

TIME-LAPSE MONITORING OF LOCALIZED
CHANGES WITHIN HETEROGENEOUS
MEDIA WITH SCATTERED WAVES

by

Kanu Chinaemerem

© Copyright by Kanu Chinaemerem, 2014

All Rights Reserved

A thesis submitted to the Faculty and the Board of Trustees of the Colorado School of Mines in partial fulfillment of the requirements for the degree of Doctor of Philosophy (Geophysics).

Golden, Colorado

Date _____

Signed: _____

Kanu Chinaemerem

Signed: _____

Dr. Roel Snieder
Thesis Advisor

Golden, Colorado

Date _____

Signed: _____

Dr. Terry Young
Professor and Head
Department of Geophysics

ABSTRACT

Time-lapse monitoring of geological and mechanical media has been the focus of various studies over the past four decades because of the information that the inferred changes within the medium provides insight into the dynamic characteristics of the medium. Time-lapse changes within a medium can be used to characterize the temporal evolution of the medium, evaluate the forces driving the changes within the medium and make predictions on the future state of the monitored medium. The detectability of the changes within a material depends on the characteristics of the change to be imaged, the sensitivity of the monitoring data to the change, and the time-lapse monitoring parameters such as the monitoring source-receiver array and the spectral content of the monitoring waves. Various time-lapse monitoring tools have been used to monitor changes within media ranging from the earth's surface to tumors within the human body. These monitoring tools include the use of 4D active surveys where an imprint of the change within the medium is extracted from the time-lapse surveys and the use of interferometric techniques that use singly or multiply scattered waves.

My major goal in this study is to image and localize changes present within a scattering medium using time-lapse multiply scattered waves generated within the monitored medium. The changes to be imaged are generally localized in space. This work is an extension of coda wave interferometry. Coda wave interferometry focuses on the identification and extraction of average velocity change occurring within a scattering medium. Due to the non-linear characteristics of multiply scattered waves and limited information of the origin of the multiply scattered waves, coda wave interferometry resolves the average velocity change within the scattering medium with no or limited indication of the location of the change. In this study, I demonstrate that time-lapse changes can be imaged and localized within scattering media using travel-time changes or decorrelation estimated from the time-lapse coda waves. The imaging algorithm is defined to invert for the location and magnitude of changes within both

statistically homogeneous and statistically heterogeneous scattering media. The imaging of the localized change requires an appropriate computation of the sensitivity of the scattered waves to the monitored change.

I develop a novel approach to compute the sensitivity kernel needed to image localized changes present within a scattering medium. I compute the sensitivity kernel, using an a-priori scattering model that has similar statistical properties as the actual medium, by computing the intensity of the scattered waves generated at both the source and the receiver locations. This approach of the kernel computation allows one to compute the sensitivity kernel for any heterogeneous scattering medium with a prescribed boundary condition. Generating the kernel with the a priori model prevents one from invoking a homogeneity assumption of the scattering model.

I apply the imaging algorithm on both numerical and laboratory experiments. The numerical experiment provides an opportunity to evaluate the resolution of the monitored change for each coda lapse time. In the laboratory experiment, I accurately resolve the change induced within two concrete blocks due to localized stress and heat changes. I also monitored velocity changes present within the subsurface beneath the Eastern section of the Basin and Range Province, Western US. Time-lapse monitoring with coda waves, generated with repeating active sources, over a period of four months suggests of the presence of a maximum velocity change of approximately 0.2% with the Eastern section of the Basin and Range Province. This observed velocity change are likely induced by the deformation within the Basin and Range Province.

TABLE OF CONTENTS

ABSTRACT	iii
LIST OF FIGURES	x
LIST OF TABLES	xxi
ACKNOWLEDGMENTS	xxii
DEDICATION	xxv
CHAPTER 1 INTRODUCTION	1
CHAPTER 2 ESTIMATION OF VELOCITY CHANGE USING REPEATING EARTHQUAKES WITH DIFFERENT LOCATIONS AND FOCAL MECHANISMS	6
2.1 Abstract	6
2.2 Introduction	6
2.3 Mathematical Consideration	8
2.4 Numerical Validation	11
2.4.1 Data processing	15
2.4.2 Effect of perturbation of source properties on the estimated velocity change	16
2.4.3 Limiting regimes of the estimations	20
2.5 Discussion and Conclusion	25
2.6 Acknowledgments	28
CHAPTER 3 A COMPARISON OF THREE METHODS FOR ESTIMATING VELOCITY CHANGES BETWEEN TIME-LAPSE MICROSEISMIC SIGNALS	29

3.1	Abstract	29
3.2	Introduction	29
3.3	Methods	30
3.3.1	Windowed cross-correlation	31
3.3.2	Stretching method	33
3.3.3	Smooth dynamic time warping	35
3.4	Real microseismic signals	36
3.5	Monitoring with downhole arrays	41
3.6	Conclusion	44
3.7	Acknowledgments	46
CHAPTER 4 NUMERICAL COMPUTATION OF THE SENSITIVITY KERNEL FOR TIME-LAPSE MONITORING WITH MULTIPLY SCATTERED ACOUSTIC WAVES		47
4.1	Abstract	47
4.2	Introduction	47
4.3	Sensitivity Kernel	50
4.4	Numerical computation	51
4.4.1	Numerical vs. analytical computation	53
4.4.2	Scattering Velocity models	58
4.4.3	Topography-induced Scattering	65
4.5	Discussion and Conclusion	72
4.6	Acknowledgments	76
CHAPTER 5 NUMERICAL COMPUTATION OF THE SENSITIVITY KERNEL FOR TIME-LAPSE MONITORING WITH MULTIPLY SCATTERED ELASTIC WAVES		77

5.1	Abstract	77
5.2	Introduction	77
5.3	Mean travel-time change in an elastic coda interferometry	79
5.4	Mean travel-time change with multiply scattered elastic intensity	80
5.5	Random isotropic scattering model	83
5.5.1	Sensitivity to perturbations in P-wave velocity	87
5.5.2	Sensitivity to perturbations in S-wave velocity	89
5.6	Heterogeneous scattering model with free-surface	92
5.6.1	Sensitivity to perturbations in P-wave velocity	95
5.6.2	Sensitivity to perturbations in S-wave velocity	99
5.7	Discussion and Conclusion	100
5.8	Acknowledgments	101
CHAPTER 6 TIME-LAPSE IMAGING OF LOCALIZED WEAK CHANGES WITH MULTIPLY SCATTERED WAVES: NUMERICAL EXPERIMENT		102
6.1	Abstract	102
6.2	Introduction	102
6.3	Theory	104
6.4	Model setup:	106
6.5	Model and Data resolution	108
6.6	Time-lapse inversion	114
6.7	Conclusions	115
6.8	Acknowledgments	117

CHAPTER 7 TIME-LAPSE IMAGING OF LOCALIZED WEAK CHANGES WITH MULTIPLY SCATTERED WAVES: LABORATORY EXPERIMENT	118
7.1 Abstract	118
7.2 Introduction	118
7.3 Theory	119
7.4 Laboratory experiment in a concrete block	121
7.5 Data analysis	130
7.6 Time-lapse inversion	133
7.7 Conclusion	137
CHAPTER 8 TIME-LAPSE MONITORING ACROSS UTAH AND EASTERN SECTION OF BASIN AND RANGE	138
8.1 Abstract	138
8.2 Introduction	138
8.3 Data processing	141
8.4 Time-lapse velocity change	145
8.4.1 Spatial distribution of velocity change	146
8.4.2 Coda time window analysis of $\langle \epsilon \rangle$	146
8.4.3 Parameter Estimation	152
8.5 Causes for the velocity changes	156
8.5.1 Seasonal loading	156
8.5.2 Local seismicity	161
8.6 Discussion and Conclusions	163
8.7 Acknowledgments	167

CHAPTER 9 CONCLUSION AND FUTURE WORK	170
REFERENCES CITED	173
APPENDIX A - THE TIME PERTURBATION DUE TO A PERTURBED SOURCE	183
APPENDIX B - VARIANCE OF THE TIME PERTURBATION	185
APPENDIX C - ERROR ESTIMATION	186
APPENDIX D - COMPARATIVE TIME SHIFT BETWEEN CHANGES IN VELOCITY AND SOURCE LOCATION	188
APPENDIX E - ANALYTICAL APPROXIMATION OF THE MODEL OF PACHECO AND SNIEDER [70]	190

LIST OF FIGURES

Figure 2.1	<p>Geometry of wave paths. Source, S_1, produces the unperturbed signal while Source, S_2, produces the perturbed signal. Path T shows the scattering path for the unperturbed signal and the scattering path for the perturbed signal is defined by Path T'. The sources are separated by a distance D and the source distances are L_T and $L_{T'}$ distance away from the first scatterer along path T and T', respectively. The unit vector \hat{r}_T defines the direction traveled by the signal before the signal first encounters a scatterer. 9</p>	9
Figure 2.2	<p>The experiment geometry of the numerical simulation. The receivers (squares) are surrounding the point scatterers (black dots). The source is positioned in the origin (cross). All perturbations of the source location is done from this position. The stations marked (NW, NE, E, SE, and SW) are used in the presentation of results in Figure 2.7 and Figure 2.8. 12</p>	12
Figure 2.3	<p>Recorded seismic signals at station E (Figure 2.2), the reference signal (red line) and the time-lapse signal (black line) with 0.4% relative velocity change (I), the time-lapse signal (black line) with $0.14\lambda_d$ source displacement (II), and the time-lapse signal (black line) with 20° source angle perturbations (III). Inset A shows the late coda while inset B shows the first arrivals of the two signals. The black bold line is the time window used for data processing. Time 0 is the source rupture time. . 14</p>	14
Figure 2.4	<p>The objective function $R(\epsilon)$ (solid line) as a function of the stretch factor ϵ. The objective function is minimum for $\epsilon = 0.4\%$, which corresponds to the time-lapse velocity change. The corresponding maximum correlation of the stretch factors is given by the dash lines. . . 17</p>	17
Figure 2.5	<p>Estimated relative velocity change for model velocity change of $\langle \frac{\delta V}{V_0} \rangle = 0.1\%$ (blue), $\langle \frac{\delta V}{V_0} \rangle = 0.2\%$ (red), $\langle \frac{\delta V}{V_0} \rangle = 0.3\%$ (black), and $\langle \frac{\delta V}{V_0} \rangle = 0.4\%$ (green). The receiver numbers are counted counter-clockwise from the W station in Figure 2.2. 18</p>	18

Figure 2.6	Estimated relative velocity change due to perturbation in the source location and the source radiation. A. The estimated velocity change for perturbed source location (divided by the dominant wavelength; inset in the top right) and B. The estimated velocity change caused by changes in source radiation angles (inset in the top right). The value of ζ is given by equation 2.15. The receiver numbers are counted counter-clockwise from the W station in Figure 2.2.	19
Figure 2.7	Estimated relative velocity change after a 0.1% velocity change and various source location perturbations (Table 2.1). The shift in the source locations are divided by the dominant wavelength λ_d of the recorded signals. For values of the source location shift greater than $\lambda_d/4$, we have incorrect estimates for the velocity change due to the distortion of the perturbed signal. Stations SW, SE, NE, and NW positions are given in Figure 2.2. The red line indicates the model (accurate) velocity change.	22
Figure 2.8	Effect of source angle perturbation on estimated velocity change. A. The estimated relative velocity changes are from a 0.1% model velocity change (Red line) and various source radiation perturbations (Table 2.2). B. The decorrelation of the doublets, due to source angle perturbations, measured by maximum cross-correlation values. Stations SW, SE, NE, and NW positions are given in Figure 2.2.	24
Figure 2.9	Source radiation pattern of the modeled earthquake sources before and after simultaneous perturbation of the source angles (strike $\Delta\phi$, rake $\Delta\lambda$ and dip $\Delta\delta$) of 20 degree each.	26
Figure 3.1	Synthetic time-lapse signals (a) and recorded microseismic time lapse signals (b). The blue curve is the baseline signal and the red curve is the time-lapse signal.	30
Figure 3.2	The stability of the windowed cross-correlation method for time shift estimation. The time shifts are estimated within time windows whose widths $2t_w$ are relative to the dominant period T of the signal: $2t_w = 37.5T$ (a), $2t_w = 75T$ (b), and $2t_w = 112.5T$ (c), where $T = 0.033$ s. . . .	32
Figure 3.3	The stability of the windowed stretching method for relative velocity change estimation. The relative velocity changes are estimated within time windows whose widths are relative to the dominant period T of the signal: $37.5T$ (a), $75T$ (b), and $112.5T$ (c), where $T = 0.033$ s. The red line shows the exact relative velocity change.	34

Figure 3.4	Time shifts and relative velocity changes estimated via SDTW. The time shifts (a) and the relative velocity changes (b) are computed from the synthetic time-lapse signals shown in Figure 3.1a. We compare the exact velocity change (red) to the estimated relative velocity changes (blue) (b).	37
Figure 3.5	Time shifts computed from the unfiltered time-lapse microseismic signals (a) using windowed cross-correlation (b), the windowed stretching method (c), and SDTW (d).	38
Figure 3.6	Time shifts computed from the 5-15Hz bandpassed time-lapse microseismic signals (a) using windowed cross-correlation (b), the windowed stretching method (c), and SDTW (d).	39
Figure 3.7	Relative velocity changes (b) computed from the 5-15Hz bandpassed time-lapse microseismic signals (a) using SDTW and multiple bounds on du/dt . Time shifts are sampled on an amplitude-aligned coarse grid (red points) (a).	41
Figure 3.8	Numerical model for time-lapse localized velocity change. The reference velocity (scattering) model (a) with the source-receiver setup, and the exact localized velocity change (b) with the source-receiver setup.	42
Figure 3.9	A comparison of the estimated time shifts (a) and relative velocity changes (b) using stretching method (black) and smooth dynamic warping (red). These timeshifts and velocity changes are estimated using the time-lapse signals for Source 2 and Receiver 3 pair shown in Figure 3.8.	43
Figure 3.10	The early (near $t = 1.6$ s) and late (near $t = 3.4$ s) coda of the time-lapse signals (a) are highlighted. Time shifts from the early coda are computed using the stretching method (b) and SDTW (c), and time shifts in the late coda are also computed using the stretching method (d) and SDTW (e). The colored lines indicate the magnitude of the estimated traveltime changes.	45
Figure 3.11	Distribution of the relative velocity changes between time-lapse signals computed using the stretching method (a) and SDTW (b) among source-receiver pairs. The velocity changes are estimated using the early part of the time-lapse coda. Blue circles are the receivers while the red circles are the sources. The blue rectangle gives the localized time-lapse velocity change of 5%. The colored lines indicate the magnitude of the estimated relative velocity changes.	46

Figure 4.1	Velocity model for numerical computation of sensitivity kernel for comparison with the analytical solution.	54
Figure 4.2	Temporal and spatial evolution of the sensitivity kernel (numerical solution).	54
Figure 4.3	Temporal and spatial evolution of the sensitivity kernel using the radiative transfer model.	55
Figure 4.4	Temporal and spatial evolution of the sensitivity kernel using the diffusion model.	56
Figure 4.5	Comparison between numerical sensitivity kernel (black line) and diffusion- (blue line) and radiative transfer- (red line) based kernel along the source- (at 2 km) receiver- (at 5 km) line.	59
Figure 4.6	Compassion of the kernel at $t = 2.0$ s using a number of scattering model realizations	60
Figure 4.7	The inline subsection (A) and the crossline subsection (B) of the kernel at $t = 2.0$ s after averaging over 1, 5, 10, and 20 realizations of the scattering model with the same statistical properties.	61
Figure 4.8	Velocity model with a vertical-fractured-like reservoir.	64
Figure 4.9	Temporal and spatial evolution of the sensitivity kernel (numerical solution) in a reservoir with vertical-fractured-like velocity perturbation with a near-surface receiver. S'' corresponds to the reflected scattered phase.	66
Figure 4.10	Temporal and spatial evolution of the sensitivity kernel (numerical solution) in a reservoir with vertical-fractured-like velocity perturbation with a receiver within the reservoir.	67
Figure 4.11	Velocity model with a shale-like reservoir.	68
Figure 4.12	Temporal and spatial evolution of the sensitivity kernel (numerical solution) in a reservoir with shale-like velocity perturbation. S'' corresponds to the reflected scattered phase.	69
Figure 4.13	Temporal and spatial evolution of the sensitivity kernel (numerical solution) in a reservoir with shale-like velocity perturbation.	70
Figure 4.14	Velocity model with variable topography.	74

Figure 4.15	Temporal and spatial evolution of the sensitivity kernel (numerical solution) showing topography-induced scattering using vertical source-receiver line.	74
Figure 4.16	Temporal and spatial evolution of the sensitivity kernel (numerical solution) showing topography-induced scattering using horizontal source-receiver line.	75
Figure 5.1	Scattering diagram illustrating the scattering interactions of the scattered waves within a scattering medium.	81
Figure 5.2	Statistically homogeneous velocity models: P-wave velocity (left) and S-wave velocity (right).	84
Figure 5.3	P-wave sensitivity kernel K_p^i of the scattered waves generated by a vertically aligned point force source for the $i = x$ component (left) and the $i = z$ component (right). The source (yellow arrow, S) is located at $[x, z] = [1.5, 1.5]km$ and the receiver (orange arrow, R) at $[x, z] = [1.5, 0.7]km$. The direction of the arrows at the source and receiver indicates the direction of the source radiation and the direction of the displacement component at the receiver, respectively. The base of the arrows are the locations of either the source or the receiver.	85
Figure 5.4	The P-wave intensity fields used for the kernel computation at travel-time $0.35 s$ in the statistically homogeneous model (Figure 5.2). Top: The source intensity field due to a vertical point force located at $[x, z] = [1.5, 1.5]km$ (yellow arrow, S). Middle: The receiver intensity field due to a horizontal point force located at $[x, z] = [1.5, 0.7]km$ (orange arrow) for the x-component kernel. Bottom: The receiver intensity field due to a vertical point force located at $[x, z] = [1.5, 0.7]km$ (orange arrow) for the z-component kernel. The direction of the arrow at the source indicates the direction of the source radiation and at the receiver indicates the direction of the displacement component at the receiver. The base of the arrows are the locations of either the source or the receiver.	86

Figure 5.5	The S-wave intensity fields used for the kernel computation at travel-time 0.35 s in the statistically homogeneous model (Figure 5.2). Top: The source intensity field due to a vertical point force located at $[x, z] = [1.5, 1.5]km$ (yellow arrow, S). Middle: The receiver intensity field due to a horizontal point force located at $[x, z] = [1.5, 0.7]km$ (orange arrow) for the x-component kernel. Bottom: The receiver intensity field due to a vertical point force located at $[x, z] = [1.5, 0.7]km$ (orange arrow) for the z-component kernel. The direction of the arrows at the source and receiver indicates the direction of the source radiation and the direction of the displacement component at the receiver, respectively. The base of the arrows are the locations of either the source or the receiver.	89
Figure 5.6	S-wave sensitivity kernel K_s^i of the scattered waves generated by a vertically aligned point force source for the $i = x$ component (left) and the $i = z$ component (right). The source (yellow arrow, S) is located at $[x, z] = [1.5, 1.5]km$ and the receiver (orange arrow, R) at $[x, z] = [1.5, 0.7]km$. The direction of the arrows at the source and receiver indicates the direction of the source radiation and the direction of the displacement component at the receiver, respectively. The base of the arrows are the locations of either the source or the receiver.	90
Figure 5.7	Heterogeneous velocity models with free surface: P-wave velocity (left) and S-wave velocity (right).	93
Figure 5.8	The P-wave intensity fields used for the kernel computation at travel-time 0.25 s in the statistically heterogeneous model (Figure 5.7). Top: The source intensity field due to a vertical point force located at $[x, z] = [1.0, 0.25]km$ (yellow arrow, S). Middle: The receiver intensity field due to a horizontal point force located at $[x, z] = [2.0, 0.25]km$ (orange arrow) for the x-component kernel. Bottom: The receiver intensity field due to a vertical point force located at $[x, z] = [2.0, 0.25]km$ (orange arrow) for the z-component kernel. The direction of the arrows at the source and receiver indicates the direction of the source radiation and the direction of the displacement component at the receiver, respectively. The base of the arrows are the locations of either the source or the receiver.	94

Figure 5.9	P-wave sensitivity kernel K_p^i of the scattered waves generated by a vertically aligned point force source for the $i = x$ component (left) and the $i = z$ component (right). The source (yellow arrow, S) is located at $[x, z] = [1.0, 0.25]km$ and the receiver (orange arrow, R) at $[x, z] = [2.0, 0.25]km$. The direction of the arrows at the source and receiver indicates the direction of the source radiation and the direction of the displacement component at the receiver, respectively. The base of the arrows are the locations of either the source or the receiver.	96
Figure 5.10	The S-wave intensity fields used for the kernel computation at travel-time 0.25 s in the statistically heterogeneous model (Figure 5.7). Top: The source intensity field due to a vertical point force located at $[x, z] = [1.0, 0.25]km$ (yellow arrow, S). Middle: The receiver intensity field due to a horizontal point force located at $[x, z] = [2.0, 0.25]km$ (orange arrow) for the x-component kernel. Bottom: The receiver intensity field due to a vertical point force located at $[x, z] = [2.0, 0.25]km$ (orange arrow) for the z-component kernel. The direction of the arrows at the source and receiver indicates the direction of the source radiation and the direction of the displacement component at the receiver, respectively. The base of the arrows are the locations of either the source or the receiver.	97
Figure 5.11	S-wave sensitivity kernel K_s^i of the scattered waves generated by a vertically aligned point force source for the $i = x$ component (left) and the $i = z$ component (right). The source (yellow arrow, S) is located at $[x, z] = [1.0, 0.25]km$ and the receiver (orange arrow, R) at $[x, z] = [2.0, 0.25]km$. The direction of the arrows at the source and receiver indicates the direction of the source radiation and the direction of the displacement component at the receiver, respectively. The base of the arrows are the locations of either the source or the receiver.	98
Figure 6.1	Sensitivity kernel $K(\mathbf{s}, \mathbf{x}_o, \mathbf{r}, t)$ for the source-receiver pair (S-R) within a statistical homogeneous scattering velocity model.	105
Figure 6.2	Numerical model for time-lapse inversion of localized velocity change with the used sources (red circles) and receivers (blue circles). Top: the reference velocity (scattering) model with the source-receiver setup and Bottom: the true localized velocity change with the source-receiver setup.	107
Figure 6.3	Azimuthal dependence of the estimated velocity change due to a Gaussian positive velocity change along the source-receiver pair at azimuth 90^0 (red line). The figure panels are the estimated velocity changes at various coda lapse times measured by the the transport mean free time t^* of the scattering model.	109

Figure 6.4	The model geometry use for data averaging test. A Gaussian velocity change is centered at location $[x, z] = [3, 5]$ km within a statistically homogeneous velocity model. The data averaging test used a ring of receivers (black dots) and s source (blue dot) located at $[x, z] = [5, 5]$ km. The azimuth of the receivers is specified by the degrees. The yellow arrow points to the location of the velocity change.	109
Figure 6.5	The coda time windows use for resolution analysis for the time-lapse imaging. Top: The used time windows for Category 1 resolution analysis and Bottom: The used time windows for Category 2 resolution analysis.	111
Figure 6.6	The point spread function \mathbf{p}^i for the inverted model at $[x, z] = [5, 3]$ km using the Top: Category 1 and Bottom: Category 2 time-windows. The point spread function \mathbf{p}^i uses time-windows: I (black window), II (red window), III (blue window), IV (green window), and V (yellow window) in Figure 6.5.	112
Figure 6.7	Data spread function for the inverted model using the Top: Category 1 time-windows and Bottom: Category 2 time-windows. Each value is an estimated fractional velocity change for a given source-receiver pair. . .	113
Figure 6.8	Inverted fractional velocity change using various coda time windows. Top inset: a typical recorded coda signal with time windows use to invert the velocity changes. Inverted velocity change in A: with black time window, B: with red time window, C: with blue time window, and D. with green time window. The black box shows the extent of the velocity change.	116
Figure 7.1	Schematic of the 3D concrete block for time-lapse monitoring	122
Figure 7.2	Outline of the 3D concrete block with the locations of the used transducers. The transducers are embedded within the concrete block. The transducer locations are the projection along the z-axis (left) and along the x-axis (right).	122
Figure 7.3	The electrical and mechanical setup of the stress loading experiment. . .	123
Figure 7.4	Typical time-lapse coda signals recorded at transducer 17 due to a source at transducer 16 from the stress loading experiment. The black ellipse indicate the electrical signal use to book-keep the source unset time.	124

Figure 7.5	The pictorial (Top) and the schematics (bottom) of the concrete block use for the time-lapse temperature monitoring experiment. The cyan line gives the heating cartridge probe.	125
Figure 7.6	The electrical and mechanical setup of the stress loading experiment. . .	126
Figure 7.7	Typical coda signal recorded by sensor R5 due to a source at sensor S1 from the temperature experiment.	126
Figure 7.8	Temperature history of the time-lapse heating experiment. The question mark indicates that the temperature curve between 1:11pm (4 th of April) and 8am (5 th of April) is unknown.	127
Figure 7.9	Normalized temperature distribution across the heated concrete medium at the end of the temperature history in Figure 7.8 using equation 7.10. The cyan line is the heating cartridge probe.	129
Figure 7.10	Record of the estimated time-lapse decorrelation due to a load jump from 5 <i>kN</i> to 10 <i>kN</i> (left) and a load jump from 5 <i>kN</i> to 15 <i>kN</i> (right). The record contains 90 traces (due to 10 pairs of sensors with no trace for the same sensor combination). The records are arranged according to the source sensor records.	131
Figure 7.11	Record of the estimated time-lapse relative velocity change in % due to a load jump from 5 <i>kN</i> to 10 <i>kN</i> (left) and a load jump from 5 <i>kN</i> to 15 <i>kN</i> (right). The record contains 90 traces (due to 10 pairs of sensors with no trace for the same sensor combination). The records are arranged according to the source sensor records.	131
Figure 7.12	Time-lapse decorrelation due to stress loading from 5 <i>kN</i> to 10 <i>kN</i> (left) and from 5 <i>kN</i> to 15 <i>kN</i> (right) at X. The colored lines between two sensors are the estimated average decorrelation between the time lapse signals using equation	132
Figure 7.13	Time-lapse fractional velocity change (%) and decorrelation due to temperature change within the concrete block. The colored lines between two sensors are the estimated changes (fractional velocity change (left) and decorrelation (left)) between the time lapse signals for the time-window in time-lapse coda (top). The changes for each sensor pairs are not restricted to the connecting colored lines.	133
Figure 7.14	Inverted change due to stress loading from 5 <i>kN</i> to 10 <i>kN</i> (left) and from 5 <i>kN</i> to 15 <i>kN</i> (right) at X. Top inset: Time-lapse coda showing the time-window used for the inversion.	135

Figure 7.15	Inverted change due to localized temperature change due to a heating cartridge at H (Figure Figure 7.5 (Bottom)) using the travel-time changes and decorrelation estimated at the coda time window (black rectangle) in Top inset. In the Bottom inset: (left) the inverted relative velocity change (in percentage) using estimated travel-time changes and (right) the inverted change in the scattering cross-section (in m^2) using estimated decorrelation.	136
Figure 8.1	USArray transportable array given by the red squares. The location of the explosion (source) is given by the yellow star. The blue and the green squares give the locations of the groundwater wells and the GPS stations, respectively.	140
Figure 8.2	Example recording of typical blast events. Event 09/10/2007 recorded at station L13A. The three components, N-S (blue), Up-Down (U-D) (red) and the E-W (black) are all used in the time-lapse analysis.	142
Figure 8.3	Typical recordings of the blast events bandpass filtered between 1-5 Hz. The three components, N-S (blue), Up-Down (U-D) (red) and the E-W (black) are all used in the time-lapse analysis. The black rectangle gives the coda section of the blast signal.	143
Figure 8.4	A typical time-lapse coda of the 1-5 Hz filtered recorded blast events for the Up-Down (U-D) component.	145
Figure 8.5	The cumulative relative velocity changes expressed in percentages for N-S (red), Up-Down (U-D) (green) and the E-W (black) components. Here the average is computed using all the stations in the USArray displayed in Figure 8.1. Missing first five estimates in Case 3 is because only signals from August 1 is processed in Case 3.	147
Figure 8.6	Relative velocity changes in % estimated from the 8 blast doublets using vertical component of the stations. The blue points are the surface stations. The source location is the point where all the colored lines meet. The color lines are the estimated percentage velocity changes for each source-receiver pair.	148
Figure 8.7	The relative velocity change estimated for each of the time-lapse periods as a function of source-receiver distance. Power law fitting of the estimated velocity changes in Utah Wasatch fault region. Fit E-W, N-S, and U-D are the fitting solutions for the estimated velocity changes of E-W, N-S, and U-D components, respectively.	149

Figure 8.8	Estimated velocity change difference Δ_T for each time-lapse period. The plots show the estimated velocity change difference Δ_T versus the source-receiver distance for the A: N-S component, B: Up-Down (U-D) component, and C: N-S component.	150
Figure 8.9	Estimated velocity change $\langle \epsilon \rangle$ versus time in the coda for each time-lapse period using the N-S component (top), the Up-Down (U-D) component (middle), and the E-W component (bottom).	151
Figure 8.10	Dependence of the estimated velocity change on the dimensionless parameter η . The definition of η is given in equation 6. The black rectangle corresponds to the range of velocity changes estimated with station J13.	153
Figure 8.11	Correlation of average velocity change with groundwater level change measured in meters (positive meters mean deepening of the groundwater level). Each plot shows the fit of the average velocity changes from the three signal components. S1 to S9 are the names of the groundwater wells.	157
Figure 8.12	Linear regression between the E-W strain derived from E-W GPS detrended displacement and the individual components of average velocity change (E-W, N-S, and vertical components). The linear regression is computed using A, all the available GPS displacement, B, only the Basin and Range GPS displacements, C, only the Wasatch fault displacements, and D, only the Snake River Plain GPS displacements.	159
Figure 8.13	Comparison of the peak ground acceleration (PGA) with average relative velocity change estimated in Case 2. The PGA values are estimated from the local seismicity ($M > -0.36$) that occurred during the monitored time-lapse period. The PGA values are estimated using relationship between PGA and the magnitude of an earthquake Chiou et al.	162
Figure 8.14	Increased sensitivity due to the presence of Moho interface at depth 25km based on the ratio of the volume integral of the sensitivity kernel with and without the Moho interface.	165

LIST OF TABLES

Table 1.1	Summary of my contributions and the contributions of my co-authors to my dissertation.	4
Table 2.1	Modeling parameters for shift in the source location.	21
Table 2.2	Modeling parameters for source radiation perturbation.	23
Table 7.1	Transducer coordinates.	123
Table 8.1	Estimated model parameters using the inverse R relation.	168
Table 8.2	Goodness of fit between average relative velocity changes and groundwater (GWL) subsidence based on the R^2 value (Case 2).	169
Table 8.3	Goodness of fit between average relative velocity changes and seasonal variation of (detrended) GPS displacement based on the R^2 value (Case 2).	169
Table 8.4	Goodness of fit between relative velocity change and PGA based on the R^2 value (Case 2).	169

ACKNOWLEDGMENTS

If I have seen further it is by standing on ye sholders of Giants. The accomplishment of this dissertation echoes these words from Isaac Newton. The progress in earning my graduate degree and in the completion of this thesis work has been the result of a huge amount of support I have received along the way. I doubt the space here is enough to show my true appreciation and thanks to all who have supported, encouraged, and inspired me.

First, I am grateful to my advisor Dr. Roel Snieder. I first met him briefly during the CWP meeting at the 2009 SEG Annual meeting in Houston. Then, I came to scout some of the research groups I was interested in applying to. He was one of those I met on that day that made me feel comfortable applying to CWP. I later met him again on my first day at CWP with Yuanzhong Fan (a CWP alumnus), who introduced me to him. I did receive my first dose of Roel's jokes during this meeting, some of them I still remember. He's that kind of person. He has always been encouraging and funny, even as he demanded the best from me. I believe I have grown in no small way because of his guidance. This growth includes the way I now tackle scientific problems and improvement in my communication skills. I don't think I am yet where I need to be, but his tutoring gives me the right foundation as I move forward.

I am grateful to Roel for the opportunity he gave me to work on diverse research projects. While with him, I have had the opportunities to work with both real and numerical data, work on both individual and collaborative projects, and acquire research experience in a couple of oil companies through internships. A lot of these opportunities have come from his ability to both guide me in the right direction through his suggestions and to give me the freedom to pursue projects that I have interest in. His guidance and relationship I will still highly regard even beyond my PhD studies. I am also grateful to the wonderful research minds of Dan O'Connell, Kristine Pankow, Ernst Niederleithinger, and Andrew Muñoz,

whom I had the opportunity to work with. Our discussions have enormously enriched me personally and in my thesis work.

I thank the members of my thesis committee - Dr. Masami Nakagawa, Dr. Paul Sava, Dr. Thomas Davis, Dr. David Wald and Dr. Michael Walls - for all their guidance and revision of my thesis work. A lot of the advice I have received both during my defenses and our one-on-one meetings have been useful to improve the quality of this dissertation. I am also grateful for their encouragement during the difficult time of the thesis process. I ever remain grateful. My regard also goes to the faculty and students of CWP and the Geophysics Department in general. I am grateful for colleagues and friends who in no small ways have made the last four years wonderful. The diversity both in research interests and personal backgrounds was what drew my interest to this research group. I wasn't disappointed but rather gained far more than I could imagine. CWP's demand on its students to develop into well-rounded scientists in terms of the content of their research, the communication of their work, and direct interaction with the big players in industry is unmatched. Fan, my official graduate buddy the year I joined CWP, deserves credit. He was my first contact with CWP during our SEG/Exxonmobil SEP program. I later learned that his recommendation was instrumental to my joining CWP as a graduate student. Fan, thank you.

Diane Witters, I am really grateful for your help with all the writing, communication, and pronunciation skills. My meetings with Diane opened my eyes to the nuances of technical writing, made me aware of the common mistakes I make, and helped me work on the clarity of my oral delivery. Although I am far from where she will want me to be at mastering these skills, I now have the confidence to critically evaluate my own writing and communication. I am at times amazed at her patience. Thank you, Diane, for your help and encouragement which have, in a lot of ways, made this dissertation a reality. I am also grateful to Pamela Kraus, Shingo Ishida, John Stockwell and Michelle Szobody for their help with administrative details surrounding my PhD studies which have allowed me to concentrate on my research.

My journey through graduate school started when Dr. G. U. Chukwu, one of my undergraduate lecturers, pointed my attention to the scholarship program in Earth System Physics at International Center for Theoretical Physics (ICTP), Italy. This opportunity opened the door to the rest of my graduate studies. I am immensely grateful to him for his foresight.

I am really grateful to my parents and sisters back in Nigeria. Their patience with me throughout all the process of graduate school since I left home about seven years ago cannot be matched. I am sincerely grateful for their prayers, belief, support, jokes, and stories. I do own them all.

To Almighty God

CHAPTER 1

INTRODUCTION

Time-lapse monitoring tools in geophysics provide ways for monitoring changes within the earth, geomechanical structures, and mechanical structures. The information inferred from the observed changes can be used to describe various geomechanical or mechanical processes, such as fluid migration and geological or structural deformations, within the medium in which the change occurs. Time-lapse monitoring is used in petroleum engineering activities such as in hydrocarbon production and fluid injection [22, 43], in global seismology such as for monitoring volcanic activities [56, 88] and for preseismic to post-seismic deformations near and far away from fault rupture zones [16, 117], in geohazard evaluations such as for monitoring stress changes in the near surface [62, 89] and in monitoring mechanical structures like cracks or defects in buildings, roads, and machines [31, 100]. Various monitoring methods and tools are used for characterizing time-lapse changes. These monitoring tools differ from one disciplinary field to another depending on what the monitoring objectives are.

The challenge of monitoring with seismic waves depends, in general, on whether the waves are transmitted, singly scattered, or multiply scattered within the scattering medium. Usually the complexity of the waves with respect to the scattering medium increases from transmitted waves (direct or diving waves) to the multiply scattering waves. However, increased scattering of the waves within the scattering medium usually provides better illumination of the scattering medium [26, 28], additional redundancy that is useful for improving the resolution and increasing the signal-to-noise ratio of images [8, 9], and increased sensitivity of the waves to changes within the scattering medium [97, 108]. Coda wave interferometry provides a means of monitoring weak changes with multiply scattered waves, especially changes which are poorly detected by singly scattered waves [76]. The challenge in using

multiply scattered waves for monitoring weak and localized time-lapse changes, in order to take advantage of their increased sensitivity, is to develop a relatively cheap and efficient way of imaging the time-lapse changes with multiply scattered waves.

In this dissertation, I work with both numerical and field-collected multiply scattered waves (coda waves), which I use to study the capability of monitoring and imaging weak localized time-lapse changes within scattering media. The scattering media to which we apply this work cover a wide range of structures from the geological subsurface to mechanical structures. Specifically, we use scattered waves generated within the earth's subsurface for time-lapse monitoring of the eastern part of the Basin and Range in the western US (Chapter 8) and ultrasonic waves generated within heterogeneous concrete blocks for time-lapse monitoring of localized changes within the blocks due to either stress or temperature changes (Chapters 6 and 7). We also perform a number of numerical tests to characterize other scattering media.

In Chapter 2, I explore the use of time-lapse scattered waves generated by repeating sources with varying source properties; specifically, I analyze the impact of differences in their locations and focal mechanisms. The focus in this chapter is to characterize the limits of the repeating sources generating the time-lapse scattered waves; the repeating sources we can use for monitoring time-lapse velocity changes within a scattering medium. Understanding these limits allows us to pick sources for the time-lapse scattered waves within a pre-defined region and a range of source radiation angles, without working under the strong restriction of using perfectly repeating scattering signals. This is vital in cases where we have limited control over the sources such as when using the coda from earthquakes or microseismic events for time-lapse monitoring. I use simple numerical models with a homogeneous distribution of scatterers and a uniform time-lapse velocity change in the scattering models. I define a limiting criterion for selecting the maximum allowable distance between the repeating sources, and suggest the use of the maximum cross-correlation of the time-lapse coda as a proxy for the error due to the deviation in the source radiation angles.

The backbone of this dissertation lies in characterizing and localizing changes within a scattering medium, i.e. the changes are localized in space and are weak within the time-lapse monitoring period. Using multiply scattered waves, I develop an algorithm that images localized changes within heterogeneous media. Chapters 4 and 5 describe the sensitivity of time-lapse changes within the coda waves to changes within a heterogeneous medium using either acoustic and elastic intensity fields, respectively. Pacheco and Snieder [70] and Rossetto et al. [82], using a statistical formulation and the ladder approximation, respectively, provide similar sensitivity kernels relating time-lapse changes within the coda waves to the changes in the scattering medium. In Chapters 4 and 5, I suggest a novel approach to compute the sensitivity kernel which is based on the adjoint method [25]. This approach allows for the computation of the sensitivity kernel for an arbitrary scattering medium. The adjoint method for the computation of the sensitivity kernel, which involves the simulation of the source and receiver intensity fields, provides an efficient means of computing the sensitivity kernel in models with inhomogeneities both in the background model and scattering properties. The models can include anisotropic scattering structures and free surface conditions. This ability to compute the sensitivity kernel for a generic model has an advantage over other methods of kernel computation that assume statistical homogeneity of the scattering model.

In Chapters 6 and 7, I apply the imaging algorithm I developed to localizing weak changes within heterogeneous media to numerical and laboratory time-lapse experiments. In the numerical experiment, I explore imaging a localized time-lapse velocity change within a statistically heterogeneous model using finite-difference generated intensity fields and applying the adjoint method [25]. In Chapter 7, I extend the imaging algorithm to two laboratory time-lapse experiments. One experiment images changes within a concrete block due to a localized compressive stress applied to adjacent faces of the concrete block; the second experiment, images changes due to a localized temperature change within a heterogeneous concrete block.

A vital part of the work in this dissertation involves the extraction of the time-lapse changes (travel-time shifts) within the multiply scattered waves. In Chapter 3, I explore the use of dynamic time warping (DTW) algorithm [35] for time shift extractions in order to characterize their strengths and weaknesses in regard to time-lapse monitoring of the weak changes within scattering media. I compared the DTW algorithm with two existing methods (time-shift cross-correlation and stretching methods) for estimating travel-time change within time-lapse coda waves. In Chapter 8, I apply coda wave interferometry to monitor time-lapse velocity changes within the subsurface beneath the eastern flank of the Basin and Range. This region is an actively deforming region of the western US and the study suggests a consistent velocity change of less than 0.2 % within a time period of 5 months. Comparison of the velocity changes with temporal variation of the E-W strain suggests that the velocity change is driven by the extensional deformation within Basin and Range.

Table 1.1: Summary of my contributions and the contributions of my co-authors to my dissertation.

Chapter	My contribution	Contribution of others
2	Define sensitivity analysis and conducted numerical analysis	Discussion on monitoring with micro-seismicity with Dan O’Connell
3	Develop cross-correlation/stretching codes	Andrew Munoz developed (S)-DTW codes
7	Develop inversion code and doing inversions	Setup of laboratory experiment and time-lapse data collection by S.Grothe and E. Niederleithinger (BAM).
8	Data analysis, code development and analytical/numerical analysis	Collection of time-lapse data via IRIS and GPS measurements by K. Pankow.
4/5/6	Develop novel computation of sensitivity kernel, code development, and numerical analysis	

My contribution to the field of geophysics and time-lapse monitoring via this dissertation, is the development and implementation of an approach to image localized and weak changes present within statistically heterogeneous media using multiply scattered waves. The changes my imaging algorithm provides spatial resolution to include velocity changes within volca-

noes, geomechanical perturbations within stimulated or depleting hydrocarbon reservoirs, changes in the thermal properties of an enhanced geothermal system (EGS), defects within mechanical structures and tumors within the human body. I developed the theoretical and the numerical background of all the studies presented in this dissertation. Table 1.1 gives a brief description of the contributions of my co-authors. I used the Madagascar open-source software package (<http://www.ahay.org>) to develop the numerical codes I used to compute the sensitivity kernels. Other codes I used for data analysis, various numerical tests and inversion, I developed using the MATLAB software.

The work in this dissertation is, or will be, documented in the following publications:

Chapter 2: Kanu, C.O., R. Snieder, and D. O’Connell (2013), Estimation of velocity change using repeating earthquakes with different locations and focal mechanisms, *J. Geophys. Res. Solid Earth*, 118, 29052914, doi:10.1002/jgrb.50206.

Chapter 4: Kanu, C.O., and R. Snieder, Numerical computation of the sensitivity kernel for time-lapse monitoring with multiply scattered acoustic waves, *Geophysical Journal International*. (*submitted*).

Chapter 5: Kanu, C. O., and R. Snieder, Numerical computation of the sensitivity kernel for time-lapse monitoring with multiply scattered elastic waves, *Geophysical Journal International*. (*submitted*).

Chapter 6: Kanu, C. O., and R. Snieder, Time-lapse imaging of localized weak changes with multiply scattered waves: Numerical experiment, *Journal Geophysical Research* (*submitted*).

Chapter 7: Kanu, C. O., R. Snieder, E. Niederleithinger, and S. Grothe, Time-lapse imaging of localized weak changes with multiply scattered waves: Laboratory experiment, *Ultrasonics* (*submitted*).

Chapter 8: Kanu, C., R. Snieder, and K. Pankow (2014), Time-lapse monitoring of velocity changes in Utah, *J. Geophys. Res. Solid Earth*, 119, doi:10.1002/2014JB011092.

CHAPTER 2

ESTIMATION OF VELOCITY CHANGE USING REPEATING EARTHQUAKES WITH DIFFERENT LOCATIONS AND FOCAL MECHANISMS

Chinaemerem O. Kanu¹, Roel Snieder¹ and Dan O’Connell²

Published in Journal Geophysical Research (2013)

2.1 Abstract

Codas of repeating earthquakes carry information about the time-lapse changes in the subsurface or reservoirs. Some of the changes within a reservoir change the seismic velocity and thereby the seismic signals that travel through the reservoir. We investigate, both theoretically and numerically, the impact of the perturbations in seismic source properties of used repeating earthquakes on time-lapse velocity estimation. We derive a criterion for selecting seismic events that can be used in velocity analysis. This criterion depends on the dominant frequency of the signals, the centertime of the used time window in a signal, and the estimated relative velocity change. The criterion provides a consistent framework for monitoring changes in subsurface velocities using microseismic events and the ability to assess the accuracy of the velocity estimations.

2.2 Introduction

Monitoring temporal changes within the Earth’s subsurface is a topic of interest in many areas of geophysics. These changes can result from an earthquake and its associated change in stress [16], fluid injection or hydrofracturing [22], and oil and gas production [116]. Some of the subsurface perturbations induced by these processes include temporal and spatial velocity changes, stress perturbations, changes in anisotropic properties of the subsurface, and

¹Center for wave phenomena, Colorado School of Mines

²Fugro Consultants, Inc., William Lettis Associates Division, Lakewood, CO 80401

fluid migration. Many of these changes span over a broad period of time and might even influence tectonic processes, such as induced seismicity [117]. For example, Kilauea, Hawaii (which erupted in November 1975) is suggested to have triggered a magnitude 7.2 earthquake within a half hour of the eruption [47]. A seismic velocity perturbation of the subsurface leads to progressive time shifts across the recorded seismic signals. Various methods and data have been used to resolve the velocity perturbations. These methods include seismic coda wave interferometry [97], doublet analysis of repeating microseismic and earthquake codas [76], time-lapse tomography [107], and ambient seismic noise analysis [12, 16, 58, 88, 111]. Earthquake codas have higher sensitivity to the changes in the subsurface because multiple scattering allows these signals to sample the area of interest multiple times. However, there are inherent challenges in the use of these signals. Doublet analysis of the earthquake (microseismic) codas requires repeating events. Failure to satisfy the requirement that the events are identical can compromise the accuracy of the estimated velocity changes. In this study, we focus on the estimation of velocity changes using codas of repeating earthquakes that are not quite identical in their locations and source mechanisms.

Fluid-triggered microseismic events often are repeatable, but in practice events occur at slightly different positions with somewhat different source mechanisms [30, 59, 85]. Changes in the source properties might result from coseismic stress changes [5] or changes in the properties of the event rupture locations [57]. Imprints of the source perturbation and the velocity change on the seismic waveforms can be subtle. Therefore, we will need to ask, how do the source location, source mechanism, and subsurface perturbations affect the estimated velocity changes? Snieder [96] shows that we can retrieve velocity changes from the coda of the waveforms recorded prior to and after the change. Robinson et al. [79] develop a formulation using coda wave interferometry to estimate changes in source parameters of double-couple sources from correlation of the coda waves of doublets. Snieder and Vrijlandt [99], using a similar formulation, relate the shift in the source location to the variance of the travel time perturbations between the doublet signals. In all these studies, the authors

assume that the expected (average) change in travel time of the coda (due to either changes in the source locations or source mechanisms) is zero.

In this study, we investigate the impact of changes in source properties on the estimation of relative velocity changes. Knowledge of the impact of these perturbations on the estimated velocity change allows for a consistent framework for selecting pairs of earthquakes or microearthquakes used for analyzing the velocity changes. This results in a more robust estimation of velocity change. In Section 2.3, we explore the theoretical relationships between the velocity changes and perturbations in the earthquake source properties. Following this section is a numerical validation of the theoretical results. We explain the implications and limitations of our results in Section 2.5. In the appendices, we explain the mathematical foundation of our results in this study.

2.3 Mathematical Consideration

In this section, we use the time-shifted cross-correlation [96, 97] to develop an expression for the average value of the time perturbation of scattered waves that are excited by sources with varying source properties. This perturbation is due to changes in the velocity of the subsurface and to changes in the source properties. These changes, we assume, may occur concurrently. Figure 2.1 is a schematic figure showing the general setup of the problem we are investigating. Two sources (S_1 and S_2) represent a doublet (repeating seismic events). These events occur at different locations and may have different rupture patterns. We assume that these events can be described by a double couple. We investigate the ability of using the signals of these sources for time-lapse monitoring of velocity changes, assuming that these sources occur at different times. We express the signals of the two sources as unperturbed and perturbed signals, where the perturbation refers to any change in the signal due to changes within the subsurface and/or the source properties.

The unperturbed seismic signal $U(t)$ is given as

$$U(t) = A \sum_T U^{(T)}(t) \quad (2.1)$$

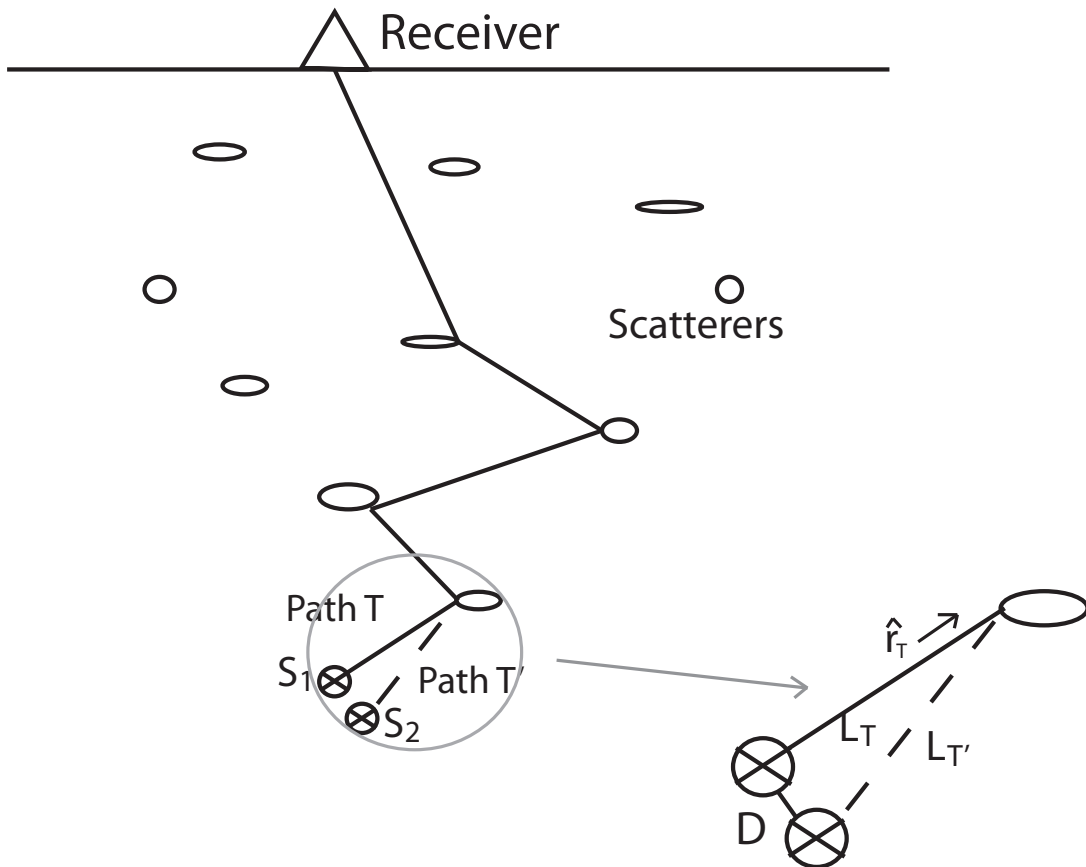


Figure 2.1: Geometry of wave paths. Source, S_1 , produces the unperturbed signal while Source, S_2 , produces the perturbed signal. Path T shows the scattering path for the unperturbed signal and the scattering path for the perturbed signal is defined by Path T' . The sources are separated by a distance D and the source distances are L_T and $L_{T'}$ distance away from the first scatterer along path T and T' , respectively. The unit vector \hat{r}_T defines the direction traveled by the signal before the signal first encounters a scatterer.

and the perturbed seismic signal $\hat{U}(t)$ is given as

$$\hat{U}(t) = \hat{A} \sum_T (1 + \zeta^{(T)}) U^{(T)}(t - t_p^T), \quad (2.2)$$

where A and \hat{A} are the amplitudes of the unperturbed and perturbed source signals, respectively. These amplitudes represent the strengths of the sources. The recorded waves are a superposition of wave propagation along all travel paths as denoted by the summation over paths T . The change in the source focal mechanism only affects the amplitude of the wave traveling along each trajectory T because the excitation of waves by a double couple is real [2]. The change in the signal amplitudes - due to changes in the source mechanism angles - is defined by $\zeta^{(T)}$ for path T , and t_p^T is the time shift on the unperturbed signal due to the medium perturbation for path T . The change in the signal amplitudes along path T depends on the source radiation angles. In this study, we assume that the medium perturbation results from the velocity change within the subsurface and changes in the source properties. The time-shifted cross-correlation of the two signals is given as

$$C(t_s) = \int_{t-t_w}^{t+t_w} U(t') \hat{U}(t' + t_s) dt', \quad (2.3)$$

where t is the centertime of the employed time window and $2t_w$ is the window length. The normalized time-shifted cross-correlation $R(t_s)$ can be expressed as follows:

$$R(t_s) = \frac{\int_{t-t_w}^{t+t_w} U(t') \hat{U}(t' + t_s) dt'}{(\int_{t-t_w}^{t+t_w} U^2(t') dt' \int_{t-t_w}^{t+t_w} \hat{U}^2(t') dt')^{\frac{1}{2}}}. \quad (2.4)$$

The time-shifted cross-correlation has a maximum at a time lag equal to the average time perturbation ($t_s = \langle t_p \rangle$) of all waves that arrive in the used time window [96]:

$$\left. \frac{\partial C(t_s)}{\partial t_s} \right|_{(t_s = \langle t_p \rangle)} = 0. \quad (2.5)$$

Equation 2.5 allows for the extraction of the average travel-time perturbation from the cross-correlation. In this study, the average of a quantity f is a normalized intensity weighted sum of the quantity [96]:

$$\langle f \rangle = \frac{\sum_T A_T^2 f_T}{\sum_T A_T^2}, \quad (2.6)$$

where $A_T^2 = \int (U^T(t'))^2 dt'$ is the intensity of the wave that has propagated along path T .

We show in Appendices A and B that the expected value of the time perturbation and its variance are given by

$$\langle t_p \rangle = - \left\langle \frac{\delta V}{V_o} \right\rangle t \quad (2.7)$$

and

$$\sigma_t^2 = \langle t_p^2 \rangle - \langle t_p \rangle^2 \simeq \frac{D^2}{3V_0^2}. \quad (2.8)$$

In the above equations, $\langle \delta V/V_0 \rangle$ is the average relative velocity change, D is the shift in the source location, and V_0 is the unperturbed velocity of a wave mode. This result is applicable to any wave mode. Equation 2.7 suggests that the average time shift in the multiple scattered signals depends only on the velocity changes within the subsurface. The variance of the time shifts depends, however, on the perturbations of the source location.

2.4 Numerical Validation

We test the equations in section 2.3 with a numerical simulation using Foldy's multiply scattering theory [27] described by Groenenboom [32]. The theory models multiple scattering of waves by isotropic point scatterers. We conduct our numerical experiments using a circular 2D geometry (Figure 2.2) with point scatterers surrounded by 96 receiver stations. We uniformly assign the imaginary component of the scattering amplitude $ImA = -4$ to all the scatterers. In 2D, this is the maximum scattering strength that is consistent with the optical theorem that accounts for conservation of energy [32]. The wave radiated by the earthquakes is modulated by the far-field P-wave radiation pattern F^P :

$$U_0(\mathbf{r}) = F^P G^{(0)}(\mathbf{r}, \mathbf{r}_s), \quad (2.9)$$

where $G^{(0)}(\mathbf{r}, \mathbf{r}_s)$ is the green's function between the source location \mathbf{r}_s and any other point \mathbf{r} . In 2D, where the take-off direction is restricted within the 2D plane, F^P is given as [2]

$$F^P = \cos \lambda \sin \delta \sin 2(\psi - \phi) - \sin \lambda \sin 2\delta \sin^2(\psi - \phi), \quad (2.10)$$

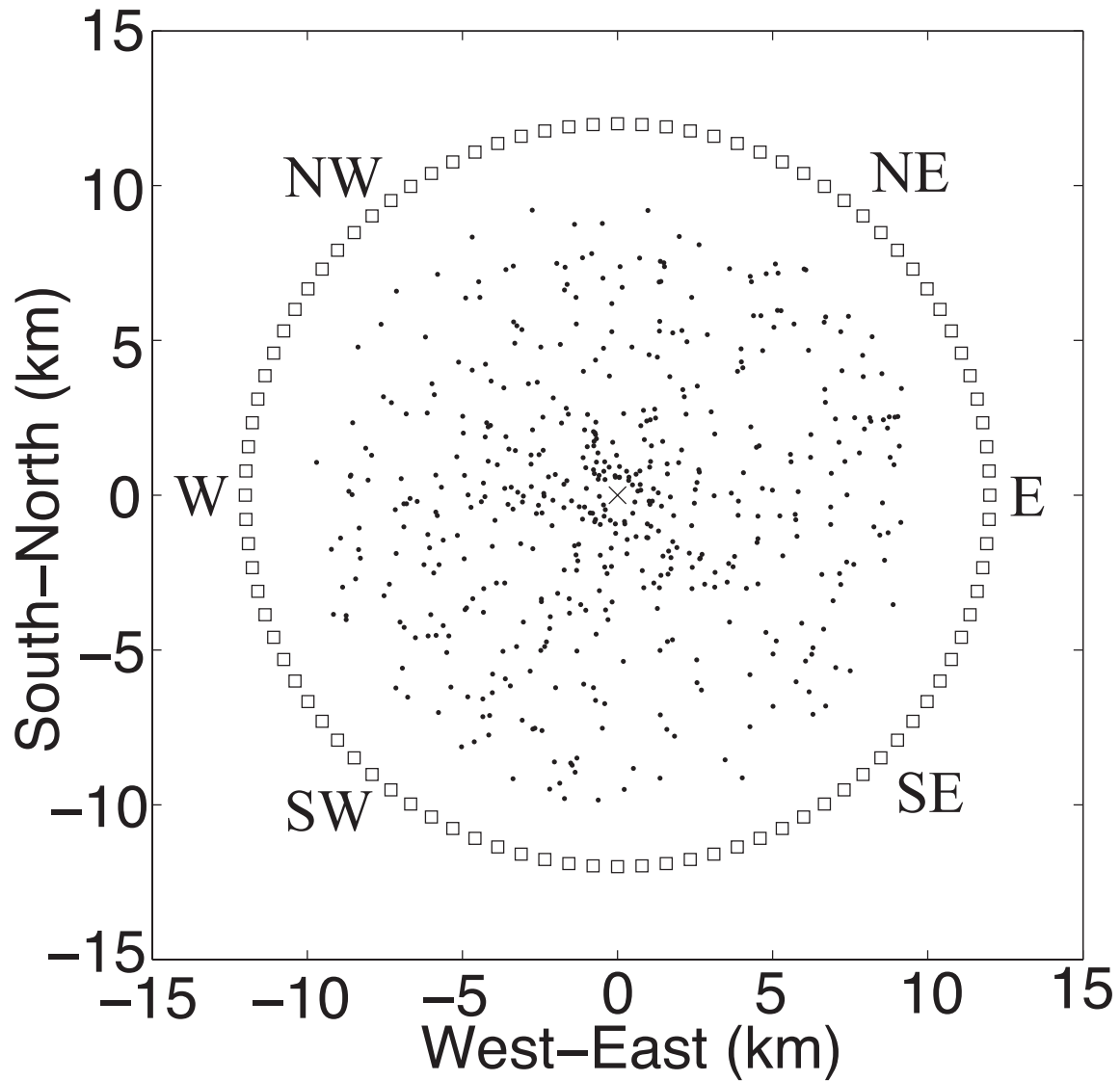


Figure 2.2: The experiment geometry of the numerical simulation. The receivers (squares) are surrounding the point scatterers (black dots). The source is positioned in the origin (cross). All perturbations of the source location is done from this position. The stations marked (NW, NE, E, SE, and SW) are used in the presentation of results in Figure 2.7 and Figure 2.8.

where ψ is the azimuth of the outgoing wave and λ , δ , and ϕ are the source parameters (rake, dip and strike, respectively). Sources are located at the center of the scattering area. The source spectrum has a dominant frequency f_d of approximately 30 Hz and a frequency range of 10-50 Hz. The source spectrum tapers off at the frequency extremes by a cosine taper with a length given by half of the bandwidth. We assume a reference velocity $V_0 = 3500$ m/s. Because the model we are using is an isotropic multiple scattering model, the transport mean free path is the same as the scattering mean free path: $l^* = l$. The scattering mean free path l^* [14, 32] is given by

$$l^* = \frac{k_o}{\rho |ImA|}, \quad (2.11)$$

where k_o is the wavenumber of the scattered signal and ρ is the scatterer density. For our model, the mean free path l^* is approximately 30.5 km. There is no intrinsic attenuation in the numerical model.

We generate multiple scattered signals, which are recorded at the receivers, using the numerical model in Figure 2.2. These signals are generated with a reference model defined by the following reference parameter values: the source radiation parameters $\phi = 0^\circ$, $\lambda = 0^\circ$, $\delta = 90^\circ$; change in medium velocity $\Delta V = 0$ m/s; and shift in the source location $D = 0$ m. We refer to signals generated by this reference model as the reference signals. In order to understand the effect of the perturbation of these parameters on velocity change estimation, we also generate synthetic signals from the perturbed version of the model. The perturbed model consists of perturbation of either the source locations, source radiation parameters, the medium velocity, or a combination of these. Synthetic signals from the reference and the 0.4% velocity perturbed models are shown in Figure 2.3I with zoom insets showing the stretching of the waveform by the velocity perturbation. The result of the velocity perturbation on the signals is a progressive time shift of the arriving seismic phases in the signals. Similarly, the effect of the independent perturbation of the source locations and the source radiation parameters are shown in Figure 2.3II and Figure 2.3III, respectively. The source location perturbation is $0.14\lambda_d$ along the z direction and the source radiation perturbation is 20° for

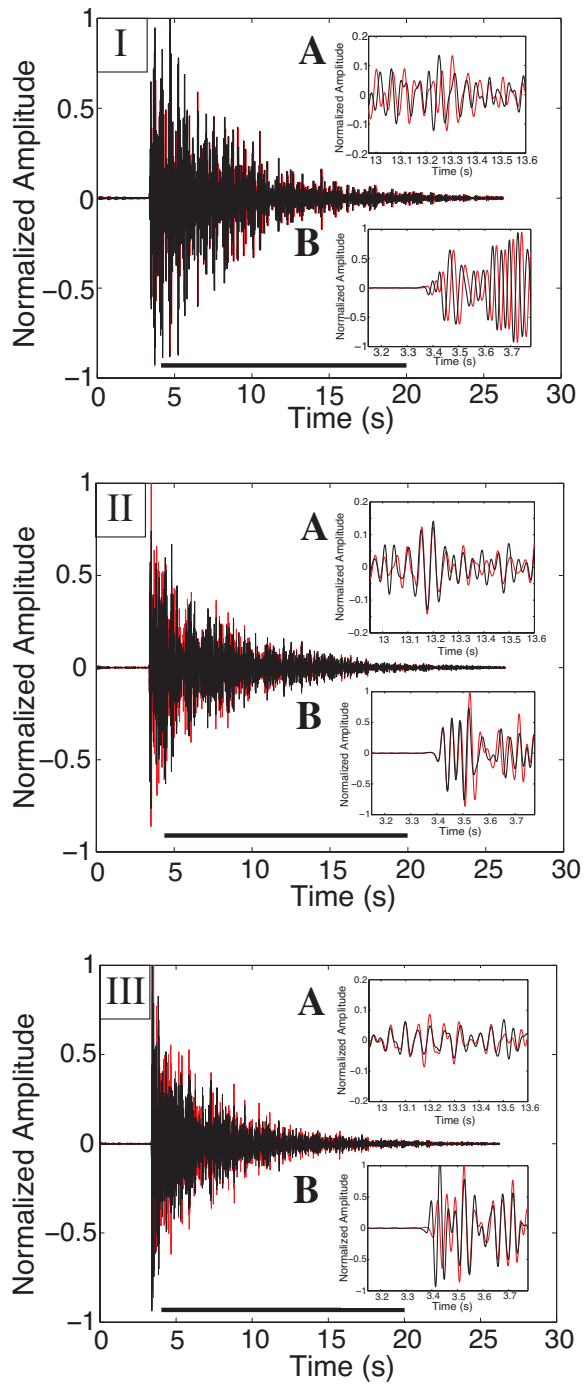


Figure 2.3: Recorded seismic signals at station E (Figure 2.2), the reference signal (red line) and the time-lapse signal (black line) with 0.4% relative velocity change (I), the time-lapse signal (black line) with $0.14\lambda_d$ source displacement (II), and the time-lapse signal (black line) with 20° source angle perturbations (III). Inset A shows the late coda while inset B shows the first arrivals of the two signals. The black bold line is the time window used for data processing. Time 0 is the source rupture time.

both the strike, rake and dip angles. The zoom insets in these Figure 2.3II and Figure 2.3III show that the changes in the source properties result in amplitude differences between the time-lapse signals. There are also phase differences between the time-lapse signals due to the perturbation of the source locations.

2.4.1 Data processing

To estimate the velocity perturbations or possible velocity change imprints on the synthetic signals due to the perturbation of the source location or its radiation properties, we use the stretching algorithm of Hadziioannou et al. [33] who demonstrate the stability and robustness of the algorithm relative to the moving time-window cross-correlation of Snieder et al. [97] and the moving time-window cross-spectral analysis of Poupinet et al. [76]. Both algorithms satisfy the relative velocity change equation [96]:

$$\left\langle \frac{t_p}{t} \right\rangle = -\epsilon, \quad (2.12)$$

where $\epsilon = \langle \delta V / V_o \rangle$ is the relative velocity change.

In the stretching algorithm, we multiply the time of the perturbed signal with a stretching factor $(1 - \epsilon)$ and interpolate the perturbed signal at this stretched time. The time window we use in all our analysis is given by the black bold line in Figure 2.3. We then stretch the perturbed signal at a regular interval of ϵ values. The range of the ϵ values can be arbitrarily defined or predicted by prior information on the range of changes in the subsurface velocity. To resolve the value of ϵ , we use an L_2 objective function rather than the cross-correlation algorithm as suggested by Hadziioannou et al. [33]. For events of equal magnitude ($A = \hat{A}$), the objective function is

$$R(\epsilon) = \|\hat{U}(t(1 - \epsilon)) - U(t)\|_2, \quad (2.13)$$

where $\|\dots\|_2$ is the L_2 norm. Figure 2.4 shows the objective function based on the L_2 norm and the maximum cross-correlation for the case of a 0.4% velocity change. The L_2 norm more accurately constrains the velocity change than the maximum cross-correlation. The

minimum of the objective function based on the L_2 norm depends on the amplitude changes between the two signals and on the travel time perturbations due to velocity changes and shifts in the source location. The signals have uniform magnitudes. The amplitude changes between the signals are due to changes in the orientation of the source angles.

The error in the estimated relative velocity change $\sigma_{\delta v}$ is given by

$$\sigma_{\delta v} \leq \frac{\sigma_U}{2\pi f_d A t}, \quad (2.14)$$

where f_d is the dominant frequency, t is the centertime of the signal, A is the amplitude of the signals, and σ_U is the standard deviation of the recorded waveforms. The derivation of equation 2.14 is given in Appendix C. The error associated with the velocity change depends on additive noise in the signals and on differences in the signals both in amplitude and in phase due to perturbation in source properties.

2.4.2 Effect of perturbation of source properties on the estimated velocity change

To understand the effect of the changes in the source properties on the estimation of the relative velocity changes, we conduct our numerical experiment over a range of parameter changes. We perturb the source location and the orientation of the source angles. The perturbation of the source radiation parameters is characterized by the weighted root mean square change in source parameters $\langle \zeta \rangle$ [80]:

$$\langle \zeta \rangle = -\frac{1}{2}(4\Delta\phi^2 + \Delta\lambda^2 + \Delta\delta^2), \quad (2.15)$$

where $\Delta\phi$ is the change in strike, $\Delta\lambda$ is the change in rake, and $\Delta\delta$ is the change in dip, between the two sources.

Figure 2.5 and Figure 2.6 show the estimated velocity changes due to the perturbation of medium velocity and the source properties (location and radiation parameters), respectively. For Figure 2.5, we generate signals with the following perturbation in the model velocity $\langle \delta V/V_0 \rangle$: 0.1%, 0.2%, 0.3%, and 0.4%. In these models, we keep the source parameters unchanged. Using the stretching method, we are able to recover the velocity changes we impose

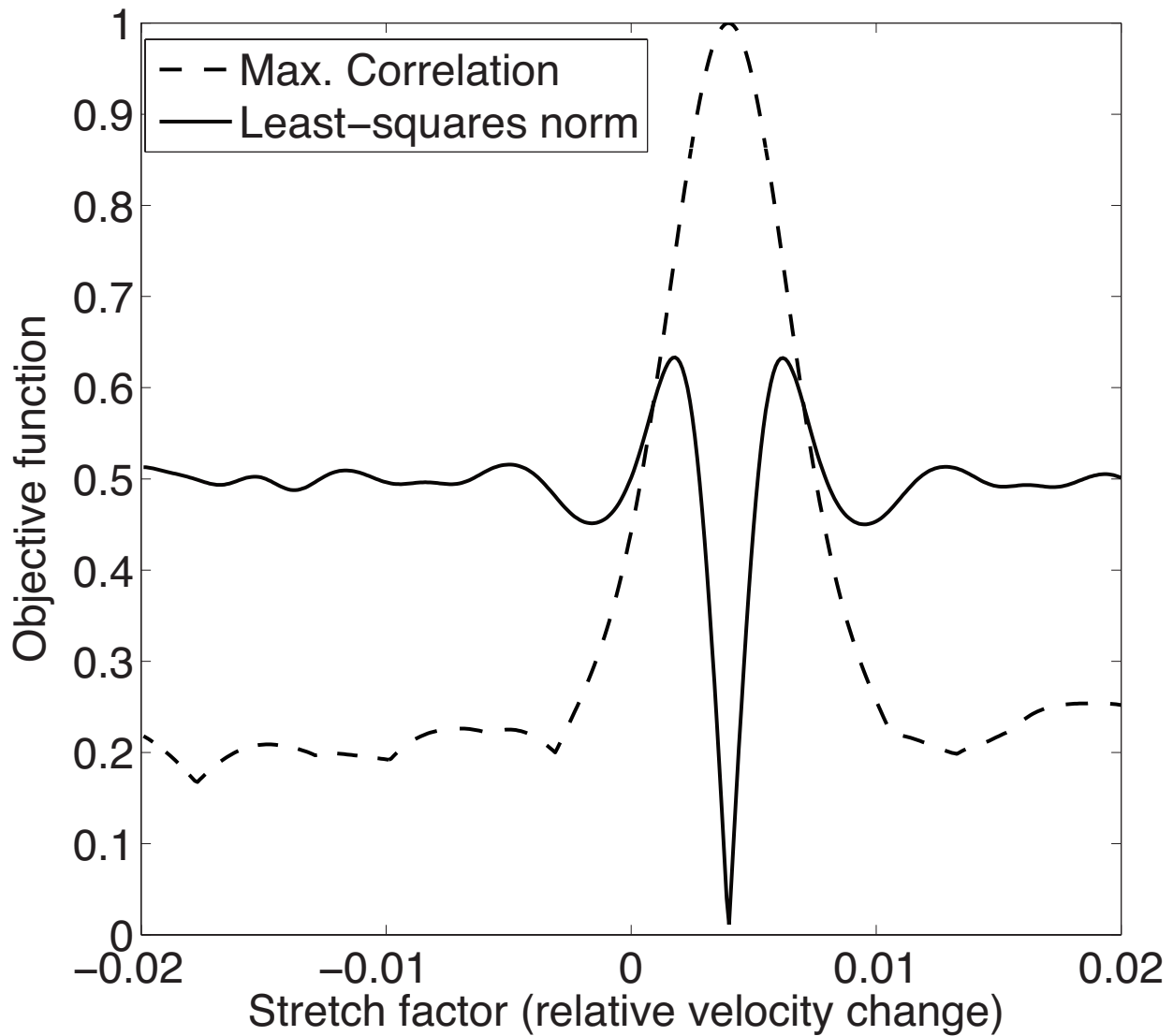


Figure 2.4: The objective function $R(\epsilon)$ (solid line) as a function of the stretch factor ϵ . The objective function is minimum for $\epsilon = 0.4\%$, which corresponds to the time-lapse velocity change. The corresponding maximum correlation of the stretch factors is given by the dash lines.

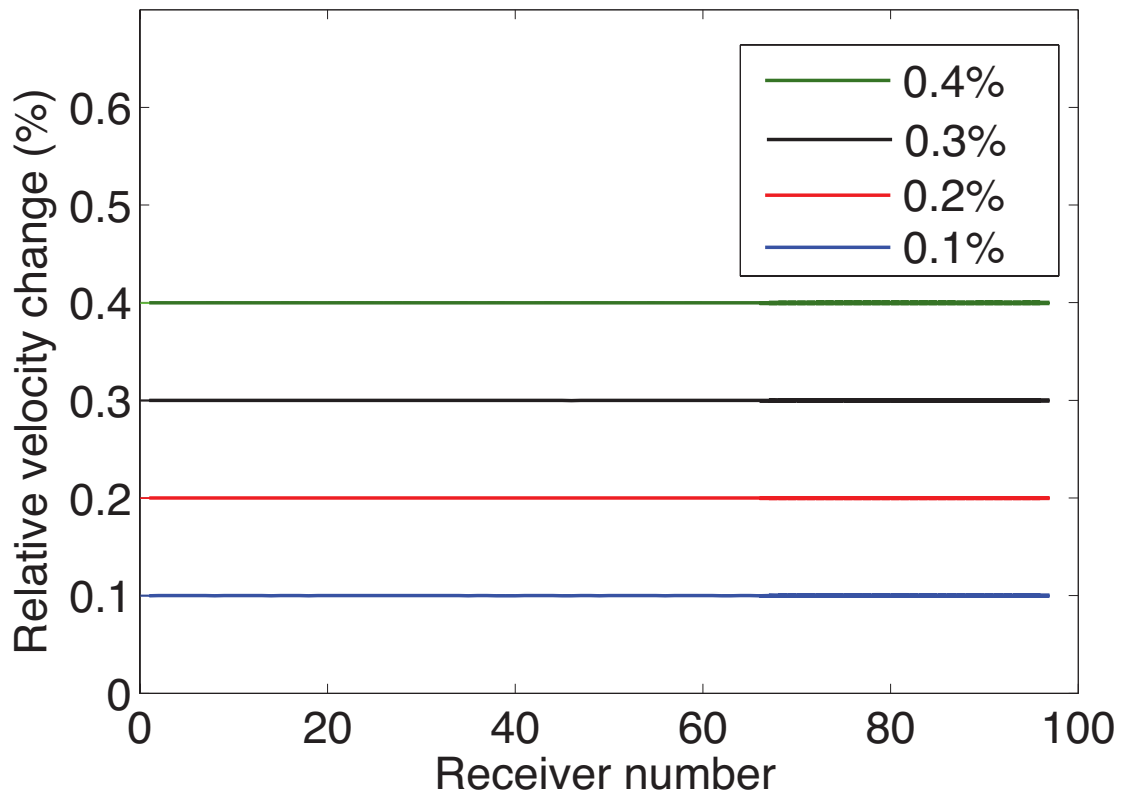


Figure 2.5: Estimated relative velocity change for model velocity change of $\langle \frac{\delta V}{V_0} \rangle = 0.1\%$ (blue), $\langle \frac{\delta V}{V_0} \rangle = 0.2\%$ (red), $\langle \frac{\delta V}{V_0} \rangle = 0.3\%$ (black), and $\langle \frac{\delta V}{V_0} \rangle = 0.4\%$ (green). The receiver numbers are counted counter-clockwise from the W station in Figure 2.2.

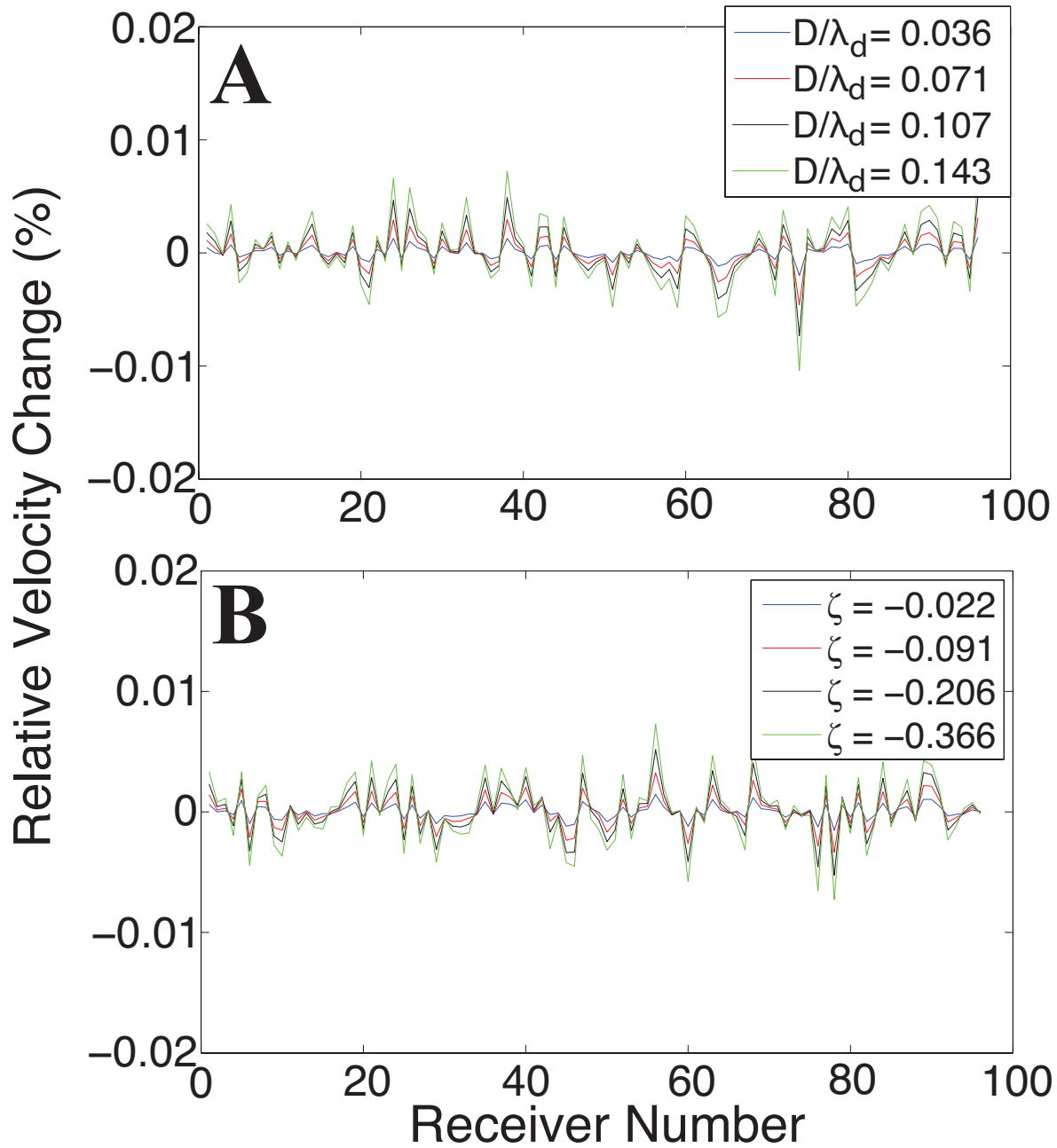


Figure 2.6: Estimated relative velocity change due to perturbation in the source location and the source radiation. A. The estimated velocity change for perturbed source location (divided by the dominant wavelength; inset in the top right) and B. The estimated velocity change caused by changes in source radiation angles (inset in the top right). The value of ζ is given by equation 2.15. The receiver numbers are counted counter-clockwise from the W station in Figure 2.2.

in the model from the codas of each of the perturbed signals and that of the reference signal (Figure 2.5). The method accurately estimates the model velocity change in all the receivers. We also generate signals with perturbations in the source locations and mechanisms only. In this case, the true velocity change is zero. Figure 2.6 shows that the estimated relative velocity changes $\langle \delta V/V_o \rangle$ are near the true value ($\delta V = 0$) for models with perturbations of either the source location or the source radiation parameters. The velocity change estimated from individual stations varies around zero, but with a shift in the source location of $D = 0.143\lambda_d$, with λ_d the dominant wavelength and source angle perturbations as large as $\Delta\phi = 20^\circ$, $\Delta\lambda = 20^\circ$, and $\Delta\delta = 20^\circ$ ($\langle \zeta \rangle = -0.366$), the magnitude of the estimated velocity change is smaller than 1/20th of the typical velocity changes inferred from seismic signals (Figure 2.6). These variations in the velocity change inferred from different stations can be used to estimate the errors in the estimated velocity change. These results agree with equation 2.7 which predicts that the average value of time shifts in the perturbed signal results only from changes in the medium velocity and is not affected by changes in source properties. We will need to know how effectively we can resolve the velocity changes in our model in the presence of the other model parameter perturbations.

2.4.3 Limiting regimes of the estimations

To investigate the extent of the perturbation in the source location and source radiation perturbations that can be allowed in the estimation of relative velocity changes, we generate synthetic signals with models having a 0.1% relative velocity change and various perturbations of the source parameters. The values of the source parameter perturbations are given in Table 2.1 and Table 2.2. Figure 2.7 shows the estimated relative velocity changes from signals generated from sources at different locations. The figure shows that we can recover the relative velocity change of 0.1% using doublets (two sources) within a sphere of radius $\lambda_d/4$, where λ_d is the dominant wavelength of the seismic signal which is approximately 140 m. This is consistent with the criterion we derived in Appendix D, which predicts that for an accurate estimation of the subsurface velocity change, the shift in the source location has

to satisfy

$$\frac{D}{\lambda_d} < \sqrt{2} \left| \left\langle \frac{\delta V}{V_o} \right\rangle \right| f_d t, \quad (2.16)$$

where f_d is the dominant frequency of the signals, $\langle \delta V/V_o \rangle$ is the average velocity change in the subsurface, and t is the centertime of the processed signal. The criterion is derived from a comparison of the phase changes due to velocity changes with those due to shifts in the source location. For the results in Figure 2.7, our model parameters are $\langle \delta V/V_o \rangle = 0.1\%$, $t = 10$ s, and $f_d \simeq 25$ Hz. With these values, the constraint on the source location shift for Figure 2.7 is

$$\frac{D}{\lambda_d} < 0.35. \quad (2.17)$$

Table 2.1: Modeling parameters for shift in the source location.

Case	$\frac{\Delta V}{V}(\%)$	D/λ_d
Reference	0	0
Case 1	0.1	0.0274
Case 2	0.1	0.0547
Case 3	0.1	0.0820
Case 4	0.1	0.1094
Case 5	0.1	0.1367
Case 6	0.1	0.1642
Case 7	0.1	0.1918
Case 8	0.1	0.2197
Case 9	0.1	0.2477
Case 10	0.1	0.2760
Case 11	0.1	0.3047
Case 12	0.1	0.3337
Case 13	0.1	0.3627
Case 14	0.1	0.3916
Case 15	0.1	0.4202

Figure 2.7 shows that for $D/\lambda_d \geq 0.3$, the estimated velocity change deviates significantly from the real velocity change; this is in agreement with equation 2.17. The criterion in equation 2.16 imposes a constraint on the spacing requirements for the source locations of the doublets used for time-lapse velocity change monitoring with microearthquakes. Alterna-

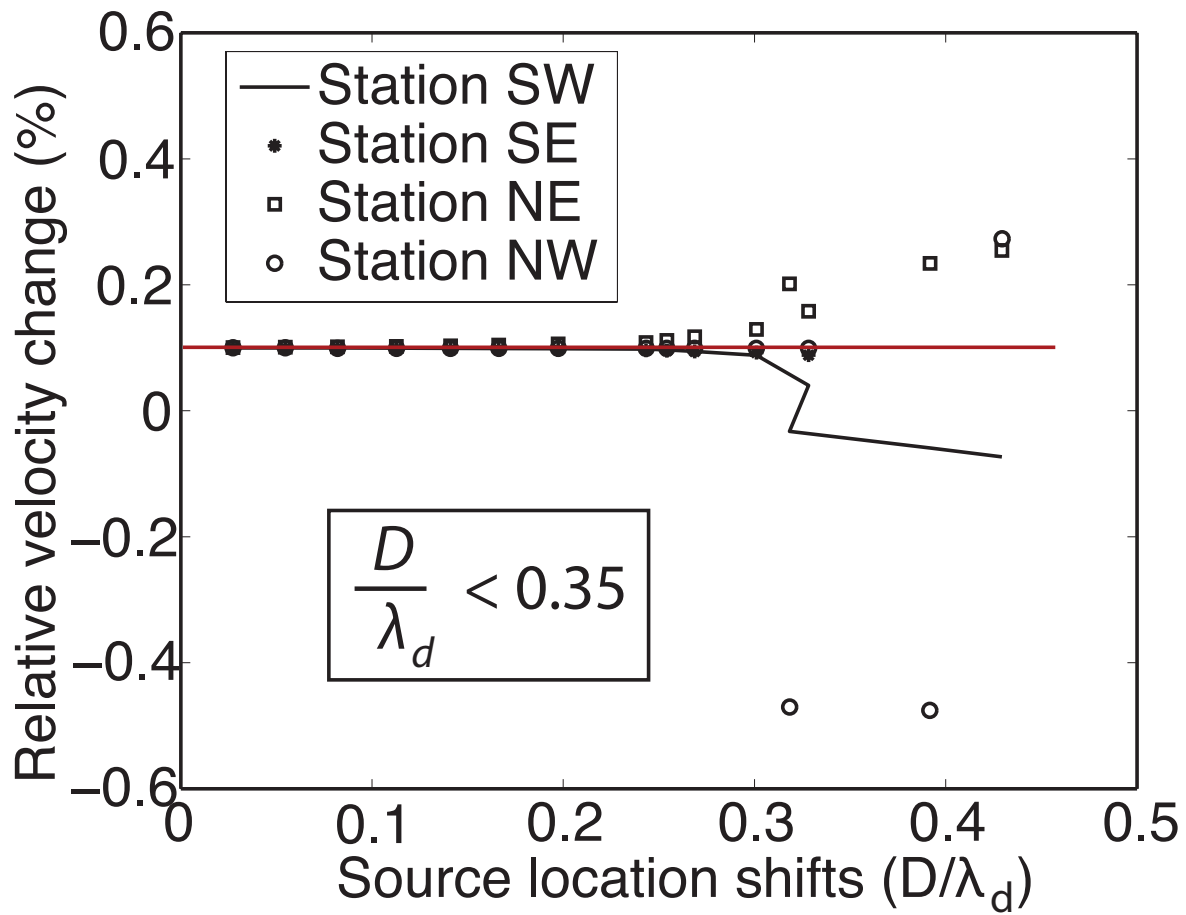


Figure 2.7: Estimated relative velocity change after a 0.1% velocity change and various source location perturbations (Table 2.1). The shift in the source locations are divided by the dominant wavelength λ_d of the recorded signals. For values of the source location shift greater than $\lambda_d/4$, we have incorrect estimates for the velocity change due to the distortion of the perturbed signal. Stations SW, SE, NE, and NW positions are given in Figure 2.2. The red line indicates the model (accurate) velocity change.

Table 2.2: Modeling parameters for source radiation perturbation.

Case	$\frac{\Delta V}{V}$	$\Delta\phi(^{\circ})$	$\Delta\lambda(^{\circ})$	$\Delta\delta(^{\circ})$	$-\langle\zeta\rangle$
Reference	0	0	0	0	0
Case 1	0.1	0	0	0	0
Case 2	0.1	2	2	2	0.0037
Case 3	0.1	4	4	4	0.0146
Case 4	0.1	6	6	6	0.0329
Case 5	0.1	8	8	8	0.0585
Case 6	0.1	10	10	10	0.0914
Case 7	0.1	12	12	12	0.1316
Case 8	0.1	14	14	14	0.1791
Case 9	0.1	16	16	16	0.2339
Case 10	0.1	18	18	18	0.2961
Case 11	0.1	20	20	20	0.3655
Case 12	0.1	22	22	22	0.4423
Case 13	0.1	24	24	24	0.5264
Case 14	0.1	26	26	26	0.6178
Case 15	0.1	28	28	28	0.7165

tively, equation 2.16 gives the magnitude of a velocity change that is resolvable with a given shift in the source location. According to equation 2.16, the allowable source separation increases with the centertime t of the employed time window. This is due to the fact that the imprint of the velocity change is more pronounced as the waves have propagated over a greater distance through the perturbed medium. However, signals at later times in the coda are more affected by the presence of additive noise because the signal-to-noise ratio usually decreases towards the late coda.

We also investigate the effect of the source radiation properties on the estimated velocity change of the medium of interest. Figure 2.8 shows the estimated velocity changes from a model with 0.1% velocity change using sources with perturbed radiation angles (measured by $\langle\zeta\rangle$). The values of the perturbed source radiation angles are given in Table 2.2. In Figure 2.8A, the estimated velocity change at the individual stations progressively deviates from the true velocity change of 0.1% with increasing change in the orientations of the source angles. This deviation is due to the decorrelation between the perturbed and the unperturbed

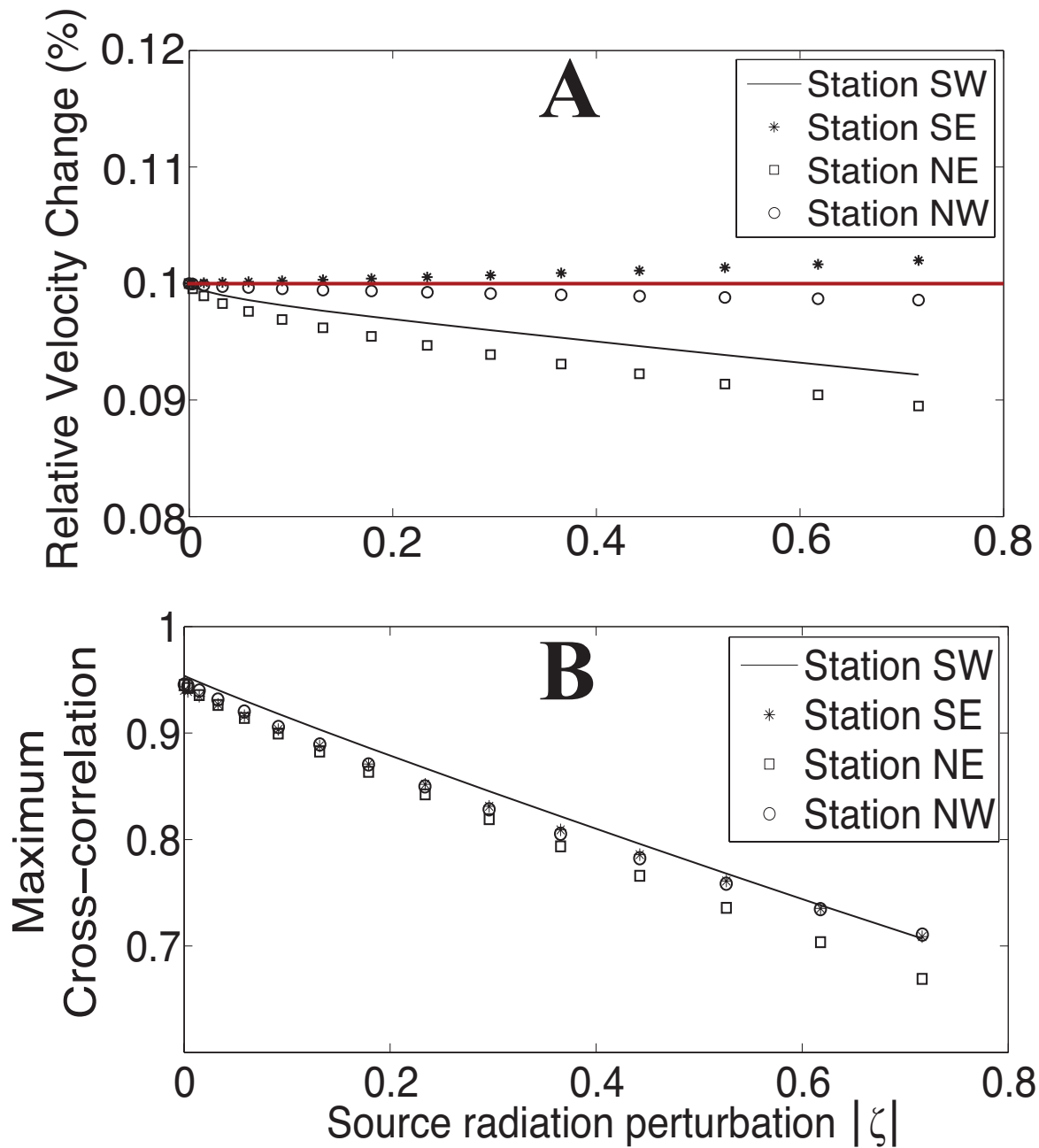


Figure 2.8: Effect of source angle perturbation on estimated velocity change. A. The estimated relative velocity changes are from a 0.1% model velocity change (Red line) and various source radiation perturbations (Table 2.2). B. The decorrelation of the doublets, due to source angle perturbations, measured by maximum cross-correlation values. Stations SW, SE, NE, and NW positions are given in Figure 2.2.

signals as shown in Figure 2.8B, which shows the maximum normalized cross-correlation of the codas within the processed time window. With an increasing change in the orientation of the sources, the maximum cross-correlation value of the waves excited by the doublets decreases. However, for source angle perturbations as large as $\Delta\phi = 28^\circ$, $\Delta\lambda = 28^\circ$, and $\Delta\delta = 28^\circ$, which corresponds to $|\langle\zeta\rangle| = 0.72$ (Figure 2.8A), the maximum deviation from the 0.1% model velocity change is approximately 0.01%. This is a small change compared to velocity changes resolved from seismic signals in practice. The maximum cross-correlation (Figure 2.8B) can be retrieved from the data and can be used as a diagnostic of the accuracy of the estimated velocity change. In this example, a maximum cross-correlation of 0.7 indicates an error of about 10% in the estimated velocity change. The difference in the errors observed among the 4 stations (SW, SE, NE and NW) is due to the differences in the amplitude perturbations resulting from the changes in the source angles. Figure 2.9 shows that with source angle perturbations of $\Delta\phi = 20^\circ$, $\Delta\lambda = 20^\circ$, and $\Delta\delta = 20^\circ$ the loops in the radiation pattern in the NE and SW directions change more dramatically than those in the NW and SE directions. For the parameters used in this experiment, the transport mean free time t^* , defined as the time over which the scattered waves loses their directions, is given by $t^* = l^*/c = 8.7$ s. c is the propagation velocity of the scattered waves. The time interval used for the analysis of the coda waves is 3.6 to 20 s (Figure 2.3). This means that the coda waves in the early part of the time interval used still retains information about the direction in which they were radiated. The changes in the radiation pattern thereby result to a higher error in velocity changes estimated with stations NE and SW than those with stations NW and SE.

2.5 Discussion and Conclusion

In this study, we investigate the influence of perturbation in source properties (location and radiation) on the estimation of velocity changes. These velocity changes are extracted from multiply scattered signals (codas) of repeating events. We show that we can resolve accurate values of relative velocity changes if the shift in the source location satisfies equa-

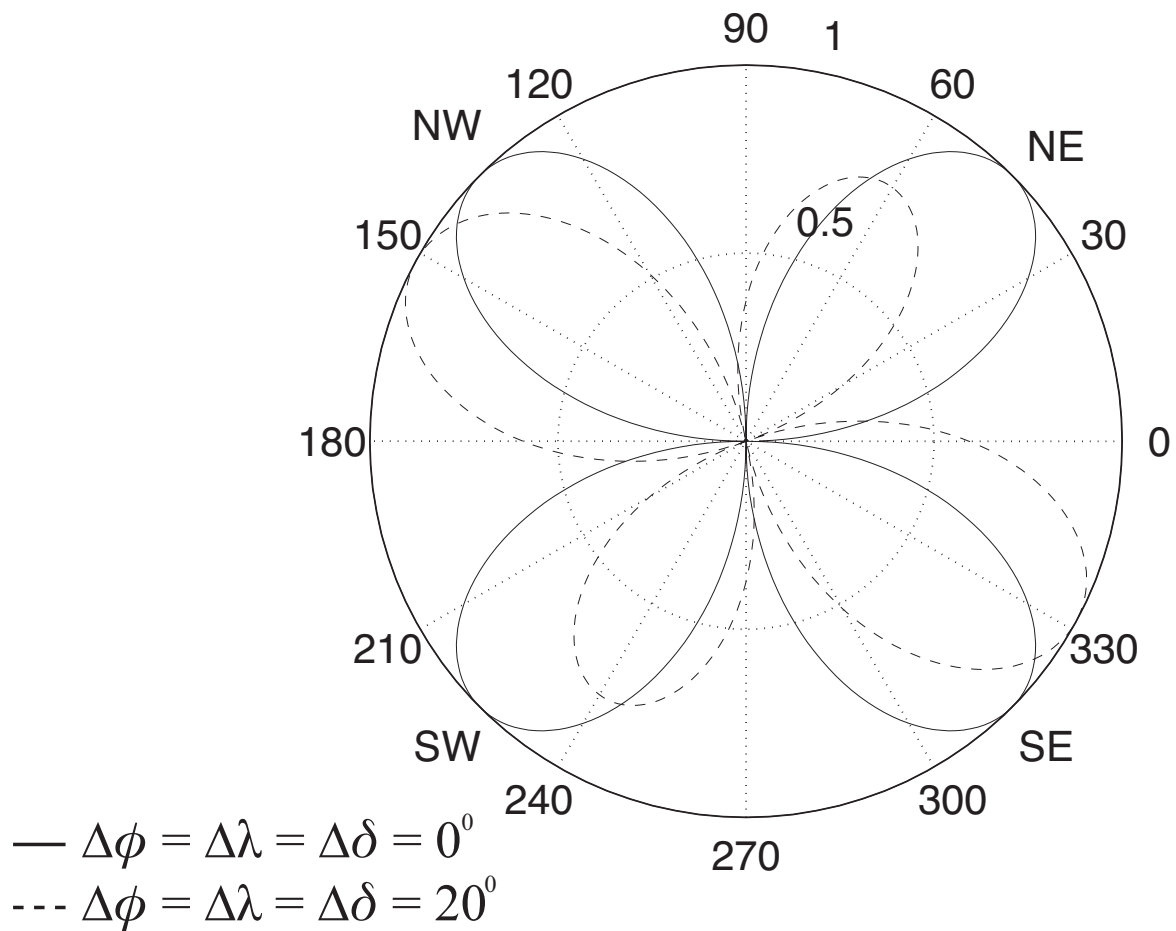


Figure 2.9: Source radiation pattern of the modeled earthquake sources before and after simultaneous perturbation of the source angles (strike $\Delta\phi$, rake $\Delta\lambda$ and dip $\Delta\delta$) of 20 degree each.

tion 2.16. This constraint depends on the dominant frequency of the signal, the estimated relative velocity change, and the centertime of the employed time window. This places a restriction on the relative event locations that can be used to estimate the relative velocity change of the subsurface. However, to use this constraint, we need to know the magnitude of the relative velocity change we seek to measure. Preliminary results on the velocity change can be used to pick events satisfying equation 2.16 for an accurate estimation of the velocity changes. Using doublets that do not satisfy the constraint result in an inaccurate estimate of the velocity change. Weaver et al. [110] similarly showed that changes in noise sources induce error in velocity change estimated from correlation signals obtained from the noise signals. Although our study differs from Weaver et al. [110] in that we are using the coda signals from the earthquake sources, the actual velocity changes can be estimated from the signal in the presence of the source perturbation as shown by Weaver et al. [110], except when the criterion in equation 2.16 is violated.

A significant change in the source mechanism of double couple sources can introduce a bias in the estimation of relative velocity change. This bias is due to the decorrelation of the perturbed and unperturbed signals which lowers the accuracy of the estimated velocity change. As shown in Figure 2.6B and Figure 2.8A, some of the stations underestimate while others overestimate the velocity change. However, this bias is negligible for the typical velocity changes resolved from seismic signals in practice. This result permits the use of sources of different orientations for the estimation of velocity changes, provided that the maximum cross-correlation of the source signals is greater than 0.7 as shown in Figure 2.8B. For a consistent estimate of the velocity change, using multiple stations is useful to ascertain the accuracy of the estimated velocity change in an isotropic subsurface.

The theory presented in this study is based on a number of simplifications and assumptions. First, we assume a uniform velocity change across our model. For the case of a localized isotropic velocity change, the resolved velocity change is a fraction of the local velocity change, where the fraction is dependent on the amount of time the codas spend

within the perturbed region relative to the unperturbed region.

In this study, we assume that the scatterer density is uniform in all directions from the source. We also ignore changes in the scattering properties which might include shifts in scatterer locations [65, 98] and changes in the scattering strength of the scatterers. These changes in the scatterer properties can be due to changes in fluid properties such as fluid migration or opening and closing of fractures and pre-existing faults. If the shifts in the scatterer location are random, the average travel time perturbation due to scatterer location shift is zero. However, if the shifts in the scatterer locations are non-random or directional, the average time perturbation due to scatterer location shift over all take-off angles is a non-zero mean traveltime change. A non-zero mean traveltime perturbation is also expected for non-uniform scatterer density. The scattered signals lag behind while traveling through a higher scatterer density region compared to a lower scatterer density region. These introduce a bias in the estimated relative velocity changes if the changes in scatterer properties or density are significant.

We used point scatterers in our numerical modeling even though in the real world, scattering can be caused by faults, fractures, horizontal or dipping layers. The employed modeling uses scalar waves, hence it does not account for mode conversions of elastic waves (for example, P-to-S or S-to-P and surface waves) that might result due to the presence of layers, free surface, and fractures. The coda is usually dominated by S wave [1, 97], hence the mode conversions between P and S waves do not dominate the details of the scattering processes.

2.6 Acknowledgments

We thank two anonymous reviewers for the critical and constructive comments. This work was supported by the U.S. Dept. of Energy through grant DE-EE0002758.

CHAPTER 3

A COMPARISON OF THREE METHODS FOR ESTIMATING VELOCITY CHANGES BETWEEN TIME-LAPSE MICROSEISMIC SIGNALS

Chinaemerem O. Kanu and Andrew Muñoz

3.1 Abstract

Time-lapse seismic signals provide information about subsurface velocity changes. The accuracy with which we measure these velocity changes is dependent on the accuracy of time shift measurements. We compare three methods of estimating time shifts using real and synthetic microseismic time-lapse signals, and use these time shifts to estimate relative velocity changes. We compare: 1) time-shift cross-correlation, 2) stretching method, and 3) smooth dynamic time warping (SDTW); SDTW provides the most detailed estimation of both time shifts and relative velocity changes among the three methods.

3.2 Introduction

Subsurface time-lapse velocity changes can be monitored using repeating earthquakes and microseismic events [76]. Velocity changes might be caused by fluid injection from hydraulic activities [22], hydrocarbon migration and production [116], and stress-induced changes. Velocity changes that are weak, localized, or embedded within a noisy signal are challenging to detect. We seek a method that estimates the relative velocity changes in the presence of noise and without any prior knowledge of the subsurface velocity structure.

These velocity changes are heterogeneous and vary non-linearly with travelttime. Estimating accurate velocity changes requires that we use a high-resolution travelttime estimation method. Windowed cross-correlation (sometimes known as moving window cross-correlation)

is a well known method used for estimating time shifts. Another well-known method, the stretching method, better estimates traveltime changes and also directly estimates relative velocity changes. We introduce a new technique for time-lapse time-shift estimation called dynamic time warping, which is a well-known signal processing method. To compute these traveltime changes, we use a modified version called smooth dynamic time warping (SDTW) [35]. We then compute relative velocity changes from these time shifts. To compare these three methods, we measure the time shifts between both synthetic and recorded microseismic time-lapse signals (Figure 3.1) using each method and compute relative velocity changes.

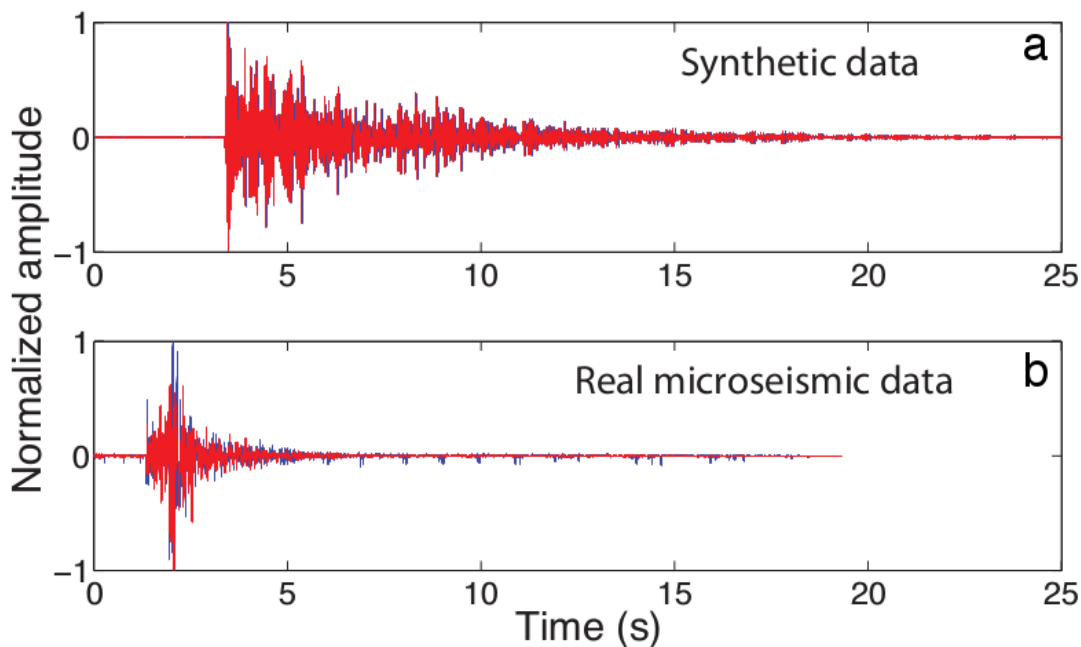


Figure 3.1: Synthetic time-lapse signals (a) and recorded microseismic time lapse signals (b). The blue curve is the baseline signal and the red curve is the time-lapse signal.

3.3 Methods

Time-lapse velocity changes within the subsurface, like in a stimulated reservoir, induce travel time delays on seismic waves. We estimate these delays and use them to compute relative velocity changes.

3.3.1 Windowed cross-correlation

Windowed cross-correlation of paired signals is a common technique used for time-shift estimation. This technique has specifically been used for time shift estimation in time-lapse studies [88] and for computing traveltimes misfits between the real data and model predicted data in geophysical inverse problems [49, 106]. Its extensive use stems from the efficient computation cost of cross-correlation.

For a constant relative velocity change $\delta v/v$, we can estimate the relative velocity change [96]

$$\frac{\delta v}{v} = -\frac{\delta t}{t} \quad (3.1)$$

where δt is the traveltime change between the time-lapse seismic signals and t is the traveltime of the seismic wave.

The time shifts between the seismic codas can be estimated using the maximum cross-correlation given by

$$R(t_s) = \frac{\int_{t-t_w}^{t+t_w} d(t') \hat{d}(t' + t_s) dt'}{\sqrt{\int_{t-t_w}^{t+t_w} d^2(t') dt' \int_{t-t_w}^{t+t_w} \hat{d}^2(t') dt'}}, \quad (3.2)$$

where $d(t)$ is the baseline coda and $\hat{d}(t)$ is the time-lapse coda. The traveltime difference δt between the two cross-correlated codas corresponds to the timeshift t_s that maximizes $R(t_s)$ [97]. The maximum cross-correlation is computed over a time window $2t_w$ centered at traveltime t . The accuracy of the relative velocity change depends on the accuracy and stability of the estimated time shifts. The estimation of time shifts is influenced by cycle-skipping, especially for large traveltime changes, while the stability of the estimated time shifts depends on the size of the cross-correlation window. Figure 3.2 shows the time shifts estimated from noise-free synthetic time-lapse codas using three different window sizes. By increasing the window size, the stability of the estimated time shifts increases. However, each time shift estimation is influenced by cycle-skipping, regardless of the window size. For instance, at $t = 8.2$ s in Figure 3.2, there is a discontinuity in the estimated time shifts. This

discontinuity corresponds to a cycle-skip. The cycle-skip is solely dependent on the time shifts between the time-lapse signals and on the dominant period of the signals.

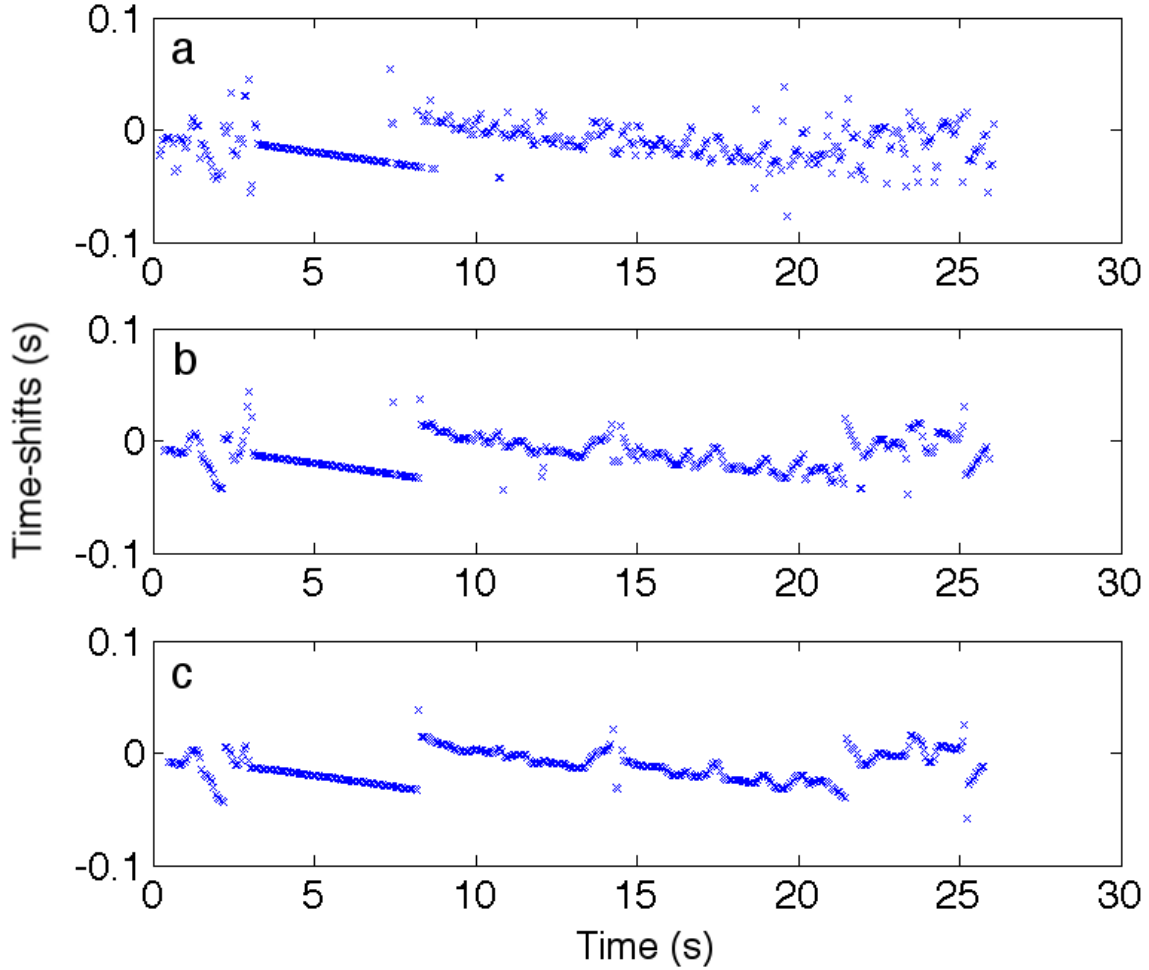


Figure 3.2: The stability of the windowed cross-correlation method for time shift estimation. The time shifts are estimated within time windows whose widths $2t_w$ are relative to the dominant period T of the signal: $2t_w = 37.5T$ (a), $2t_w = 75T$ (b), and $2t_w = 112.5T$ (c), where $T = 0.033$ s.

Time shifts between time-lapse codas can also be estimated in the frequency domain using the moving-window cross-spectrum technique [76]. Using this technique, the time shifts δt are estimated from the phase spectrum $\phi(f)$:

$$\delta t = \frac{\phi(f)}{2\pi f}. \quad (3.3)$$

3.3.2 Stretching method

The stretching method proposed by Hadziioannou et al. [33] provides a direct estimate of the relative velocity change $\delta v/v$ by shrinking or stretching the time-lapse coda signal relative to the baseline coda signal using an estimated stretch factor ϵ . We stretch the signals by

$$\hat{d}(\hat{t}) \rightarrow \hat{d}(t(1 + \epsilon)), \quad (3.4)$$

where \rightarrow is the stretching operation.

The estimation of the optimal stretching factor ϵ can be obtained using either the cross-correlation

$$R(\epsilon) = \frac{\int_{t_{min}}^{t_{max}} d(t') \hat{d}(t'(1 + \epsilon)) dt'}{\sqrt{\int_{t_{min}}^{t_{max}} d^2(t') dt' \int_{t_{min}}^{t_{max}} \hat{d}^2(t'(1 + \epsilon)) dt'}}, \quad (3.5)$$

where t_{min} and t_{max} are the minimum and the maximum traveltimes of the stretched time-lapse signals, or the L_2 norm of the difference between the time-lapse and baseline coda signals:

$$R(\epsilon) = \|\hat{d}(t(1 + \epsilon)) - d(t)\|_2. \quad (3.6)$$

The optimal ϵ is determined by the ϵ that maximizes the cross-correlation or minimizes the L_2 norm between the baseline coda and the time-lapse coda. In this study, we use the L_2 norm to pick the optimal ϵ value. This optimal stretching factor ϵ is equal to $-\delta t/t$, which according to equation 3.1 is also equal to the estimated relative velocity change $\delta v/v$.

Hadziioannou et al. [33] show, using laboratory data, that the stretching method is a more accurate and robust estimate of $\delta v/v$ compared to the window cross-correlation method. The stretching method is limited to a constant $\delta v/v$ over the time window that the stretch factor is computed. To compute a time-varying $\delta v/v$, we compute the stretch factor over smaller time windows, or we use a predefined functional relationship between the stretch factor and traveltime $\epsilon = f(t)$. To use this predefined function, we must know how the relative velocity change varies along the seismic coda. By computing the stretch factors with small coda time windows (windowed stretching method), we only need to assume the stretching

window length. In the windowed stretching method, the stability of the extracted stretch factors depends on the time window length relative to the dominant period of the time-lapse signals; this dependence is similar to that found with the windowed cross-correlation method. Figure 3.3 shows the impact of the window length on the stability of the estimated velocity changes. The stability of the estimated relative velocity changes increases with length of the stretching window, especially in the presence of large time shifts in the signals.

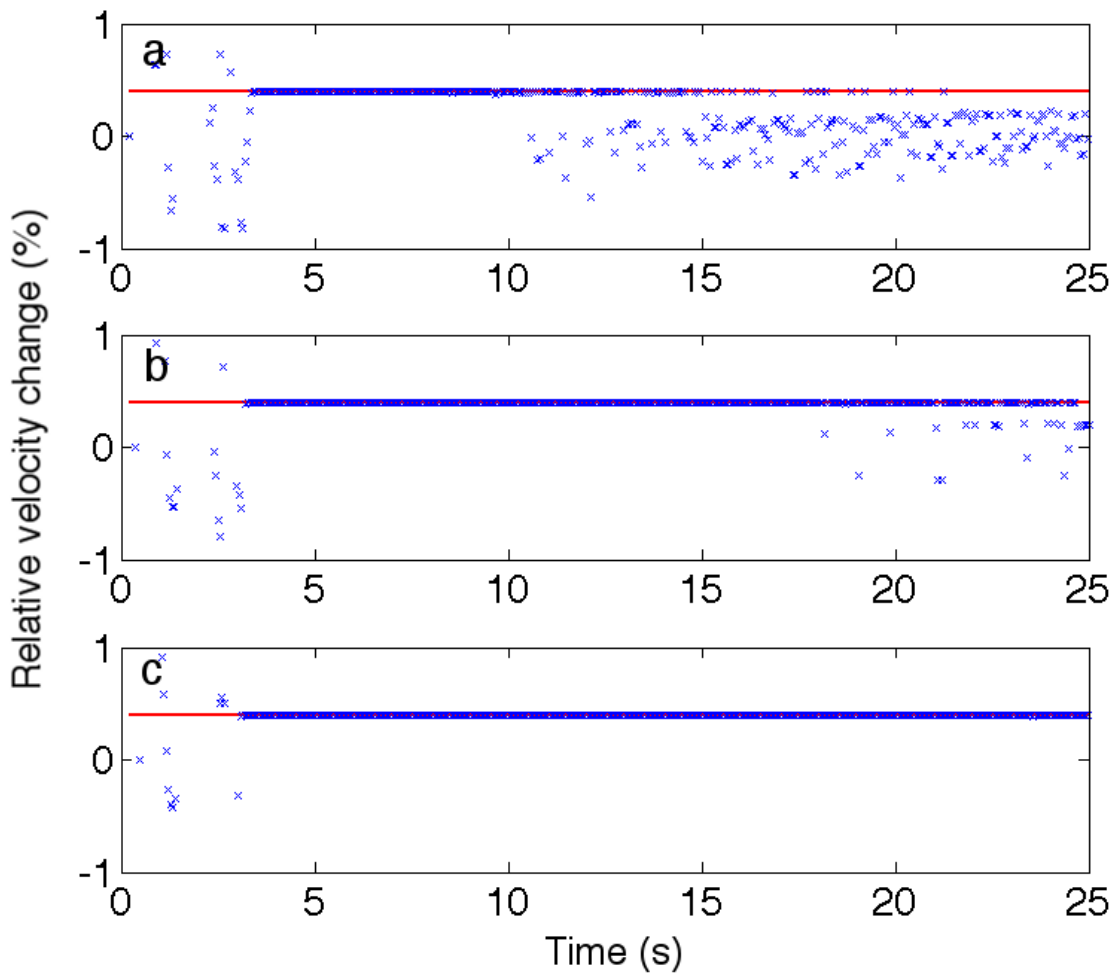


Figure 3.3: The stability of the windowed stretching method for relative velocity change estimation. The relative velocity changes are estimated within time windows whose widths are relative to the dominant period T of the signal: $37.5T$ (a), $75T$ (b), and $112.5T$ (c), where $T = 0.033$ s. The red line shows the exact relative velocity change.

3.3.3 Smooth dynamic time warping

Dynamic time warping (DTW) is a widely used algorithm in speech-processing and has recently been modified and applied to geophysics [19, 34, 35]. We use a modified form of DTW called smooth dynamic time warping (SDTW) [35] to compute time shifts between time-lapse signals; this modification of DTW samples time shifts at coarse intervals, which decreases the resolution of (or *smooths*) the time shifts. SDTW computes a globally optimal solution to a non-linear minimization problem (the alignment between two time-lapse signals), subject to constraints on time shifts.

Specifically, we align the baseline signal $d(t)$ to the time-lapse signal $\hat{d}(t)$ such that

$$\hat{d}(t) \approx d(t - u(t)), \quad (3.7)$$

where $u(t)$ are the time shifts that optimally align the time lapse signals. These shifts are subject to constraints on u . We follow the same analysis as Muñoz and Hale [61] to relate u to relative velocity changes:

$$\begin{aligned} \frac{du}{dt} &= \frac{v_o(t) - v(t)}{v_o(t)}, \\ &= -\frac{\delta v}{v_o}, \end{aligned} \quad (3.8)$$

where v is the velocity of the time-lapse signal, v_o is the velocity of the baseline signal, and $\delta v/v_o$ is the relative velocity change. We limit these velocity changes to constrain du/dt :

$$\min \left(\frac{\delta v}{v_o} \right) \leq \frac{du}{dt} \leq \max \left(\frac{\delta v}{v_o} \right). \quad (3.9)$$

Following Compton and Hale [19], we use an amplitude-aligned, non-uniform grid (computed from the baseline signal) to estimate time shifts. These grid points align with the largest amplitudes within a time window of at least 0.25 s. We show an example of these grid points in Figure 3.7a. The grid spacing prevents us from sampling time shifts too finely. At the grid points, we are more confident with our time shift estimates and therefore our relative velocity change estimates compared with time shifts estimated at blindly sampled

coarse grid points.

Figure 3.4a shows time shifts, computed using SDTW, that align the synthetic microseismic baseline and time-lapse signals shown in Figure 3.1, and Figure 3.4b shows the associated relative velocity changes in blue compared to the exact velocity changes in red. These computed relative velocity changes align well with the exact values.

A geophysically reasonable assumption is that relative velocity changes are smooth and continuous. Therefore, we interpolate time shifts between grid points using cubic splines, and because cubic splines have continuous first derivatives, our resulting relative velocity changes are smooth. We illustrate the sensitivity of constraints computed using equation 3.9 in Figure 3.7b, where the variation in relative velocity change is larger in the late times of the time-lapse signals than at the earlier times; this instability may be attributed to the decrease in signal to noise ratio with time.

3.4 Real microseismic signals

We use recorded time-lapse microseismic signals from a geothermal field to compare the three time shift estimation methods. These microseismic signals are shown in Figure 3.1b; their magnitude is approximately $1.5 M_w$. We anticipate a non-zero relative velocity change between the microseismic signals due to the variation in the subsurface properties over time. These recorded microseismic signals are noisy, which will affect the accuracy of the estimated time shifts and relative velocity changes [110].

We compute these time shifts using the three previously discussed methods: windowed cross-correlation, window stretching method, and SDTW. Figure 3.5 shows the estimated time shifts using the full-bandwidth microseismic signals. The time shifts estimated using windowed cross-correlation and the window stretching method are computed with overlapping window sizes of 1.0 s. Computing time shifts with the overlapping windows provides a detailed estimate of the time shifts. However, this implies that the individual measurements of the time shifts are correlated. Figure 3.5 shows that the estimated time shifts computed using windowed cross-correlation and stretching method have less variability compared to

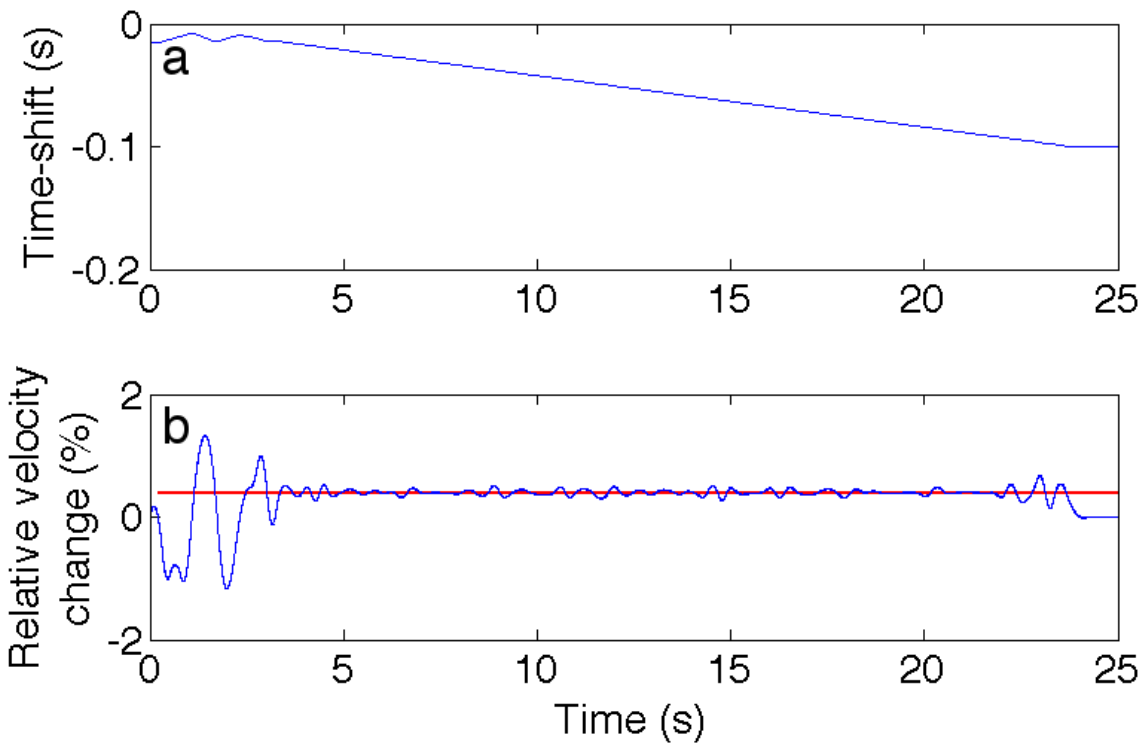


Figure 3.4: Time shifts and relative velocity changes estimated via SDTW. The time shifts (a) and the relative velocity changes (b) are computed from the synthetic time-lapse signals shown in Figure 3.1a. We compare the exact velocity change (red) to the estimated relative velocity changes (blue) (b).

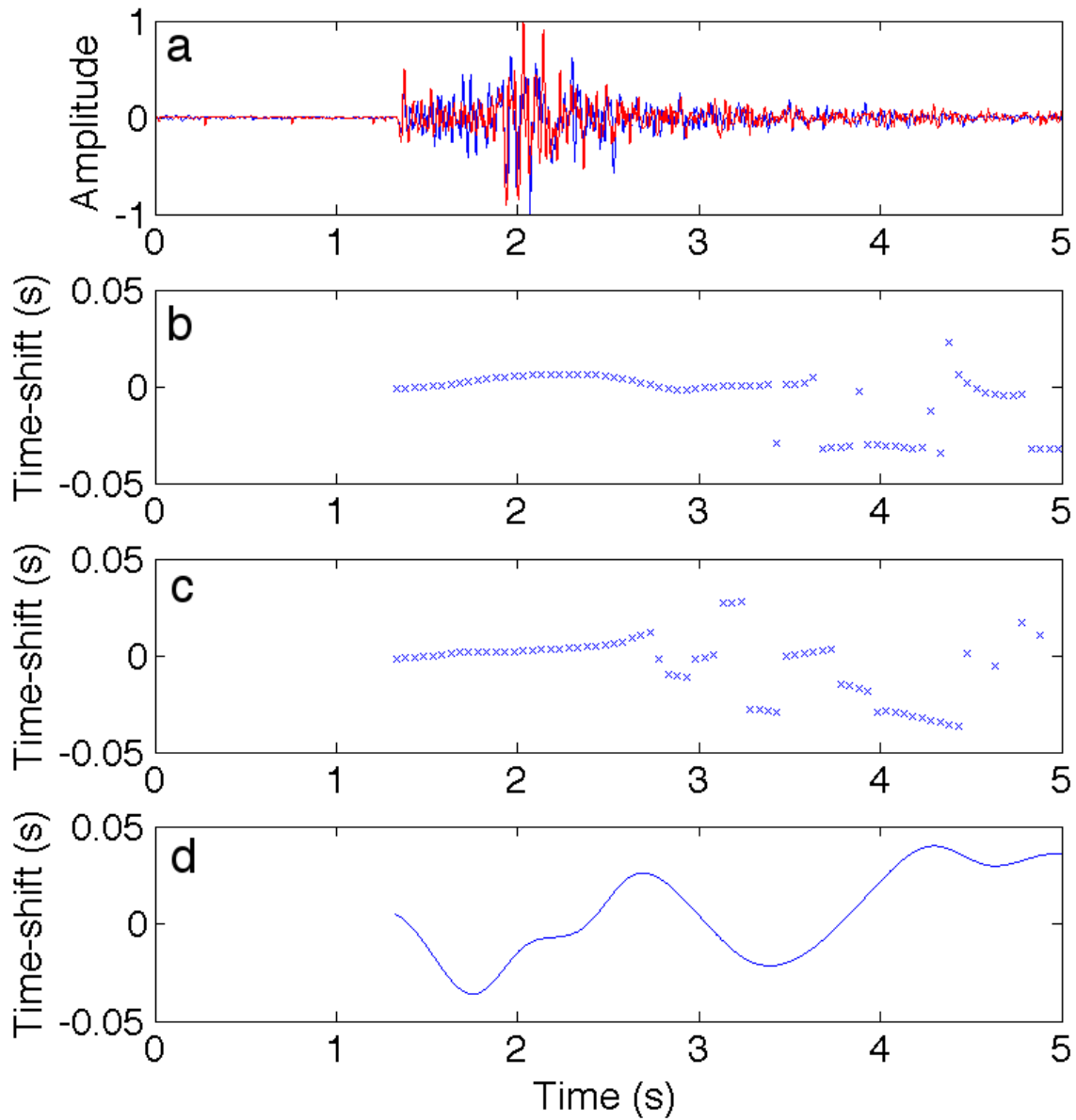


Figure 3.5: Time shifts computed from the unfiltered time-lapse microseismic signals (a) using windowed cross-correlation (b), the windowed stretching method (c), and SDTW (d).

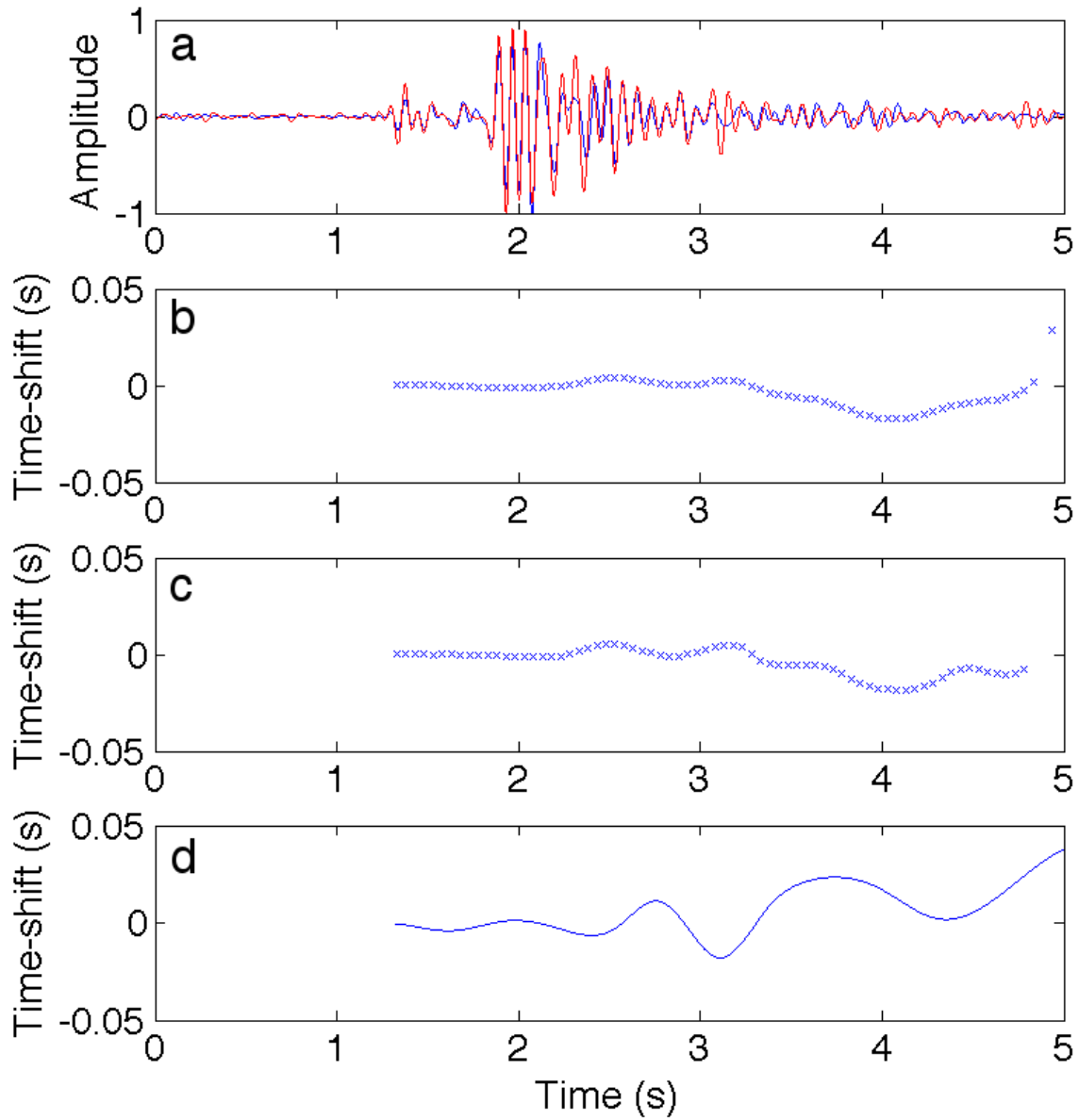


Figure 3.6: Time shifts computed from the 5-15Hz bandpassed time-lapse microseismic signals (a) using windowed cross-correlation (b), the windowed stretching method (c), and SDTW (d).

the SDTW estimates, especially at times with high signal-to-noise ratios. This is due to an averaging effect of the windowing. Late in the coda, for example at $t > 3.5$ s, the windowed cross-correlation and stretching method show more variability in time shifts compared to the early coda. This variability in the late coda is due to the low signal-to-noise ratio; this effect is also noted when computing time shifts using SDTW, as shown in Figure 3.5d. However, the estimated time shifts using SDTW are more continuous. In Figure 3.5d and Figure 3.6d, we bound $\delta v/v_o$ to $\pm 10\%$.

We also compute the time shifts using the filtered time-lapse signals shown in Figure 3.6a to improve our time shift estimates. We filter the high frequency noise from the previously shown time-lapse signals using a 5-15 Hz bandpass filter; this range spans the dominant frequencies of the signal. Figure 3.6 shows estimates of time shifts from these filtered signals using all three methods. These estimates contain smaller time shift variations compared to the time shifts estimated from unfiltered recorded data shown in Figure 3.5. The time shifts computed using SDTW show a larger variability with time compared to the time shifts estimated from windowed cross-correlation and stretching method. The averaging effect of the time windowing of the time-lapse signals via the cross-correlation and stretching methods reduces this variability of the time-shifts across the coda. The estimated time shifts from these three methods are similar from $t = 1$ s to $t = 2.7$ s (Figure 3.6). For traveltimes greater than 2.7 s, the SDTW estimated time shifts deviate from the estimated time shifts that are computed using cross-correlation and stretching methods. The time shifts computed using SDTW are dependent on the sampling of amplitude-aligned grid points and the du/dt constraints used (equation 3.9).

From the time shifts, estimated using SDTW, we compute relative velocity changes using equation 3.8, as shown in Figure 3.7. We vary these relative velocity changes by varying the bounds on the maximum and minimum relative velocity change to: $\pm 5\%$, $\pm 10\%$, $\pm 15\%$, and $\pm 20\%$. As shown in Figure 3.7b, if we vary these constraints, we also vary the resulting relative velocity changes. When the signal to noise ratio is large, the relative velocity change

is consistent, as seen in early times in the signal. When the signal to noise ratio is low, the relative velocity change varies more as we vary the constraints on $\delta v/v_o$. Figure 3.7 can be used to measure the time-varying uncertainty of our relative velocity change estimation. The red points shown in Figure 3.7a align with peaks and troughs of amplitudes in the signals. These points correspond to the grid points used to coarsely sample time shifts in SDTW. Notice a gap in grid points from 0 s to about 1 s; this is gap that we compute by measuring the first arrival time among the time-lapse signals.

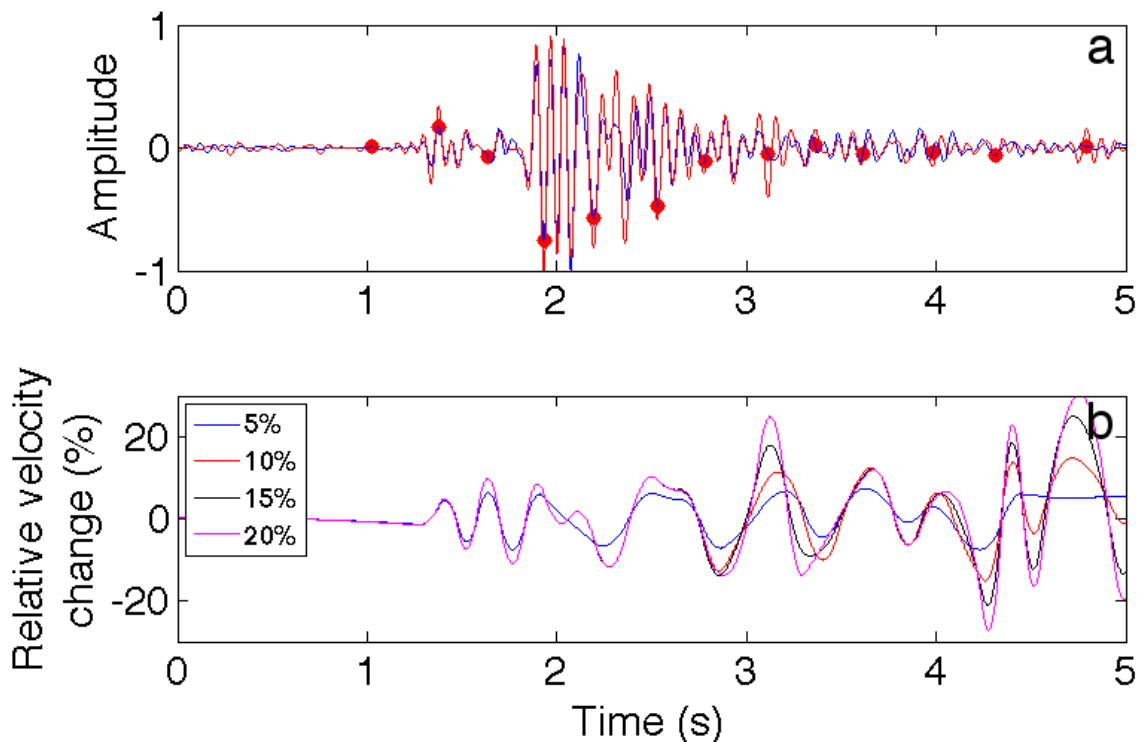


Figure 3.7: Relative velocity changes (b) computed from the 5-15Hz bandpassed time-lapse microseismic signals (a) using SDTW and multiple bounds on du/dt . Time shifts are sampled on an amplitude-aligned coarse grid (red points) (a).

3.5 Monitoring with downhole arrays

To compare the ability of these time shift estimation methods in identifying localized velocity changes within the subsurface, we consider a synthetic example with a time-lapse monitoring source (red) and receiver (blue) setup given in Figure 3.8a that shows both the

velocity (scattering) model and the time-lapse velocity change for our monitoring problem. The velocity model is a 3-layer model with each layer having scattering properties of different statistical characteristics. The statistical characteristics of the top and the bottom scattering layers are homogeneous and structurally isotropic, while the middle layer is heterogeneous and characterizes a highly fractured reservoir. There is a 5% relative velocity change shown in Figure 3.8b in a black rectangle at around 2.75 km in depth. To measure this localized change with time-lapse signals, we use two vertical receiver arrays representing two boreholes lying on opposite sides of the localized change. These arrays record scattered waves generated by the three sources indicated by the red circle in Figure 3.8b. We assume acoustic wave propagation and do not account for the effect of source radiation and elastic wave modes.

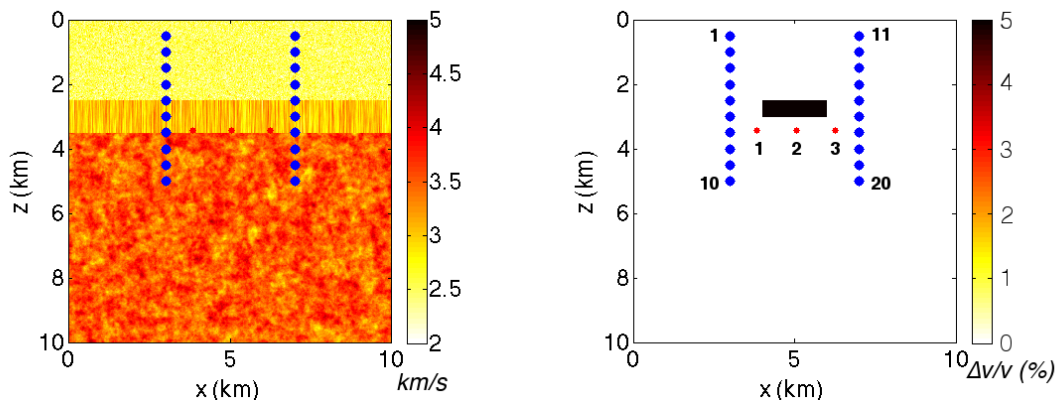


Figure 3.8: Numerical model for time-lapse localized velocity change. The reference velocity (scattering) model (a) with the source-receiver setup, and the exact localized velocity change (b) with the source-receiver setup.

Figure 3.9a and Figure 3.9b show the time shifts and the corresponding relative velocity changes computed using the stretching method and SDTW. The estimated time shifts show similar time shift variation along the coda between methods. Similar to the time shifts estimated from the recorded time-lapse microseismic signals (section 3.4), the variability in the time shifts from SDTW is larger than the time shifts variations from the stretching method. This difference in the time shift variation is a function of how time shifts are estimated with each method.

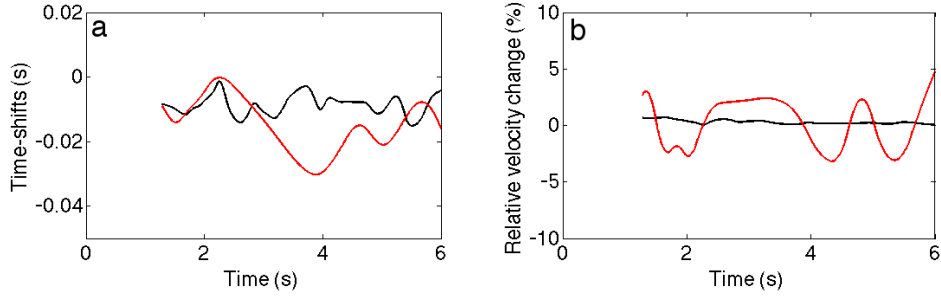


Figure 3.9: A comparison of the estimated time shifts (a) and relative velocity changes (b) using stretching method (black) and smooth dynamic warping (red). These timeshifts and velocity changes are estimated using the time-lapse signals for Source 2 and Receiver 3 pair shown in Figure 3.8.

Time shifts computed using STDW vary more with time compared to the windowed stretching method. Figure 3.9b also shows the time-varying relative velocity changes computed using SDTW and stretching method; SDTW shows more variability in the relative velocity change with time. This estimated velocity change is a fraction of the true velocity change, where the fraction depends on the relative time the scattered wave spends in the region of change relative to the traveltime of the scattered wave [75].

Figure 3.10 shows source-receiver estimated time shifts relative to the location of the velocity change both in the early and late coda. Both time shift estimation methods give similar source-receiver distribution of the time shifts. Early in the coda waves (near $t = 1.6$ s in Figure 3.10a), the estimated time shifts are larger for source-receiver paths that intersect the localized velocity change. This distribution of time shifts in the early coda is also reflected in the estimated velocity changes shown in Figure 3.11. Relative velocity changes computed using SDTW are a better indicator of the magnitude localized velocity change in our model than the relative velocity changes computed using the stretching method but the estimated relative velocity change using SDTW suggests negative velocity change which is not present in the time-lapse model.

Later in the coda (near $t = 3.4$ s in Figure 3.10a), the time shifts average across the source-receiver pairs such that the source-receiver pairs below the region of change are affected by

the localized change. This behavior of the time shifts in the late coda results from scattered waves that travel along paths other than the direct source-to-receiver path. We need the statistical properties of the scattering model to understand the behavior of the time shifts and the scattered waves late in the coda. For more details on the behavior of the scattered waves in a random scattering medium, we refer the reader to Kanu and Snieder [38]. However, the time shifts in the early coda give a preliminary indication of the location of the velocity change.

3.6 Conclusion

In this paper, we compare time shift and relative velocity change estimations using three methods: time shift cross-correlation, stretching method, and smooth dynamic time warping (SDTW). We compare these methods using both synthetic time-lapse signals and recorded time-lapse microseismic signals. The synthetic signals allow for a comparison of the results of the three methods with known exact values, while the recorded microseismic signals allow us to compare the methods in the presence of noise.

Compared to the time shift cross-correlation and the stretching method, time shifts computed using SDTW are more detailed. This is because the SDTW time shifts are computed by optimally aligning two signals. In the time shift cross-correlation and stretching methods, the time shifts and relative velocity changes are estimated within windows. This leads to an averaging of the estimated time shift or velocity change values within the time window, which smooths the variations in the time shifts. However, the averaging by the cross-correlation and stretching methods reduces the impact of signal noise on the time-shift estimations. SDTW may be inaccurate in the presence of noise if time shifts are computed on a finely sampled grid, but if we use an amplitude-aligned coarse grid, the effect of noise on the resulting time shifts is reduced. We are also able to constrain relative velocity changes by imposing constraints on du/dt , thus further limiting potential errors in our time shifts due to noise. We use the amplitude-aligned grid points and constraints on relative velocity changes that minimize the effect of noise and provide an optimal tie of the time-lapse signals. SDTW

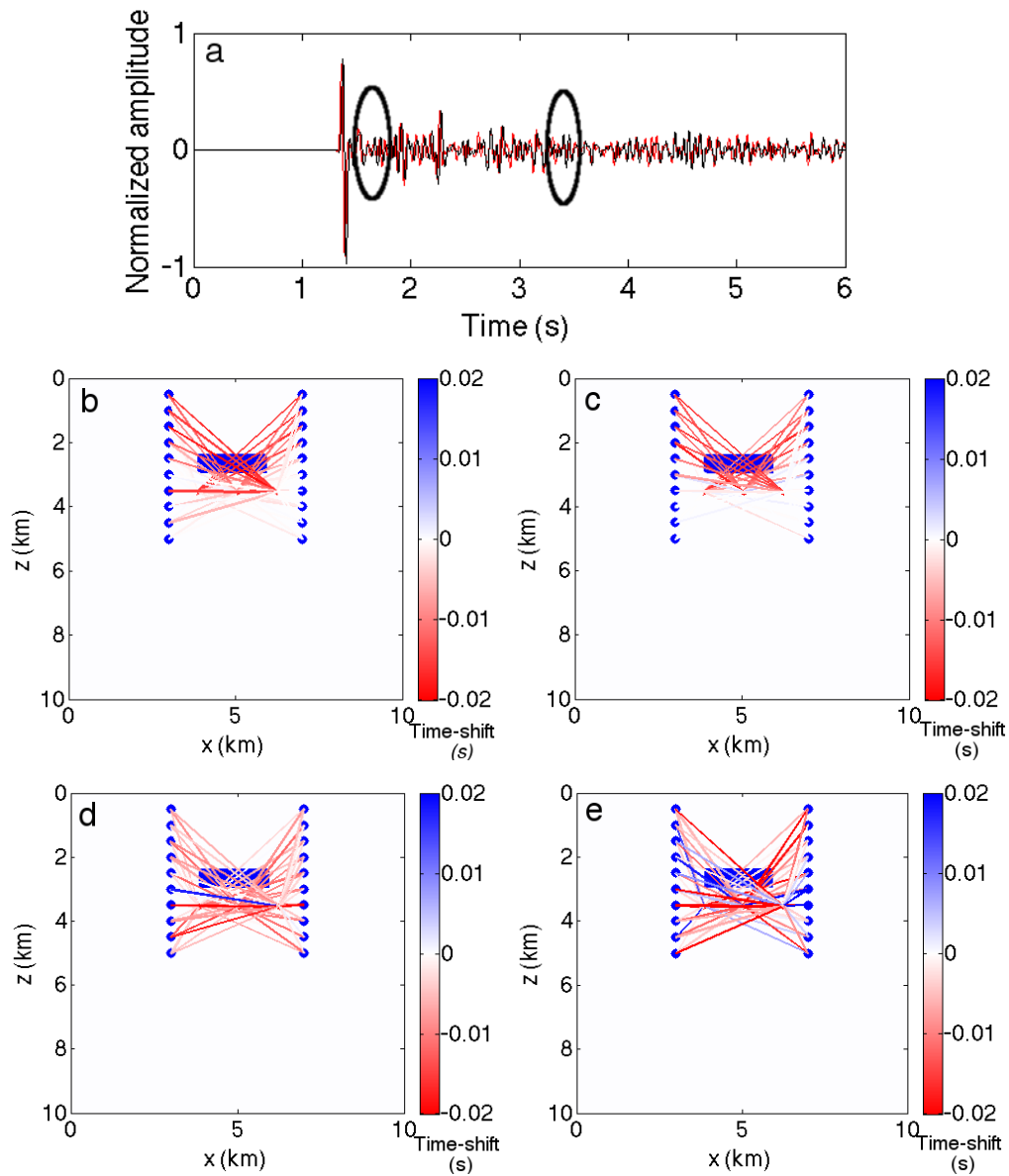


Figure 3.10: The early (near $t = 1.6$ s) and late (near $t = 3.4$ s) coda of the time-lapse signals (a) are highlighted. Time shifts from the early coda are computed using the stretching method (b) and SDTW (c), and time shifts in the late coda are also computed using the stretching method (d) and SDTW (e). The colored lines indicate the magnitude of the estimated traveltime changes.

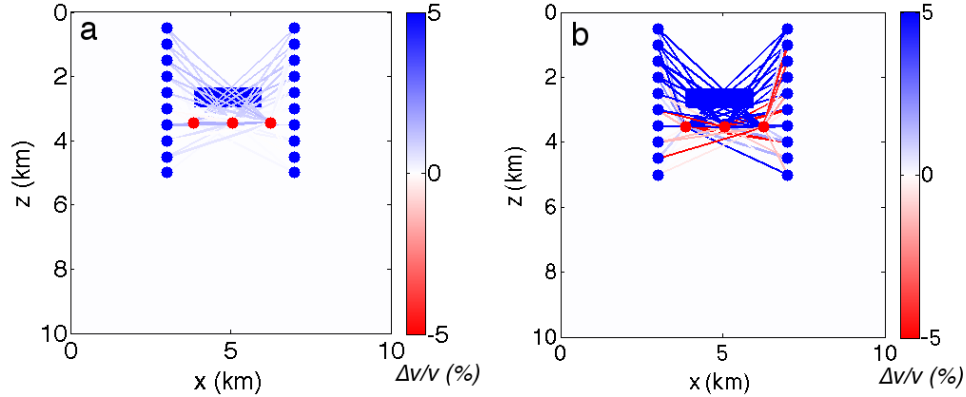


Figure 3.11: Distribution of the relative velocity changes between time-lapse signals computed using the stretching method (a) and SDTW (b) among source-receiver pairs. The velocity changes are estimated using the early part of the time-lapse coda. Blue circles are the receivers while the red circles are the sources. The blue rectangle gives the localized time-lapse velocity change of 5%. The colored lines indicate the magnitude of the estimated relative velocity changes.

is also unaffected by cycle-skipping, which causes errors in estimating time shifts using the cross-correlation method.

3.7 Acknowledgments

We thank the sponsors of the Consortium Project on Seismic Inverse Methods for Complex Structures, whose support made this research possible. We are also grateful to Roel Snieder for initiating the idea of this study, his helpful suggestions, and his witty jokes.

CHAPTER 4

NUMERICAL COMPUTATION OF THE SENSITIVITY KERNEL FOR TIME-LAPSE MONITORING WITH MULTIPLY SCATTERED ACOUSTIC WAVES

Chinaemerem Kanu and Roel Snieder

To be submitted to Geophysical Journal International (2015)

4.1 Abstract

In time-lapse monitoring of weak localized changes within a medium using coda waves, we can either use the resulting decorrelation and/or the phase shift of the coda waves. The formulation for both the decorrelation and the phase-shift of the coda waves resulting from the weak time-lapse changes contains a common sensitivity kernel that is needed to image the weak localized changes. We provide a novel approach to compute the sensitivity kernel which uses numerical modeling (finite difference) of the wavefields from the source and the receiver with an a priori scattering model. These wavefields give the intensities needed to compute the sensitivity kernels. This approach is different from common methods of computing the sensitivity kernel that use analytical approximations of the scattered intensity. The numerical solution of the sensitivity kernel allows us to use arbitrary earth model that may include a free surface without simplifying the property of the scattering model. We demonstrate the behavior of the numerical solution of the sensitivity kernel with end members of heterogeneous scattering models.

4.2 Introduction

Multiple scattering of seismic waves along their travel paths potentially provides information about the subsurface that can be used to increase the resolution of an imaged subsurface (with multiple reflected waves) [8], increase illumination especially within a poorly illuminated subsurface [26, 28] and monitor weak time-lapse changes within the earth's subsurface

[76, 87, 97]. Using scattered waves, especially for monitoring temporal weak changes within the subsurface, we can increase the illumination and resolution of time-lapse changes within a subsurface [10, 52]. Multiply scattered waves are used for monitoring weak changes such as velocity changes as weak as 0.1% [97] and monitoring defects within mechanical structures [55]. However, the complexity in the travel paths of the multiply scattered waves, which depends on the scattering properties of the medium of interest, makes it challenging to accurately describe the origin, travel paths, and distribution of the scattered waves within the medium. In a strongly scattering medium, the multiply scattered waves for late lapse time can be described as a diffusive process [72, 92, 112]. The diffusion model has been used successfully in imaging algorithms that use multiply scattered waves in medical imaging [113] or in imaging of missing scatterers [82]. But, the validity of using the diffusion intensity model in explaining the multiple scattering of waves depends on the strength of the scattering process. Even in a strongly scattering medium, the diffusion intensity model is only accurate at large lapse times, i.e. for $t \gg r/c$, where t is the travel-time, r is the source-receiver distance and c is the average velocity of the medium. Alternatively, the scattered intensity can be modeled using the radiative transfer intensity model, which more accurately predicts the scattered intensity for all scattering regimes [69, 105]. The diffusion and radiative transfer intensity models are analytical models developed under the assumption of a stochastic wave equation. These analytical intensity models, as well as most other intensity models for the scattered waves, are based on homogeneous or simple scattering media. The scattered intensity can easily become complicated if the statistical properties of the scattering medium are heterogeneous. We show that for more realistic media, a more accurate scattered intensity can be modeled numerically using, for example, finite-difference modeling rather than using the analytical intensity models.

Time-lapse changes within the earth's subsurface (both natural and induced) are usually either gradual, weak, or localized both in space and time. Detecting these changes in many cases requires data that are highly sensitive to the changes. Vlastos et al. [108] show that

the sensitivity of multiply scattered waves to the weak changes is significantly higher than the sensitivity of the ballistic or direct part of the seismic waves to the weak changes. This increase in the sensitivity is due to the repeated sampling of the weak velocity changes by the scattered waves [81]. The high sensitivity of the multiply scattered waves has led to successful detection of time-lapse velocity changes within the earth’s subsurface. Poupinet et al. [76] use coda waves generated by repeating earthquakes to observe an average S wave velocity change of 0.2% after the 1979 M_w 5.9 Coyote Lake earthquake on the Calaveras Fault, California. Using correlation functions generated from seismic noise, Wegler and Sens-Schönfelder [111] detect a sudden decrease in the seismic velocity of the region surrounding the 2004 M_w 6.6 Mid-Niigata earthquake rupture. Using controlled-source monitoring Nishimura et al. [64] detected a velocity decrease of 0.3-1.0 % due to the 1998 M_w 6.1 Mount Iwate earthquake. However, Pacheco and Snieder [70] show that the spatial sensitivity of the multiply scattered waves to the time lapse changes is not uniformly distributed but is dependent on the source and receiver locations.

Most time-lapse monitoring of weak changes within the earth’s subsurface using multiply scattered waves has been limited to identifying weak changes rather than localizing these changes. Except in very densely distributed source and receiver set-ups, the velocity changes detected by coda wave interferometry are spatially averaged velocity changes. Recently, successful efforts have been made not only in identifying the weak changes using multiply scattered waves, but also in localizing the changes in a statistically homogeneous scattering medium [82]. However, to localize changes within the earth’s subsurface - a scattering medium which is most likely to be inhomogeneous - we will need to appropriately handle the inhomogeneities of the earth’s subsurface. Because of the prominence of surface waves, we also need to account for the presence of a free surface.

In this study, we explore the capability of computing the sensitivity kernel that we need for time-lapse monitoring and localizing the weak changes within a medium. In the next subsection, we describe the theoretical connection of the sensitivity kernel to the estimated

time lapse time-shifts or the decorrelations in the time lapse scattered waves resulting from the weak changes. In section 4.4, we develop a novel approach for computing the kernel numerically for any scattering model and explore the behavior of the kernel using various end-member scattering models. In section 4.5, we discuss the practicality of the kernel computation.

4.3 Sensitivity Kernel

Pacheco and Snieder [70] use the intensity of multiply scattered waves to develop a sensitivity kernel $K(\mathbf{s}, \mathbf{x}_o, \mathbf{r}, t)$ which relates the mean travel time changes $\langle \tau \rangle$ to the localized relative velocity change within the subsurface $\delta v/v(\mathbf{x}_o)$:

$$\langle \tau(t) \rangle = - \int_V K(\mathbf{s}, \mathbf{x}_o, \mathbf{r}, t) \frac{\delta v}{v}(\mathbf{x}_o) dV(\mathbf{x}_o), \quad (4.1)$$

where t is the travel-time of the scattered wave, V is the scattering volume, and \mathbf{s} and \mathbf{r} are the source and the receiver locations, respectively. The sensitivity kernel $K(\mathbf{s}, \mathbf{x}_o, \mathbf{r}, t)$ depends on the source and receiver locations, the scattering property of the medium, and the travel-time of the scattered wave.

Rossetto et al. [82] consider a different problem where the local scattering strength changes. This change is accounted for by a change in scattering cross-subsection $\delta\sigma(\mathbf{x}_o)$. Using the correlation function $C(\mathbf{s}, \mathbf{r}, t)$ of the multiply scattered waves in a medium with this time-lapse change, they relate the decorrelation $1 - C(\mathbf{s}, \mathbf{r}, t)$ of the time lapse scattered waves to the time lapse change in the total scattering cross-subsection of the medium:

$$1 - C(\mathbf{s}, \mathbf{r}, t) = \int_V \frac{v(\mathbf{x}_o)\delta\sigma(\mathbf{x}_o)}{2} K(\mathbf{s}, \mathbf{x}_o, \mathbf{r}, t) dV(\mathbf{x}_o). \quad (4.2)$$

Using either the time-shifts or the decorrelation values from the time-lapse multiply scattered waves for resolving localized weak changes, the sensitivity kernel $K(\mathbf{s}, \mathbf{x}_o, \mathbf{r}, t)$ forms the building block for the Fréchet derivatives needed to resolve the weak changes. The

sensitivity kernel $K(\mathbf{s}, \mathbf{x}_o, \mathbf{r}, t)$ is given by

$$K(\mathbf{s}, \mathbf{x}_o, \mathbf{r}, t) = \frac{\int_0^t P(\mathbf{s}, \mathbf{x}_o, t') P(\mathbf{x}_o, \mathbf{r}, t - t') dt'}{P(\mathbf{s}, \mathbf{r}, t)}, \quad (4.3)$$

where P is the normalized intensity of the multiply scattered waves [70].

The normalized intensity in a homogeneous scattering medium in the diffusion approximation is given by [69]:

$$P(\mathbf{s}, \mathbf{r}, t) = \frac{1}{(4\pi Dt)^{d/2}} \exp\left(-\frac{R_{sr}^2}{4Dt}\right), \quad (4.4)$$

where d is the dimension of the scattering medium, $R_{sr} = |\mathbf{r} - \mathbf{s}|$ is the source-receiver distance and D is the diffusion coefficient. The normalized intensity can also be described by the radiative transfer model. The 2D radiative transfer intensity [69] is

$$P(\mathbf{s}, \mathbf{r}, t) = \frac{\exp(-vt/l)}{2\pi R_{sr}} \delta(vt - R_{sr}) + \frac{1}{2\pi lvt} (1 - R_{sr}^2/v^2t^2)^{-1/2} \times \exp\left(\sqrt{v^2t^2 - R_{sr}^2}/l - vt\right) \Theta(vt - R_{sr}), \quad (4.5)$$

where l is the scattering mean free path length; δ and Θ are the Dirac delta and the Heaviside step functions, respectively. Complex heterogeneous models require a more complex mathematical intensity model to describe the intensity of the scattered waves [54]. These complex heterogeneous media include heterogeneously layered media [36, 53] and media with nondiffusive regions [78]. In addition, one may also need to account for the presence of a free surface.

4.4 Numerical computation

For most scattering media, especially for complex heterogeneous scattering media, one might need to compute the sensitivity kernel $K(\mathbf{s}, \mathbf{x}_o, \mathbf{r}, t)$ numerically. For these scattering media, one might not have an exact analytical formulation for either the intensity of the scattered waves or the corresponding sensitivity kernel for imaging the weak changes. Using

equation 4.3 and a model of the scattering medium, we can numerically compute the sensitivity kernel by simulating the scattered wavefield with the scattering model, then compute the intensity field from the simulated wavefield. However, the numerical computation of the sensitivity kernel depends on how well one knows the statistical properties of the scattering medium. The characteristics of the heterogeneous medium, such as the scattering mean free path length and the average velocity, can be estimated from the analysis of the coda waves in the recorded data or using additional information such as velocity values from well log measurements when available or a velocity model obtained from other geophysical methods.

In the following subsection, we compute the sensitivity kernel using equation 4.3. We generate the source and receiver wavefields by numerical computation of waves excited at the source and receiver locations, respectively. Here, we use acoustic modeling. We also use absorbing boundary conditions at the boundaries of our models. We do not account of effects due free-surface boundary conditions except in the model with variable topography (subsection 3.3). The respective normalized intensities are the square of the envelope of the generated wavefields normalized by the spatial integral of the intensity $\int_V P(\mathbf{x}_o, t) dV(\mathbf{x}_o)$ [86]. The normalization of the scattered intensity removes imprint of the the source time function from the acoustic intensity field. To compute the sensitivity kernel $K(\mathbf{s}, \mathbf{x}_o, \mathbf{r}, t)$, we convolve the source and the receiver intensity fields and normalize with the denominator in equation 4.3. We simulate the wavefields with finite difference modeling using a realization of a von-Karman random velocity model [86]. The 2D von-Karman power spectral density function (PSDF) \tilde{P}_{2D} is given by

$$\tilde{P}_{2D}(k_x, k_z) = \frac{4\pi\Gamma(\kappa + 1)\epsilon^2\sqrt{a_x^2 + a_z^2}}{\Gamma(\kappa)(1 + [k_x^2 a_x^2 + k_z^2 a_z^2])^{\kappa+1}}, \quad (4.6)$$

where κ is the von-Karman exponent, ϵ is the fluctuation strength of the scattering model, a_x and a_z are the correlation lengths along the x - and z - directions, respectively, and k_x and k_z are the wavenumbers along the x - and z - directions, respectively. The correlation length is $a = \sqrt{a_x^2 + a_z^2}$. A wide range of values have been associated with the von-Karman

parameters for the earth subsurface. The values of the von-Karman parameters depend on the subsurface lithology and the depth of the subsurface. Using the autocorrelation function of surface rock samples from Westerly and Oshima granite, Spetzler et al. [101] estimate for the Westerly granite $\epsilon = 8.5\%$ and $a = 0.22\text{ mm}$ while $\epsilon = 9.3\%$ and $a = 0.46\text{ mm}$ for the Oshima granite. Yoshimoto and Sato [114], using 149 waveforms in the frequency band of 8 - 16 Hz from 10 earthquakes occurring at depths shallower than 10 km , estimates the range of ϵ and a values to be 5 - 8 % and 0.3 - 0.8 km , respectively, in the Nilko area of Japan.

The scattering model we use for kernel computation consists of the random velocity fluctuations defined by the von-Karman parameters and constant density. The velocity model is given as

$$v(\mathbf{x}) = v_0(\mathbf{x})[1 + \zeta(\mathbf{x})], \quad (4.7)$$

where $v_0(\mathbf{x})$ is the background velocity and $\zeta(\mathbf{x})$ is a realization of the random velocity fluctuation for the von-Karman PSDF in equation 4.6 [86].

4.4.1 Numerical vs. analytical computation

The sensitivity kernel can be estimated from analytical models of the scattered intensity (the diffusion and radiative transfer approximation of the scattered intensity). To compare the analytical and numerical solution of the sensitivity kernel, we use a von-Karman scattering model defined by the following parameters: $a_x = a_y = 0.01\text{ km}$, $\epsilon = 0.1$, $\kappa = 0.5$, and $f = 15\text{ Hz}$ ($\lambda = 0.23\text{ km}$). This scattering model and the dominant scattering wavenumber correspond to $ka \simeq 0.27$. The scattering velocity model is given in Figure 4.1 with an average velocity of 3.5 km/s . The theoretical scattering mean free path length (l_{VK}) and transport mean free path length (l_{VK}^*) for these von-Karman parameters and the scattered waves are 5.7 km and 6.9 km , respectively [86].

We compute the analytical solution of the sensitivity kernel by using the corresponding theoretical mean free path lengths and the approximations of the scattered intensity using the diffusion (equation 4.4) and the radiative transfer (equation 4.5) models. We also convolve

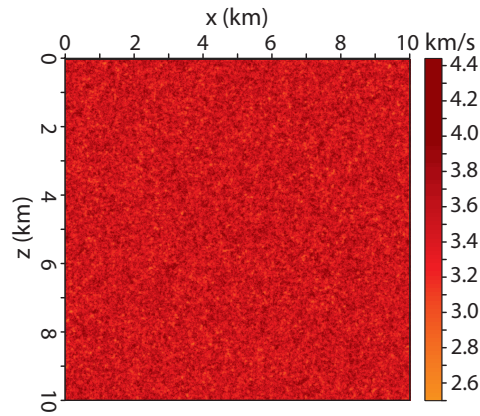


Figure 4.1: Velocity model for numerical computation of sensitivity kernel for comparison with the analytical solution.

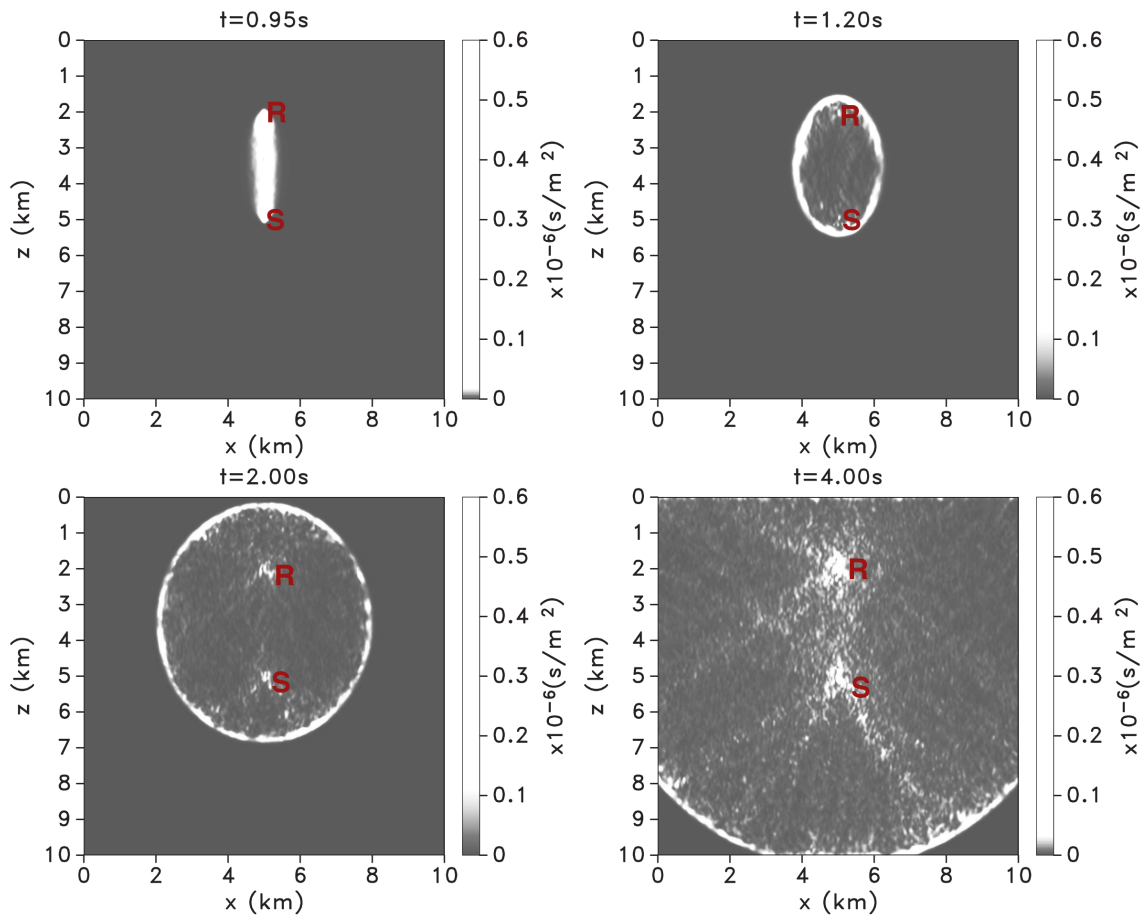


Figure 4.2: Temporal and spatial evolution of the sensitivity kernel (numerical solution).

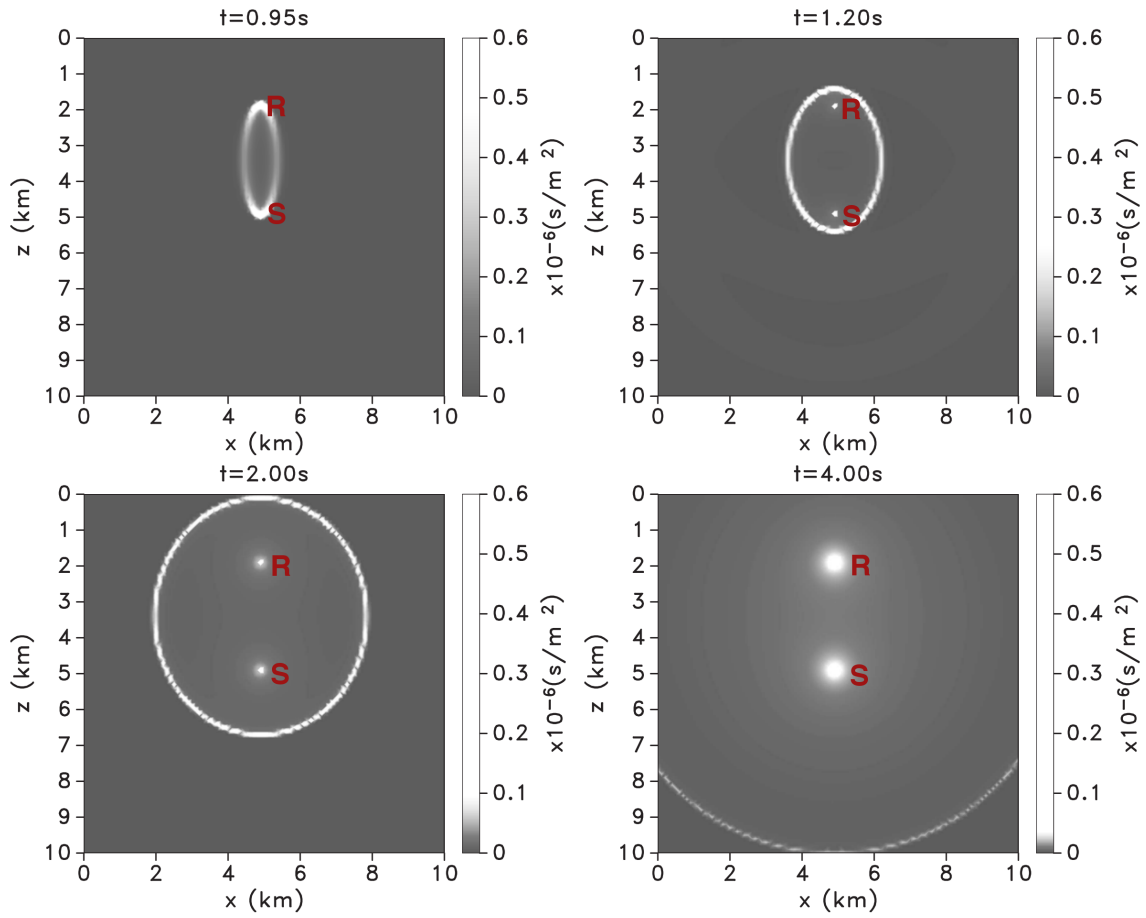


Figure 4.3: Temporal and spatial evolution of the sensitivity kernel using the radiative transfer model.

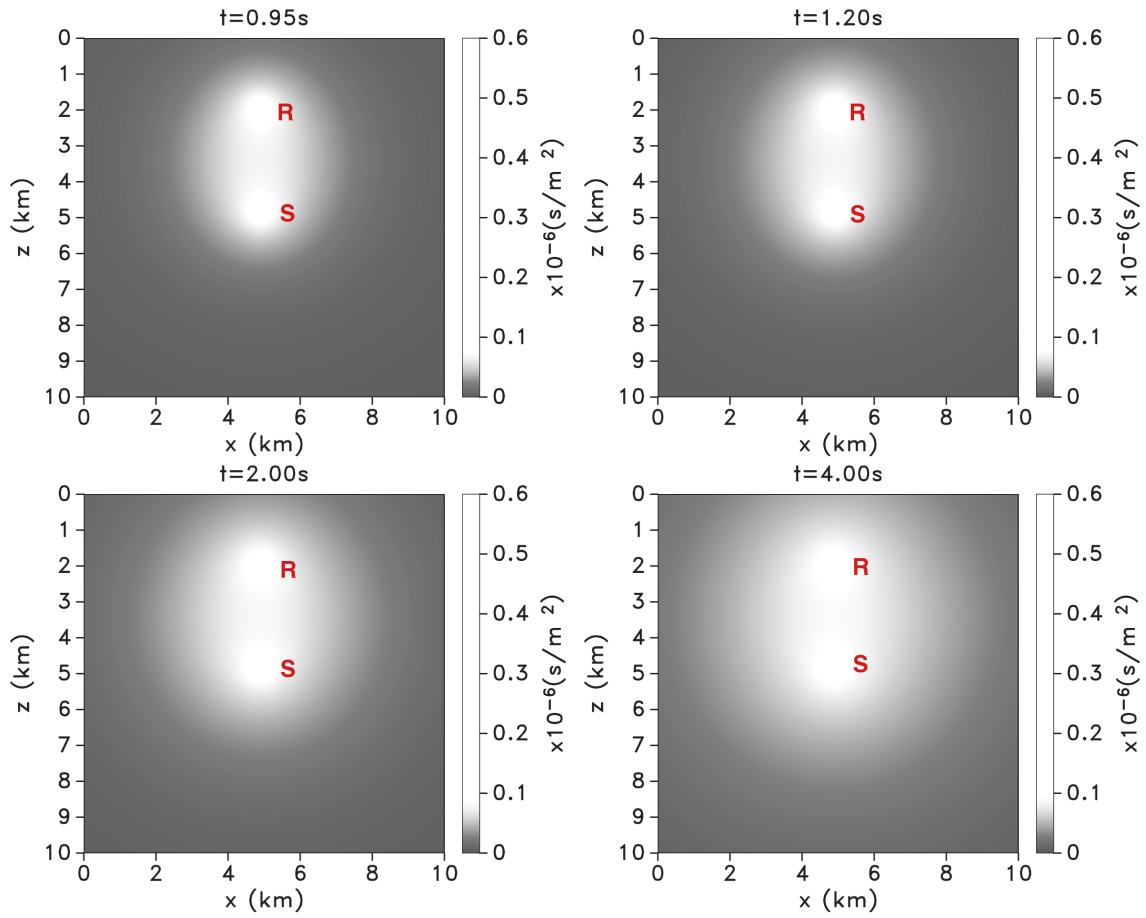


Figure 4.4: Temporal and spatial evolution of the sensitivity kernel using the diffusion model.

the analytical intensities with the intensity of the source wavelet used for the computation of the numerical kernel. Figure 4.2, Figure 4.3 and Figure 4.4 show time snapshots of the temporal evolution of the sensitivity kernel for both the numerical and the analytical solutions, respectively. In Figure 4.2, Figure 4.3 and Figure 4.4, the time-shots are taken at 0.95 s, 1.20 s, 2.00 s, and 4.00 s. The numerical solution of the sensitivity kernel is bound by the a kernel front which is defined as the edge of the kernel that is dominantly composed of single scattering and bounds the multiple scattering contributions. The numerical sensitivity kernel shows similar features represented in the radiative transfer model (Figure 4.3) of the sensitivity kernel including the direct line-of-sight characteristic of the ballistic kernel (0.95 s) and the elliptical shape of the kernel front at lapse times after the first arrival time. The major difference between the numerical kernel and the radiative transfer kernel is the fluctuations in the numerical kernel. The numerical kernel in Figure 4.2 is computed with one realization of the scattering model. These kernel fluctuations are suppressed by averaging the numerical kernel over many realizations of the scattering model. The diffusion approximation of the sensitivity kernel (Figure 4.4), as expected, only reproduces the spatial features of the kernel at long lapse times ($ct/R_{sr} \gg 1$) [69] with no clear ellipsoidal edge. Figure 4.5 shows a cross-subsection of the kernel along the source-receiver line. The diffusion kernel fails to explain the zero or near-zero sensitivity of the kernel beyond the kernel front, evident in both the numerical and the radiative transfer kernels.

The spatial and temporal behavior of the kernel implies that to resolve time-lapse changes within a scattering medium with homogeneous statistical properties, the radiative transfer kernel can closely substitute for the numerical kernel solution. Figure 4.5 shows that the numerical kernel has more fluctuations compared to the analytical solutions. This numerical kernel is computed with one realization of the scattering model. The kernel fluctuations which are due to isolated scatterers within the scattering model, are present in the multiply scattering contribution to the kernel. We can suppress the kernel fluctuations by averaging the kernel over a number of the realizations of the scattering model with the same statistical

properties. Figure 4.6 shows the averaged kernel at travel-time 2.00 s over 1, 5, 10 and 20 realizations of the scattering model. Increasing the number of realizations of the model used for the kernel computation reduces the fluctuations both at the singly scattered and multiply scattered part of the kernel. With few realizations of the random model (5-10 realizations) we can achieve stability in the sensitivity kernel (Figure 4.7).

4.4.2 Scattering Velocity models

Random isotropic scattering model

Figure 4.2 shows the kernel for a given source-receiver pair (S-R) at the following time snapshots: 0.95 s , 1.20 s , 2.00 s , and 4.00 s . The direct wave excited by a source S arrives at the receiver R at travel-time $t = 0.90 s$ with an average velocity of 3.5 km/s . The time snapshots of the kernel shown in Figure 4.2 show the sensitivity to the changes in the scattering model for the scattered phases arriving at a specific travel-time t . The kernel at $t = 0.95 s$ corresponds to the sensitivity of scattered waves dominated by direct and forward scattered waves. With increasing time, the area covered by the sensitivity kernel progressively increases. The spatial broadening of the kernel with time increases the detectability of any change in the scattering property of the medium due to multiple interaction between the scattered waves and the change with time, especially changes away from the path of the direct wave (which is along the source-receiver line in this case). However, the resolving power of the kernel is expected to decrease with increasing time because of the spatial broadening of the kernel. The shape of the kernel with increasing time depends on the source and receiver locations, the corresponding travel-time, and the properties of the scattering medium. At times $t > 0.95 s$, the kernel assumes an elliptical shape with the major axes along the source-receiver line and the minor axes perpendicular to the source-receiver line. The edge of the kernel is dominated by contributions from single scattering. The kernel for the singly scattered waves is given by [71]

$$K(\mathbf{x}_o, t) = \frac{1}{2\pi h \sqrt{(ct/R_{sr} - 1)}} \left[\frac{r_s}{s} + \frac{r_r}{r} \right], \quad (4.8)$$

where s and r are the distances from the point \mathbf{x}_o to the source and receiver, respectively; r_s and r_r are the distances from any point on the kernel front to the source and receiver, respectively.

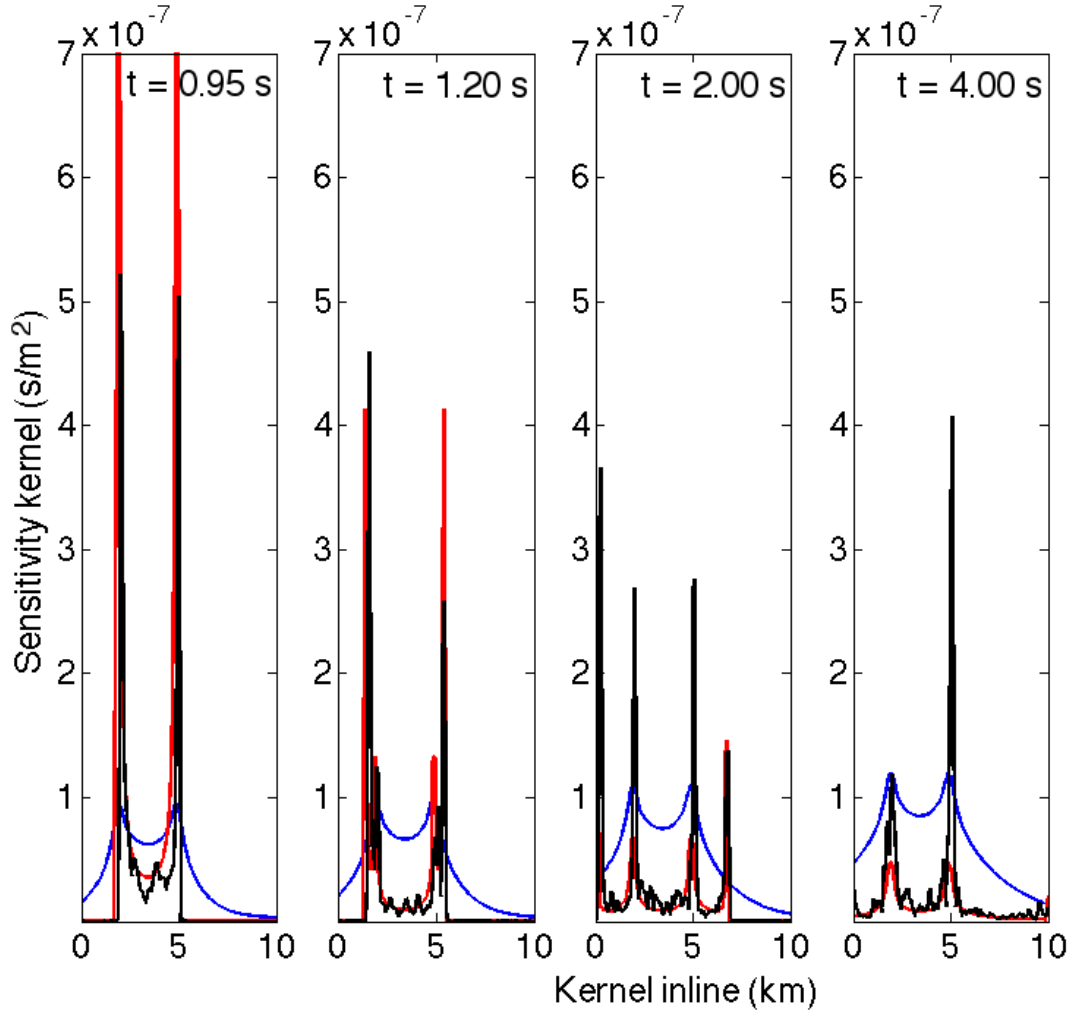


Figure 4.5: Comparison between numerical sensitivity kernel (black line) and diffusion- (blue line) and radiative transfer- (red line) based kernel along the source- (at 2 km) receiver- (at 5 km) line.

The single-scattering-dominated part of the kernel spatially bounds the multiple scattering part of the kernel. The inner part of the kernel accounts for multiple scattering, which has lower amplitude compared to the kernel contribution from the single scattering. Within the multiple-scattering-dominated part of the kernel, there are high sensitivities at

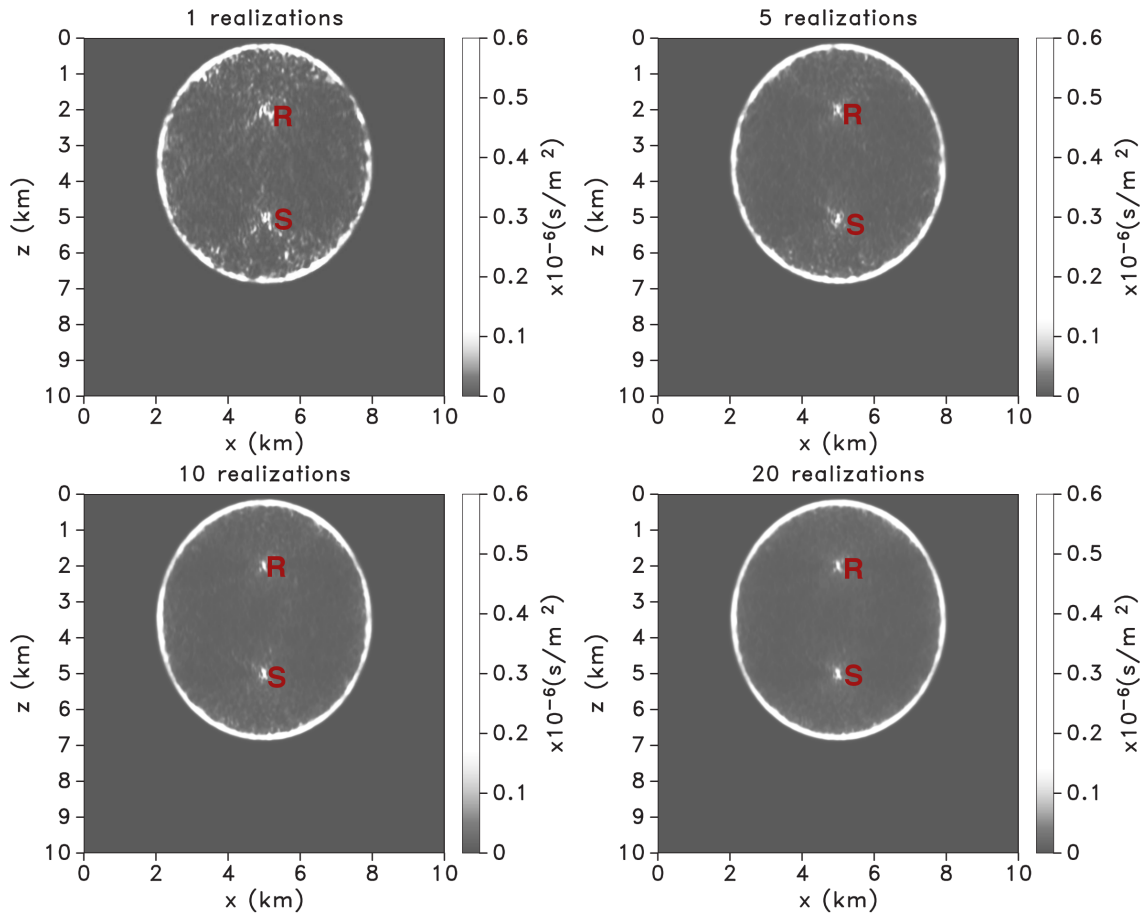


Figure 4.6: Comparison of the kernel at $t = 2.0$ s using a number of scattering model realizations

the source and receiver locations which are predicted accurately by the analytical solutions in Figure 4.5. These high sensitivities at or near the source and receiver locations suggest that the dominant contribution to the multiply scattered waves recorded at receiver R due to a source S originates from scattering near the source and receiver locations.

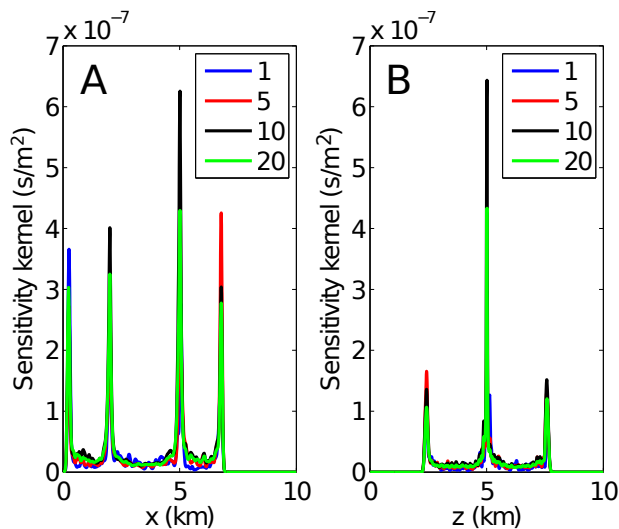


Figure 4.7: The inline subsection (A) and the crossline subsection (B) of the kernel at $t = 2.0$ s after averaging over 1, 5, 10, and 20 realizations of the scattering model with the same statistical properties.

Random non-isotropic scattering model

The scattering properties within the earth's subsurface are generally complex and inhomogeneous. The scattering characteristics of the subsurface can vary from place to place depending on both the underlying lithology and overlaying stress conditions of the local and regional subsurface. The scattering properties of the earth's subsurface also vary with depth [93]. The stress- and depth- dependent scattering properties of the subsurface controls the scattering process of the seismic wave traveling through the subsurface. The effective scattering of the subsurface are defined by both the scattering properties of the subsurface and the characteristics of the incident seismic phase that is scattered. The characteristics of the incident phase include the incidence angle of the wave, the spectral properties of the incident wave, and the wave mode of the incident wave [45].

To explore the dependence of the sensitivity kernel on the scattering medium, we test two scattering models whose background velocity is a 3-layered velocity model. In both models (Figure 4.8 and Figure 4.11), the top and bottom layers have the same scattering properties given by the von-Karman PSDF. For the top layer, $\kappa = 0.5$, $\epsilon = 0.5$, and $a_z = a_x = 0.05 \text{ km}$; for the bottom layer, $\kappa = 0.8$, $\epsilon = 0.1$, and $a_z = a_x = 0.1 \text{ km}$. However, in the middle layer, one model consists of vertical velocity perturbations while the other model is composed of horizontal velocity perturbations. The model with vertical velocity perturbations mimics a highly vertically fractured reservoir while the model with horizontal velocity perturbations represents a shale-like reservoir with a thin laminated layering. The middle layer for both models is defined by the following von-Karman parameters. For the vertically fractured model, $a_z = 0.5 \text{ km}$ and $a_x = 0.0001 \text{ km}$; for the shale-like model, $a_z = 0.0001 \text{ km}$ and $a_x = 0.5 \text{ km}$. In both models, $\kappa = 0.1$ and $\epsilon = 0.5$ for the middle layer. In both scattering models, we compute the sensitivity kernels using two source-receiver configurations. In one configuration, the source-receiver line is vertical while in the second configuration the source-receiver line is horizontal and is embedded within the middle layer. These source-receiver configurations resemble a source such as a microseismic event or an earthquake embedded within the subsurface with either a receiver at the near surface (for the vertical source-receiver line) or a receiver within a borehole (for the horizontal source-receiver line).

Figure 4.9 and Figure 4.10 give time snapshots of the sensitivity kernel in the vertically fractured model for the vertical and horizontal source-receiver configurations, respectively. In both source-receiver configurations, the kernels show many of the features present in the kernel of the random isotropic model (Figure 4.2), which include the spatial broadening of the kernel with increasing time, the high sensitivity at the source and receiver locations, and the presence of the single scattering contributions to the kernel at the kernel front. However, the heterogeneity in the scattering model introduces extra features to the kernel of the vertically fractured model which are not present in the random isotropic kernel (Figure 4.2). In both source-receiver configurations, the width of the kernel (along the minor axes of the kernel)

at each layer of the model depends on the effective velocity in that layer (see Figure 4.9 and Figure 4.10 at $t = 2.50$ s). In the vertical source-receiver configuration at $t = 2.50$ s and 5.00 s, there are extra scattered fronts marked as S'' within the kernel; these fronts are secondary scattered intensity fronts due to reflections from the layer interfaces in the model. These reflected fronts lag behind the singly scattered front. In the horizontal source-receiver configuration (Figure 4.10), the direct wave refracts through the top interface of the bottom layer because of the higher velocity of the bottom layer (Figure 4.10 at $t = 1.38$ s). A few milliseconds later, many of the forward scattered waves are confined within the middle layer (Figure 4.10 at $t = 1.40$ s). At later lapse times, the singly scattered kernel front propagates out from the middle layer into the top and the bottom layers. The extent of the front propagation depends on the average velocity of the layer. The reflected wavefronts S'' seen in the vertical source-receiver configuration are absent in the kernel with the horizontal source-receiver configuration. This is because the reflectors are parallel to the source-receiver line in the horizontal configuration. The sensitivity is dominant within the middle layer because the vertical velocity perturbations within the middle layer persistently reflects back and forth waves traveling horizontally between the source and the receiver. The orientations of the velocity perturbations are perpendicular to the dominant forward propagation of the waves which is along the source-receiver line (Figure 4.10 at $t = 2.50$ s and 5.00 s). This dominance of the kernel in the middle layer is not present with the vertical source-receiver setup (Figure 4.9), where in the middle layer the wave propagation direction is along the direction of the velocity perturbation. The lack of the kernel dominance within the middle layer with a vertical source-receiver setup is because of the relative orientation of the source-receiver line and the orientation of the scatterers which results to minimal scattering of the waves compared to the horizontal source-receiver setup. Also the scattered waves recorded at the receiver has a higher probability of exploring the whole model space without being trapped within middle layer due to scattering. With the horizontal source-receiver setup, much of the recorded scattered waves are generated within the middle layer.

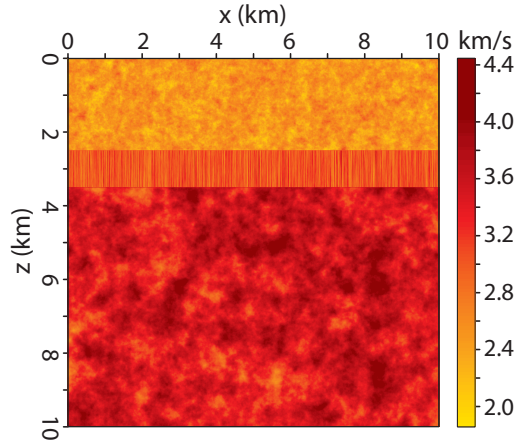


Figure 4.8: Velocity model with a vertical-fractured-like reservoir.

Figure 4.12 and Figure 4.13 give time snapshots of the sensitivity kernel in the shale-like model using the vertical and horizontal source-receiver configurations, respectively. The kernel for the shale-like model, which uses a vertical source-receiver configuration, exhibits similar features present in the vertically fractured model with a similar source-receiver setup. Differences in the kernels are in the multiply scattered part of the kernel in the middle layer of the vertically fractured model where there are more scattering close to the source. However, with the horizontal source-receiver configuration (Figure 4.13), the kernel at late lapse time ($t = 2.50$ s and 5.00 s) shows features different from those present in the kernel with the vertically fractured model using the horizontal source-receiver configuration. The high sensitivity present in the vertically fractured model using the horizontal source-receiver setup is absent from the model with the horizontal velocity perturbation in the middle layer because the direction of wave propagation between the source and the receiver is parallel to the velocity layering in the middle layer, which results in relatively less scattering of the seismic wave. The effect of the source-receiver setup on the kernel behavior implies that the setup of the source and receiver pairs relative to the location of a particular time-lapse change within a scattering medium has large implications for the capability of detecting and resolving

the time-lapse change. For example, if there is a change in the middle layer, the horizontal source-receiver setup provides a better scenario for detecting and resolving the time-lapse change in the middle layer than will the vertical source-receiver setup. This connection between the source-receiver setup and the behavior of the sensitivity kernel suggests the need for the source and receiver to be in close proximity to the location of the time-lapse change. The relative direction of the forward scattering between the source and the receiver to the orientation of the length of the scatterers impacts the relative magnitude of the sensitivity of the scattered intensity to the time-lapse change. This impact is evident in a comparison of the kernel strength in the middle layers of the vertically fractured model to the kernel strength in the middle layer of the shale-like model. The relative strength of the kernel is higher in the vertically fractured model where the perpendicular alignment of the scatterers allows for a stronger generation of multiply scattered waves.

The kernels at early lapse times are almost identical in both models (Figure 4.9, Figure 4.10, Figure 4.12 and Figure 4.13 at $t = 1.38 s$ and $1.40 s$). The kernels at these times consist of mainly direct, refracted, and forward scattered waves.

4.4.3 Topography-induced Scattering

Seismic waves are not only scattered by heterogeneities within the earth's subsurface, but also by near-surface heterogeneities such as variable topography or low velocity unconsolidated lithology in the near-surface layers. Due to the high impedance contrast across the free surface and the higher heterogeneities within the near-surface compared to the heterogeneities deeper in the subsurface [93], the multiple scattering from variable topography and near-surface scattering effects can dominate bulk scattering. Rough or variable topography plus the presence of the free surface can focus or defocus seismic waves and can convert seismic waves from one wave mode to another such as conversion of body waves to surface waves and vice versa [45]. Bouchon et al. [11] show that a simple symmetric ridge can induce amplification of a monochromatic SH wave by up to a factor of 1.5 at the crest of the ridge. The amplification factor of the incident wave depends on the incident angle of the wave and

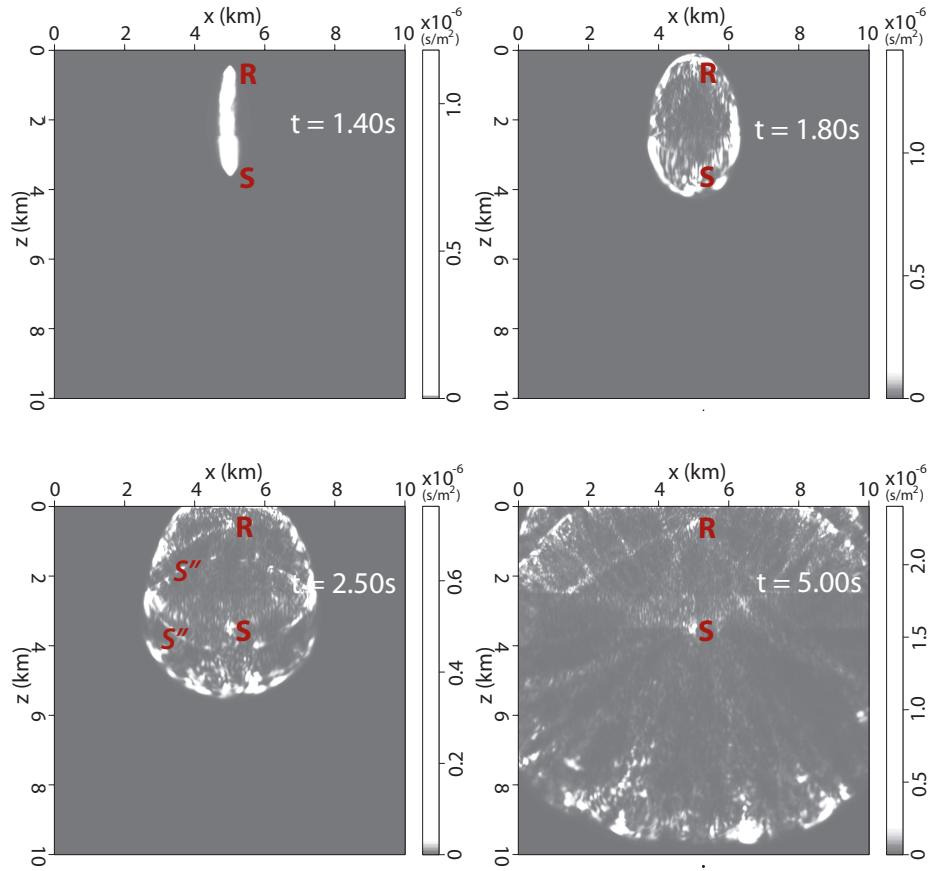


Figure 4.9: Temporal and spatial evolution of the sensitivity kernel (numerical solution) in a reservoir with vertical-fractured-like velocity perturbation with a near-surface receiver. S'' corresponds to the reflected scattered phase.

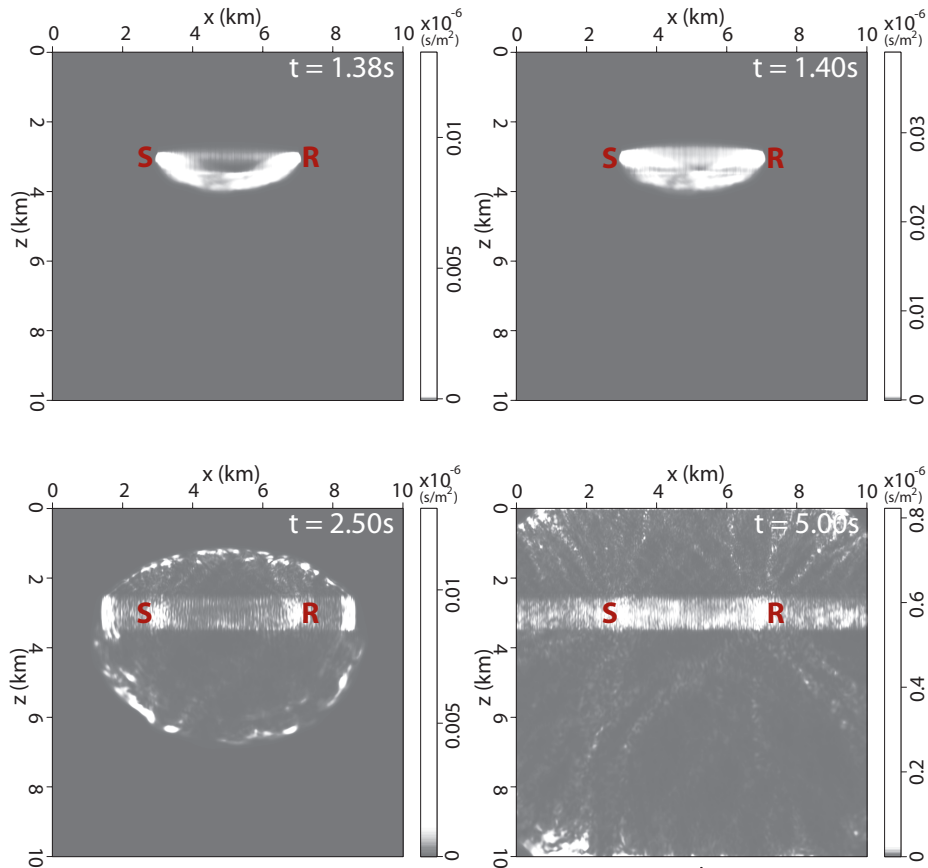


Figure 4.10: Temporal and spatial evolution of the sensitivity kernel (numerical solution) in a reservoir with vertical-fractured-like velocity perturbation with a receiver within the reservoir.

the height to width ratio of the topography perturbation.

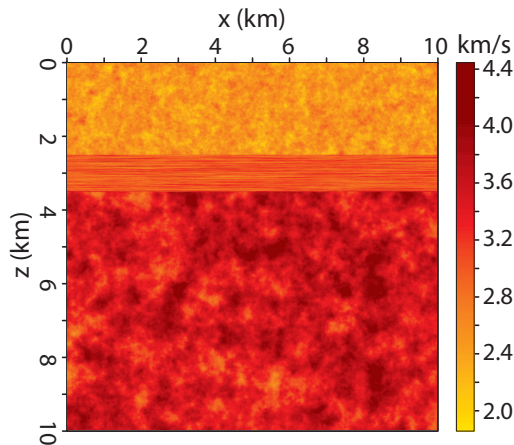


Figure 4.11: Velocity model with a shale-like reservoir.

To explore the effect of topography on the sensitivity kernel, we simulate an acoustic wavefield using a homogeneous velocity model with a variable topography. The velocity model consists of 3 homogeneous layers: a top air layer with a velocity of 330m/s, a thin layer under the topography with a velocity of 2000 m/s , and the rest of the model with a velocity of 3000 m/s (Figure 4.14). The free-surface is approximated using the air-subsurface interface based on the velocity discontinuity assuming a constant density [103]. We model the variable topography using a 1D von-Karman PSDF in order to create a random variable topography with a correlation across the topography defined by a correlation distance of 0.5 km .

We compute the sensitivity kernel with the scattered waves induced by the variable topography using a vertical source-receiver setup (Figure 4.15) and a horizontal source-receiver setup (Figure 4.16). At time $t = 1.40 s$, the kernel accounts for the direct wave between source S and receiver R. The direct wave kernel using the vertical source-receiver setup is shown in Figure 4.15 at $t = 1.40 s$. At later lapse time (Figure 4.15; $t > 1.40 s$), the kernel expands into a singly scattered front which broadens with time. The kernel has a

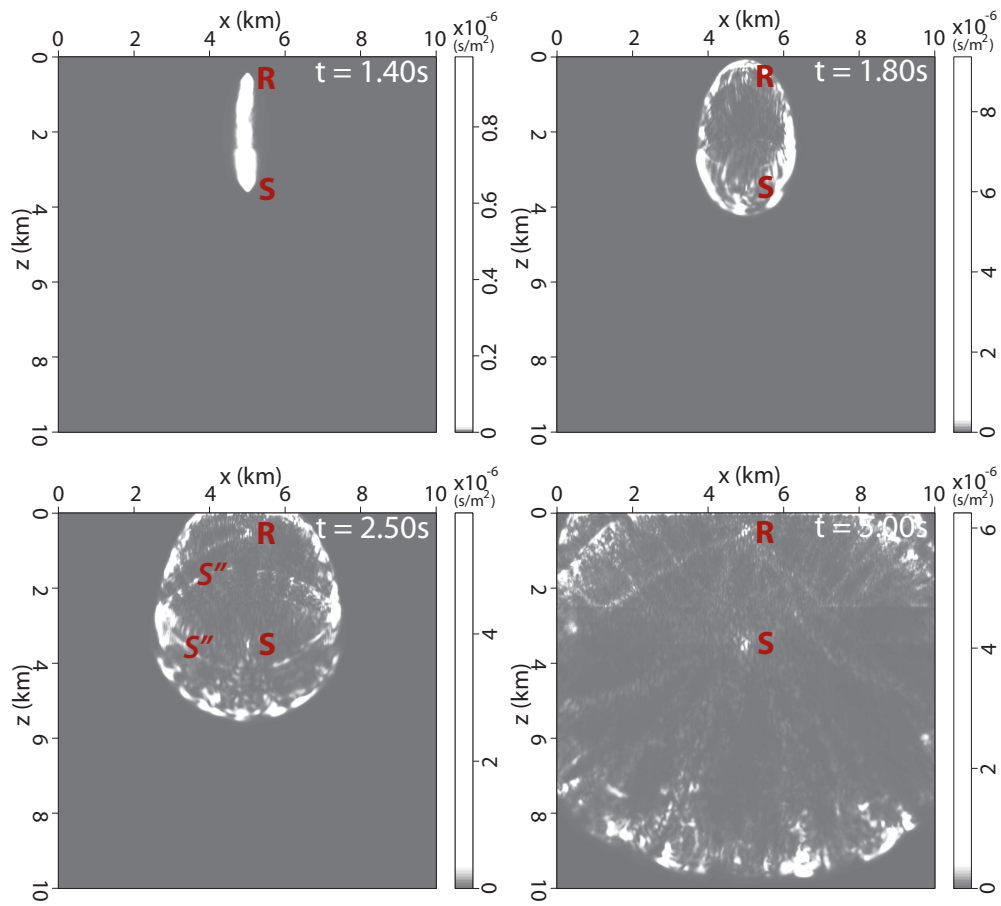


Figure 4.12: Temporal and spatial evolution of the sensitivity kernel (numerical solution) in a reservoir with shale-like velocity perturbation. S'' corresponds to the reflected scattered phase.

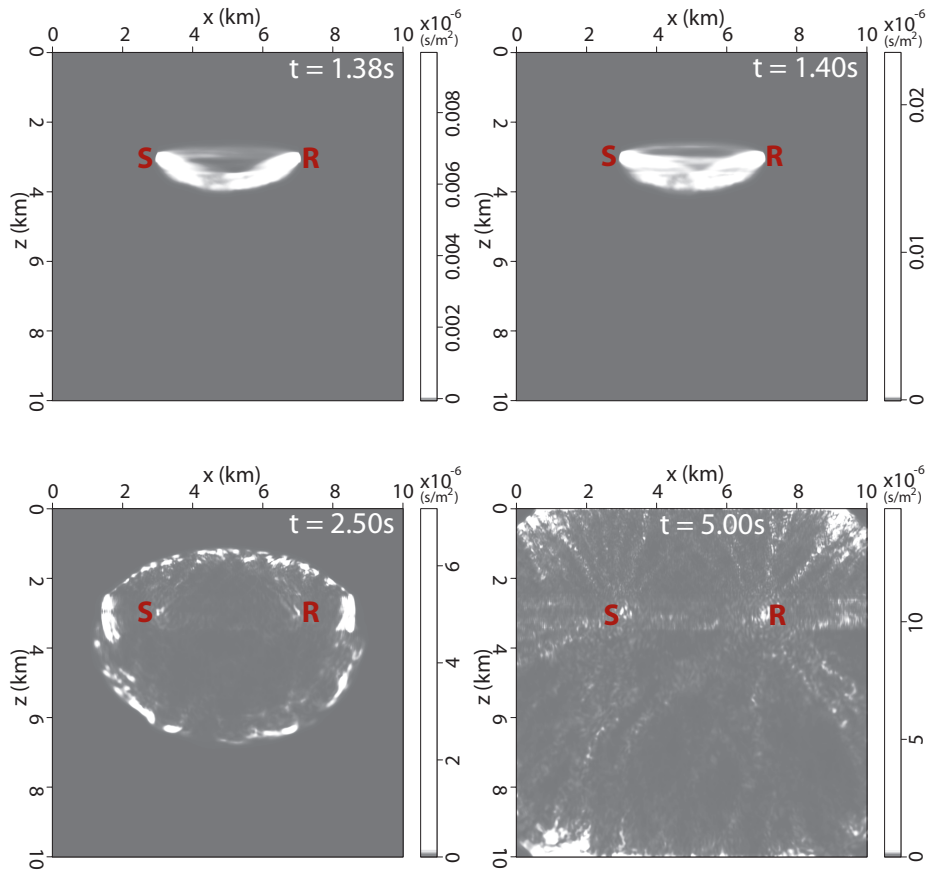


Figure 4.13: Temporal and spatial evolution of the sensitivity kernel (numerical solution) in a reservoir with shale-like velocity perturbation.

relatively large magnitude within the tiny low velocity layer underneath the topography (Figure 4.15, $t = 2.5$ s and 5.0 s). This part of the kernel is due to scattering contributions from the topography-induced scattering which are trapped in the near-surface layer. This topography-induced sensitivity is contained predominantly within the near-surface layer by the velocity interface on top of the high velocity halfspace. The topography-induced sensitivity, however, increases and broadens away from the receiver location within the near-surface layer with an increase in time.

When the source and receiver are embedded within the near-surface layer underneath the variable topography, the kernel of the first arrival consists of refracted waves off of the higher velocity halfspace underneath the near-surface low velocity layer (Figure 4.16, $t = 1.6$ s). Similar to the vertical source and receiver setup, the direct/refracted kernel with the horizontal source and receiver setup splits for $t = 1.8$ s into the singly scattered kernel. In Figure 4.16, only the downward subsection of the singly scattered kernel is present because the high velocity contrast across the topography prevents propagation of scattered waves into the air. At later lapse time ($t = 2.50$ s and 5.00 s, Figure 4.16), the dominant part of the kernel lies within the low velocity layer which results from the topography-induced scattering and the trapped waves within the low velocity layer. The presence of the thin low velocity layer underneath the topography induces kernels with similar behavior at large lapse time for both source-receiver setups.

The behavior of the kernel in the presence of variable topography and a thin low velocity layer in the above results demonstrates the need to accurately characterize the scattering properties of the medium being monitored. Incorporating both the topography and the appropriate velocity (scattering) model in the kernel computation provides the distribution and origin of the scattered waves via the kernel that can be used for time-lapse monitoring. Due to the effect of variable topography and of a heterogeneous scattering medium on the kernel, we will need to use an appropriate source-receiver array setup to image a time-lapse change within the subsurface. For example, in a case of monitoring velocity changes within

a reservoir that might be due to fluid production or injection within the reservoir, a borehole array in close proximity to the change might be a more effective source-receiver setup for monitoring than using a surface-receiver array. In this case, the borehole array records more of the scattered waves generated within a given layer. This results in higher sensitivity to a change in that layer. Also, the borehole array, depending on its relative depth to the free-surface, will have less of the topography- or near-surface- induced scattering.

4.5 Discussion and Conclusion

We propose a novel approach to compute the sensitivity kernel that can be used to resolve weak changes within the earth’s subsurface or any other medium using multiply scattered waves. These are changes which are usually irresolvable with singly scattered waves. Our approach does not rely on analytical models of the scattered intensity such as the diffusion and radiative transfer models. To compute the sensitivity kernel, we compute the scattered intensity field needed for the kernel computation using an a priori model of the scattering medium from numerically generated scattered wavefield. In this paper, we use the finite-difference modeling for the computation of the seismic wavefield. The numerical modeling of the scattered intensity can take advantage of various numerical methods for seismic wavefield computation. Using our approach we can incorporate any complexities of the scattering medium and any boundary conditions of the medium. With an appropriate a priori scattering model, we can obtain a more accurate estimate of the sensitivity kernel which accurately describes the intensity of the scattered wave recorded by a given source-receiver pair. Our kernel computation approach is suitable for a medium such as the earth’s subsurface where in most cases the scattering properties are heterogeneous and whose scattered intensity may not be described analytically.

The caveat to the computation of the scattered intensity and in extension the sensitivity kernel for the time lapse monitoring, are the computation cost of both the scattered intensity and the corresponding kernel and the need for an accurate a priori model of the statistical properties of the scattering medium. The cost of the kernel computation mostly depends

on the travel-time of the scattered phase for the kernel, the sum of number of sources and receivers, the number of the scattering model realizations needed, the cost of the forward modeling of the scattered intensity for both the source and receiver intensity fields, and the cost for the convolution between the source and receiver intensity fields. The cost for the forward modeling of the scattered intensity depends on the spatial dimensions of the scattering model used for modeling the intensity field which makes a significant difference if the medium is 2D or 3D and the temporal or the frequency dimension of the scattered waves. All numerical examples we show in this paper uses 2D models but the computation of the numerical kernel in 3D follows exactly the same procedure.

Another limitation of the numerical computation of the sensitivity kernel is the need to know the statistical property of the a priori model. This limitation is also inherent to the analytical computation of the kernel where the scattering parameter such the diffusion coefficient and the mean free path length are needed for the diffusion and the radiative transfer models, respectively. The details of the a priori scattering model needed for the kernel computation can be relaxed, with the requirement that the a priori model used should have similar statistical property to that of the true model and that the corresponding scattered intensity should explain significantly the envelope of the scattered wave rather than the individual phases of the multiply scattered waves. The effect of the fluctuations in the microscopic properties between the a priori scattering model and the true scattering medium can be suppressed while computing the kernel with multiple realizations of the scattering model. A few realizations of the scattering model (for example, 5-10 realizations) can significantly stabilize the fluctuations in the sensitivity kernel.

The numerical examples in this study are based on acoustic wave propagation with isotropic source radiation. This acoustic wave assumption can be considered valid at the equipartition regime of multiply scattered waves at which S-wave energy dominates the scattered waves [37, 109]. Equipartitioning of the scattered waves is achieved late in the coda (travel-times at which diffusion approximation is usually considered). However, our recipe

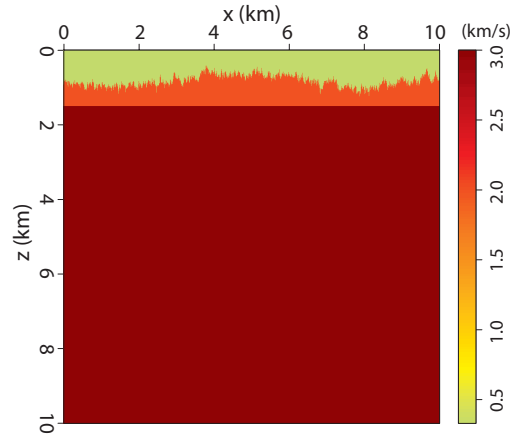


Figure 4.14: Velocity model with variable topography.

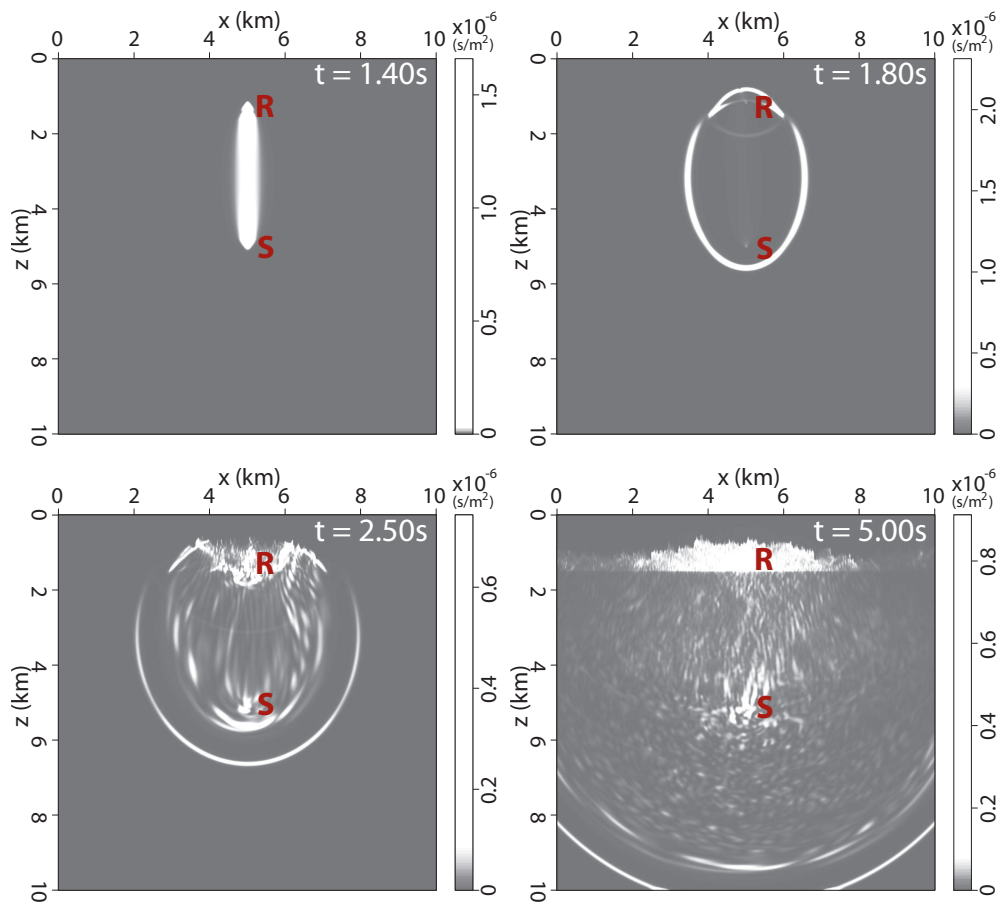


Figure 4.15: Temporal and spatial evolution of the sensitivity kernel (numerical solution) showing topography-induced scattering using vertical source-receiver line.

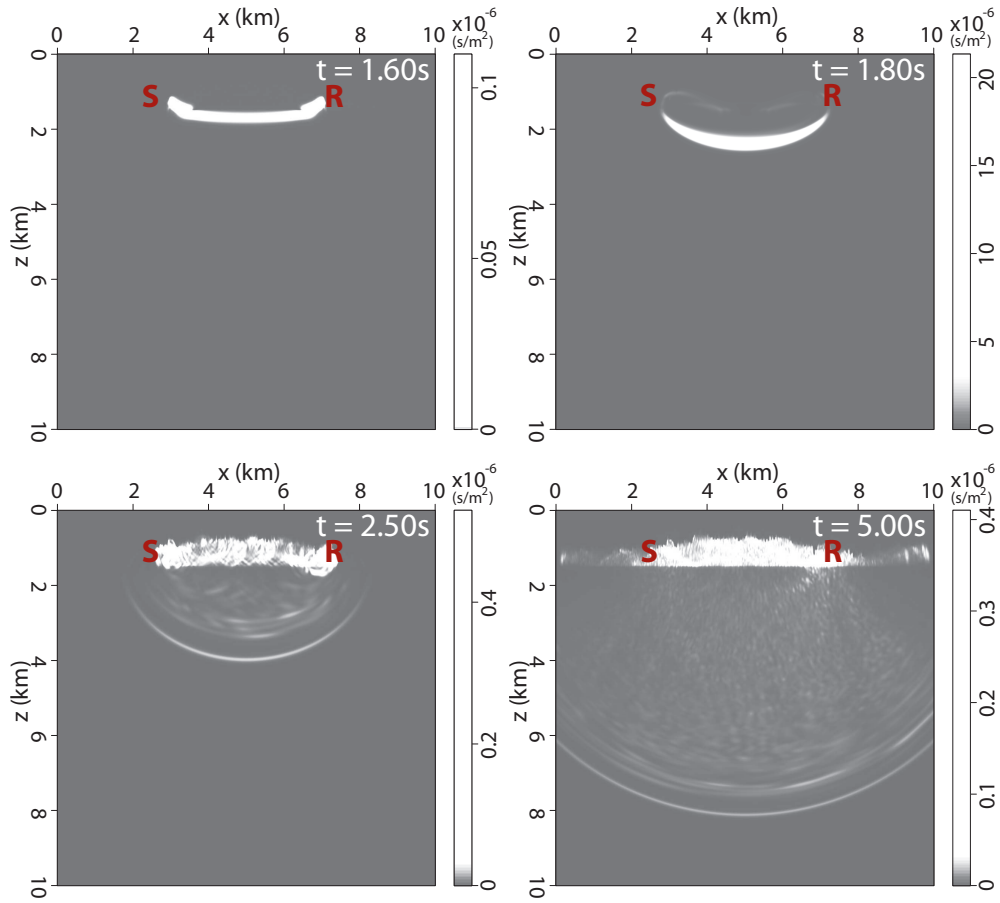


Figure 4.16: Temporal and spatial evolution of the sensitivity kernel (numerical solution) showing topography-induced scattering using horizontal source-receiver line.

for computing the numerical sensitivity kernel remains valid for elastic wave propagation. For elastic waves, we expect to get the sensitivities to the change in P- and S-wave velocities. The computation of the elastic sensitivity kernels will involve additional considerations. Some of these considerations include, separating the P- and S- wave modes in order to get the sensitivities to P- and S-wave velocity changes and using the appropriate radiation pattern for the receiver intensity field that depends on the propagation directions of either the recorded P- or S-wave. The details on the elastic sensitivity kernel will be in a forthcoming publication.

4.6 Acknowledgments

This research was supported by sponsors of the Consortium Project on Seismic Inverse Methods for Complex Structures. The reproducible numerical examples in this paper use the Madagascar open-source software package freely available from <http://www.ahay.org>.

CHAPTER 5

NUMERICAL COMPUTATION OF THE SENSITIVITY KERNEL FOR TIME-LAPSE MONITORING WITH MULTIPLY SCATTERED ELASTIC WAVES

Chinaemerem Kanu and Roel Snieder

To be submitted to Geophysical Journal International (2015)

5.1 Abstract

Coda wave interferometry has been used extensively to monitor average velocity changes within elastic media, where the average velocity changes are weighted averages of the P- and S-wave velocity changes. However, in most cases, obtaining the individual values of the P- and S-wave velocity changes provides more detailed information on the change present within an elastic medium compared to using the weighted average of the P- and S-wave velocity changes. We provide a novel approach to evaluate the sensitivity of elastic travel-time changes to fractional changes in the P- or S-wave velocity. This approach involves a numerical computation of the sensitivity kernel using P- and S-wave scattered intensity fields within any arbitrary scattering medium with a prescribed boundary condition. The P- and S- sensitivity kernels allow one to evaluate the contributions of the P- and S-wave velocity changes to the travel-time changes for a specific displacement component of the elastic time-lapse coda.

5.2 Introduction

The earth's subsurface and mechanical structures undergo changes in their elastic properties which can be monitored over a period of time. The changes in the elastic properties, such as perturbations in the P- or S-wave velocities, result from the changes in the lattice material of the medium (rock properties in the case of the earth's subsurface) or changes in the properties of fluid present within the pores of the medium. Time-lapse tools have

been used in various disciplines to monitor changes both in lithology and in fluid properties or movements. The time-lapse tools used include 4D active surveys where the interest is to extract differences between the time-lapse surveys [90], monitor changes with repeating earthquakes [76], and use passive interferometry for time-lapse monitoring [50, 88]. For each of these time-lapse monitoring tools, one needs time-lapse data where the only differences in the time-lapse data result from changes within the medium that is monitored. The capability for achieving high sensitivity of the time-lapse data to changes within the monitored medium varies according to the monitoring method used.

Multiply scattered waves, due to their redundant sampling of the monitored medium, have higher sensitivity to perturbations in the elastic properties of the scattering medium compared to singly scattered waves. The increase in sensitivity allows for identification of changes within the medium and detectability of changes as weak as 0.1% [96]. Multiply scattered waves have been used to monitor S-wave velocity changes due to coseismic stress changes [76, 87, 111], to characterize P- and S-wave velocity changes resulting from CO₂ or water injection into reservoirs [4, 41], to monitor volcanoes, landslides, geothermal reservoirs or dams [13, 50, 51, 56], and to characterize concrete [31].

Notwithstanding the successful use of multiply scattered waves in monitoring time-lapse changes in the elastic properties of a scattering medium, little has been done to characterize the spatial distribution and the location of the time-lapse changes. In most cases, the location and the spatial distribution of the perturbations are as important as the temporal changes. The location of the change provides additional information such as the origin of the observed change, the dynamics of the change, and potentially the driving forces for the perturbation of the elastic properties. Prior efforts to characterize the spatial component of the time-lapse changes hinged on the distribution of the monitoring sources and receivers [15, 50] which generally characterizes the variation of the estimated changes across the monitoring stations. This aspect of the spatial characterization is dependent on having a sufficiently dense station distribution. Usually only limited information about the location of the change is obtained.

Pacheco and Snieder [70], assuming multiple scattering of scalar waves, provide the relationship between a localized velocity change and the travel-time changes due to the localized velocity change. This theory is extended to changes in the scattering properties of a scattering medium by Rossetto et al. [82]. Implicit in both studies is the assumption of acoustic wave scattering. However, to monitor and image perturbations in the elastic properties of the scattering medium, we need an imaging algorithm that resolves the elastic properties (for example, P- and S-wave velocities). The imaging algorithm needs to resolve both the spatial and temporal component of the time-lapse change. In this study, we provide the imaging equation for time-lapse elastic velocity change and explore the characteristics of the sensitivities of the travel-time change to P- and S-wave velocity changes using a non-isotropic source.

5.3 Mean travel-time change in an elastic coda interferometry

The travel-time t^ζ of an elastic scattered wave along the scattering path ζ can be defined as

$$t^{\zeta i} = t_p^{\zeta i} + t_s^{\zeta i}, \quad (5.1)$$

where t_p^{ζ} and t_s^{ζ} are the time spent either as a P- or a S-wave before the scattered wave is recorded. The index i is the recorded component of scattered elastic displacement which in this study is $i = x, z$ for 2D elastic scattering. Although the examples in this study are for 2D elastic media, the theory is equally valid in 3D. Equation 5.1 can be expressed as

$$t^{\zeta i} = \frac{l_p^{\zeta i}}{\alpha} + \frac{l_s^{\zeta i}}{\beta} = s_p l_p^{\zeta i} + s_s l_s^{\zeta i}, \quad (5.2)$$

where α and β are the P- and S-wave velocities, s_p and s_s are the P- and S-wave slownesses, and l_p and l_s are the traveled distance for the P- and S-waves, respectively. Assuming there are perturbations in the P- or the S- wave velocities such that the perturbed slownesses are $\dot{s}_p(\mathbf{x}) = s_p(\mathbf{x}) + \delta s_p(\mathbf{x})$ and $\dot{s}_s(\mathbf{x}) = s_s(\mathbf{x}) + \delta s_s(\mathbf{x})$, the perturbed travel-time is

$$t^{\zeta i} + \tau^{\zeta i} = s_p l_p^{\zeta i} + \delta s_p l_p^{\zeta i} + s_s l_s^{\zeta i} + \delta s_s l_s^{\zeta i}. \quad (5.3)$$

From equation 5.3, the travel-time change τ^{ζ^i} is

$$\tau^{\zeta^i} = \delta s_p l_p^{\zeta^i} + \delta s_s l_s^{\zeta^i} = \frac{\delta s_p}{s_p} t_p^{\zeta^i} + \frac{\delta s_s}{s_s} t_s^{\zeta^i}. \quad (5.4)$$

In equation 5.4, $t_p^{\zeta^i}$ and $t_s^{\zeta^i}$ provide the weights for the contribution of the P- and S- wave fractional velocity change to the travel-time change τ^{ζ^i} . Averaging over all paths arriving at a particular travel-time, the average travel-time change $\langle \tau^i \rangle$ is

$$\langle \tau^i \rangle = \frac{\delta s_p}{s_p} \langle t_p^i \rangle + \frac{\delta s_s}{s_s} \langle t_s^i \rangle. \quad (5.5)$$

The time spent by the P- or S-wave in the scattering medium thus explains the sensitivity of the scattered elastic waves to the fractional change in the P- or S-wave velocity [81, 97]. So if we replace the time spent by the scattered waves within the scattering medium with sensitivity kernels ($K(\mathbf{x}, t)$) [71], we obtain

$$\langle \tau^i \rangle = \int_V K_p^i(\mathbf{x}, t) \frac{\delta s_p}{s_p} d\mathbf{x} + \int_V K_s^i(\mathbf{x}, t) \frac{\delta s_s}{s_s} d\mathbf{x}, \quad (5.6)$$

where $K_p^i(\mathbf{x}, t)$ and $K_s^i(\mathbf{x}, t)$ are the kernels that represent the sensitivity of the travel-time change to the fractional changes in the P- and S- wave velocities, respectively. We define equation 5.6 as the kernel-based travel-time change.

5.4 Mean travel-time change with multiply scattered elastic intensity

To find the relationship between the travel-time changes and the fractional velocity changes, we need to determine the time spent within the scattering medium (therefore the sensitivity kernel) by the P- and S-wave contributions. Equation 5.6 gives the contributions of the fractional change in the P- or S-wave velocity to the travel-time change for a given component i of the time-lapse scattered waves via the P- and S-wave sensitivity kernels $K_p^i(\mathbf{x}, t)$ and $K_s^i(\mathbf{x}, t)$, respectively. Using Helmholtz decomposition for an isotropic elastic medium, we can split the intensity of the scattered waves $W(\mathbf{x}, t)$ into the intensities for the compressive wave W_p and the shear wave W_s [84, 91], assuming a displacement field $\mathbf{u}(\mathbf{x}, \mathbf{t})$:

$$W(\mathbf{x}, t) = W_p(\mathbf{x}, t) + W_s(\mathbf{x}, t) = \overline{\left(\frac{\lambda}{2} + \mu\right) (\nabla \cdot \mathbf{u}(\mathbf{x}, \mathbf{t}))^2} + \overline{\frac{\mu}{2} (\nabla \times \mathbf{u}(\mathbf{x}, \mathbf{t}))^2}, \quad (5.7)$$

where λ and μ are the Lamè parameters and the bar denotes an ensemble average. Equation 5.7 splits the scattered intensity into P- and S-wave intensities by evaluating the divergence and curl of the displacement field. We can re-express equation 5.7 as

$$W(\mathbf{x}, t) = \frac{\overline{\alpha^2 \rho} (\nabla \cdot \mathbf{u}(\mathbf{x}, \mathbf{t}))^2}{2} + \frac{\overline{\beta^2 \rho} (\nabla \times \mathbf{u}(\mathbf{x}, \mathbf{t}))^2}{2}, \quad (5.8)$$

where ρ is the density of the scattering medium. Following [70], the probability for an elastic

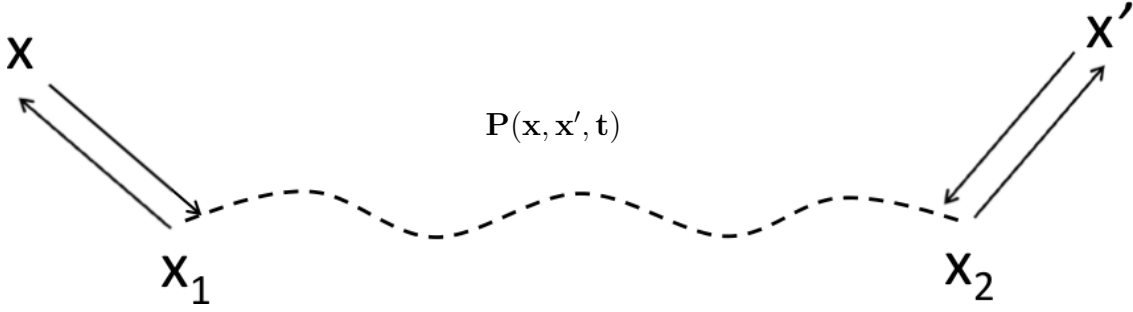


Figure 5.1: Scattering diagram illustrating the scattering interactions of the scattered waves within a scattering medium.

wave travelling from a source \mathbf{s} to a receiver \mathbf{r} with a travel-time t via \mathbf{x} at travel-time t' for the i^{th} displacement component ($P^i(\mathbf{x}, \mathbf{r}, \mathbf{s}, t', t)$), assuming the ladder approximation [3], is

$$P^i(\mathbf{x}, \mathbf{r}, \mathbf{s}, t', t) = P^i(\mathbf{x}, \mathbf{s}, t') P^i(\mathbf{r}, \mathbf{x}, t - t'), \quad (5.9)$$

where $P^i(\mathbf{x}, \mathbf{x}', t)$ is all the scattering contributions from locations \mathbf{x}' to \mathbf{x} at travel-time t for the i^{th} displacement component, described in Figure 5.1. The scattering contributions consist of all scattering events between scatterers at \mathbf{x}_1 and \mathbf{x}_2 (Figure 5.1) which allow for scattering between P- and S- wave modes. The scattering consists of wave propagation from \mathbf{x} to the first scatterer along the path considered at \mathbf{x}_1 , all the scattering between scatterers at \mathbf{x}_1 and \mathbf{x}_2 , and the scattered wave from the last scatterer along the path at location \mathbf{x}_2 to the location \mathbf{x}' . Equation 5.9 is then expressed with the P- and S-wave contributions:

$$\begin{aligned} P^i(\mathbf{x}, \mathbf{r}, \mathbf{s}, t', t) &= P_p^i(\mathbf{x}, \mathbf{s}, t') P_p^i(\mathbf{r}, \mathbf{x}, t - t') + P_s^i(\mathbf{x}, \mathbf{s}, t') P_s^i(\mathbf{r}, \mathbf{x}, t - t') \\ &= P_p^i(\mathbf{x}, \mathbf{s}, t') P_p^i(\mathbf{x}, \mathbf{r}, t - t') + P_s^i(\mathbf{x}, \mathbf{s}, t') P_s^i(\mathbf{x}, \mathbf{r}, t - t'), \end{aligned} \quad (5.10)$$

where $P_p^i(\mathbf{x}, \mathbf{x}', t)$ or $P_s^i(\mathbf{x}, \mathbf{x}', t)$ are the probabilities that the scattered waves travel either as a P- or S-wave between scatterers from locations \mathbf{x}' to \mathbf{x} at travel-time t , respectively, for the i^{th} displacement component. The probability $P^i(\mathbf{x}, \mathbf{r}, \mathbf{s}, t', t)$ contains all the contributions of the scattered intensity visiting the location \mathbf{x} at travel-time t' , generated by a source at location \mathbf{s} , and recorded by the receiver at location \mathbf{r} . We invoke the reciprocity theorem in the last line of equation 5.10. We assume that along a given scattering path at a given travel-time, the elastic wave occupies either the P- or S- wave state. The probabilities $P(\mathbf{x}, t)$ are the normalized scattered intensities $I(\mathbf{x}, t)$ which are given as

$$I(\mathbf{x}, t) = \frac{W(\mathbf{x}, t)}{\int_R W(\mathbf{x}, t) d\mathbf{x}}, \quad (5.11)$$

where $\int_R \dots d\mathbf{x}$ is the integration of the scattering region R . Using equation 5.10, we have

$$I^i(\mathbf{x}, \mathbf{r}, \mathbf{s}, t', t) = I_p^i(\mathbf{x}, \mathbf{s}, t')I_p^i(\mathbf{x}, \mathbf{r}, t - t') + I_s^i(\mathbf{x}, \mathbf{s}, t')I_s^i(\mathbf{x}, \mathbf{r}, t - t'). \quad (5.12)$$

The scattered intensity $I^i(\mathbf{x}, \mathbf{s}, t')$ at location \mathbf{x} is generated by a source at \mathbf{s} with the source mechanism that generated the time-lapse signals used for monitoring; contrastingly, the scattered intensity $I^i(\mathbf{x}, \mathbf{r}, t')$ from the location \mathbf{r} to a location \mathbf{x} is generated by placing a point force source at \mathbf{r} in the direction of component i of the recorded scattered intensity. At the receiver location, the recorded displacement field for a specific component is the displacement whose particle motion is aligned in the direction of the component of the recorded displacement field.

Averaging over all possible path contributions that visit all intermediate points \mathbf{x} ,

$$\begin{aligned} I^i(\mathbf{r}, \mathbf{s}, t) &= \int_A I^i(\mathbf{x}, \mathbf{r}, \mathbf{s}, t', t) d\mathbf{x} \\ &= \int_A [I_p^i(\mathbf{x}, \mathbf{s}, t')I_p^i(\mathbf{x}, \mathbf{r}, t - t') + I_s^i(\mathbf{x}, \mathbf{s}, t')I_s^i(\mathbf{x}, \mathbf{r}, t - t')] d\mathbf{x}. \end{aligned} \quad (5.13)$$

Integrating both sides over travel-time t ,

$$tI^i(\mathbf{r}, \mathbf{s}, t) = \int_A \int_0^t [I_p^i(\mathbf{x}, \mathbf{s}, t')I_p^i(\mathbf{x}, \mathbf{r}, t - t') + I_s^i(\mathbf{x}, \mathbf{s}, t')I_s^i(\mathbf{x}, \mathbf{r}, t - t')] dt' d\mathbf{x}. \quad (5.14)$$

Then, the travel-time t is

$$t = \frac{1}{I^i(\mathbf{r}, \mathbf{s}, t)} \int_A \int_0^t [I_p^i(\mathbf{x}, \mathbf{s}, t')I_p^i(\mathbf{x}, \mathbf{r}, t - t') + I_s^i(\mathbf{x}, \mathbf{s}, t')I_s^i(\mathbf{x}, \mathbf{r}, t - t')] dt' d\mathbf{x}, \quad (5.15)$$

where $I^i(\mathbf{r}, \mathbf{s}, t)$ corresponds to the normalized scattered intensity of the i^{th} component of the displacement field recorded at \mathbf{r} due to a source at \mathbf{s} . Equation 5.15 gives

$$t = \int_A [K_p^i(\mathbf{x}, t) + K_s^i(\mathbf{x}, t)] d\mathbf{x}, \quad (5.16)$$

where

$$K_p^i(\mathbf{x}, t) = \frac{\int_0^t [I_p^i(\mathbf{x}, \mathbf{s}, t')I_p^i(\mathbf{x}, \mathbf{r}, t - t')] dt'}{I^i(\mathbf{r}, \mathbf{s}, t)}, \quad (5.17)$$

and

$$K_s^i(\mathbf{x}, t) = \frac{\int_0^t [I_s^i(\mathbf{x}, \mathbf{s}, t')I_s^i(\mathbf{x}, \mathbf{r}, t - t')] dt'}{I^i(\mathbf{r}, \mathbf{s}, t)}. \quad (5.18)$$

The mean travel-time change is obtained by inserting 5.17 and 5.18 into equations 5.6. Therefore the kernel-based travel-time (KBT) change within the time-lapse coda waves can be estimated using equations 5.6, 5.17 and 5.18. The computation of the kernel-based travel-time (KBT) change requires a numerical simulation of the displacement field $\mathbf{u}(\mathbf{x}, \mathbf{t})$, computation of the normalized intensity field $I(\mathbf{x}, t)$ using equations 5.8 and 5.11, and the evaluation of equation 5.6 using equations 5.17 and 5.18.

5.5 Random isotropic scattering model

To explore the properties of the elastic sensitivity kernel, we compute $K_p^i(\mathbf{x}, t)$ and $K_s^i(\mathbf{x}, t)$ using equations 5.17 and 5.18, respectively, in a statistically homogeneous scattering

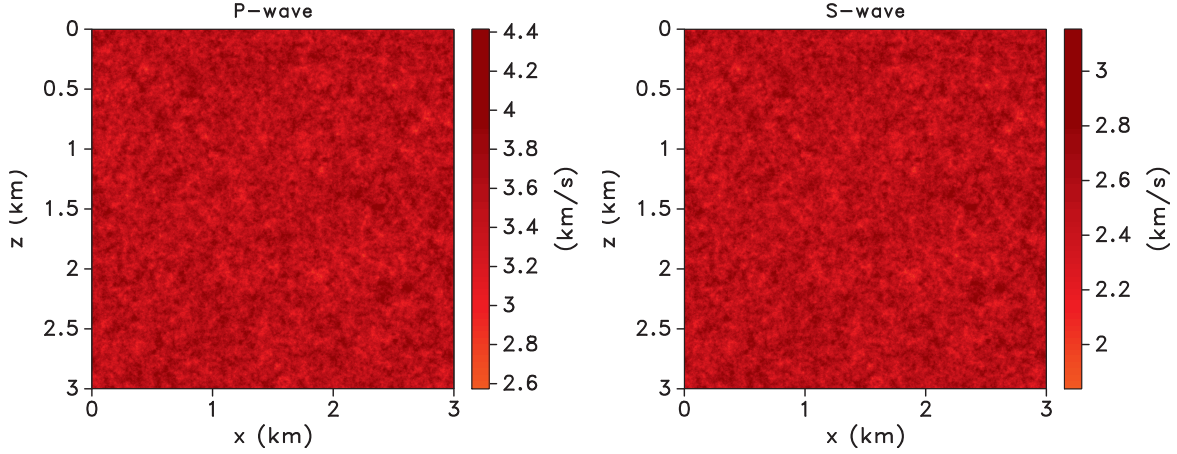


Figure 5.2: Statistically homogeneous velocity models: P-wave velocity (left) and S-wave velocity (right).

model. To compute the sensitivity kernels $K_p^i(\mathbf{x}, t)$ and $K_s^i(\mathbf{x}, t)$, we use elastic waveform modeling to compute the displacement field. Then using equation 5.8, we obtain the intensity fields of the compressive and the shear waves. With equations 5.17 and 5.18, we then get the sensitivity kernels. The used scattering model is a von-Karman scattering velocity model [86] defined by the following parameters: $a_x = a_z = 0.01 \text{ km}$, $\epsilon = 0.8$, and $\kappa = 0.5$. Figure 5.2 shows the P- and S-wave velocity models with an average velocity of 3.5 km/s and 2.5 km/s , respectively. Using a source wavelet with a dominant frequency of 30 Hz , we get a dominant elastic wave scattering wavenumber ka that yields values of 0.54 and 0.75 for the P- and S-waves, respectively. The P- and S-wave scattering models are characterized by the transport mean free paths (l_{VK}^*) of 0.032 km and 0.021 km , respectively [86]. Each von-Karman scattering velocity model is generated with a random realization. The sensitivity kernels are usually computed with multiple realizations of the scattering models [38] to stabilize the sensitivity kernel. However, the kernel examples we show in this study involve only one realization of the scattering model.

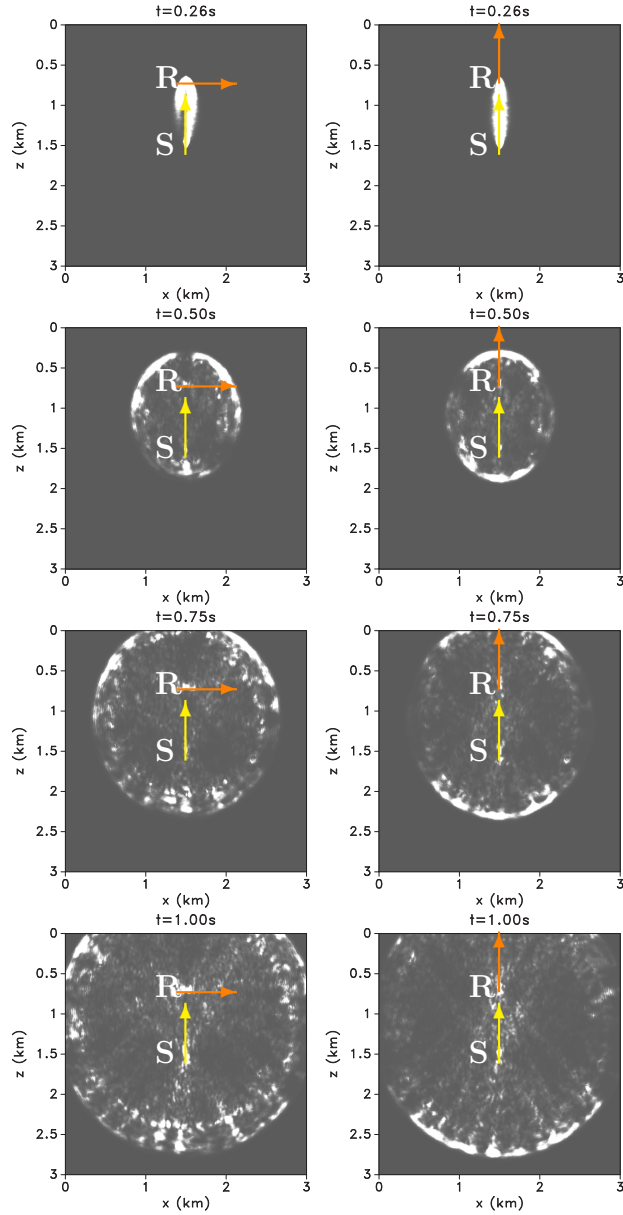


Figure 5.3: P-wave sensitivity kernel K_p^i of the scattered waves generated by a vertically aligned point force source for the $i = x$ component (left) and the $i = z$ component (right). The source (yellow arrow, S) is located at $[x, z] = [1.5, 1.5]km$ and the receiver (orange arrow, R) at $[x, z] = [1.5, 0.7]km$. The direction of the arrows at the source and receiver indicates the direction of the source radiation and the direction of the displacement component at the receiver, respectively. The base of the arrows are the locations of either the source or the receiver.

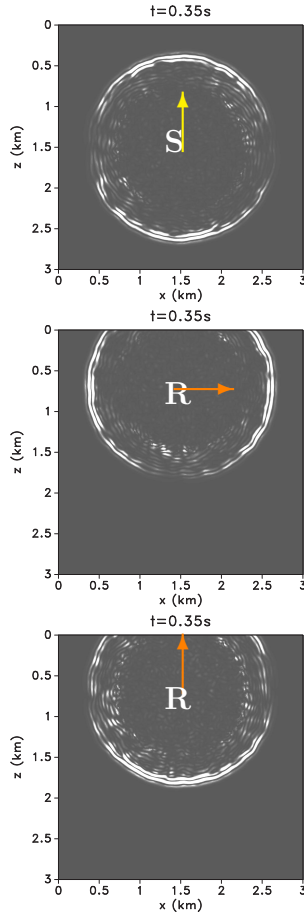


Figure 5.4: The P-wave intensity fields used for the kernel computation at travel-time 0.35 s in the statistically homogeneous model (Figure 5.2). Top: The source intensity field due to a vertical point force located at $[x, z] = [1.5, 1.5]\text{ km}$ (yellow arrow, S). Middle: The receiver intensity field due to a horizontal point force located at $[x, z] = [1.5, 0.7]\text{ km}$ (orange arrow) for the x-component kernel. Bottom: The receiver intensity field due to a vertical point force located at $[x, z] = [1.5, 0.7]\text{ km}$ (orange arrow) for the z-component kernel. The direction of the arrow at the source indicates the direction of the source radiation and at the receiver indicates the direction of the displacement component at the receiver. The base of the arrows are the locations of either the source or the receiver.

5.5.1 Sensitivity to perturbations in P-wave velocity

Using equation 5.17, we compute the sensitivity of the travel-time change due to perturbations in P-wave velocity for waves excited by a point force oriented in the z-direction. The sensitivity kernel is computed using the velocity models in Figure 5.2. The locations of the source and receiver for the kernel computation are shown in Figure 5.3 by the yellow and orange arrows, respectively. Given that the radiation of the source and receiver wavefields is directional, the orientation of the source-receiver pair affects the radiation of the sensitivity kernel especially across the kernel front. The radiation pattern of the source and the directional sensitivity of the displacement sensor cause the sensitivity kernels to be dependent on direction, especially for the early arriving waves whose direction is not yet influenced by multiple scattering. Figure 5.3 shows the P-wave sensitivity kernel for the x- (left) and z- (right) displacement components. The four panels for each component (x , z) of the kernel correspond to the kernels at travel-times $t = 0.26$ s, 0.50 s, 0.75 s, and 1.00 s, for waves that are excited by a vertical point force. The first arrival time of the P-wave is approximately 0.24 s.

We compute the sensitivity kernels using numerically generated intensity fields (Figure 5.4) and we simulate the intensity fields with a finite difference elastic modeling algorithm in Madagascar (<http://www.ahay.org>). The intensity field for either the P- or the S-wave is computed by evaluating equation 5.8.

The edge of the sensitivity kernels is defined by the kernel front [38] which is dominated by single scattering contributions and bounds the interior of the kernel where multiple scattering waves dominate. However, because the source radiation is non-isotropic and the wavefield is recorded along either the x- or the z- direction (Figure 5.3), the kernel front is also non-isotropic. Figure 5.3 (left) shows the sensitivity kernel for the displacement field along the x-direction. There are vanishing amplitudes on the kernel front along the z-direction above the receiver location and in the lower hemiellipse of the kernel front, except along the z-direction below the source location. The nodal sensitivity at the kernel front above the

receiver location is due to the lack of a singly scattered P-wave recorded by the x-component of the receiver along the z-direction (Figure 5.4, middle panel). The vanishing amplitude of the kernel front in the lower hemiellipse (Figure 5.3) results from the fact that the vertical point source radiates a vanishing P-wave front along the horizontal direction (Figure 5.4, top panel) and the x-component of the receiver records no vertical propagating P-wave (Figure 5.4, middle panel). However, since the vertical point force preferentially radiates the P-wave in the vertical direction and the scattered P-waves are recorded horizontally by the x-component of the receiver, there is non-zero amplitude along the kernel front in the upper hemiellipse, except along the z-direction above the receiver location.

For the sensitivity kernel along the z-direction (Figure 5.3 (right)), there is vanishing sensitivity at the kernel front propagating horizontally from the source-receiver line. This horizontally propagating part of the kernel results from a vanishing P-wave radiated horizontally by the vertical point force (Figure 5.4, top panel) and recorded horizontally by the z-component of the receiver. This part of the kernel front propagating horizontally from the source-receiver line decays with coda lapse time, i.e., as the eccentricity of the kernel front decreases toward zero. With increasing coda lapse time, the contributing P-wave radiation to the horizontally propagating part of the kernel originates from near the node of the source P-wave intensity front (Figure 5.4, top panel). However, the vertically propagating part of the kernel front (Figure 5.3 (right)) is generated by the P-waves radiated and recorded along the z direction (Figure 5.4, top and bottom panel).

Within the kernel front lies the multiply scattering contribution to the kernel. Given that for late times, the intensity field is directionally randomized due to multiple scattering, the multiple scattering contributions to the kernel do not retain the radiation characteristics of the kernel front. At the source and receiver locations, the sensitivity is elevated similar to that predicted by acoustic scattering [38, 70]. This elevated sensitivity, which is present for all coda lapse times, is due to the large amplitude of waves that are scattered near the source or the receiver.

5.5.2 Sensitivity to perturbations in S-wave velocity

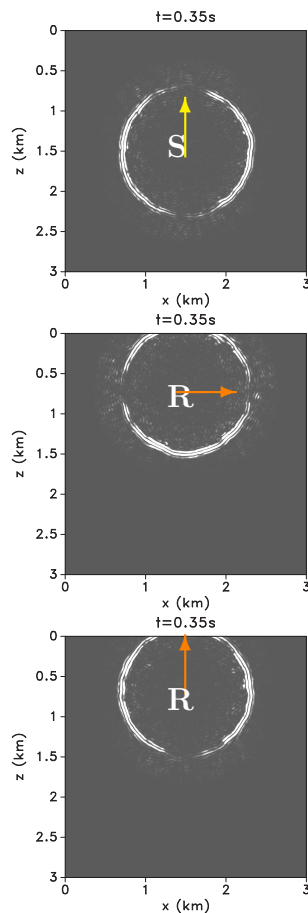


Figure 5.5: The S-wave intensity fields used for the kernel computation at travel-time 0.35 s in the statistically homogeneous model (Figure 5.2). Top: The source intensity field due to a vertical point force located at $[x, z] = [1.5, 1.5]km$ (yellow arrow, S). Middle: The receiver intensity field due to a horizontal point force located at $[x, z] = [1.5, 0.7]km$ (orange arrow) for the x-component kernel. Bottom: The receiver intensity field due to a vertical point force located at $[x, z] = [1.5, 0.7]km$ (orange arrow) for the z-component kernel. The direction of the arrows at the source and receiver indicates the direction of the source radiation and the direction of the displacement component at the receiver, respectively. The base of the arrows are the locations of either the source or the receiver.

To compute the S-wave sensitivity kernel, we evaluate equation 5.18 using the shear intensity field I_s . Figure 5.5 shows the scattered intensity field at 0.35s. The arrival time of the direct S-wave is approximately 0.33 s. The figure shows the S-wave intensity field generated at the source location by a point force aligned along the z-direction (Figure 5.5,

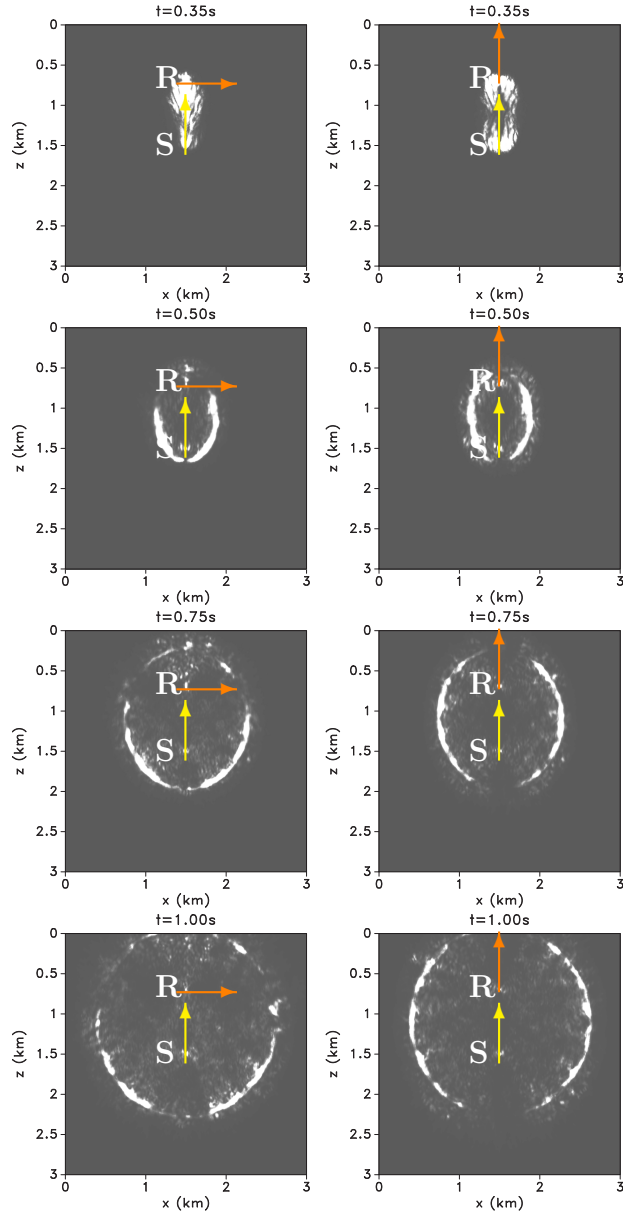


Figure 5.6: S-wave sensitivity kernel K_s^i of the scattered waves generated by a vertically aligned point force source for the $i = x$ component (left) and the $i = z$ component (right). The source (yellow arrow, S) is located at $[x, z] = [1.5, 1.5]km$ and the receiver (orange arrow, R) at $[x, z] = [1.5, 0.7]km$. The direction of the arrows at the source and receiver indicates the direction of the source radiation and the direction of the displacement component at the receiver, respectively. The base of the arrows are the locations of either the source or the receiver.

top panel). The receiver intensity fields are also shown, which are generated at the receiver location by a point source aligned along the x-direction (Figure 5.5, middle panel) or along the z-direction (Figure 5.5, bottom panel) for the computation of the sensitivity kernel along the x- or z- component of the displacement field, respectively. The source and the receiver locations are indicated by the yellow and orange arrows, respectively. The S-wave intensity fields show scattered phases propagating beyond the S-wave scattered front. These scattered phases are due to P-to-S converted waves.

In Figure 5.6, we show the S-wave sensitivity kernel for the x- and z- components of the displacement field generated by a vertical point source. The panels in Figure 5.6 correspond to the kernels at travel-times $t = 0.35 \text{ s}$, 0.50 s , 0.75 s , and 1.00 s . As was the case for the P-wave kernels, the kernel fronts are significantly larger than the contributions elsewhere in the kernel. The S-wave kernel consists of the kernel front defining the single scattering contribution, the sensitivity due to multiple scattering beyond and bounded by the kernel front, and the elevated sensitivity at or near the source and the receiver locations. The sensitivity beyond the kernel front is the sensitivity to the S-wave velocity perturbation due to S waves converted from originally travelling P-waves. The part of the sensitivity kernel bounded by the kernel front results from S-waves multiply scattering from both P- and S-waves.

The kernel fronts show a radiation pattern defined by the source radiation pattern, the orientation of the source-receiver line, and the component of the recorded displacement field. The radiation pattern of the kernel front in the x-component of the S-wave kernel is a 180° rotation of the radiation pattern of the kernel front in the x-component of the P-wave kernel (compare the left panels of Figure 5.3 and Figure 5.6). The rotation results from the 90° rotations in the radiation patterns in both the source and receiver S-wave intensities relative to the source and receiver P-wave intensities. In the kernel front of the x-component of the displacement field (Figure 5.6 (left)), a node is present along the z-direction below the source location because of the node in the S-wave radiation in the z-direction along the wavefront

of the source S-wave intensity field (Figure 5.5, top panel). The vanishing sensitivity along the kernel front at the upper hemiellipse is generated by the vanishing S-wave radiated in the vertical direction by a vertical point source. However, given that the S-wave front is radiated horizontally from the source location, the kernel front in the lower hemiellipse of the kernel front is non-zero.

The S-wave sensitivity kernel for the z-component shows a different radiation pattern. The kernel shows a nodal sensitivity along the the z-direction except at the source and the receiver locations. The nodal sensitivity at the kernel front along the z-direction is due to the nodal line (in 2D) of the S-wave radiated vertically by the vertical point force. The nodal sensitivity splits the kernel symmetrically into a left and right horizontally propagating kernel front. The horizontally propagating part of the kernel front is generated by the S-waves radiating in the horizontal direction.

5.6 Heterogeneous scattering model with free-surface

The earth's subsurface is usually statistically heterogeneous and is a sphere or half space bounded by a free surface. The presence of the heterogeneity and the free-surface adds additional complexity to the scattered wavefield. For seismic waves propagating within the earth, we expect the presence of both surface waves and body waves and the continuous conversion between these two wave types. To explore the characteristics of the sensitivity kernel in the presence of these complexities in wave scattering, we compute the kernel with the scattering models in Figure 5.7, which shows a two-layered scattering velocity model bound at the top by a free surface. The top layers of the P- and S-wave velocity models are strongly scattering layer defined by the von-Karman parameters $a_x = a_z = 0.01 \text{ km}$, $\epsilon = 1.0$, and $\kappa = 0.2$. In the bottom half-spaces, the von-Karman parameters are $a_x = a_z = 0.1 \text{ km}$, $\epsilon = 0.1$, and $\kappa = 0.8$. The average P-wave velocity of the top layer is 2.5 km/s while that of the bottom half-space is 3.5 km/s . The average S-wave velocity for the top and the bottom layers are 1.78 km/s and 2.5 km/s , respectively. We assume a constant density of 1.5 g/cm^3 .

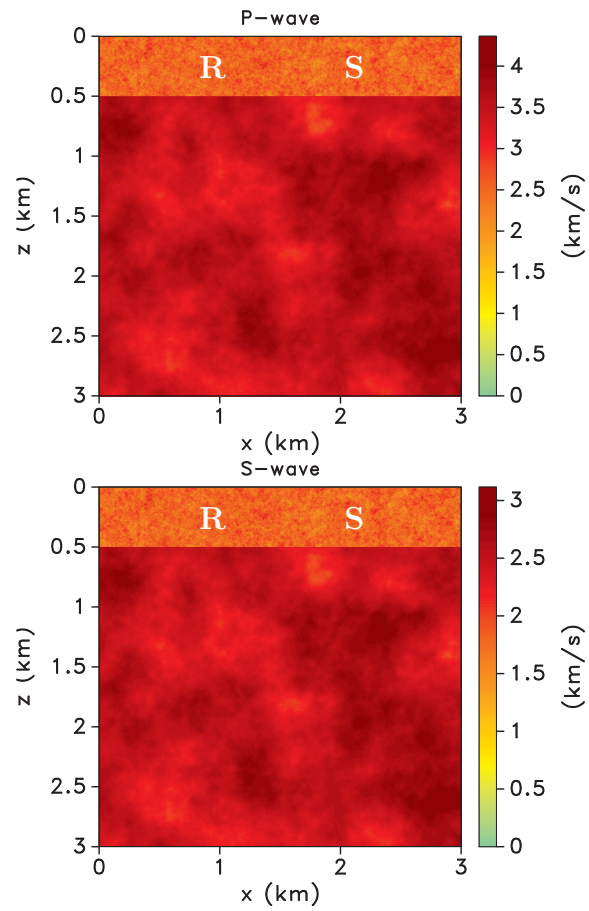


Figure 5.7: Heterogeneous velocity models with free surface: P-wave velocity (left) and S-wave velocity (right).

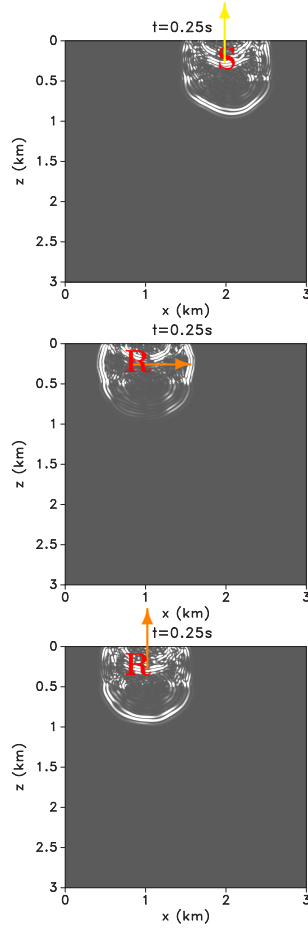


Figure 5.8: The P-wave intensity fields used for the kernel computation at travel-time 0.25 s in the statistically heterogeneous model (Figure 5.7). Top: The source intensity field due to a vertical point force located at $[x, z] = [1.0, 0.25]\text{ km}$ (yellow arrow, S). Middle: The receiver intensity field due to a horizontal point force located at $[x, z] = [2.0, 0.25]\text{ km}$ (orange arrow) for the x-component kernel. Bottom: The receiver intensity field due to a vertical point force located at $[x, z] = [2.0, 0.25]\text{ km}$ (orange arrow) for the z-component kernel. The direction of the arrows at the source and receiver indicates the direction of the source radiation and the direction of the displacement component at the receiver, respectively. The base of the arrows are the locations of either the source or the receiver.

5.6.1 Sensitivity to perturbations in P-wave velocity

We compute the sensitivity kernels for a source-receiver pair embedded within the strongly heterogeneous top layer (Figure 5.7). The source is a vertical point force located at $[x, z] = [1.0, 0.25]km$ (yellow arrow, Figure 5.7). Figure 5.8 shows the intensity field generated by the point force and the receiver intensity fields with horizontal and vertical point forces for the computation of the x- and z-components of the kernels, respectively. The intensity fields are composed of scattered intensities from the free-surface and the reflector, a multiply scattered intensity field, and a scattered intensity due to surface waves propagating along the top layer. Due to the lower velocity, strong heterogeneity, free surface, and an embedded source within the top layer, most of the scattered intensity is trapped within the top layer.

In the bottom layer, we have mostly coherently scattered waves propagating across the layer. The forward propagating front is distorted due to the relatively broad velocity variations in the bottom layer. Figure 5.9 shows the P-wave sensitivity kernels for the x- and z-components of the displacement fields at travel-times 0.425 s, 0.50 s, 0.75 s, and 1.00 s. The travel-time of the first arrival is approximately 0.4 s. At the top panels of Figure 5.9 for both kernel components, the sensitivity is dominated mostly by forwardly propagating scattered waves. The source radiation and components of the displacement fields define the radiation of the kernel fronts shown in the top two figure panels of the kernel (Figure 5.9; $t = 0.425s$ and $0.5s$). However for longer coda lapse times, the kernel is chaotic within the top layer. In the two lower figure panels of Figure 5.9, the sensitivity is larger in the top layer than in the bottom layer. Also, the kernel sensitivity within the top layer is randomized and the kernel front is weak. The randomized nature of the kernel in the top layer results from multiple scattering because of the strong heterogeneity within the top layer. The propagating kernel front in the bottom layer is still present but with smaller magnitude compared with the kernel in the top layer.

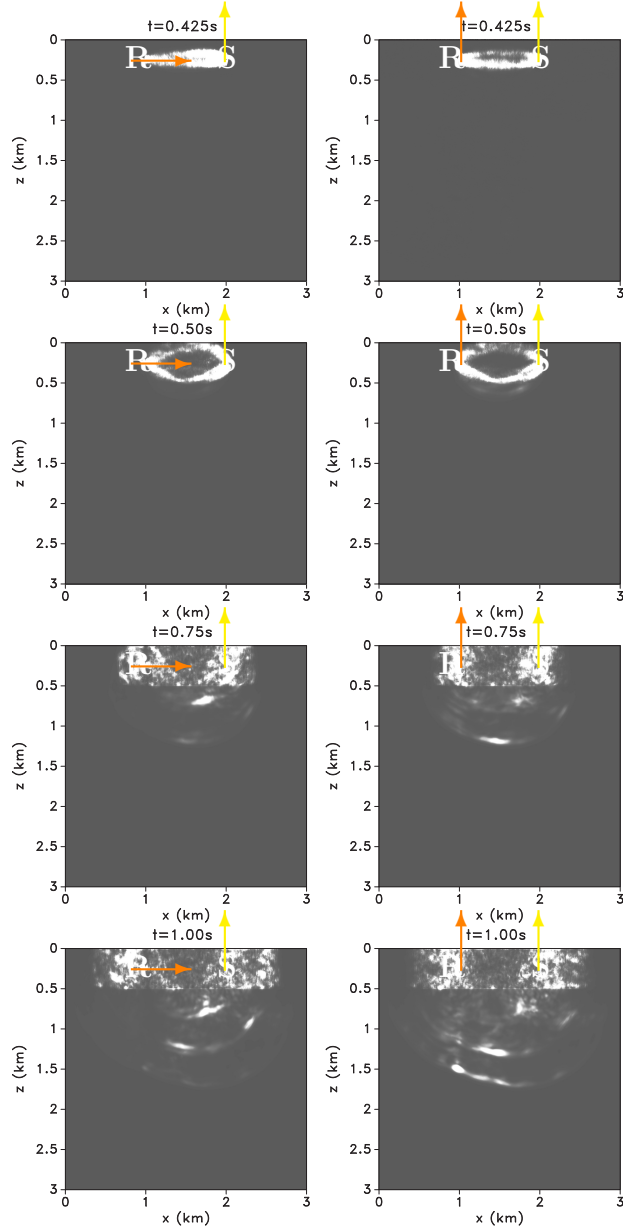


Figure 5.9: P-wave sensitivity kernel K_p^i of the scattered waves generated by a vertically aligned point force source for the $i = x$ component (left) and the $i = z$ component (right). The source (yellow arrow, S) is located at $[x, z] = [1.0, 0.25]km$ and the receiver (orange arrow, R) at $[x, z] = [2.0, 0.25]km$. The direction of the arrows at the source and receiver indicates the direction of the source radiation and the direction of the displacement component at the receiver, respectively. The base of the arrows are the locations of either the source or the receiver.

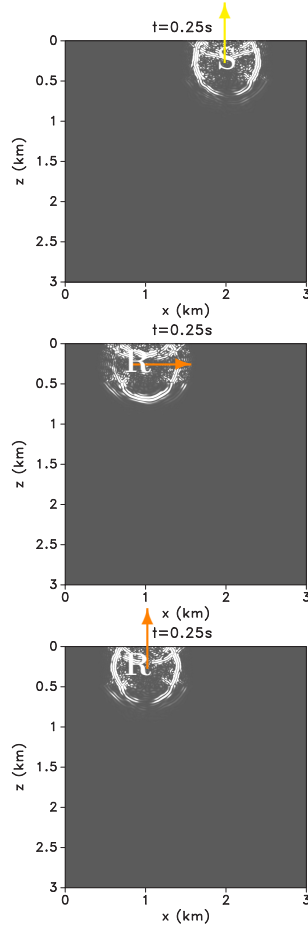


Figure 5.10: The S-wave intensity fields used for the kernel computation at travel-time 0.25 s in the statistically heterogeneous model (Figure 5.7). Top: The source intensity field due to a vertical point force located at $[x, z] = [1.0, 0.25]\text{ km}$ (yellow arrow, S). Middle: The receiver intensity field due to a horizontal point force located at $[x, z] = [2.0, 0.25]\text{ km}$ (orange arrow) for the x-component kernel. Bottom: The receiver intensity field due to a vertical point force located at $[x, z] = [2.0, 0.25]\text{ km}$ (orange arrow) for the z-component kernel. The direction of the arrows at the source and receiver indicates the direction of the source radiation and the direction of the displacement component at the receiver, respectively. The base of the arrows are the locations of either the source or the receiver.

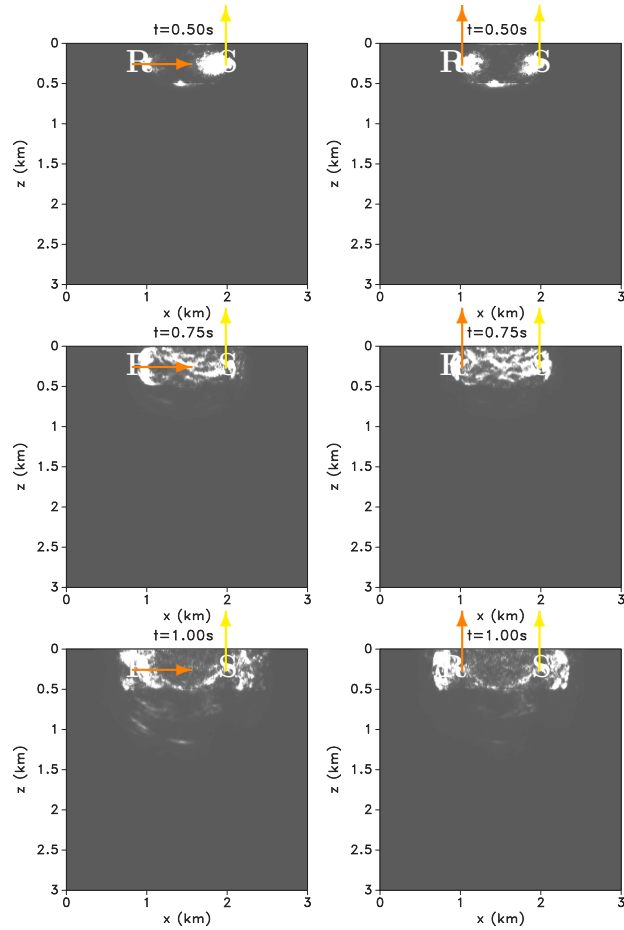


Figure 5.11: S-wave sensitivity kernel K_s^i of the scattered waves generated by a vertically aligned point force source for the $i = x$ component (left) and the $i = z$ component (right). The source (yellow arrow, S) is located at $[x, z] = [1.0, 0.25]km$ and the receiver (orange arrow, R) at $[x, z] = [2.0, 0.25]km$. The direction of the arrows at the source and receiver indicates the direction of the source radiation and the direction of the displacement component at the receiver, respectively. The base of the arrows are the locations of either the source or the receiver.

5.6.2 Sensitivity to perturbations in S-wave velocity

The computation of S-wave kernels uses the scattered S-wave intensities from both the source and the receiver locations. Figure 5.10 shows the source S-wave intensity field due to a vertical point force located at $[x, z] = [1, 0.25]$ km (yellow arrow, S) and the receiver S-wave intensity fields for the x and z-components of the S-wave kernels. We compute the S-wave intensity using the decomposed S-wave displacement field (equation 5.8). The receiver S-wave displacement fields are generated by the point forces, aligned to the x and z-directions for the x and z-components of the kernel, respectively, and located at $[x, z] = [2, 0.25]$ km (orange arrows; Figure 5.10, middle and bottom panel). These intensity fields contain both the intensity of the surface waves propagating within the top layer, reflected intensities both from the free-surface and the reflector, and transmitted intensity propagating through the bottom layer. At travel-time 0.25s, Figure 5.10 shows the nodal lines of the intensities present in the forward propagating and reflected intensities.

Figure 5.11 shows the x- and z-components of the S-wave sensitivity kernel for travel-times 0.50 s, 0.75 s, and 1.00 s. At travel-time 0.50 s, the x-component of the sensitivity kernel is relatively higher at the source location (yellow arrow) compared to the receiver location (orange arrow, S) because the amplitude is largest along the x-direction for the source intensity field (Figure 5.10, middle panel). In the z-component of the kernel, the sensitivities at the source and receiver locations have comparable magnitude with little indication of the kernel split along the x-direction because the scattering occurs close to the source and receiver locations. In the two bottom panels of Figure 5.11 (travel-times 0.75 s and 1.00 s), the sensitivity within the top layer is mostly randomized but is still bounded by a suppressed kernel front. The sensitivity within the bottom layer has relatively smaller magnitude compared to the top layer.

The reduced sensitivities within the bottom layer (using the source-receiver pair embedded within the strongly heterogeneous top layer) imply that there is weaker scattering contributions to the scattered waves from the bottom layer across the coda lapse time. This

means that the source-receiver setup in Figure 5.7 will be less sensitive to changes (both P- and S-wave velocity changes) within the bottom layer. The sensitivity distribution across the heterogeneous model (Figure 5.7) will be different when the source-receiver pair is embedded within the bottom layer of the scattering model.

5.7 Discussion and Conclusion

Changes in the elastic properties of a scattering medium can induce changes in the P- and S-wave velocities of the scattering medium. These changes in the elastic properties depend on changes in the mechanical and fluid properties of the medium. In this study, we provide an approach to characterize the sensitivities of the travel-time changes estimated across the elastic time-lapse coda to the fractional change in the P- and S-wave velocities. Assuming that the scattered P- and S-waves are independently sensitive to the P- and S-wave velocity changes, respectively, the sensitivity kernel for the P- and S-wave velocity changes can be accounted for by equations 5.17 and 5.18. We provide an approach to numerically compute the sensitivity kernels using multiply scattered waves. This approach allows for the computation of the sensitivity kernels within an arbitrary scattering model without an assumption of homogeneity in the scattering model. Also, any boundary condition, such as the free-surface boundary conditions, can be incorporated within the numerical computation of the sensitivity kernels. The computation of the sensitivity kernel also allows us to evaluate the relative contribution of the velocity changes (P- or S-wave velocities) to an estimated travel-time change across the coda lapse time for a given scattering medium. The contribution of the velocity changes to an estimated travel-time change depends on the scattering medium, the relative location of the change to the monitoring source-receiver pairs, the relative magnitude of the P- and S-wave velocity changes, the source radiation pattern, the component of the monitoring time-lapse coda, and the travel-time of the monitoring coda waves.

However, there lies a challenge in using equation 5.6 for imaging either P- or S-wave velocity change. In equation 5.6, the travel-time changes due to changes in the elastic

velocities are coupled. Equation 5.6 can be expressed in the matrix form

$$\hat{\tau} = \hat{\tau}_p + \hat{\tau}_s = [K_p d\mathbf{x} \quad K_s d\mathbf{x}] \times \begin{bmatrix} \hat{\delta s}_p \\ s_p \\ \hat{\delta s}_s \\ s_s \end{bmatrix}, \quad (5.19)$$

where $\hat{\tau}$ is an $M \times 1$ vector of the travel-time changes and $\frac{\hat{\delta s}_{p,s}}{s_{p,s}}$ is a $N \times 1$ vector of the discretized slowness model of either the P- or S-wave. The discretized kernels $K_p d\mathbf{x}$ and $K_s d\mathbf{x}$ are an $M \times N$ matrix of the P- and S-wave sensitivity kernel, respectively, where M is the dimension of the estimated travel-time change and N is the dimension of the discretized monitored medium.

The travel-time changes estimated from the time-lapse coda of a particular component contain the contributions from both the P- and S-wave velocity changes. The coupled travel-time changes will provide trade-offs for the inverted fractional changes in the P- and S-wave velocities. The trade-off can be limited by using estimates of the travel-time change from travel-times at which the relative magnitude of one of the sensitivity kernels (P or S) is significantly larger than the other. At travel-times close to the direct P-wave arrival time, the P-wave sensitivity is expected to be greater than the S-wave sensitivity; conversely at travel-times close to the direct S-wave arrival time, the S-wave sensitivity is greater. Also at travel-times $t \gg r/c$, where r is the source-receiver distance and c average velocity, the coda is expected to be dominated by the S-waves [1, 97, 109] due to equipartitioning of the scattered waves. At these travel-times one expects greater contribution of the S-velocity change to the travel-time change. Comparison of the contributions of the kernels to the travel-time changes across the elastic coda may provide a constraint on the relative magnitude of the fractional velocity changes in either the P- or S- wave velocity.

5.8 Acknowledgments

This research was supported by sponsors of the Consortium Project on Seismic Inverse Methods for Complex Structures. The reproducible numerical examples in this paper use the Madagascar open-source software package freely available from <http://www.ahay.org>.

CHAPTER 6

TIME-LAPSE IMAGING OF LOCALIZED WEAK CHANGES WITH MULTIPLY SCATTERED WAVES: NUMERICAL EXPERIMENT

Chinaemerem Kanu and Roel Snieder

To be submitted to Journal Geophysical Research (2015)

6.1 Abstract

Multiply scattered seismic waves, due to their long path length within a finite volume, provide information that can be used to detect and image weak time-lapse changes within a medium. Such weak changes are usually not resolved with singly scattered waves. Previous use of multiply scattered waves for time-lapse monitoring assume some level of statistical homogeneity about the scattering medium. This homogeneity is usually characterized either by a constant mean free path or diffusion coefficient. In a realistic medium, however, this assumption of homogeneity likely breaks down. We demonstrate the capability of resolving a localized time-lapse velocity change within a 3-layer scattering model using multiply scattered waves. The layers within the model have different scattering properties. We localize the weak velocity change but the resolution of the imaged change degrades with increasing coda travel-time.

6.2 Introduction

Various monitoring tools have been developed to monitor and characterize weak changes within a wide spectrum of media which includes the earth's subsurface, mechanical structures such as buildings, and medical specimens. These monitoring tools range from single-scattering wave methods (such as sonic/seismic tomography [48, 66], reflection/transmission methods [21], and time-lapse microscopy [43]) to multiply-scattering wave methods (such as diffusion (acoustic) wave spectroscopy (D(A)WS) [20, 74] and coda wave interferometry

(CWI) [96, 97]). The strengths and limitations of these monitoring tools depend on both the sensitivity of the monitoring data to the change in the medium and how accessible the imaging data is for the monitoring process. It has been demonstrated that multiply scattered waves are more likely to identify weak temporal changes than do single-scattered waves [31, 44]. Multiply scattered waves, due to increased scattering, provide information about the monitored medium that can be used to increase the resolution of the imaged medium (for example, using reflected multiples) [8], increase illumination especially within poorly illuminated subsurface [28], and increase the detection of weak time-lapse changes within the medium [76]. Increased scattering of seismic waves potentially improves the detectability of the weak changes especially in cases where these weak changes are not resolvable with singly scattered waves. However, because of the averaging effect of multiply scattered waves and the complexity in the travel paths of the multiply scattered waves, the spatial resolution of the weak changes is usually not high.

Initial efforts in using multiply scattered waves for time-lapse monitoring were successfully used for detecting changes within a monitored medium [64, 76, 97, 111]. Techniques like D(A)WS and CWI are geared toward measuring global change within a medium thereby averaging the changes present across the monitored medium regardless of whether the changes are localized or not. However, imaging the locations of weak time-lapse changes was a focus of recent research. The first known recipe for inverting a localized change using multiply scattered waves is given by Pacheco and Snieder [70] who relate the mean travel-time changes to a localized slowness change. Rossetto et al. [82] introduce a technique, called LOCADIFF, which uses the decorrelation of the time-lapse scattered waves to image a localized change in the scattering medium. These efforts at localizing changes within a scattering medium assume statistically homogeneous scattering models. How well these methods resolve weak changes in complexly heterogeneous media especially in media where the scattered waves have non-diffusive behavior is yet unknown.

In this study, we investigate the capability of imaging a localized weak velocity change within a scattering medium with heterogeneous statistical properties. Using a numerical example of structurally heterogeneous model, we demonstrate the use of travel-time changes to image a localized time-lapse velocity change within a scattering medium. In section 6.5, we describe how the resolution of the imaged change in the model depends on the spatial broadening of the sensitivity kernel and on the averaging out of the estimated fractional velocity change.

6.3 Theory

Pacheco and Snieder [70] developed a sensitivity kernel $K(\mathbf{s}, \mathbf{x}_o, \mathbf{r}, t)$ that is based on the intensity of multiply scattered waves which relates mean travel-time changes $\langle \tau(t) \rangle$ to a localized relative velocity change $\delta v/v(\mathbf{x}_o)$ at \mathbf{x}_o :

$$\langle \tau(t) \rangle = - \int_V K(\mathbf{s}, \mathbf{x}_o, \mathbf{r}, t) \frac{\delta v}{v}(\mathbf{x}_o) dV(\mathbf{x}_o), \quad (6.1)$$

where V is the scattering volume, and \mathbf{s} and \mathbf{r} are the source and the receiver locations, respectively. We estimate the travel-time changes ($\langle \tau(t) \rangle = -\epsilon t$) using the stretching method [33] for a given time window of the scattered waves, where ϵ is the stretching factor. The stretching factor is equal to the estimated fractional velocity change within the time window. To obtain the optimal stretch factor, we minimize

$$\min f(\epsilon) = \|\hat{u}(t + \epsilon t) - u(t)\|_2^{t, t_w}, \quad (6.2)$$

where $u(t)$ and $\hat{u}(t)$ are the original and the time-lapse coda signals, respectively.

Perturbation of a scattering medium can result in changes in the scattering cross-section of the medium without a change in the velocity of the medium. Rossetto et al. [82] relate the decorrelation $D(\mathbf{s}, \mathbf{r}, t)$ between time-lapse multiply scattered waves to the time-lapse change in the total scattering cross-subsection $\delta\sigma(\mathbf{x}_o)$ of a medium:

$$D(\mathbf{s}, \mathbf{x}_o, \mathbf{r}, t) = \frac{v(\mathbf{x}_o)\delta\sigma(\mathbf{x}_o)}{2} K(\mathbf{s}, \mathbf{x}_o, \mathbf{r}, t). \quad (6.3)$$

The change in the total scattering cross-subsection describes changes in the scattering properties the medium. The time-windowed decorrelation is defined as

$$\begin{aligned}
 D(\mathbf{s}, \mathbf{r}, t) &= 1 - C(\mathbf{s}, \mathbf{r}, t) \\
 &= 1 - \frac{\int_{t-t_w}^{t+t_w} u(\mathbf{s}, \mathbf{r}, t') \hat{u}(\mathbf{s}, \mathbf{r}, t' + t_s) dt'}{[\int_{t-t_w}^{t+t_w} u(\mathbf{s}, \mathbf{r}, t')^2]^{1/2} [\int_{t-t_w}^{t+t_w} \hat{u}(\mathbf{s}, \mathbf{r}, t')^2]^{1/2}},
 \end{aligned} \tag{6.4}$$

where t is the travel-time and t_w is the half-length of the time-window use to compute the cross-correlation $C(\mathbf{s}, \mathbf{r}, t)$.

Equations 6.1 and 6.3 contain the same sensitivity kernel $K(\mathbf{s}, \mathbf{x}_o, \mathbf{r}, t)$ [75], which depends on the source and receiver locations, the scattering property of the medium, and the travel-time of the scattered waves. The sensitivity kernel is given by

$$K(\mathbf{s}, \mathbf{x}_o, \mathbf{r}, t) = \frac{\int_0^t P(\mathbf{s}, \mathbf{x}_o, t') P(\mathbf{x}_o, \mathbf{r}, t - t') dt'}{P(\mathbf{s}, \mathbf{r}, t)}, \tag{6.5}$$

where P is the normalized intensity of the scattered waves [70]. The normalized intensity

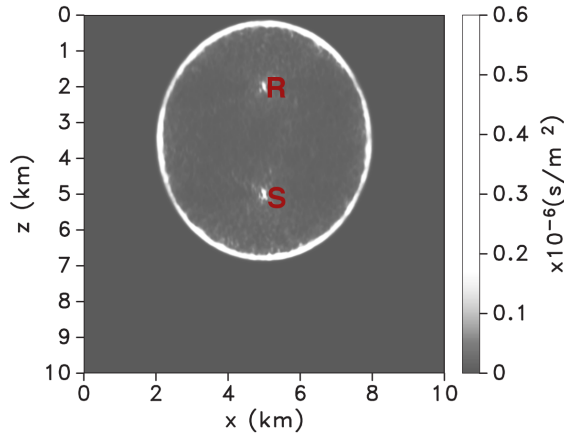


Figure 6.1: Sensitivity kernel $K(\mathbf{s}, \mathbf{x}_o, \mathbf{r}, t)$ for the source-receiver pair (S-R) within a statistical homogeneous scattering velocity model.

or the corresponding sensitivity kernel can be computed either by using analytical intensity models such as the diffusion intensity model or the radiative transfer intensity model [69]; or by using a numerical approach where the sensitivity kernel is computed by convolving numerically generated source and receiver intensity fields [38]. The intensity fields are com-

puted from numerically simulated scattered wavefields excited at the source and the receiver locations. Using the numerically generated scattered intensity fields in equation 6.5, the sensitivity kernel $K(\mathbf{s}, \mathbf{x}_o, \mathbf{r}, t)$ is obtained for every given coda lapse time t . Figure 6.1 shows a sensitivity kernel for the source-receiver pair (S-R) using a statistical homogeneous scattering velocity model. This sensitivity kernel corresponds to the scattered waves recorded at travel-time $t \simeq t^*$, where t^* is the mean free time. Given an estimate of the statistical properties of the scattering model, the numerical solution of the wavefield gives the kernel for imaging the time-lapse changes present in a medium, especially in a heterogeneously complex medium.

6.4 Model setup:

To explore the capability of resolving a localized velocity change using either the estimated travel-time change or the decorrelation of the time-lapse data, we consider the geometry shown in Figure 6.2, which shows both the velocity (scattering) model and the time-lapse velocity change for our imaging problem. The velocity model is a 3 layer model, with each layer having scattering properties of different statistical characteristics. The statistical characteristics of the top and the bottom scattering layers are structurally isotropic, while the middle layer is statistically heterogeneous characterizing a highly fractured reservoir. The time-lapse change is a 0.5% velocity change in the rectangle embedded within the middle layer shown in Figure 6.2 (bottom). To monitor and resolve this localized change, we use two vertical receiver arrays representing two boreholes located on opposite sides of the localized change. These boreholes record scattered waves generated by the 9 sources that are located along a horizontal line. This source-receiver setup depicts time-lapse monitoring with repeating microseismic events whose scattered waves (codas) are recorded in the 2 boreholes. We assume acoustic waves generated by an explosive source, hence we are not accounting for the effect of the source radiation and elastic seismic wave modes.

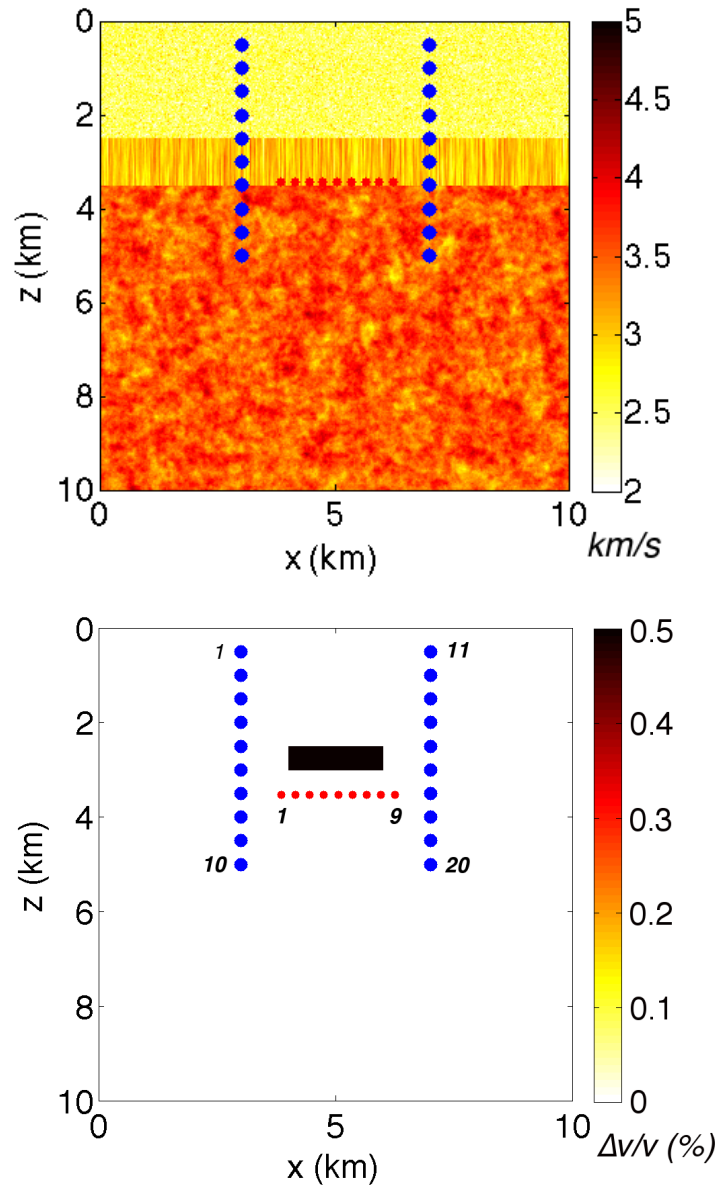


Figure 6.2: Numerical model for time-lapse inversion of localized velocity change with the used sources (red circles) and receivers (blue circles). Top: the reference velocity (scattering) model with the source-receiver setup and Bottom: the true localized velocity change with the source-receiver setup.

6.5 Model and Data resolution

The challenge of imaging localized velocity changes or other model properties with the multiply scattered waves lies in the resolution of the imaged model parameters. For our imaging of the time-lapse changes, the resolution of the imaged localized changes depends on the travel-time of the scattered waves. With increasing travel-time, the imaging data (the travel-time changes or the decorrelation) spreads out in space and the sensitivity kernel for the time-lapse changes broadens spatially. To consider the resolution of the inverse problem, we consider both the model resolution and the data resolution. The model resolution considers the impact of the spatial broadening of the kernel on the resolution of the inverse solution while the data resolution evaluates the effect of the data averaging. Data averaging within the time-lapse coda wave occurs because at increasing coda lapse time, the recorded coda results from the interference of scattered waves travelling across broader region of the scattering medium in the presence of localized change. Figure 6.3 shows an azimuthal dependence of estimated velocity changes due to a Gaussian positive velocity change (Figure 6.4, yellow arrow points to the location of the velocity change) within a statistical homogeneous scattering model (Figure 6.4) using the circular receiver array and a source embedded in the middle of the model (Figure 6.4, blue dot). The azimuth of the Gaussian velocity change is along azimuth 90° (Figure 6.3, red line) and the maximum velocity change is 1%. We show the estimated velocity change for 36 source-receiver pairs at different azimuths for 5 coda lapse times. Figure 6.3 shows non-zero estimated velocity changes for source-receiver pairs with azimuth close to the azimuth of the Gaussian velocity change early in the coda ($t < t^*$). But later in the coda time ($t > t^*$), the velocity change spreads to other source-receiver pairs far from the Gaussian velocity change. The estimated velocity change becomes isotropic at large coda lapse time ($t \gg t^*$). The estimated velocity changes are path-averaged velocity changes of all the interfering scattered waves recorded within the coda wave time-window used to estimate the velocity changes. Given that the velocity change is localized, the estimated velocity change is a fraction of the true maximum velocity change in the medium.

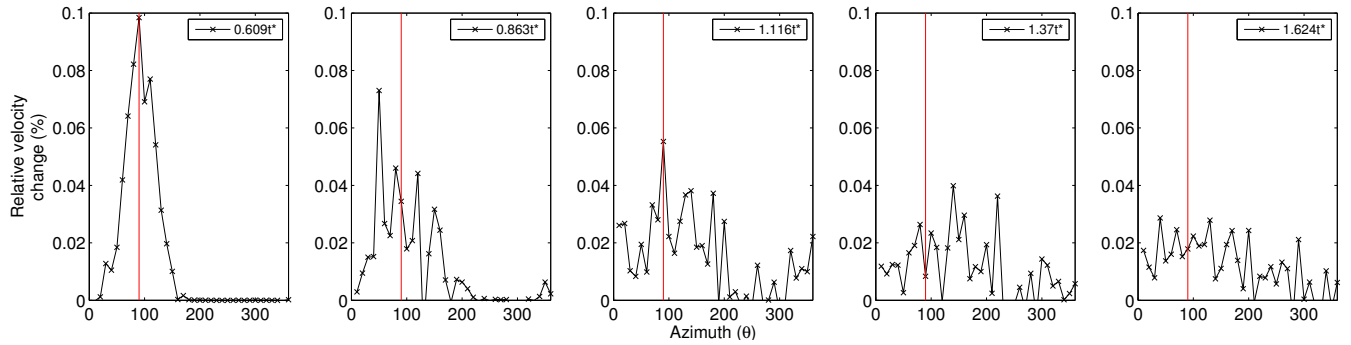


Figure 6.3: Azimuthal dependence of the estimated velocity change due to a Gaussian positive velocity change along the source-receiver pair at azimuth 90° (red line). The figure panels are the estimated velocity changes at various coda lapse times measured by the transport mean free time t^* of the scattering model.

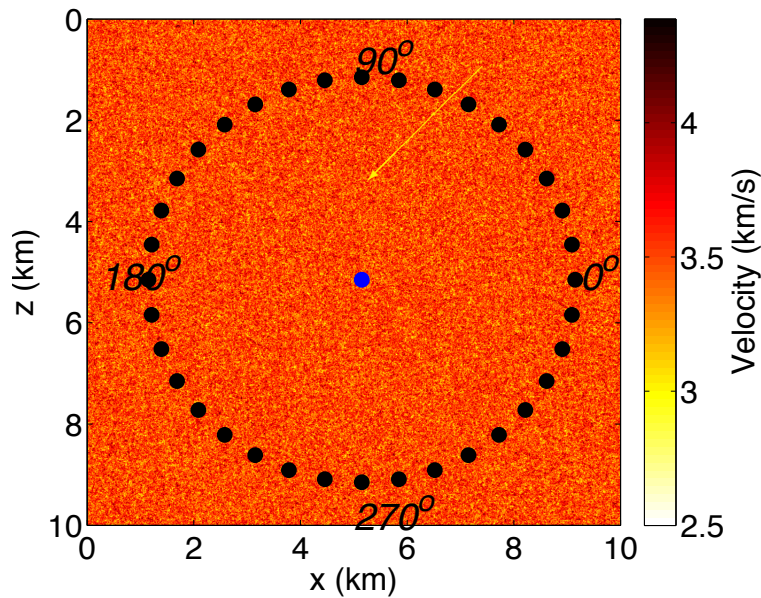


Figure 6.4: The model geometry use for data averaging test. A Gaussian velocity change is centered at location $[x, z] = [3, 5]$ km within a statistically homogeneous velocity model. The data averaging test used a ring of receivers (black dots) and a source (blue dot) located at $[x, z] = [5, 5]$ km. The azimuth of the receivers is specified by the degrees. The yellow arrow points to the location of the velocity change.

Lets consider an inverse problem $\mathbf{d} = \mathbf{K}\mathbf{m}$ (ignoring noise due either to data measurement or the model discretization), where \mathbf{m} is the model, \mathbf{d} is the data, and the \mathbf{K} is a discretized version of the Frechet derivative which describes the sensitivity of the data to the model. We minimize the regularized least-squares objective function ϕ :

$$\phi = \|\mathbf{W}_d(\mathbf{d} - \mathbf{K}\mathbf{m})\|_2^2 + \beta\|\mathbf{m}\|_2^2 \quad (6.6)$$

where β is the trade-off parameter and \mathbf{W}_d is the data weighting matrix whose diagonal elements are the standard deviation of \mathbf{d} . We determine the trade-off parameter using generalized cross-validation (GCV) [7].

The estimated model is

$$\mathbf{m} = [\mathbf{K}^T \mathbf{W}_d^T \mathbf{W}_d \mathbf{K} + \beta \mathbf{I}]^{-1} \mathbf{K}^T \mathbf{W}_d^T \mathbf{W}_d \mathbf{K} \hat{\mathbf{m}} \quad (6.7)$$

where $\hat{\mathbf{m}}$ is the actual model and \mathbf{I} is an identity matrix. Equation 6.7 can be rewritten as:

$$\mathbf{m} = \mathbf{R}_m \hat{\mathbf{m}} \quad (6.8)$$

where $\mathbf{R}_m = [\mathbf{K}^T \mathbf{W}_d^T \mathbf{W}_d \mathbf{K} + \beta \mathbf{I}]^{-1} \mathbf{K}^T \mathbf{W}_d^T \mathbf{W}_d \mathbf{K}$ is the model resolution matrix. The model resolution matrix \mathbf{R}_m explains how the inverse solution is a smeared out version of the actual model $\hat{\mathbf{m}}$. From equation 6.8,

$$\mathbf{m} = \mathbf{R}_m \hat{\mathbf{m}} = \sum_{i=1}^N \hat{m}_i \mathbf{p}^i \quad (6.9)$$

where N is the dimension of the model and \mathbf{p}^i are the column vectors of the model resolution matrix \mathbf{R}_m . The \mathbf{p}^i vectors which are usually called the point spread functions, explain how the i^{th} element of the actual model is mapped to the estimated model. Following Oldenborger and Routh [68], we can determine how well an i^{th} parameter of the model is resolved by solving

$$[\mathbf{K}^T \mathbf{W}_d^T \mathbf{W}_d \mathbf{K} + \beta \mathbf{I}] \mathbf{p}^i = \mathbf{K}^T \mathbf{W}_d^T \mathbf{W}_d \mathbf{K} \Delta_i \quad (6.10)$$

for \mathbf{p}^i using a delta function vector Δ_i which has 1 at the i^{th} vector element and zeros elsewhere. To solve for \mathbf{p}^i , we use a linear conjugate gradient algorithm. Each of the \mathbf{p}^i are

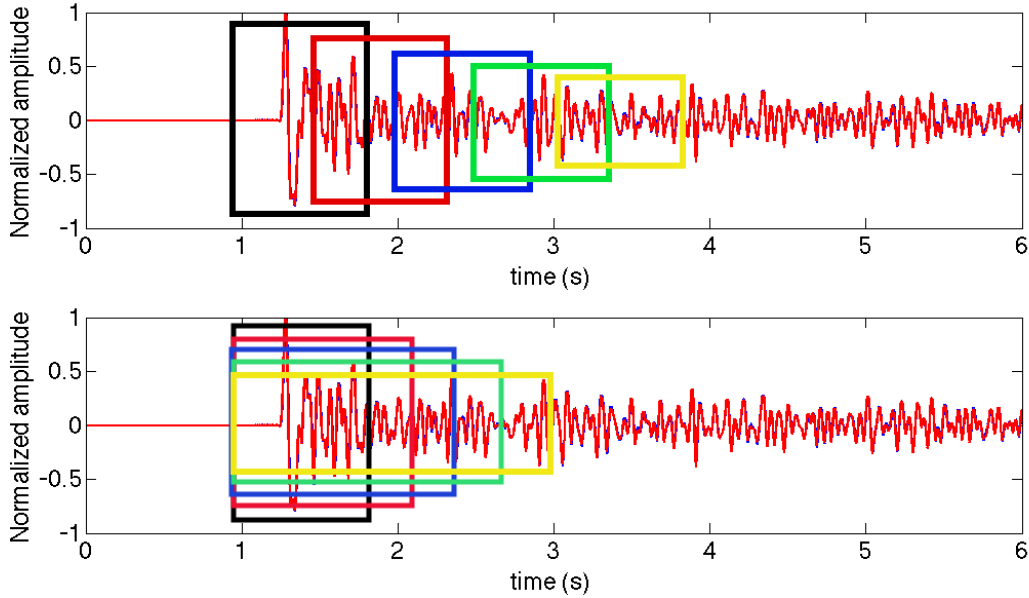


Figure 6.5: The coda time windows use for resolution analysis for the time-lapse imaging. Top: The used time windows for Category 1 resolution analysis and Bottom: The used time windows for Category 2 resolution analysis.

obtained after 5 iterations. We compare the model resolution at various time windows of the multiply scattered waves (coda). To estimate the travel-time changes across the coda, we use 0.6 s time windows with each window overlapping 0.1 s with the previous time window. Each time window contains about 10 cycles of the signal and the windowed signals are tapered with a Tukey time window. Using a time window which is 10 times the dominant period helps stabilize the estimated travel-time changes [97]. To get more data points for the inversion, we interpolate estimated travel-time changes from time-interval 0.5 s to 0.02 s. To evaluate the model resolution across the coda, we consider two time-window categories. These window categories define time-windows that contain sub-time-windows. Category 1 uses a 0.55 s time window with progressive shifts of the centertime of the window to later coda times by 0.5 s (Figure 6.5 Top). For Category 2, each of the time-windows start from 0.30 s before the first arrival. The first time window (Figure 6.5 black rectangle) extends to 0.25 s after the first arrival. The extent of the rest of the time windows increases by 0.25 s (Figure 6.5 Bottom), i.e extending to 0.80 s, 1.05 s, 1.30 s, and 1.55 s, respectively after the

travel-time of the first arrival.

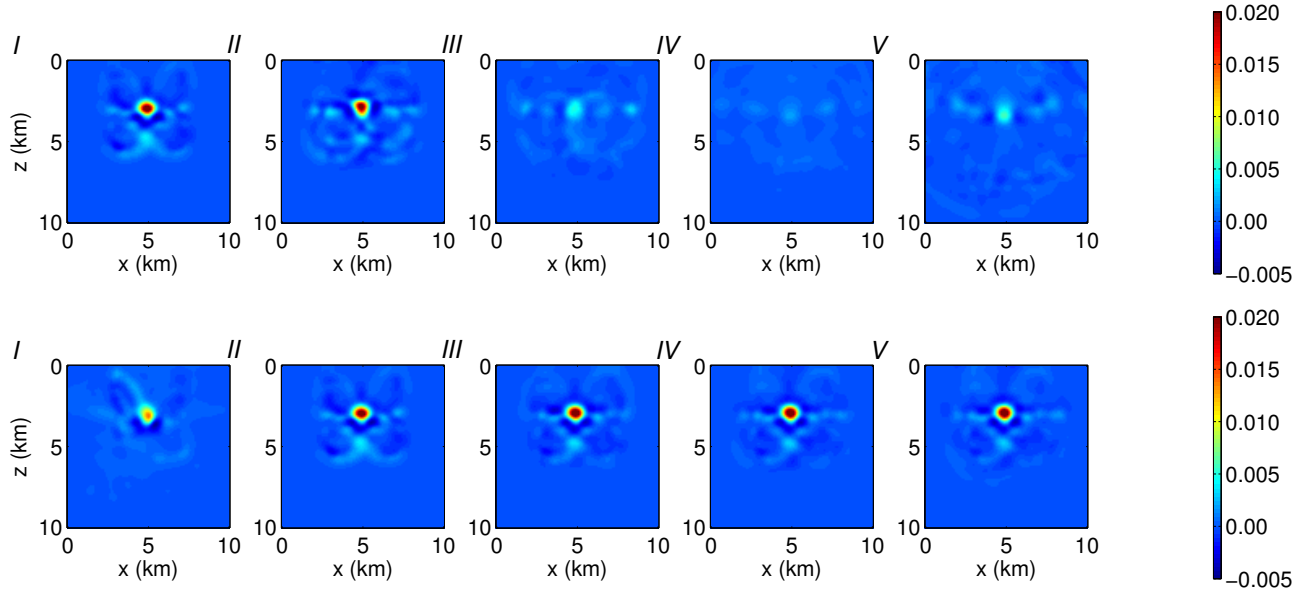


Figure 6.6: The point spread function \mathbf{p}^i for the inverted model at $[x, z] = [5, 3] \text{ km}$ using the Top: Category 1 and Bottom: Category 2 time-windows. The point spread function \mathbf{p}^i uses time-windows: I (black window), II (red window), III (blue window), IV (green window), and V (yellow window) in Figure 6.5.

Figure 6.6 (Top) shows the \mathbf{p}^i for the model elements located at $[x, z] = [5, 3] \text{ km}$ for the coda time-windows in Figure 6.5 (Top). This model element corresponds to the model location inside the middle horizon which is between z of 2.5-3.5 km (Figure 6.2). The resolved point spread functions suggest a decrease of the model resolution with increased centertime of the time-window (Figure 6.6). This reduced resolution results from the spatial broadening of the sensitivity kernel. However, using the coda time-windows in Figure 6.5 (Bottom), the velocity change \mathbf{p}^i is better resolved with increasing centertime of the time-window (Figure 6.6 Bottom). Extending the time-windows to longer coda lapse time in Category 2 (Figure 6.5 (Bottom)), we incorporate additional model information into the inverse process which helps to improve model resolution (Figure 6.6 Bottom). But the spatial control on the resolved local change in the model lies on the earlier part of the coda.

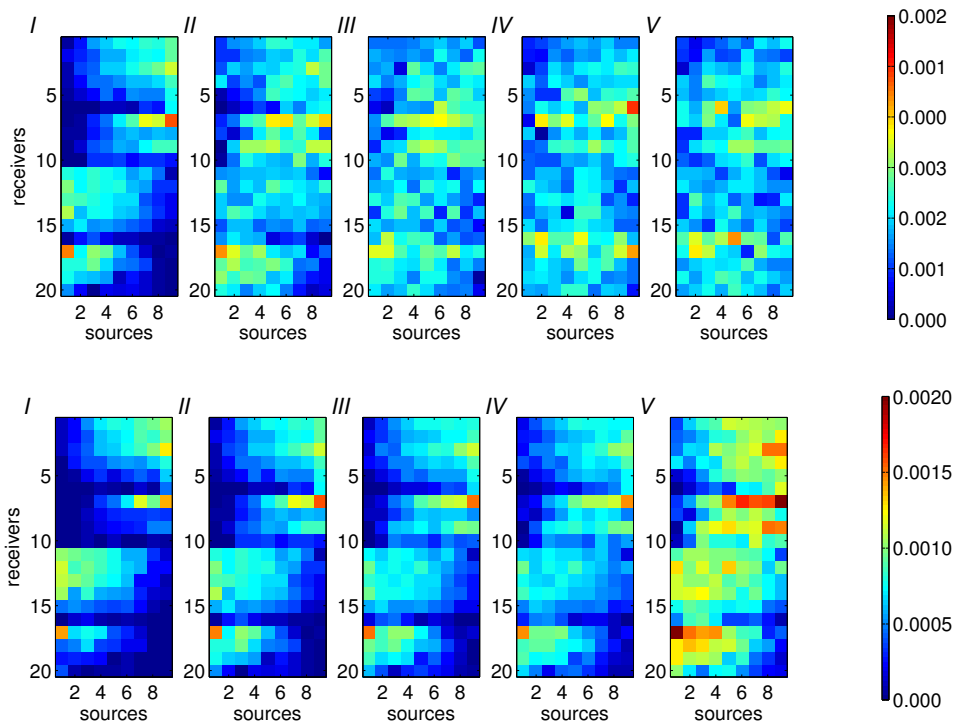


Figure 6.7: Data spread function for the inverted model using the Top: Category 1 time-windows and Bottom: Category 2 time-windows. Each value is an estimated fractional velocity change for a given source-receiver pair.

Due to multiple scattering of the waves within the scattering model, there is an averaging of the estimated travel-time change across the coda with increasing travel-time. Figure 6.7 shows the average estimated fractional velocity change across the time windows for Categories 1 and 2, as defined in Figure 6.5. These values are the average values of the subwindows in the time windows shown in the categories. The receiver and the source numbering in Figure 6.7 are shown in Figure 6.2. In Figure 6.7 (Top), the average estimated velocity changes are smeared across the source-receiver pairs with increasing the centertime of the coda waves. The smearing of the estimated velocity changes means that there are smaller or insignificant differences between the estimated velocity changes for source-receiver lines across the location of the change and the estimated velocity changes for source-receiver lines away from the location of the change (Figure 6.7, Top). Also due to the averaging of the estimated velocity changes due to multiple scattering, the estimated velocity change is a fraction of the true maximum velocity change in the medium (explained in Figure 6.3). In Category 2, the smearing of the estimated velocity change is relatively smaller than in Category 1. In Category 2, the average velocity change for all the time windows contains the estimates of the velocity change near the direct or forward scattered waves.

6.6 Time-lapse inversion

To localize the weak velocity change, we minimize the objective function ϕ (equation 6.6). The objective function ϕ corresponds to solving the following weighted least squares problem:

$$\mathbf{K}^T \mathbf{W}_d^T \mathbf{d} = [\mathbf{K}^T \mathbf{W}_d^T \mathbf{W}_d \mathbf{K} \mathbf{S}^{-1} + \beta \mathbf{I}] \mathbf{m} = [\mathbf{K}^T \mathbf{W}_d^T \mathbf{W}_d \mathbf{K} \mathbf{S}^{-1} + \beta \mathbf{I}] \mathbf{m}_S, \quad (6.11)$$

where \mathbf{d} is the estimated travel-time change δt , and $\mathbf{m} = \mathbf{S}^{-1} \mathbf{m}_S$ is the fractional velocity change. The sensitivity weighting matrix \mathbf{S} is a diagonal matrix with the elements $S_{ij} = \delta_{ij} w_j$, where the weights w_j are given by [46]:

$$w_j = \left(\sum_{k=1}^N K_{kj}^2 \right)^{1/2}, \quad j = 1, \dots, M; \quad (6.12)$$

where N is the number of data and M is the number of the discretized model space. We apply S to suppress the elevated sensitivity at the source and receiver locations [38]. The sensitivity weighting matrix acts as a preconditioner for the inversion problem. To solve equation 6.11, we use a linear conjugate-gradient method. All the imaged velocity changes in this subsection are obtained after 5 iterations.

The inverted velocity images correctly recovers the location of the velocity change, albeit with some artifacts. For the time windows shown in the top panel of Figure 6.8, the resolution of the inverted velocity change varies with different coda time windows. Figure 6.8B provides the best resolved and localized image of the velocity change. In Figure 6.8A, there are smears in the inferred velocity change towards the receivers above the velocity change. These smears are caused by the forward scattered waves that have their highest sensitivity along the source-receiver lines that cut across the location of the velocity change. At later times (Figure 6.8B, C, and D), there is an additional artifact which is centered at location $[x, z] = [5, 5.8]$ km. This artifact is induced by the intersection of kernel fronts which have relatively large amplitudes compared to the inner part of the sensitivity kernel. In Figure 6.8D the artifact is weaker due to the weakening of the kernel front with traveltime.

6.7 Conclusions

In this study, we demonstrate the capability of resolving localized weak changes within heterogeneous scattering media using multiply scattered waves. Our imaging algorithms build on the work of Pacheco and Snieder [70] and Rossetto et al. [82]. Using estimated time-lapse travel-time change, we demonstrate with a numerical example how well we can localize a weak velocity change within a heterogeneous 3-layer scattering model. We image this localized velocity change in the 3-layer model without assuming any statistical homogeneity of the scattering model. For this model, our imaging recipe resolves well the location of the velocity change especially early in the coda wave. However, the resolution of the imaged velocity change progressively decreases with increasing travel-time of the coda waves we use in the imaging. The decrease in the resolution of the velocity change results from the spatial

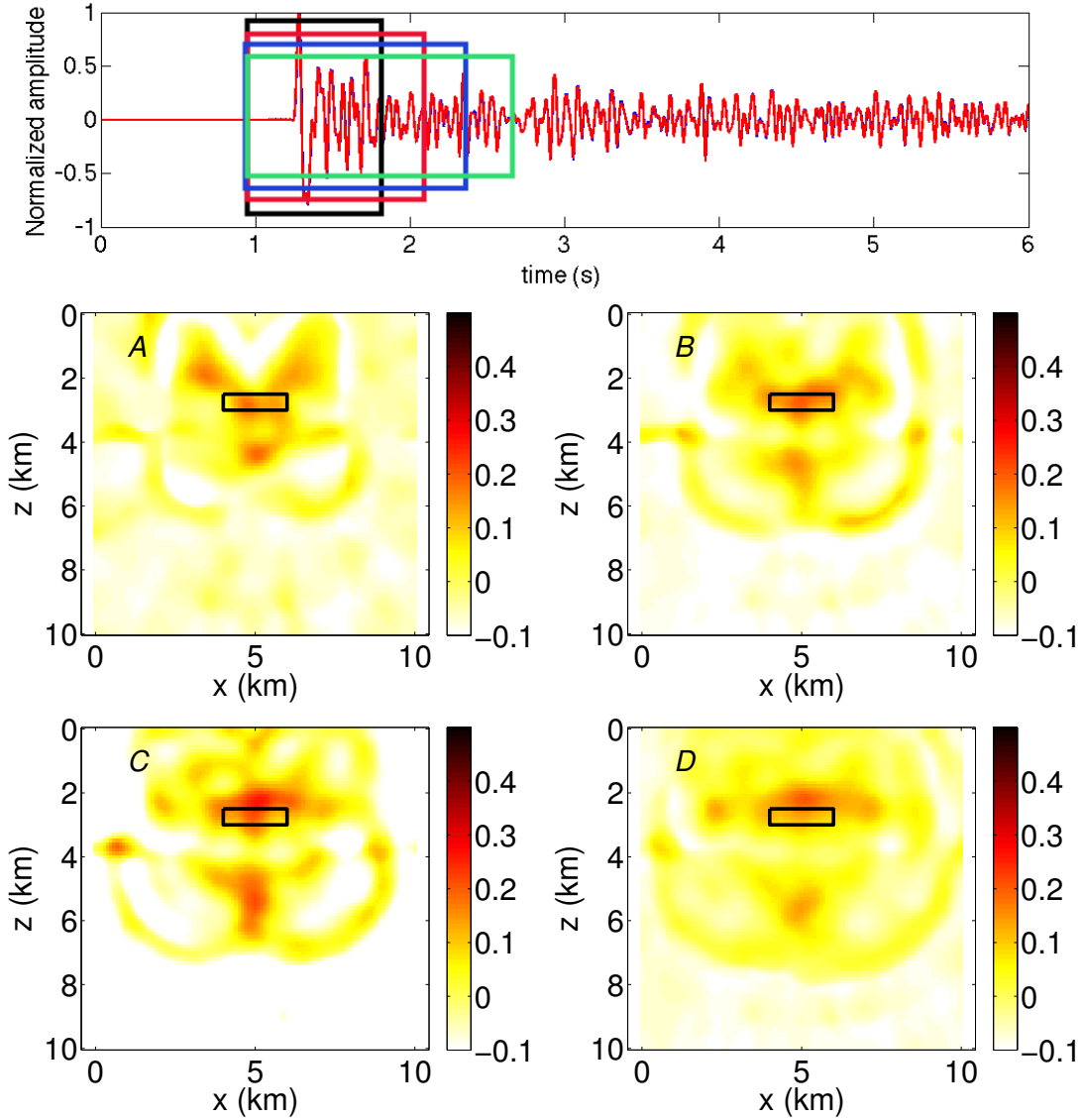


Figure 6.8: Inverted fractional velocity change using various coda time windows. Top inset: a typical recorded coda signal with time windows use to invert the velocity changes. Inverted velocity change in A: with black time window, B: with red time window, C: with blue time window, and D. with green time window. The black box shows the extent of the velocity change.

broadening of the sensitivity kernel with travel-time and the averaging out of the estimated changes across the sources and receivers.

6.8 Acknowledgments

This research was supported by sponsors of the Consortium Project on Seismic Inverse Methods for Complex Structures. The reproducible numeric examples in this paper use the Madagascar open-source software package freely available from <http://www.ahay.org>.

CHAPTER 7

TIME-LAPSE IMAGING OF LOCALIZED WEAK CHANGES WITH MULTIPLY SCATTERED WAVES: LABORATORY EXPERIMENT

Chinaemerem Kanu^{1 2}, Roel Snieder^{1 2}, Ernst Niederleithinger^{1 2}, and Sven Grothe²

To be submitted to Ultrasonics (2015)

7.1 Abstract

Mechanical structures can undergo changes due to wear and tear due to natural or man-made processes. These processes usually induce stress or temperature changes in the structures which create either irreversible or partially reversible changes on the rigidity of the structures. We demonstrate the use of multiply scattered ultrasound waves in monitoring and imaging localized changes within concrete blocks. We present a laboratory experiment with two concrete blocks where in one we apply a localized stress change and in the other a temperature change from a localized heating cartridge. Using the intensity of multiply scattered waves, we imaged the changes induced by both the stress and temperature changes within the concrete blocks. We accurately localize the change within the concrete blocks using the decorrelation of the time-lapse coda and the fractional velocity changes.

7.2 Introduction

Mechanical structures, such as buildings, roads, and bridges, are known to undergo wear and tear over time which can compromise the longevity of these structures. The resulting defects within the structures can be weak and hard to detect, so that their effect on the overall integrity of the structures are felt late. For an optimal management of the mechanical structures and the overall safety of their use, there is a need to monitor the mechanical

¹Center for wave phenomena, Colorado School of Mines

²BAM (Federal Institute for Materials Research and Testing), Berlin, Germany

structures continuously with a monitoring tool or method that has the sensitivity to identify the defects before they escalate to a destructive stage. Coda wave interferometry (CWI) provides a tool to identify weak changes or defects within a scattering medium, such as in monitoring of volcanoes [56], subsurface velocity changes near faults or in the near subsurface [76, 87], or changes in concrete blocks induced by either stress changes or temperature changes [31, 100]. The higher sensitivity of the coda waves to weak changes compared to the singly scattered waves allows for the detection of weak changes within scattering media. However, the coda waves provide spatially averaged estimates of the weak changes especially in cases where the time-lapse changes are localized. This spatial averaging limits the ability to resolve the locations of the weak changes.

We present two laboratory experiments with concrete blocks in which we monitor weak changes. In one of the experiments we monitor a weak change due to an induced compressive stress (force) at the opposite sides of the concrete block while in the second experiment we monitor changes due to temperature changes within a different concrete block. The temperature changes in the concrete block is either due to the ambient temperature fluctuations within the concrete and due to a localized heating provided by a heat cartridge within the concrete block. In this study, we apply an imaging algorithm based on the scattered intensity of the time-lapse coda to localize the weak changes within the concrete blocks [38].

7.3 Theory

Velocity changes and changes in the scattering properties of a heterogeneous medium induce changes within time-lapse coda waves. Pacheco and Snieder [70] and Rossetto et al. [82] related the travel-time changes and decorrelation of the time-lapse coda waves to velocity changes and perturbations in the scattering cross-section of the medium, respectively. Using probability density functions, Pacheco and Snieder [70] give the relationship between a localized fractional velocity change $\delta v/v(\mathbf{x}_o)$ at \mathbf{x}_o and the estimated travel-time changes

$\langle \tau(t) \rangle$ induced by the velocity change:

$$\langle \tau(t) \rangle = - \int_V K(\mathbf{s}, \mathbf{x}_o, \mathbf{r}, t) \frac{\delta v}{v}(\mathbf{x}_o) dV(\mathbf{x}_o), \quad (7.1)$$

where $K(\mathbf{s}, \mathbf{x}_o, \mathbf{r}, t)$ is the sensitivity of the travel-time change to the localized velocity change in the scattering medium. The sensitivity, which is computed using the intensity of the scattered wavefield [38], depends on the source and receiver locations, the scattering property of the medium, and the travel-time of the scattered waves. Similarly, Rossetto et al. [82] relate the decorrelation $D(\mathbf{s}, \mathbf{r}, t)$ between time-lapse multiply scattered waves to the time-lapse change in the total scattering cross-section $\delta\sigma(\mathbf{x}_o)$ of a medium:

$$D(\mathbf{s}, \mathbf{x}_o, \mathbf{r}, t) = \frac{v}{2} \int_V K(\mathbf{s}, \mathbf{x}_o, \mathbf{r}, t) \delta\sigma(\mathbf{x}_o) dV(\mathbf{x}_o), \quad (7.2)$$

The change in the total scattering cross-section describes a change in the scattering property the medium.

The travel-time changes $\langle \tau(t) \rangle$ and the decorrelation $D(\mathbf{s}, \mathbf{r}, t)$ can be estimated for a given source-receiver pair by comparing the time-lapse coda waves. Practically, the time-windowed decorrelation is obtained using

$$\begin{aligned} D(\mathbf{s}, \mathbf{r}, t) &= 1 - C(\mathbf{s}, \mathbf{r}, t) \\ &= 1 - \frac{\int_{t-t_w}^{t+t_w} u(\mathbf{s}, \mathbf{r}, t') \hat{u}(\mathbf{s}, \mathbf{r}, t' + t_s) dt'}{[\int_{t-t_w}^{t+t_w} u(\mathbf{s}, \mathbf{r}, t')^2]^{1/2} [\int_{t-t_w}^{t+t_w} \hat{u}(\mathbf{s}, \mathbf{r}, t')^2]^{1/2}}, \end{aligned} \quad (7.3)$$

where t is the travel-time and t_w is the half-length of the time-window use to compute the cross-correlation $C(\mathbf{s}, \mathbf{r}, t)$. We estimate the travel-time changes ($\langle \tau(t) \rangle = -\epsilon t$) using the stretching method [33] for a given time window of the scattered waves, where ϵ is the stretching factor. The stretching factor is equal to the estimated fractional velocity change within the time window. To obtain the optimal stretch factor, we minimize

$$\min f(\epsilon) = \|\hat{u}(t + \epsilon t) - u(t)\|_2^{t, t_w}, \quad (7.4)$$

where $u(t)$ and $\hat{u}(t)$ are the original and the time-lapse coda signals, respectively.

The sensitivity kernel is given by

$$K(\mathbf{s}, \mathbf{x}_o, \mathbf{r}, t) = \frac{\int_0^t P(\mathbf{s}, \mathbf{x}_o, t') P(\mathbf{x}_o, \mathbf{r}, t - t') dt'}{P(\mathbf{s}, \mathbf{r}, t)}, \quad (7.5)$$

where P is the normalized intensity of the multiply scattered waves [70]. The sensitivity kernel $K(\mathbf{s}, \mathbf{x}_o, \mathbf{r}, t)$ can be estimated either by using the analytical [70, 82] or numerical methods [38]. The analytical method of computing $K(\mathbf{s}, \mathbf{x}_o, \mathbf{r}, t)$ usually uses the diffusion [72, 92, 112] or the radiative transfer formulation of the scattered intensity [69]. However, the analytical methods typically assumes that the scattering medium is statistical homogeneous. In a medium where the scattering properties are spatially varying, the numerical method of computing the sensitivity kernel is preferred [38], because the sensitivity is computed numerically with an a prior estimate of the scattering model by numerically computing the normalized intensity of the multiply scattered waves.

7.4 Laboratory experiment in a concrete block

Concrete block with stress changes

To demonstrate the capability of resolving weak changes within a physical scattering medium, we invert for a change induced by a localized stress loading on the surface of a concrete block with dimensions $1.5 \times 1.5 \times 0.5 \text{ m}^3$. The concrete block, with an average P-wave velocity of 4 km/s , consists of aggregate (which act as scatterers) of size approximately 32 mm and reinforcements in half of the block (Figure 7.1). The reinforcement consists of a rebar mesh of 8 mm rods spaced at 150 mm intervals. Within the block, we embedded 18 transducers that serves both as sources and receivers. Because of coupling issues, we only use 10 of the transducers (Figure 7.2). Table 7.1 gives the locations of the used transducers. These 10 transducers are connected to ultrasound transmitting and receiving equipment via a multiplexer. The multiplexer connects an amplified signal generated by a function generator to a given transducer selected at a given time (Figure 7.3). This selected transducer acts as the source while the rest of the transducers serve as receivers. The recorded signals are sent to an Analog-to-Digital (A/D) device and then to data storage. A given load experiment

results to a total of 90 traces. The source signal has a dominant frequency of 60 kHz .

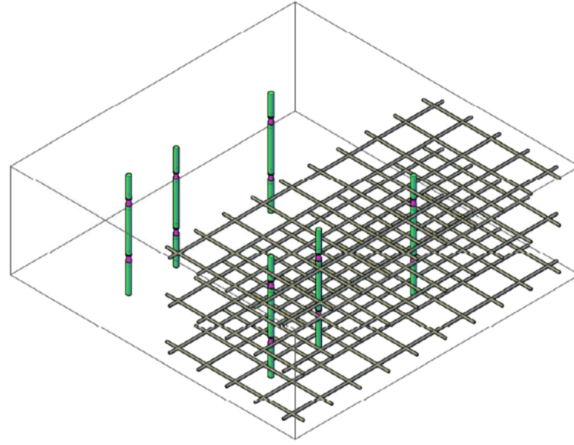


Figure 7.1: Schematic of the 3D concrete block for time-lapse monitoring

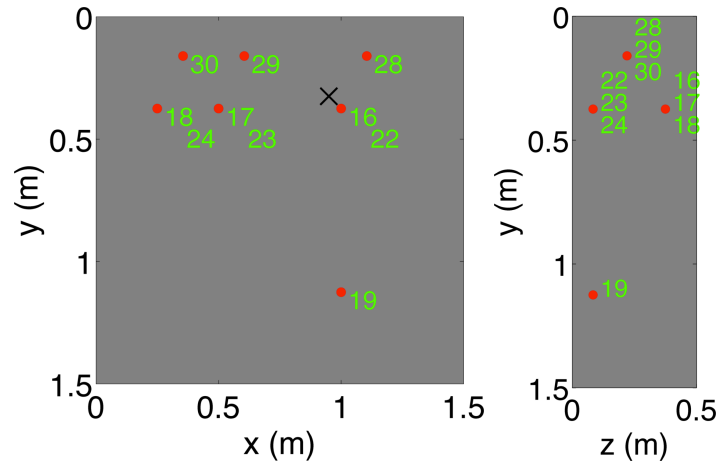


Figure 7.2: Outline of the 3D concrete block with the locations of the used transducers. The transducers are embedded within the concrete block. The transducer locations are the projection along the z -axis (left) and along the x -axis (right).

To induce a local change on the concrete block, we apply a stress loading on a 30 mm borehole drilled through the block along the z -axis. The borehole is located at $(x = 0.95\text{ m}, y = 0.325\text{ m})$. A 20 mm bolt is put through the borehole and fastened on both sides with load distribution steel plates and nuts. The load steel plates are $0.1 \times 0.1\text{ m}^2$ wide and 10 mm thick. On one side of the block, a calibrated load cell (a piezoelectric sensor) is placed between the load steel plate and an additional disc. The load cell is used for current supply

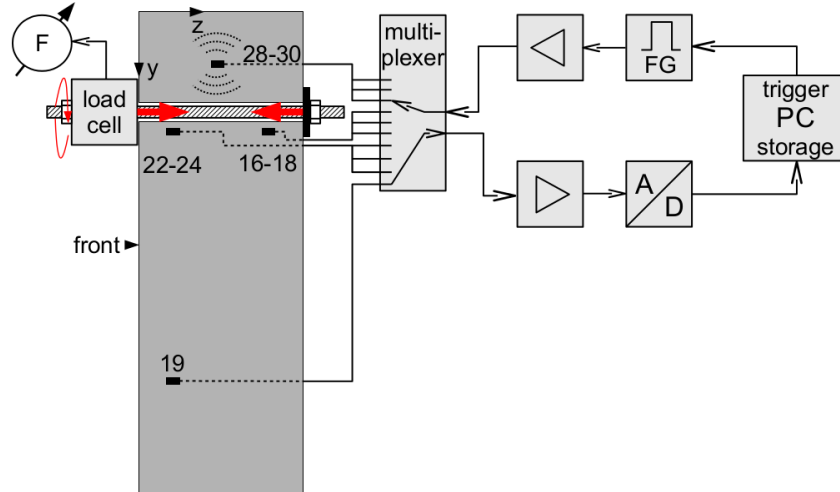


Figure 7.3: The electrical and mechanical setup of the stress loading experiment.

and voltage measurement. This experiment which was designed and setup at the Federal Institute for Materials Research and Testing, Berlin, Germany (known as BAM) involves monitoring series of stress loading ranging from 0 kN to 100 kN and back to 0 kN .

Table 7.1: Transducer coordinates.

Transducer No.	x (mm)	y (mm)	z (mm)
16	1000	375	374.5
17	500	375	374.5
18	250	375	374.5
19	1000	1125	83.5
22	1000	375	83.5
23	500	375	83.5
24	250	375	83.5
28	1105	160	220
29	605	160	220
30	355	160	220
Load	950	325	0 - 500

Figure 7.4 shows typical signals recorded at transducer 17 when transducer 16 acts as a source. At $t=0$ each receiver records a event from the source induced electrical response. We use this electrical event (Figure 7.4 (black ellipse)) to book-keep the onset time of the source signals. This event is removed prior to time-lapse analysis of the signals. The rest of the recorded scattered waves in the signals consist of ballistic and coda waves resulting from

wave scattering within the concrete block. The two signals in Figure 7.4 are from repeated experiments on a given stress load displaying the strong repeatability of the signals.

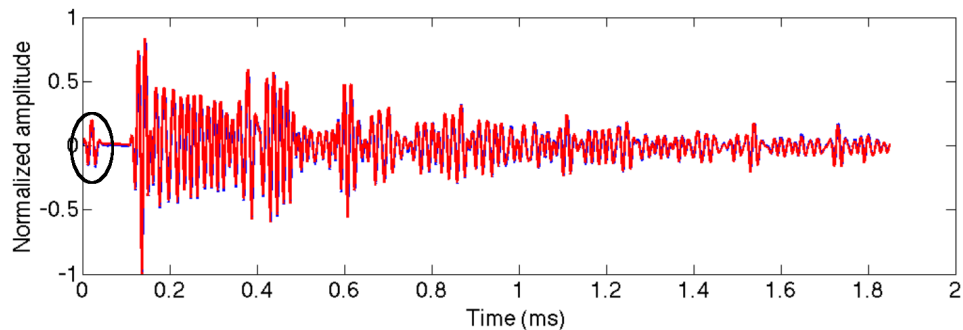


Figure 7.4: Typical time-lapse coda signals recorded at transducer 17 due to a source at transducer 16 from the stress loading experiment. The black ellipse indicate the electrical signal use to book-keep the source unset time.

Concrete block for temperature changes

Figure 7.5 shows both the pictorial and schematic views of the concrete block we use for monitoring changes due to temperature changes. The experiment was conducted in an outdoor field in Berlin that is owned by BAM. The concrete block has a dimension of $5 \times 4 \text{ m}^2$ and 0.8 m thick consisting of a concrete mix based on the C30/37 mix design given in the European (Eurocode2) or German guidelines (DIN 1045-1). There is a heat cartridge H connected via a heating pipe from outside into the concrete block to induce local temperature changes within the block (Figure 7.5 bottom, cyan line). We monitor the time-lapse local temperature changes using sensors that are attached at the side faces of the concrete block. We have ten sensors at each of the four sides of the concrete block. The sources for the monitoring ultrasonic waves are given as sensors (S1-S20) while sensors R1-R20 are the recording sensors of the scattered (ultrasonic) waves (Figure 7.5 Bottom). The electrical setup of the temperature experiment is similar to the setup in the stress experiment (Figure 7.6). However, in the temperature experiment, we use an ultrasonic source signal of a dominant frequency of 25 kHz . Figure 7.7 shows an example of the time-lapse signals recorded by sensor R5 due to source signal from sensor S5.

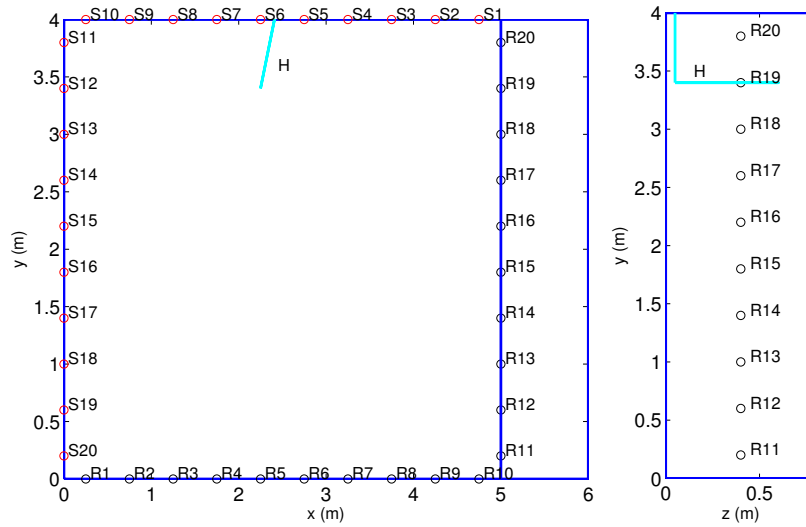


Figure 7.5: The pictorial (Top) and the schematics (bottom) of the concrete block use for the time-lapse temperature monitoring experiment. The cyan line gives the heating cartridge probe.

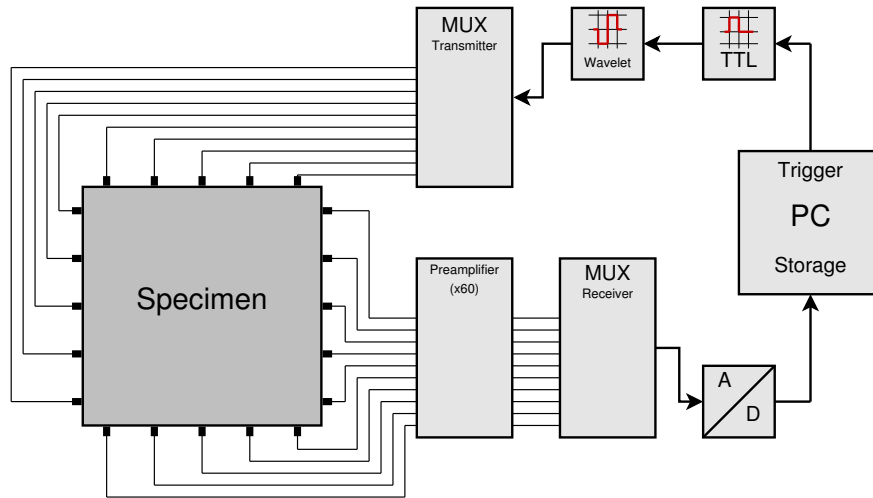


Figure 7.6: The electrical and mechanical setup of the stress loading experiment.

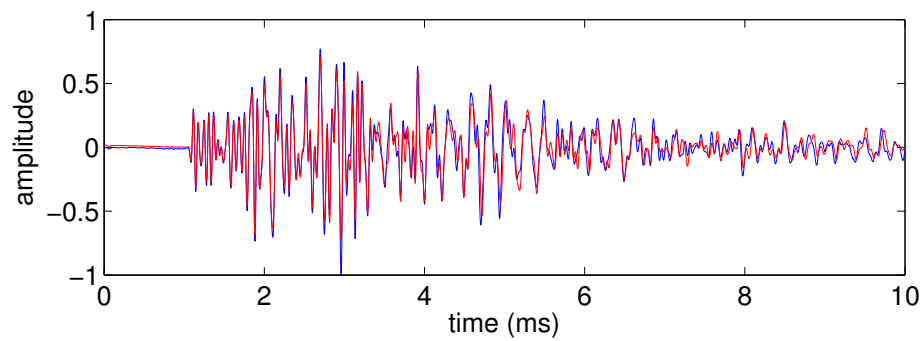


Figure 7.7: Typical coda signal recorded by sensor R5 due to a source at sensor S1 from the temperature experiment.

The fundamental solution of the heat transfer equation for an infinite 3D homogeneous medium with a thermal conductivity k using a delta temperature forcing of maximum 1°C is

$$T(\mathbf{x}, t) = \frac{1}{\sqrt{4\pi\alpha t}} e^{-\|\mathbf{x}-\mathbf{x}_0\|^2/4\alpha t}, \quad (7.6)$$

where α is the thermal diffusivity of the heated medium. The thermal diffusivity is given as $k/\rho c_p$, where ρ is the density of the medium and c_p is the specific heat capacity of the medium.

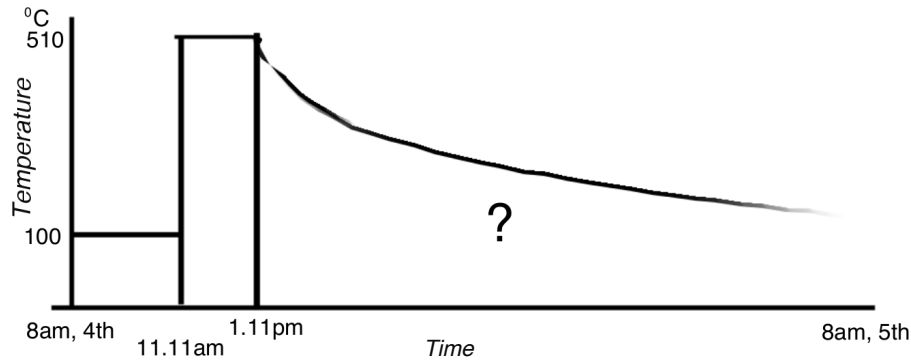


Figure 7.8: Temperature history of the time-lapse heating experiment. The question mark indicates that the temperature curve between 1:11pm (4^{th} of April) and 8am (5^{th} of April) is unknown.

Figure 7.8 shows the temperature history of the time-lapse temperature experiment at the location of the heat cartridge. The time-lapse temperature change occurs between 8am at the 4^{th} of April, 2014 and 8am at the 5^{th} of April, 2014. The ambient temperatures measured were 11.37°C on the 4^{th} and 10.41°C on the 5^{th} of April. During the baseline measurement on 4^{th} of April, the temperature of the heating cartridge was set at 100°C . However, at 11:11am on 4^{th} of April, the heating temperature was increased to 510°C for a period of 2 hours before the cartridge was turned off. The decay of the temperature after 1:11pm on the 4^{th} of April is based on the solution of the heat transfer equation in equation 7.6. To estimate the temperature distribution across the heated concrete block at the time-lapse time (8am on the 5^{th} of April), we need the initial condition of the temperature distribution across the

concrete, i.e., the temperature distribution across the concrete at 1:11pm on the 4th of April. We do have point temperature measurements at the location of the heat cartridge and 0.2 *m* away from the heat cartridge within the concrete. The temperature measurements at the location of the heat cartridge and 0.2 *m* away from the heat cartridge are 510⁰C and 47⁰C, respectively.

Let's assume that the temperature distribution at 1:11pm on the 4th of April (the initial temperature condition $T_{IC}(\mathbf{x}, t)$) has a Gaussian characteristics defined as:

$$T_{IC}(\mathbf{x}, t) = 510e^{-\|\mathbf{x}-\mathbf{x}_0\|^2/2\sigma^2}, \quad (7.7)$$

where σ is the width of the temperature anomaly during the initial temperature condition time. This assumed Gaussian characteristics ignores the effect of the reflecting boundaries. This is because we do not have the exact location of the temperature sensor 0.2 *m* away from the heat cartridge. Using the temperature measurement 0.2 *m* away from the heat cartridge, the estimated width of the temperature anomaly during the initial temperature condition time σ is 0.092 *m*. Therefore,

$$T_{IC}(\mathbf{x}, t) = 510e^{-\|\mathbf{x}-\mathbf{x}_0\|^2/0.0168m^2}. \quad (7.8)$$

Assuming $T_{IC}(\mathbf{x}, t)$ as the initial condition for the heat conduction, the solution of the heat conduction within the concrete at the time-lapse time ($T_T(\mathbf{x}, t)$) is

$$T_T(\mathbf{x}, t) = \int_V T(\mathbf{x} - \mathbf{x}', t)T_{IC}(\mathbf{x}', t) d\mathbf{x}', \quad (7.9)$$

$$T_T(\mathbf{x}, t) = \frac{510}{\sqrt{4\pi\alpha t}} e^{-\|\mathbf{x}-2\mathbf{x}_0\|^2/(4\alpha t+0.0168)m^2}. \quad (7.10)$$

The typical thermal diffusivity of concrete medium ranges from 0.002-0.007 *m*²/*hr* [115]. Using equation 7.10 and assuming a thermal diffusivity α of 0.005 *m*²/*hr* for a concrete material, the approximate distribution of the temperature (equation 7.10) within the concrete material is shown in Figure 7.9. The temperature at the location of the heat cartridge is 463.84⁰C during 8am of the 5th of April, 2014. Therefore the temperature curve in Figure 7.8 decreases to approximately 463.84⁰C on 8am of the 5th of April.

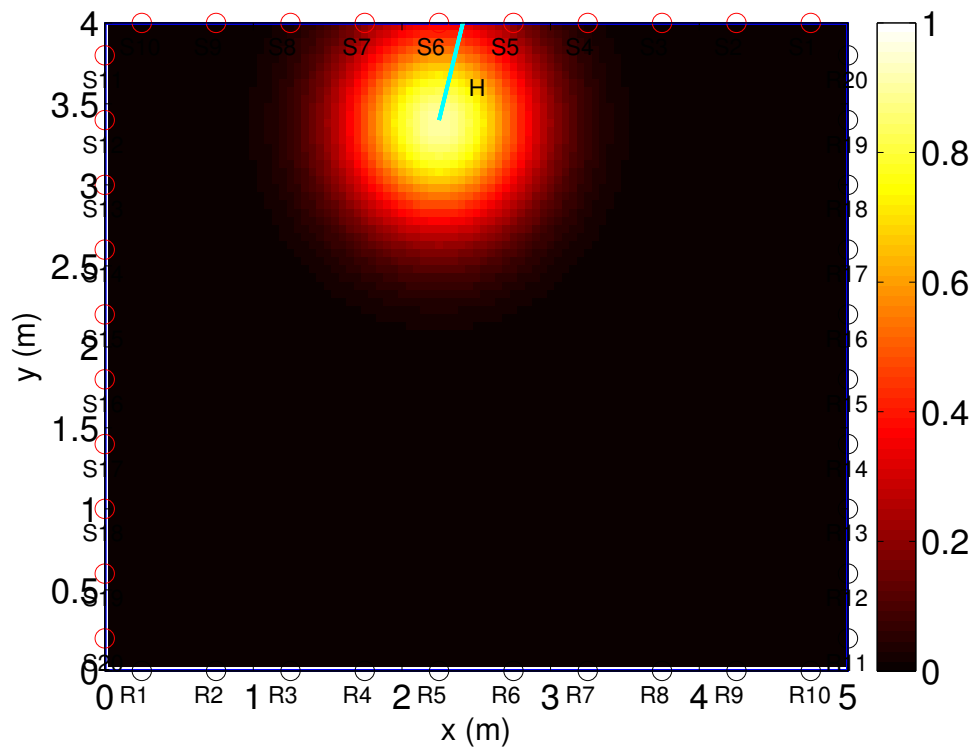


Figure 7.9: Normalized temperature distribution across the heated concrete medium at the end of the temperature history in Figure 7.8 using equation 7.10. The cyan line is the heating cartridge probe.

7.5 Data analysis

Using coda wave interferometry analysis (CWI), we can estimate the fractional velocity change $\Delta v/v$ or the decorrelation D of the time-lapse coda signals for a specific time window using either the stretching method [33], or by computing $D = 1 - C_{max}$ (equation 7.3), respectively.

In the stretching method, we stretch one of the coda signal by a constant stretch factor relative to the second time-lapse coda signal. The optimal stretch factor, which is the estimated fractional velocity change within the windowed time-lapse coda, is determined by the stretch factor that minimizes the L_2 norm of the difference between the time-lapse coda signals. Figure 7.10 and Figure 7.11 show the estimated decorrelation D and the estimated fractional velocity change $\Delta v/v$ from the 90 time-lapse coda signals in the stress experiment, respectively. The estimates of the decorrelation or the fractional velocity change is random and larger before the first arrival because of low signal-to-noise ratio. The figures compare changes due to load jumps from 5 kN to 10 kN and from 5 kN to 15 kN . The changes are larger for the 5 kN -15 kN load jump than for the 5 kN -10 kN load jump (Figure 7.10 and Figure 7.11). The estimated changes are more pronounced for later coda lapse times. Compare traces 28-35 with traces 38-45. Traces 38-45 generally have larger time-lapse velocity changes and decorrelations than traces 28-35. The differences in the time-lapse changes across the traces are due to the arrangements of the sensors. Figure 7.12 provides a picture of the recorded time-lapse change for individual transducer pairs. The figure shows an indication of a localized change. Figure 7.12 shows the average decorrelations estimated from the time-lapse scattered waves arriving between 0.28 ms and 0.58 ms after the first arrival. The decorrelations are estimated using the time-window in time-lapse coda in Figure 7.12 (top). Larger decorrelation results from the load jump of 5 kN to 15 kN compared to the load jump of 5 kN to 10 kN and also from the sensor pairs close to the location of the compressive loads.

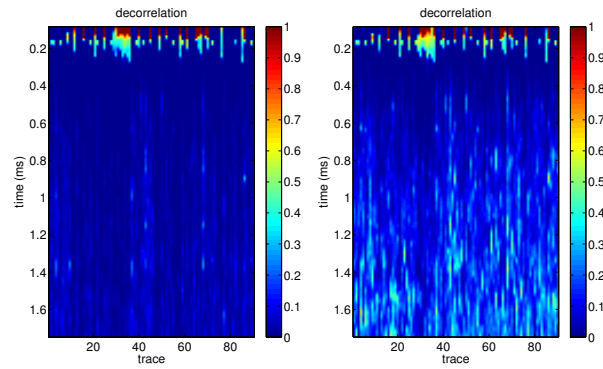


Figure 7.10: Record of the estimated time-lapse decorrelation due to a load jump from 5 kN to 10 kN (left) and a load jump from 5 kN to 15 kN (right). The record contains 90 traces (due to 10 pairs of sensors with no trace for the same sensor combination). The records are arranged according to the source sensor records.

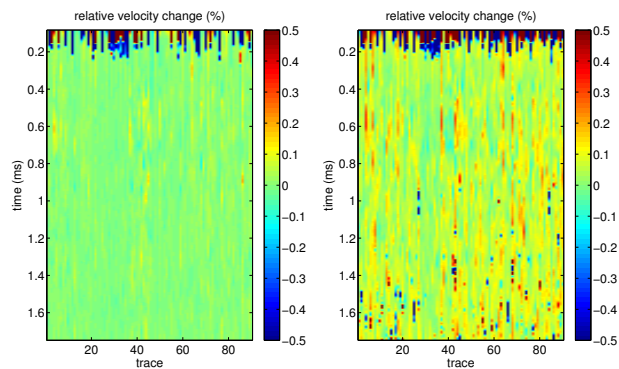


Figure 7.11: Record of the estimated time-lapse relative velocity change in % due to a load jump from 5 kN to 10 kN (left) and a load jump from 5 kN to 15 kN (right). The record contains 90 traces (due to 10 pairs of sensors with no trace for the same sensor combination). The records are arranged according to the source sensor records.

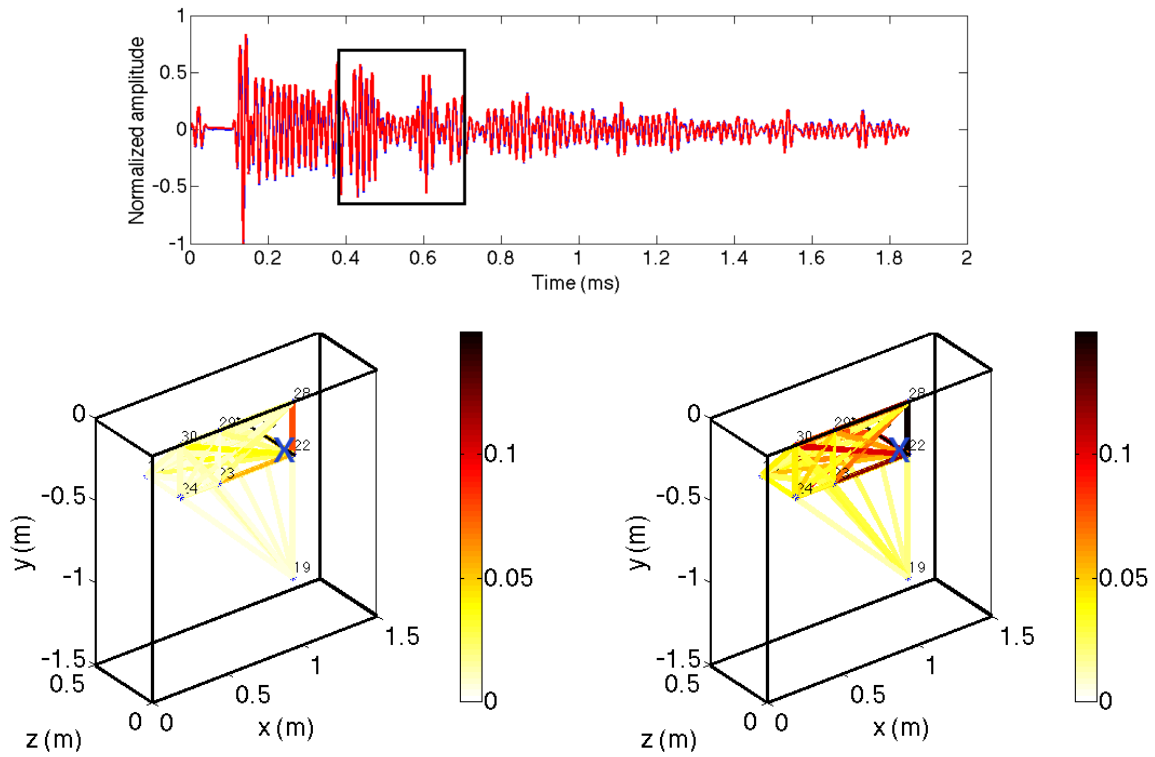


Figure 7.12: Time-lapse decorrelation due to stress loading from 5 kN to 10 kN (left) and from 5 kN to 15 kN (right) at X. The colored lines between two sensors are the estimated average decorrelation between the time lapse signals using equation 7.3 for the time-window in time-lapse coda (top). The decorrelations for each sensor pairs are not restricted to the connecting colored lines.

Figure 7.13 shows the estimated decorrelation and velocity (negative) changes for the time-lapse heating experiment for the source-receiver pairs using the time-window shown with the black box in the top panel of Figure 7.13. For each source-receiver pair, the time-window is centered at a delay time of 2.5 *ms* from the first arrival times. The decorrelation and velocity (negative) changes are spread out across the source-receiver pairs but there are larger decorrelation and velocity (negative) changes for the source-receiver pairs across the heat cartridge (lying between S5 and S6).

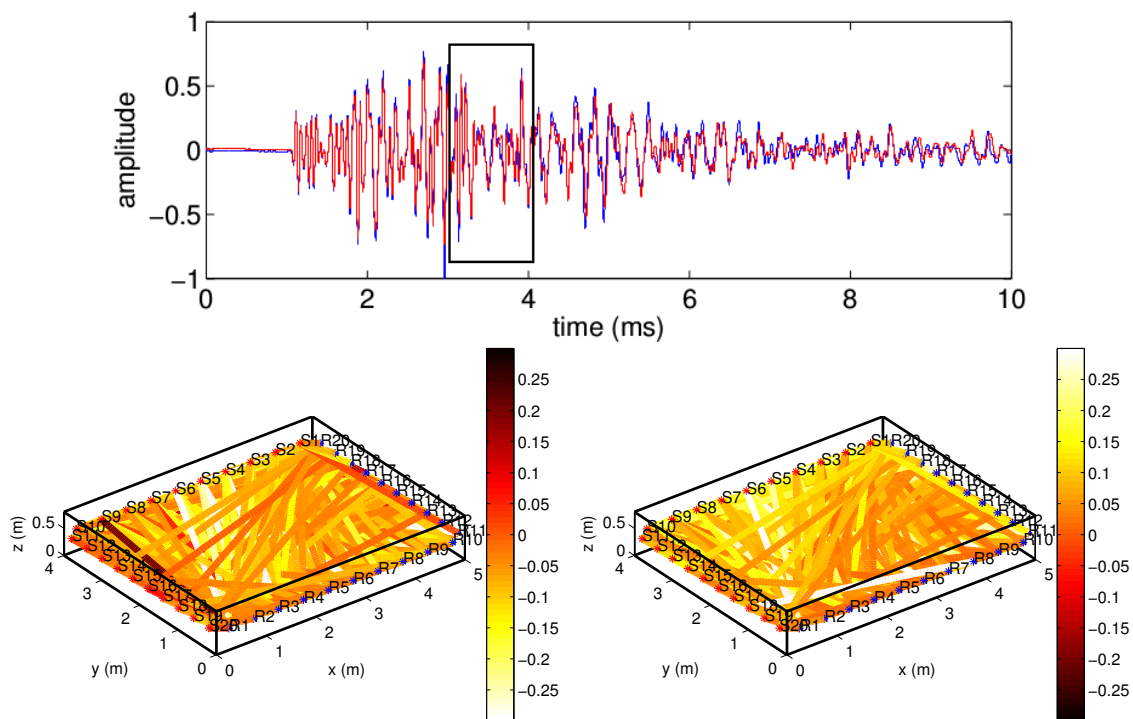


Figure 7.13: Time-lapse fractional velocity change (%) and decorrelation due to temperature change within the concrete block. The colored lines between two sensors are the estimated changes (fractional velocity change (left) and decorrelation (left)) between the time lapse signals for the time-window in time-lapse coda (top). The changes for each sensor pairs are not restricted to the connecting colored lines.

7.6 Time-lapse inversion

Here, we invert for weak changes within the heterogeneous 3D concrete blocks. These weak changes are induced either by a compressive localized stress or a localized change in

temperature within the concrete block. To invert for the changes induced by the stress loadings or the localized temperature change, we solve

$$\mathbf{K}^T \mathbf{W}_d^T \mathbf{d} = [\mathbf{K}^T \mathbf{W}_d^T \mathbf{W}_d \mathbf{K} + \beta \mathbf{I}] \mathbf{m}, \quad (7.11)$$

where \mathbf{K}^T is a discretized version of the sensitivity kernel (equation 7.5) of the travel-time change or the decorrelation to the localized change in the scattering model using multiply scattered waves, \mathbf{W}_d is the data weighting matrix, β is a regularization parameter, and \mathbf{m} defines the inverted change in the scattering medium which are either the change in velocity or the change in the scattering cross-section. The data is either the decorrelation of the time-lapse coda or the travel-time change from the time-lapse coda. To solve equation 7.11, we use linear conjugate-gradient method.

We compute the sensitivity kernel using radiative transfer model of the scattered intensity in the block [38] with fully reflecting boundary conditions [82] on the planar boundaries of the concrete block. We currently assume acoustic wave scattering but future inversions of the weak change in the concrete block will incorporate elastic scattering. To estimate the sensitivity kernel we estimate the average mean free path by fitting the intensities of the coda waves using radiative transfer intensity which depends on the mean free path. We estimate the mean free path to be approximately 1.52 *m* which corresponds to a mean free time of 0.362 *ms* using P-wave velocity for the stress experiment and a mean free path of 3.75 *m* and a mean free time of 0.893 *ms* for the temperature experiment. The time window we use for the inversion extends beyond the mean free time.

Figure 7.14 shows the inverted solution of the weak changes within the concrete block in the stress experiment at $z = 0$ *m* for stress loading of 5-10 *kN* and 5-15 *kN* using the time window in Figure 7.14 (top). For the stress experiment we use the decorrelation of the time-lapse coda for the inversion. These stress loadings induce a relatively more significant and consistent perturbation on the amplitude of the coda signals than on the phase of the coda. Figure 7.14 shows the resolved change which is at close proximity to the point of the stress loading for both stress experiments. The resolution of the weak change depends on

the source-receiver coverage and the time windows we use for the inversion due to the spatial broadening of the sensitivity kernel with travel-time [38].

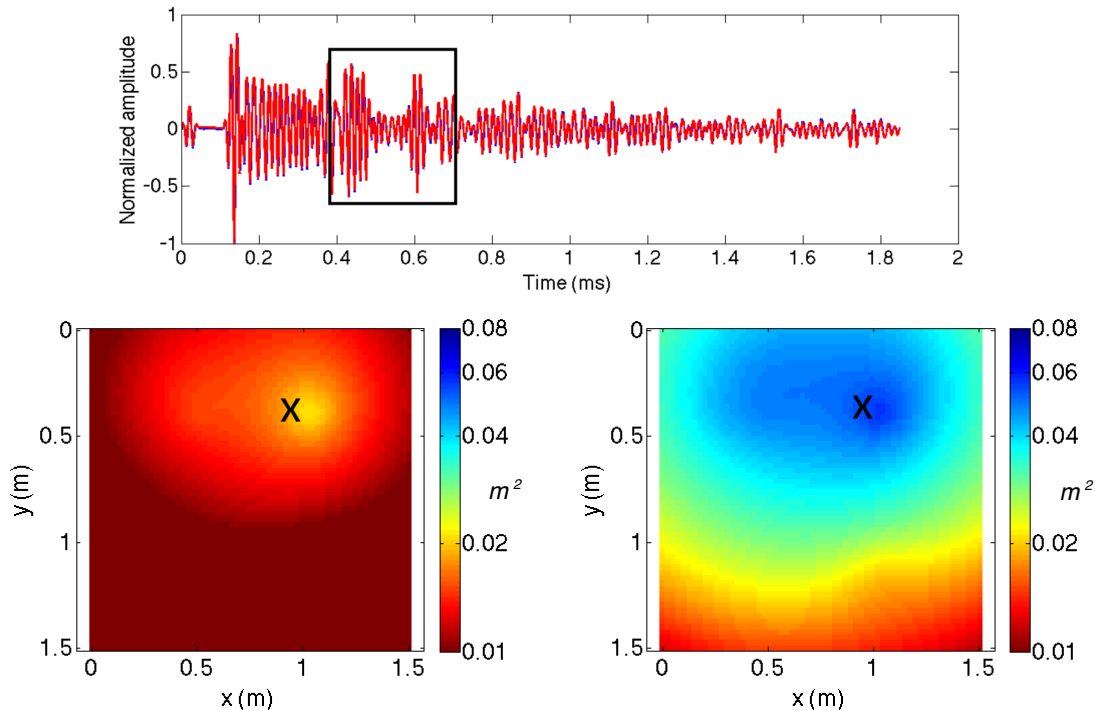


Figure 7.14: Inverted change due to stress loading from 5 kN to 10 kN (left) and from 5 kN to 15 kN (right) at X. Top inset: Time-lapse coda showing the time-window used for the inversion.

Using the same inversion algorithm, we invert for the time-lapse change within the concrete block in Figure 7.5 due to a localized temperature change. Figure 7.15 shows the inverted velocity change in percent resulting from a heating experiment at the location of the heating cartridge. We use scattered waves recorded at the same hour of the day to reduce the effect of ambient temperature change. Figure 7.15 compares the imaged velocity change and the imaged change in the scattered cross-section with the location of the heating cartridge. We use estimated fractional velocity change and decorrelation extracted from time-windows centered at around $2.5ms$ after the first arrival (Figure 7.15 top). The figures show that using the estimated change from the coda time-window beyond the mean free time, we can accurately localize the location of the temperature change induced by the heating within the concrete. The imaged velocity change suggests that temperature changes induces

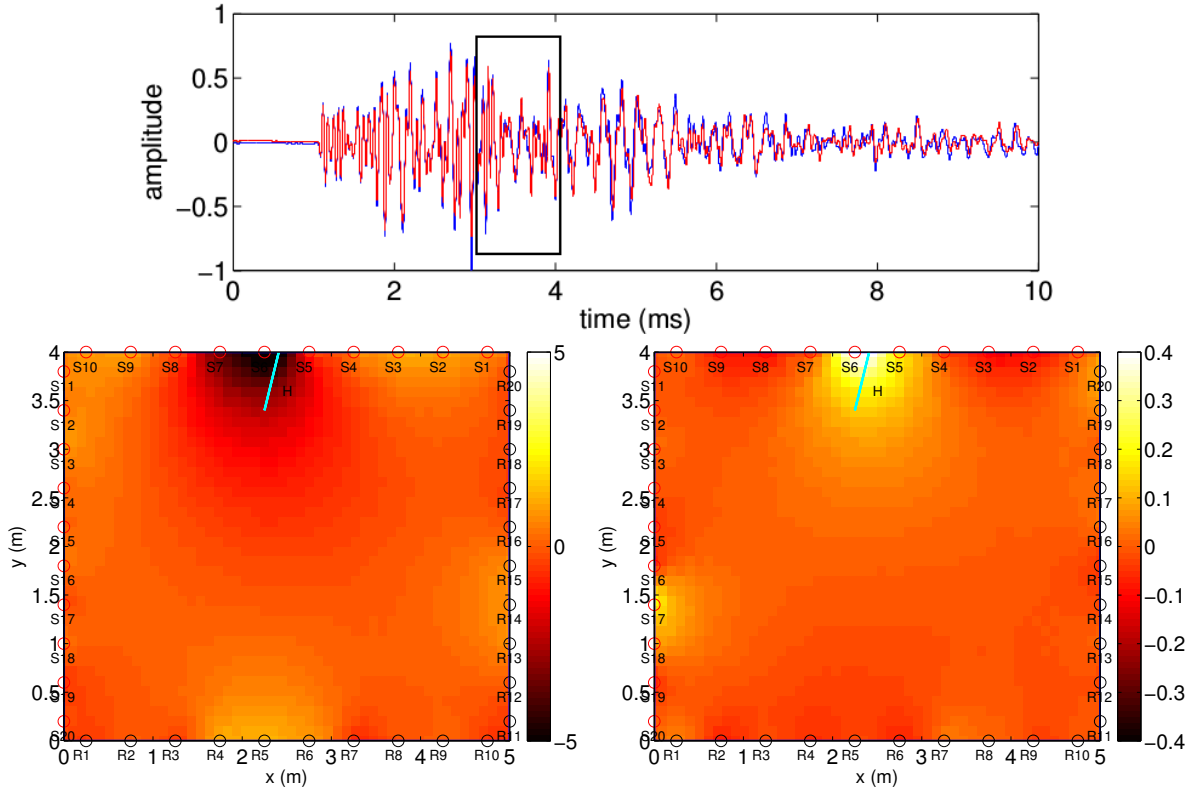


Figure 7.15: Inverted change due to localized temperature change due to a heating cartridge at H (Figure Figure 7.5 (Bottom)) using the travel-time changes and decorrelation estimated at the coda time window (black rectangle) in Top inset. In the Bottom inset: (left) the inverted relative velocity change (in percentage) using estimated travel-time changes and (right) the inverted change in the scattering cross-section (in m^2) using estimated decorrelation.

a negative velocity change around the heating cartridge. The negative velocity change implies that at 8am of 5th of April, 2014, the temperature within the concrete surrounding the heating cartridge has not dropped down to 100^o C [31, 63]. The elevated temperature at 8am of 5th of April, 2014 is supported by the modeled time-lapse temperature distribution within the medium in Figure 7.9.

7.7 Conclusion

This study demonstrates the use of time-lapse ultrasound waves to monitor changes induced within heterogeneous concrete blocks by stress and heat changes. We monitor time-lapse localized changes within a C30/37 concrete block due to an induced compressive stress applied on opposite sides of the concrete block. In another concrete block, we monitor changes induced by elevated localized heat within the block that is induced by an embedded heating cartridge. To image the changes within the concrete blocks, we use imaging algorithms based on the work of Pacheco and Snieder [70] and Rossetto et al. [82]. The imaging algorithms allow for the use of either time-lapse fractional velocity changes or the decorrelation of the time-lapse ultrasound signals to image the change. To invert for the localized change within the concrete blocks, we solve a regularized least squares problem using linear conjugate gradient. We accurately localized the change within the concrete blocks using decorrelation and fractional velocity changes estimated with coda lapse times beyond the mean free time of the concrete blocks.

CHAPTER 8
TIME-LAPSE MONITORING ACROSS UTAH AND EASTERN SECTION OF BASIN
AND RANGE

Chinaemerem Kanu¹, Roel Snieder¹ and Kristine Pankow²

Published in Journal Geophysical Research (2014)

8.1 Abstract

The Eastern part of the Basin and Range, extending to the Wasatch fault region, is an actively deforming region characterized by varieties of extensive features and prominent seismicity along the inter-mountain seismic belt. The present day deformation of the inter-mountain seismic belt and the eastern Basin and Range provinces, motivates an interest in continuous monitoring of the region. In this study we monitor time-lapse velocity changes within Utah and eastern Nevada using coda waves generated by repeatable explosions. This monitoring characterizes velocity changes within the region from June to September of 2007. We observe, both temporally and spatially, variable velocity changes within the monitored region, with a maximum path-average velocity change of 0.2%. This suggests a significant change in the velocity within the region given the short monitoring duration. Correlation of the temporal variation of the average velocity change with strains derived from GPS detrended displacements suggests that the velocity change might be driven by the broad deformation within the monitored region.

8.2 Introduction

Coda wave interferometry is an effective tool to monitor time-lapse changes within a medium, especially if these changes are weak [97]. Coda wave interferometry allows us to

¹Center for wave phenomena, Colorado School of Mines

²University of Utah Seismograph Stations, Salt Lake City, Utah

extract subsurface changes from scattered seismic waves generated from repeated sources. With identical sources and negligible noise, differences within the seismic coda (such as time shift and amplitude decay) provide information about the changes within the monitored medium through which the coda wave travels. Due to the redundancy in the coda waves and possibly increased illumination of the subsurface by the scattered waves, the sensitivity of the scattered waves to perturbations within the subsurface usually increases with increasing travel time. This sensitivity of the multiply scattered waves has allowed for monitoring weak changes in velocity that are in the order of 0.1% [96]. Multiply scattered waves have successfully been used to monitor velocity changes along fault regions [76, 87], detect in-situ velocity changes due to stress changes in a mine [31], characterize near-surface velocity changes [62, 89], monitor temporal changes within volcanic regions [56], and detect far-field stress-induced velocity changes (such as those induced by solid earth tides) [100].

The monitored region in this study covers the Basin and Range physiographic province, the transition from the Basin and Range to both the Middle Rocky Mountains and the Colorado Plateau, and the Snake River Plain (Figure 8.1). This region is characterized by active deformation, primary extension mostly east-west directions for the Basin and Range and more southeast to northwest extension in the Snake River Plain [77]. In addition to the major phisographic provinces, the region is characterized by mostly north-south trending normal faults, including the Wasatch fault. While there is diffuse seismicity throughout the region, most of the seismicity is concentrated with the Intermountain Seismic Belt (ISB), a zone of shallow seismicity that extends from Montana to Arizona [95]. Unique to western Utah are basins composed of soft sediments related to Lake Bonneville (a late Pleistocene pluvial lake). In the Salt Lake Basin these soft sediments are greater than 1 *km* deep in some locations [83]. The soft sediments are potentially susceptible to both near-field and far-field stress loadings. Taken together, the active regional deformation, localized seismicity and faulting, and surface geology, provide a complex contemporary deforming area with potentially small- and large-scale changes in both time and space.

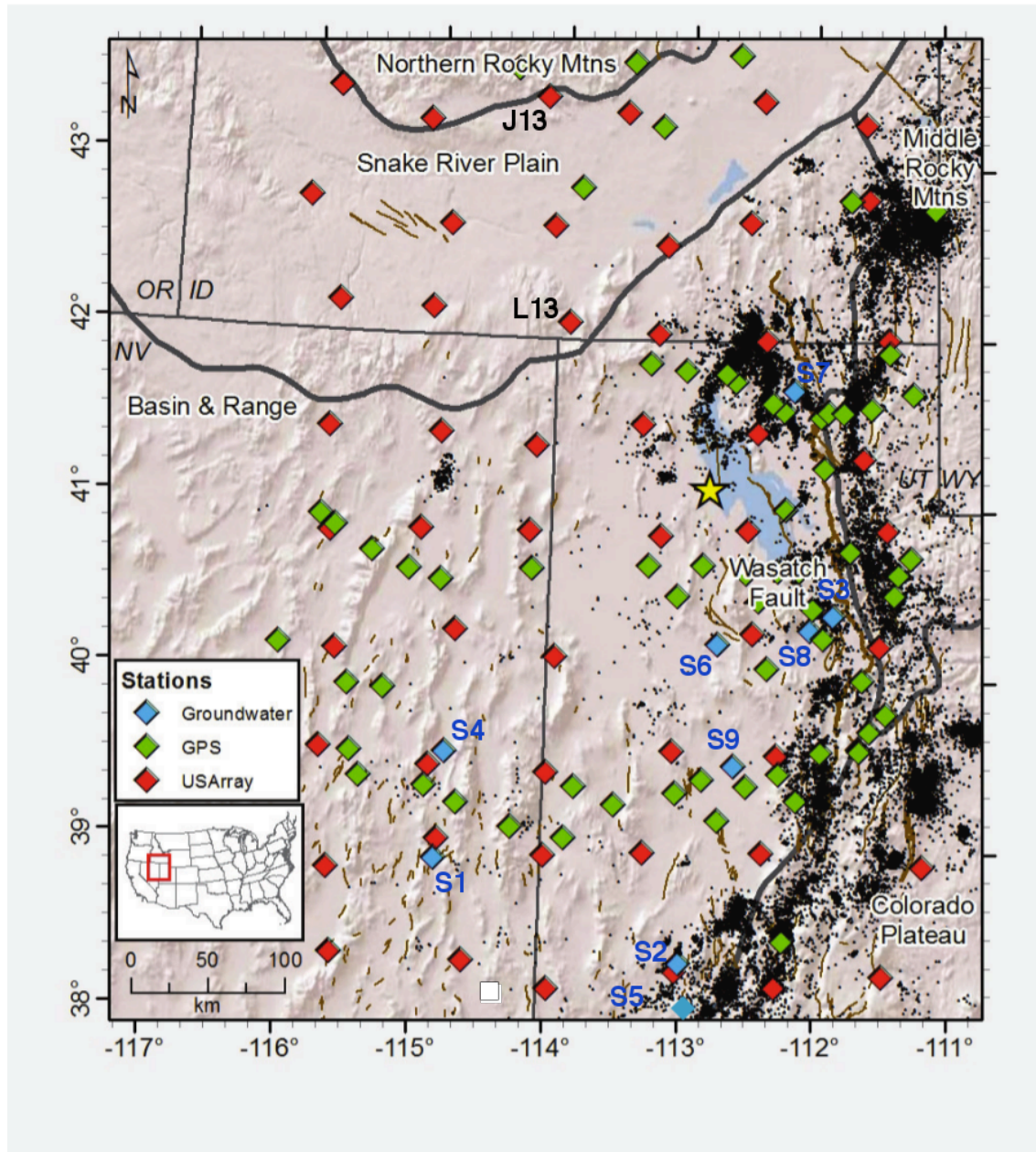


Figure 8.1: USArray transportable array given by the red squares. The location of the explosion (source) is given by the yellow star. The blue and the green squares give the locations of the groundwater wells and the GPS stations, respectively.

In this study, we monitor temporal velocity changes within the crustal sub-surface in the Great Basin and across the transition zone to the Middle Rocky Mountains and Colorado Plateau. We use coda waves generated by time-lapse active sources during the summer of 2007. These coda waves were recorded by USArray stations located in western Utah, eastern Nevada and southern Idaho (Figure 8.1). In the following section, we describe in detail the data processing routine we use in this study. In sections 8.4 and 8.5 we present the results from the time-lapse monitoring of the study area and an interpretation of the results, respectively. Section 8.6 concludes the results of the study and discusses the assumptions we use to resolve the in-situ velocity changes.

8.3 Data processing

We process coda signals generated by 9 rocket motor explosions, occurring between June 4 and September 10 2007, which were surface rocket explosions at the Utah Test and Training Range (UTTR) of Hill Air Force Base, Utah [102]. Each of the explosions was carried out at the same location with latitude and longitude of $N41.141^\circ$ and $W112.9065^\circ$, respectively. The similarity in the source properties of the monitoring signals prevents errors in the estimated relative velocity changes due to changes in the properties of the sources (such as a shift in source location or source mechanism) generating the coda signals [39, 110]. The blast signals were recorded on 54 Earthscope USArray transportable (TA) stations surrounding the blast location (Figure 8.1).

In this study we process the three (N-S, E-W and vertical) components of the recorded explosive signals. Figure 8.2 shows an example of the unfiltered velocity records. We use a 1-5Hz frequency band for the time-lapse monitoring and an example blast signal for the 1-5Hz frequency band is given in Figure 8.3. We use the S-wave coda section of the signals (i.e. the section of the signal with exponential amplitude decay) (Figure 8.4). The onset time of the coda section after the S-waves varies between stations. We normalize each signal with its maximum amplitude and resampled each of the signals from a time interval δt of 0.025s to 0.001s. The resampling increases the resolution of the estimated velocity changes. The

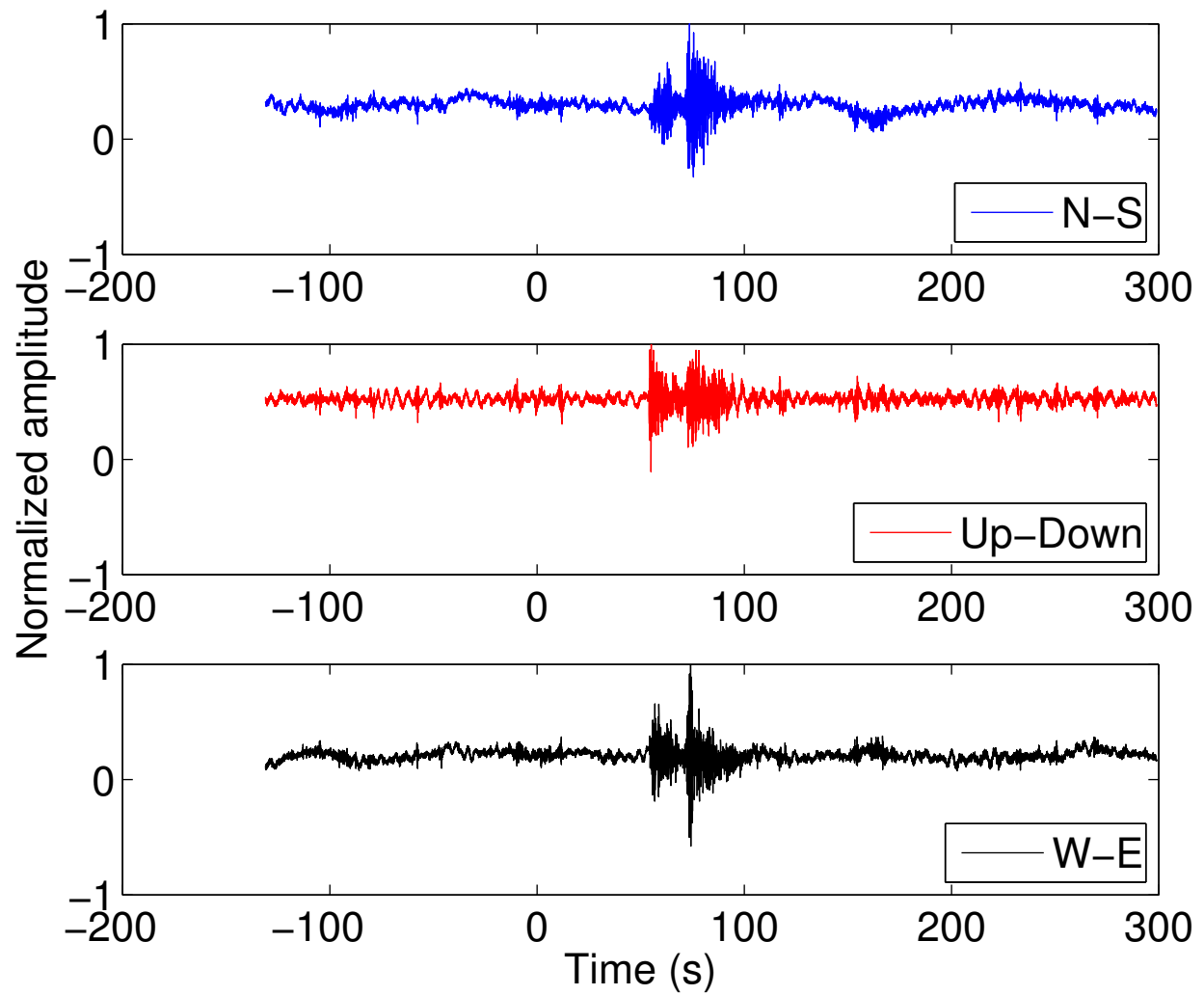


Figure 8.2: Example recording of typical blast events. Event 09/10/2007 recorded at station L13A. The three components, N-S (blue), Up-Down (U-D) (red) and the E-W (black) are all used in the time-lapse analysis.

data is processed using three cases of comparison. Case 1 consists of comparing each of the recorded signals to the first blast signal on June 4. In Case 2, each signal is compared to the previous signal (in time). For Case 3, we use only the signals from August 1 to September 10. Each of the signals in Case 3 is compared to the blast signal on August 1. The purpose for these three cases is to check for consistency in our estimate of velocity change.

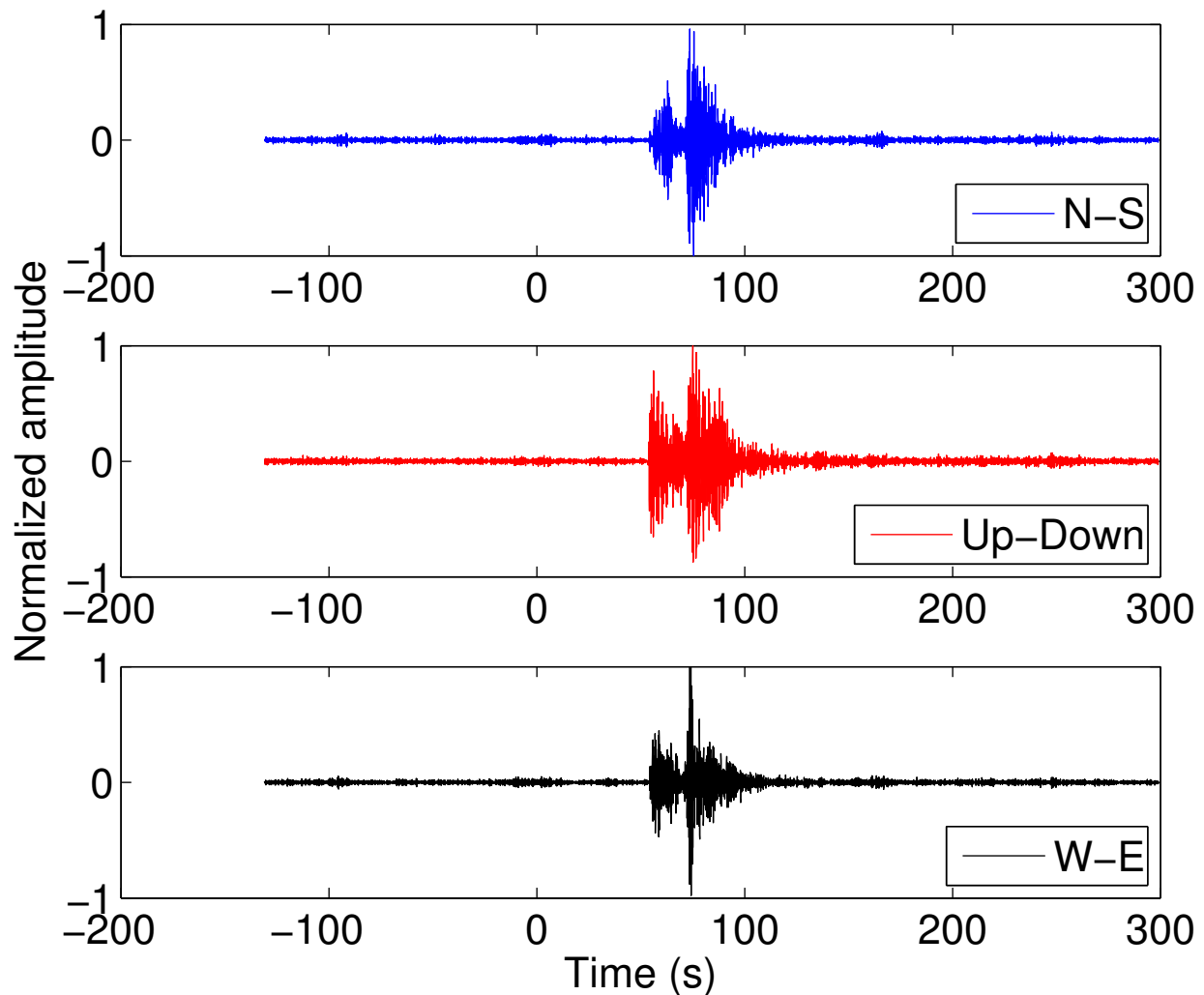


Figure 8.3: Typical recordings of the blast events bandpass filtered between 1-5 Hz. The three components, N-S (blue), Up-Down (U-D) (red) and the E-W (black) are all used in the time-lapse analysis. The black rectangle gives the coda section of the blast signal.

To extract the relative velocity change from the time-lapse data, we use the stretching method [33]. However, rather than using the maximum correlation as the misfit function for

the time-lapse objective, we use the L_2 norm as the objective function [39]. We initialize the time of the signals to the onset times of the explosive events in order to apply the stretching algorithm. A doublet consists of time-lapse signals from two explosive events. The source properties of the explosive signals are similar; therefore any difference in the signals results from either changes along the propagation path of the signals or differences in noise properties of the signals. The major challenge we encountered while analyzing this explosive data was accounting for missing data. In some cases the data were either missing one of the components or all three of the components. We only used explosive signals that are recorded on all three components of the stations.

Because of the presence of noise in the data and because the noise becomes more prominent with increasing coda time, we only use the codas where the correlation of the early part of the coda between the time-lapse signals is greater than 0.75 and the correlation of the end of the coda is greater than 0.5 (similarity criterion). This section of the coda is submitted to the stretching algorithm. In cases where this criterion is not met, we assign zero to the relative velocity change and its error. We compute the error associated with the estimated velocity change using [39]

$$e \leq \frac{\sigma_U}{2\pi f_d A t}, \quad (8.1)$$

where f_d is the dominant frequency, t is the centertime of the signal, A is the amplitude of the signals, and σ_U is the standard deviation of the recorded waveforms.

The estimated relative velocity changes $\langle \epsilon \rangle$ estimated in Cases 1 and 3 are cumulative velocity changes from the reference signals. However in Case 2, the changes estimated are interval velocity changes for each monitored time period. To express the estimated velocity changes of Case 2 in a way that is consistent with the other two cases, in Figure 8.5 we sum the estimated velocity changes and their associated error values using the following equations and ignoring the estimates where our similarity criterion was not met:

$$\alpha_j = \sum_{i=1}^j \langle \epsilon \rangle_i, \quad (8.2)$$

and

$$e_j^\alpha = \sqrt{\sum_{i=1}^j e_i^2}, \quad (8.3)$$

where α is the cumulative relative velocity change, e is the error of the relative velocity change, e^α is the error of the cumulative relative velocity change, and i and j denote the time intervals we are monitoring with values 1 to 8.

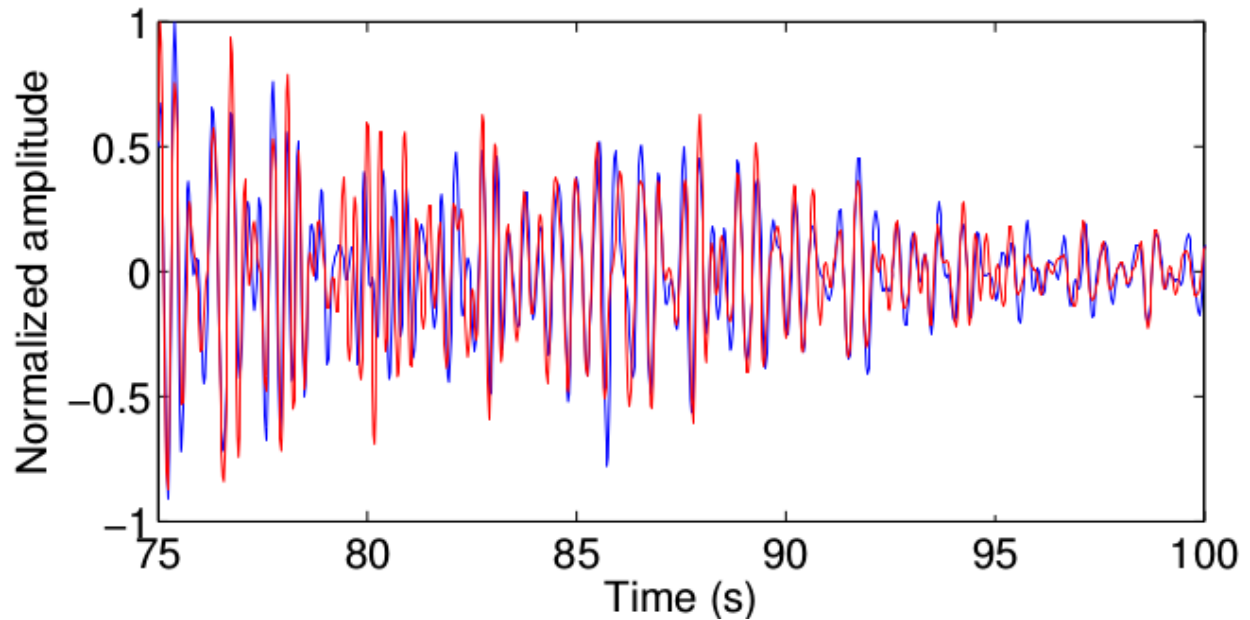


Figure 8.4: A typical time-lapse coda of the 1-5 Hz filtered recorded blast events for the Up-Down (U-D) component.

8.4 Time-lapse velocity change

Figure 8.5 shows the cumulative estimates of the average relative velocity changes for: Case 1, Case 2 and Case 3. We compute the average velocity change using all the monitoring stations with estimated velocity change. Comparison of the estimated velocity changes from all three cases reveals that the estimated average velocity changes for all three components follow a consistent trend. Cases 1 and 2 show an average velocity increase of about 0.1% between June 4 and July 9 (Figure 8.5). Most of the 0.1% velocity change occurs between

June 26 and July 9. The temporal variation of the rest of the velocity changes lie within the error level of the velocity change. The error values are the standard deviations of the mean estimated velocity changes from all the stations. However, the velocity remains fairly constant from July 9 until August 1. Given the consistency in the average velocity changes after August 1 shown by all the cases, the estimated velocity changes might be significant. But the variability of these velocity changes is hard to discern given the error level of the velocity changes.

8.4.1 Spatial distribution of velocity change

Figure 8.6 and Figure 8.7 show the velocity change for each station. The trend of the velocity changes in these figures are similar to what are observed in the average velocity changes computed using all the stations. The estimated velocity changes in Figure 8.6 and Figure 8.7 are the estimated velocity changes in Case 2 for each time-lapse period. Figure 8.6 shows the spatial distribution of the velocity changes which varies with receivers; the region of dominant velocity changes also varies from one time period to the other.

The estimated velocity changes generally decrease with increasing source-receiver distance (Figure 8.7). The dependence of the estimated velocity change on the source-receiver distance explains the high error levels in the average of the estimated velocity change shown in Figure 8.5. The spread in the velocity changes estimated at the stations is not due to random errors but due to variations in the estimated velocity change among different source-receiver pairs. The spatial distribution of the velocity changes and the dependence of the velocity change on the source-receiver distance might suggest that the velocity changes in the medium are spatially localized.

8.4.2 Coda time window analysis of $\langle \epsilon \rangle$

Obermann et al. [67] shows that the variation of the estimated velocity change with time in the coda waves can be use to differentiate between subsurface velocity change at shallow or at great depths. We estimate velocity change within 5 coda time windows: $[t_s; t_s + 3]$,

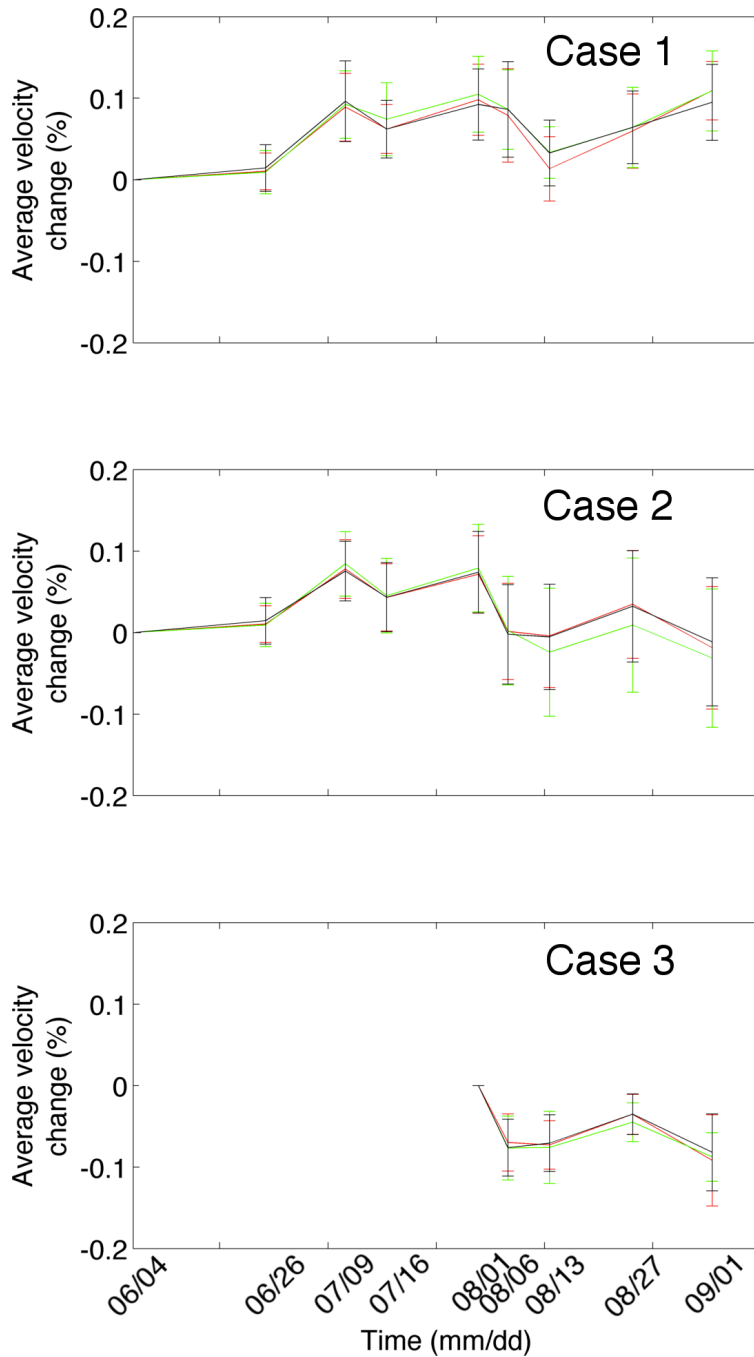


Figure 8.5: The cumulative relative velocity changes expressed in percentages for N-S (red), Up-Down (U-D) (green) and the E-W (black) components. Here the average is computed using all the stations in the USArray displayed in Figure 8.1. Missing first five estimates in Case 3 is because only signals from August 1 is processed in Case 3.

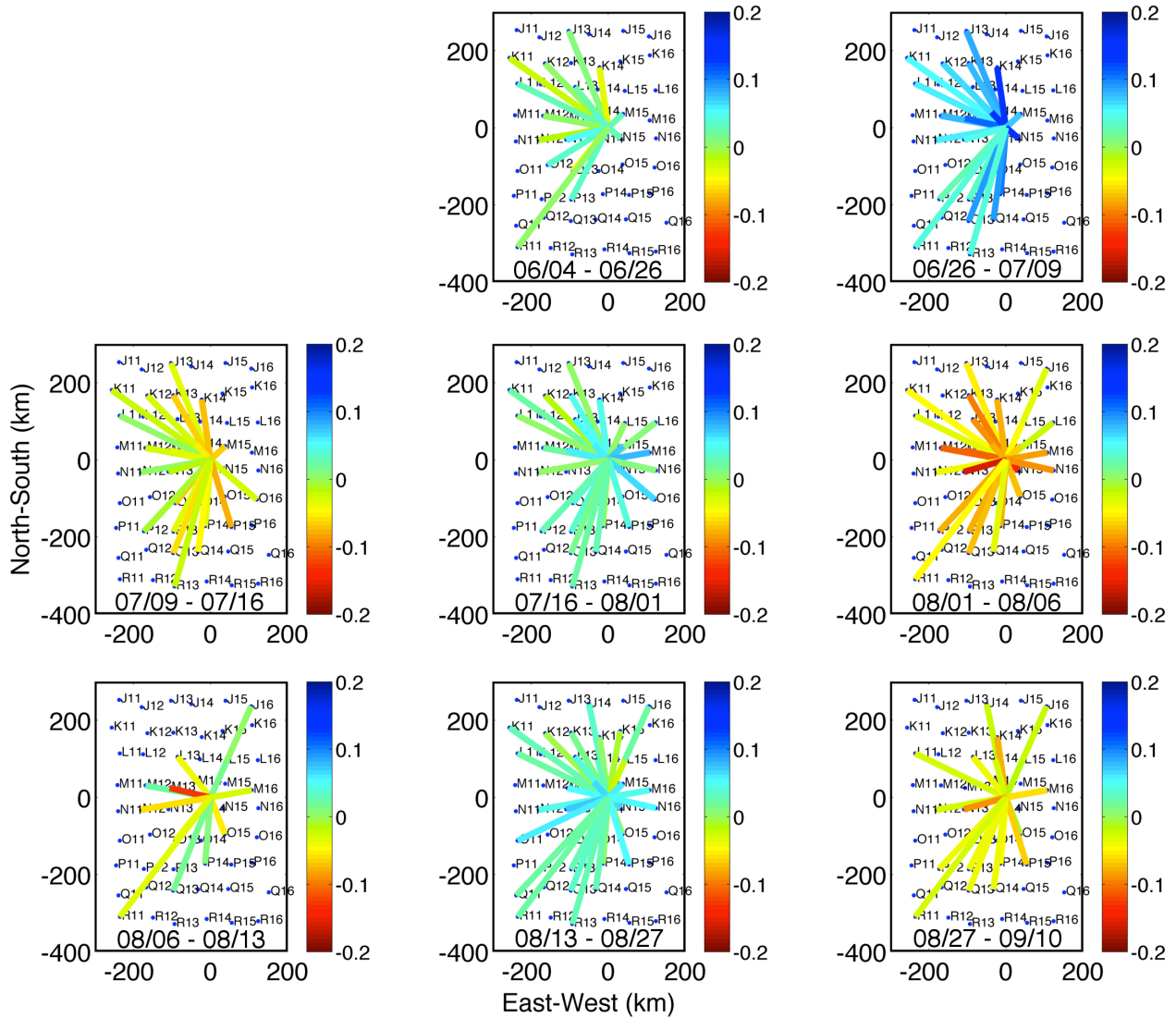


Figure 8.6: Relative velocity changes in % estimated from the 8 blast doublets using vertical component of the stations. The blue points are the surface stations. The source location is the point where all the colored lines meet. The color lines are the estimated percentage velocity changes for each source-receiver pair.

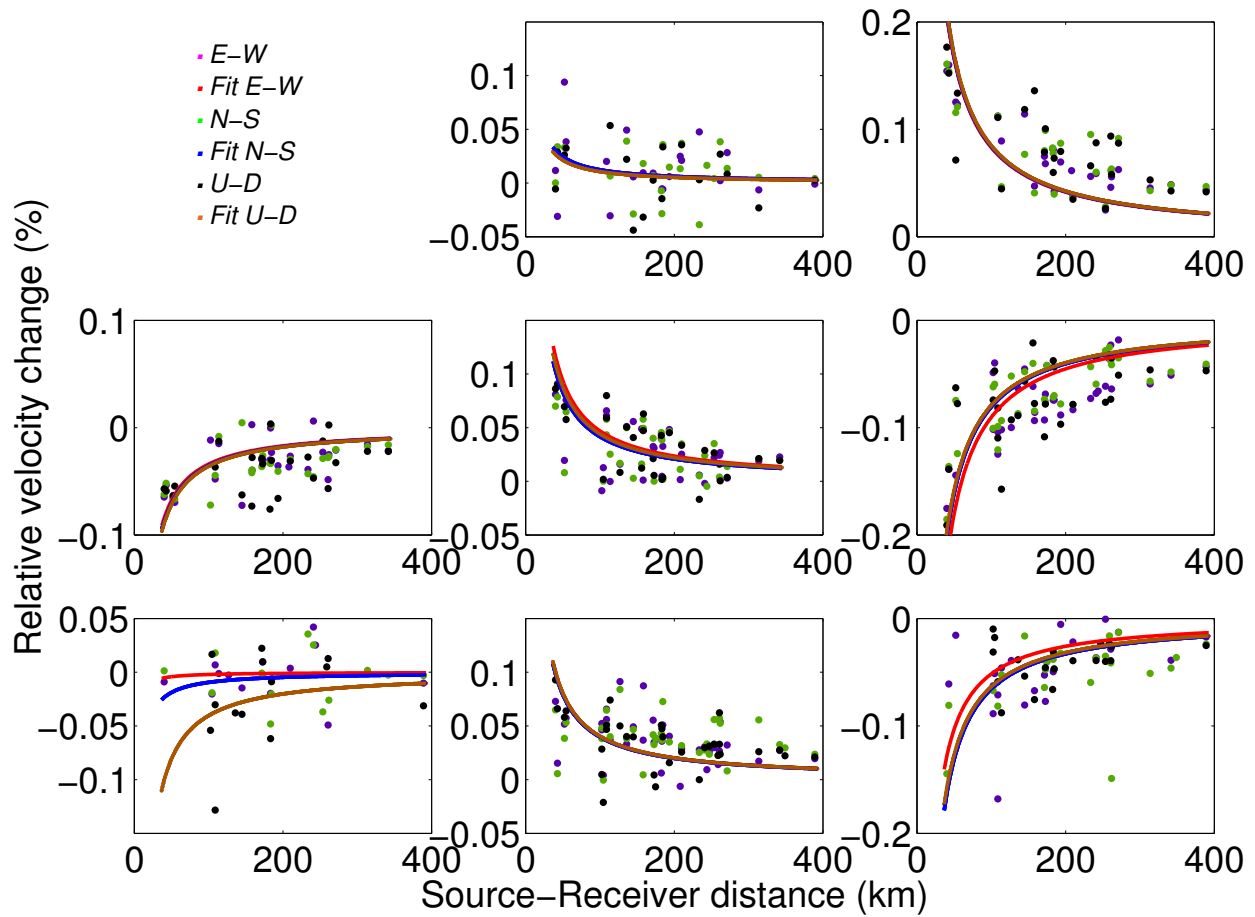


Figure 8.7: The relative velocity change estimated for each of the time-lapse periods as a function of source-receiver distance. Power law fitting of the estimated velocity changes in Utah Wasatch fault region. Fit E-W, N-S, and U-D are the fitting solutions for the estimated velocity changes of E-W, N-S, and U-D components, respectively.

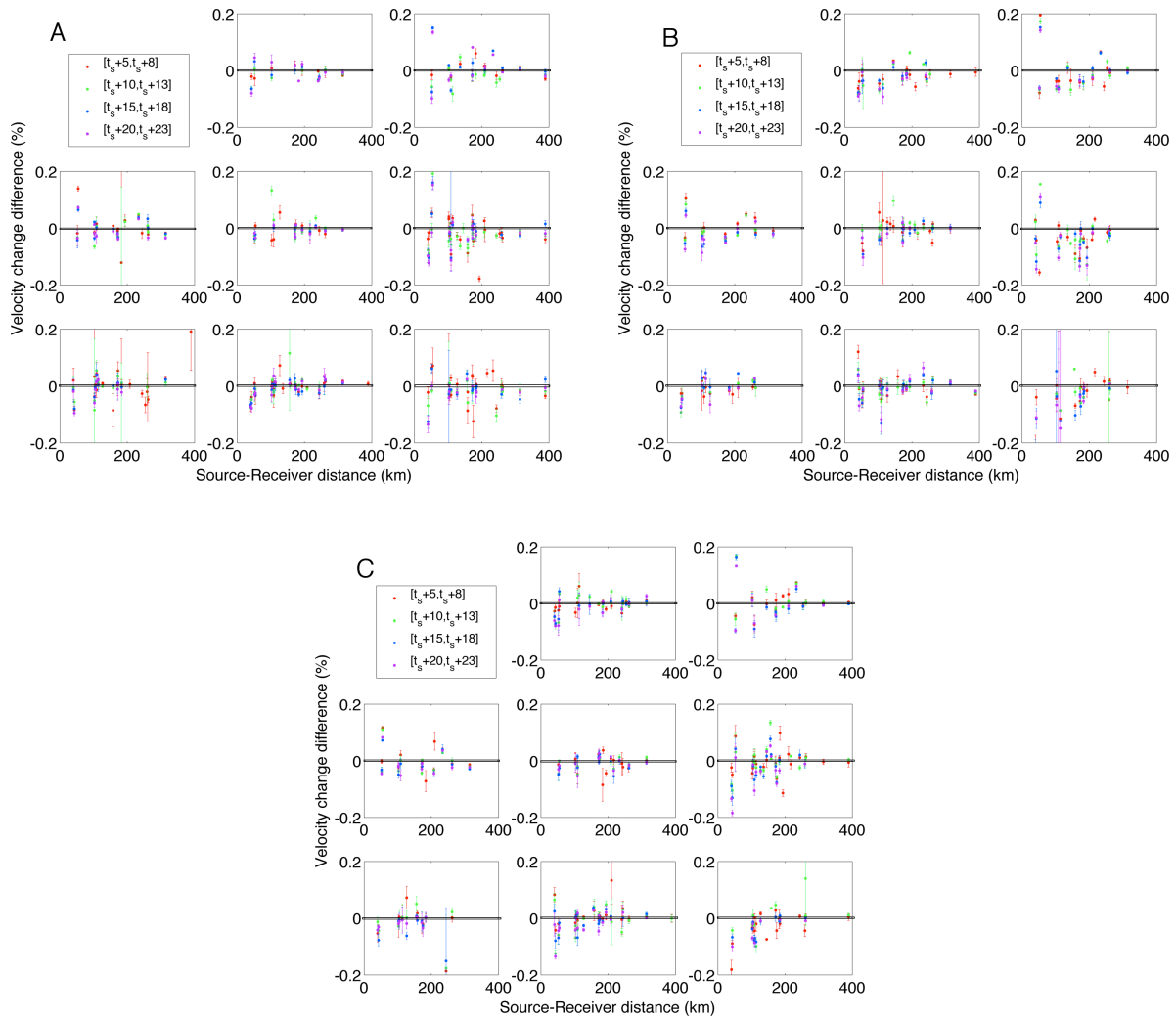


Figure 8.8: Estimated velocity change difference Δ_T for each time-lapse period. The plots show the estimated velocity change difference Δ_T versus the source-receiver distance for the A: N-S component, B: Up-Down (U-D) component, and C: N-S component.

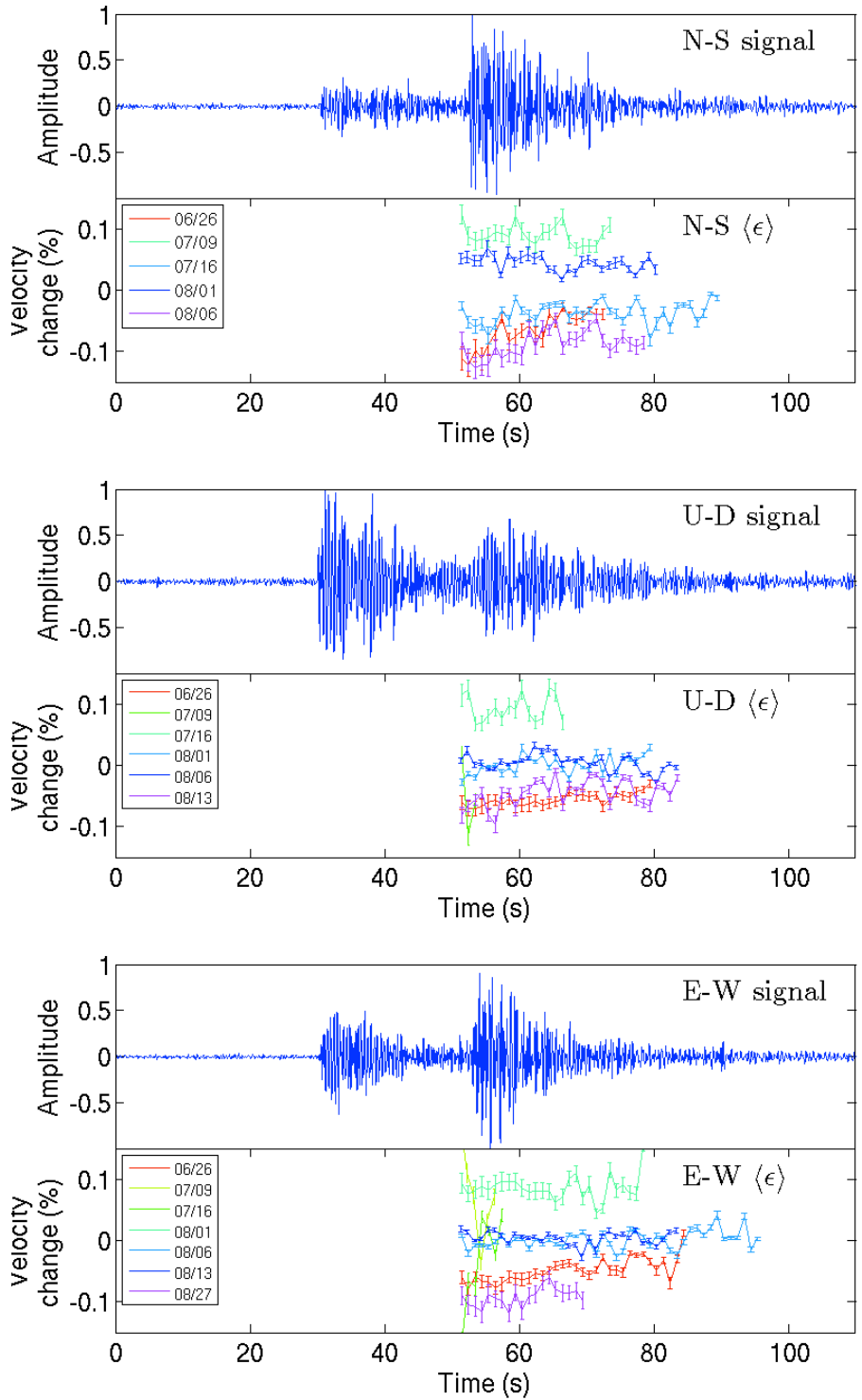


Figure 8.9: Estimated velocity change $\langle \epsilon \rangle$ versus time in the coda for each time-lapse period using the N-S component (top), the Up-Down (U-D) component (middle), and the E-W component (bottom).

$[t_s + 5; t_s + 8]$, $[t_s + 10; t_s + 13]$, $[t_s + 15; t_s + 18]$, and $[t_s + 20; t_s + 23]$, where t_s is the first arrival time of the S-wave and the units are seconds. Figure 8.8 shows estimated velocity change difference Δ_T for the three signal components - N-S, E-W, and U-D components. We define the estimated velocity change difference Δ_T as

$$\Delta_T = |\langle \epsilon \rangle|_T - |\langle \epsilon \rangle|_{[t_s; t_s+3]} \quad (8.4)$$

where, T is the coda time windows ($[t_s + 5; t_s + 8]$, $[t_s + 10; t_s + 13]$, $[t_s + 15; t_s + 18]$, and $[t_s + 20; t_s + 23]$ seconds). Figure 8.8 compares Δ_T for all the monitoring stations and time-lapse periods. We compute the errors using equation 8.3. The figure shows that the velocity change differences Δ_T are predominately negative for stations less than 50 *km* but for source-receiver distances greater than 50 *km* the Δ_T values cluster around zero. The predominately negative values of Δ_T for source-receiver distances less than 50 *km* shows that the absolute value of the estimated velocity change for the coda times 5 *s* greater than the arrival time of S-wave (t_s) are predominately smaller than the absolute value of the estimated velocity change at the coda time close to the arrival time of S-wave for these distances. These negative values of Δ_T for source-receiver distances less than 50 *km* might indicate that the subsurface velocity change extends to the near surface [67]. However, the cluster of the Δ_T values for source-receiver distances greater than 50 *km* shows no consistent variations in Δ_T . This is because the estimated velocity change is fairly constant across the coda times. Figure 8.9 shows the estimated velocity change across the coda for the three signal components using station N12A. We estimate the velocity change using 3 *s* time windows with 2 *s* overlap. The overlap allows for more estimates of the velocity changes. The estimated velocity change is fairly constant across the coda. This variation of the estimated velocity change might suggest a broad subsurface velocity change across the crust extending to the near-surface.

8.4.3 Parameter Estimation

Assuming a diffusion model for the coda waves, the traveltime shifts (and therefore the estimated velocity changes) depend on the magnitude of the subsurface in-situ velocity

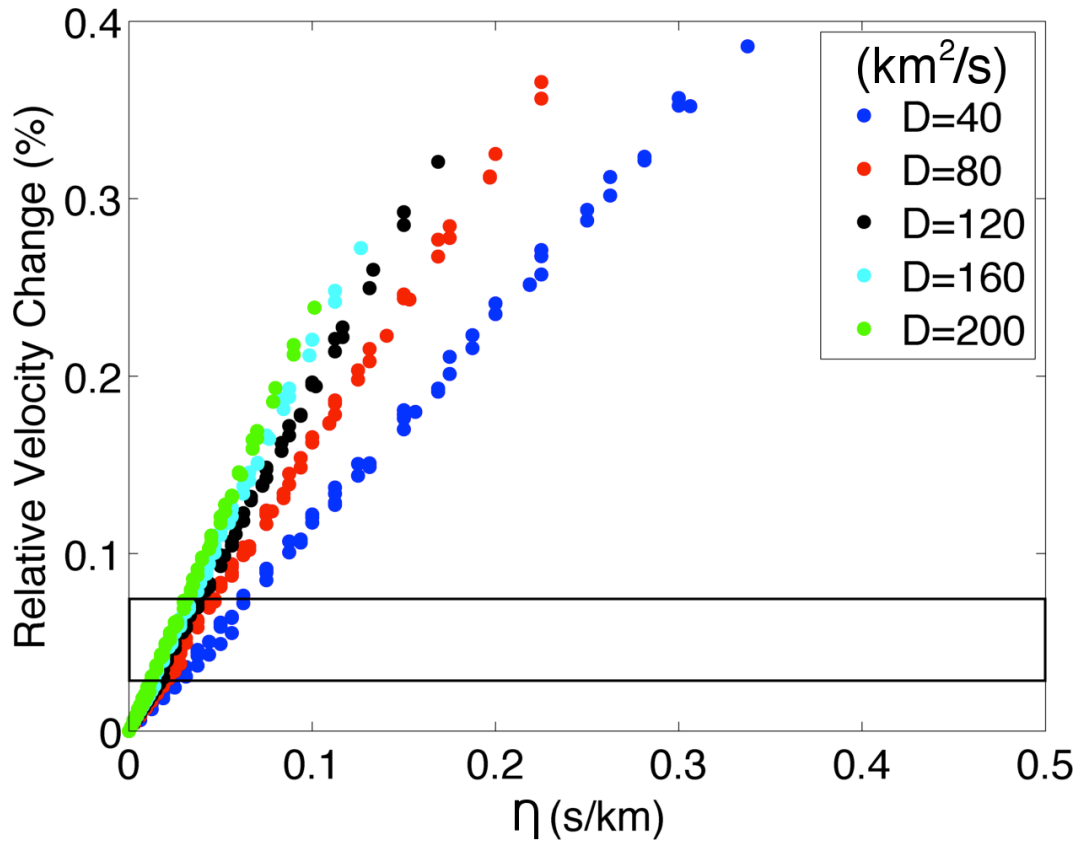


Figure 8.10: Dependence of the estimated velocity change on the dimensionless parameter η . The definition of η is given in equation 6. The black rectangle corresponds to the range of velocity changes estimated with station J13.

change Δv , the volume of the velocity change ΔV , the diffusion coefficient D of the scattered wave intensity [70], and the source-receiver distance R_{sr} . Assuming a uniform lateral velocity change within a layer of thickness h near the earth's free surface and 3D bulk wave scattering, we can formulate the parametric dependence of the estimated relative velocity change $\langle \epsilon \rangle$ as follows:

$$\langle \epsilon \rangle = F(\Delta v/v, h, D, R_{sr}). \quad (8.5)$$

The function F can be found from the theory of Pacheco and Snieder [70], which relates the estimated relative velocity change $\langle \epsilon \rangle$ to the model parameters $(\Delta v/v, h, D, R_{sr})$ through the relation:

$$\langle \epsilon \rangle = \int_V K(\mathbf{r}, t; D) \frac{\Delta v}{v}(\mathbf{r}) dV; \quad (8.6)$$

where $K(\mathbf{r}, t; D)$ is the sensitivity kernel of velocity change using multiply scattered waves, with travel time t , to subsurface relative velocity change $\Delta v/v$ at location \mathbf{r} . Here, the source-receiver distance R_{sr} is given by the known source and receiver locations. For a given source-receiver distance R_{sr} , the estimated relative velocity change depends mostly on the parameter η , defined as

$$\eta = \frac{h}{D} \frac{\Delta v}{v}. \quad (8.7)$$

Figure 8.10 shows the apparent (estimated) velocity changes using the source-receiver distance of station J13 for values of η from 0 *s/km* to 0.45 *s/km* as obtained from equation 8.5. These values of η cover the range of relative velocity change we observe in this study ($\langle \epsilon \rangle < 0.2\%$). Figure 8.10 suggests that the combined effect of the magnitude of the subsurface velocity change Δv and the depth of the velocity change h have the greatest influence on the estimated velocity change, for a given source-receiver distance R_{sr} . Assuming the diffusion model, different D values gives different slopes in Figure 8.10. With a wide range of estimated velocity change $\langle \epsilon \rangle$, these different slopes suggest that diffusion coefficient D gives a weaker trade-off with the other two parameters, the magnitude of subsurface relative

velocity change $\Delta v/v$ and the depth of velocity change h . However, for the range of velocity change we estimate in this study (black rectangle in Figure 8.10 for station J13), the dependence of $\langle \epsilon \rangle$ on the three parameters (h , D , $\Delta v/v$) is mostly through the combination of η . We cannot separate the effect of D except if we independently estimate D . Figure 8.10 is for Station J13, the other stations show a similar trade-off between the three model parameters.

We can constrain the diffusion coefficient D by using the relationship that at the peak of the coda intensity, $D = R_{sr}^2/6\langle t \rangle$ (Appendix E). The weighted average time $\langle t \rangle$ corresponds to the peak of the coda intensity. For the current dataset, the estimated average diffusion coefficient is $106 \text{ km}^2/\text{s}$. Fixing the diffusion coefficient to this average value, the velocity change is a function of the trade-off between $\Delta v/v$ and h . The trade-off between $\Delta v/v$ and h makes it impossible to independently determine each of these parameters without additional information.

According to equation E.12 in Appendix E, we can use a power law relation to describe the dependence of estimated velocity changes on distance (Figure 8.7) as:

$$\langle \epsilon \rangle = aR_{sr}^{-1}, \quad (8.8)$$

where $a = (h\Delta v/v)\Sigma$ (equation A12). Σ is a dimensionless constant of the monitored region (equation E.11) that depends on the diffusion coefficient D . Using the power-law relation in equation 8.8, we invert the values of $h\Delta v/v$ from the estimated velocity changes. Table 8.1 gives the estimated parameters for the fitting solutions of the estimated velocity changes, the goodness of fit in R^2 (a measure of regression) values, and the inverted values of $h\Delta v/v$. We use the weighted nonlinear least-squares method with the inverse of the estimated errors as weights. Negative R^2 values are encountered due to the use of a nonlinear model [18]. Based on the surface layer model, the inverted values for $h\Delta v/v$ are of the order of $1 \% \text{ km}$ (Table 8.1). This value of $h\Delta v/v$ implies, for a change extending throughout the crustal thickness of 25-40 km, the average subsurface in-situ velocity becomes less than 0.04%. However, when the thickness of the layer is limited to less than a kilometer the velocity change is large ($\simeq 1\%$). A velocity change of less than 0.04% for a crustal-scale deformation

might be realistic in the actively extending Basin and Range province.

The diffusion model in the Appendix E generally explains the decrease of the estimated velocity changes $\langle\epsilon\rangle$ with the source-receiver distance. However, as the goodness of fit in R^2 indicates (Table 8.1), equation E.12 provides a poor description of the variation of the estimated velocity changes $\langle\epsilon\rangle$ with source-receiver distance. This poor fit results from the significant scatter in the estimated velocity changes $\langle\epsilon\rangle$. The deviation of the estimated velocity changes $\langle\epsilon\rangle$ from equation E.12 can result from heterogeneity in the scattering properties of the monitored subsurface (captured by varying D values) or heterogeneity in the subsurface velocity change. These heterogeneity are ignored in the diffusion model in Appendix E.

8.5 Causes for the velocity changes

Variations in subsurface velocity at time scales similar to the ones in the observed velocity changes might be induced by fluctuations in seasonal stress loading including precipitation, hydrological cycles, thermal changes, local seismicity, and groundwater level variations [104].

8.5.1 Seasonal loading

Utah is a region that receives little precipitation. Available precipitation records for the monitored region show that the cumulative precipitation during the monitored time period is less than 5 *cm*. This amount of precipitation can not induce the amount of velocity change observed. The groundwater level, however, can vary temporally, not only due to precipitation but also to irrigation practices [6], stress loading resulting from large earthquakes [60], and solid earth tides [100]. Figure 8.11 shows the correlation between cumulative groundwater level change (positive values corresponds to deepening of the groundwater level) over the monitored period with the estimated average velocity change from Case 2, using 9 recording wells. The location of the recording wells of the groundwater level are shown in Figure 8.1. For a few of the wells (wells S4, S7, S8 and S9), a linear regression suggests that the average velocity changes show significant correlation (with regression coefficients $R^2 > 0.5$) with

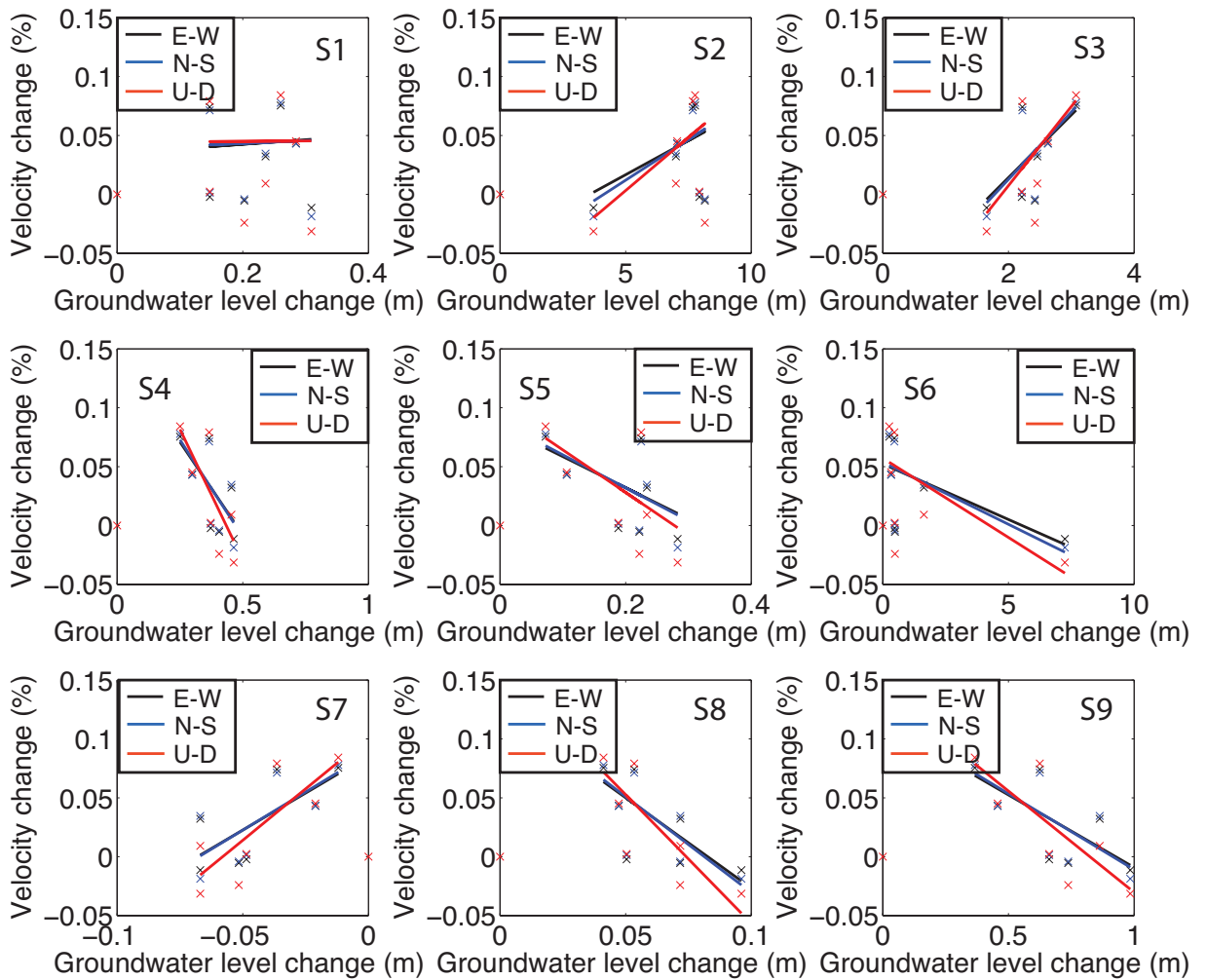


Figure 8.11: Correlation of average velocity change with groundwater level change measured in meters (positive meters mean deepening of the groundwater level). Each plot shows the fit of the average velocity changes from the three signal components. S1 to S9 are the names of the groundwater wells.

the groundwater level subsidence. We quantify the quality of the correlation using the R^2 values of the linear fit (Table 8.2) [23]. We obtain R^2 values less than 0.67 using a weighted least-squares fit, where we use the standard deviation of the estimated velocity change as the weights. Among wells S4, S7, S8 and S9, only well S7 supports a direct proportional relationship between velocity change and stress (pressure) changes, if we assume that increase in groundwater level change results in an increase in effective stress. The maximum groundwater level change within the time period monitored among the wells is less than 2 m. This corresponds to approximately a change in the effective stress of less than 2.94×10^{-2} MPa assuming that the Biot coefficient is equal to 1 and a soil density of less than 2.5 g/cm^3 . The stress sensitivity η reported in the literature is between $10^{-6}/\text{Pa}$ and $10^{-9}/\text{Pa}$ [44, 94]. These stress sensitivity values imply a range of $\Delta v/v$ values of magnitude 10^{-2} to 10^{-5} %. Given that these values of $\Delta v/v$ are orders of magnitude smaller than the estimated velocity changes $\langle \epsilon \rangle$ and that only a few of the stations show significant positive correlation with the velocity changes (Figure 8.11), the groundwater level change is unlikely to explain the observed velocity changes.

Seasonal strain changes can be recorded by detrended GPS displacement measurements. Using horizontal GPS displacements from GPS stations within our monitored region (Figure 8.1), we quantify the correlation between the estimated relative velocity change and the seasonal E-W strain using the R^2 values of the linear fit (Figure 8.12). We compute the average horizontal strain between stations using the average detrended horizontal GPS displacements denoted by $d_k^{i,j}$. Because, the horizontal distances between the stations are much larger than the elevations between the stations, we approximate the average horizontal strains by:

$$\gamma_{kk}^{ij} = \frac{d_k^j - d_k^i}{X_k^j - X_k^i}, \quad (8.9)$$

where, i and j are station indexes, X_k is either E-W ($k = 1$) or N-S ($k = 2$) GPS location, and γ is the average strain. The detrended GPS displacement $d_k^{i,j}$ is averaged two days prior

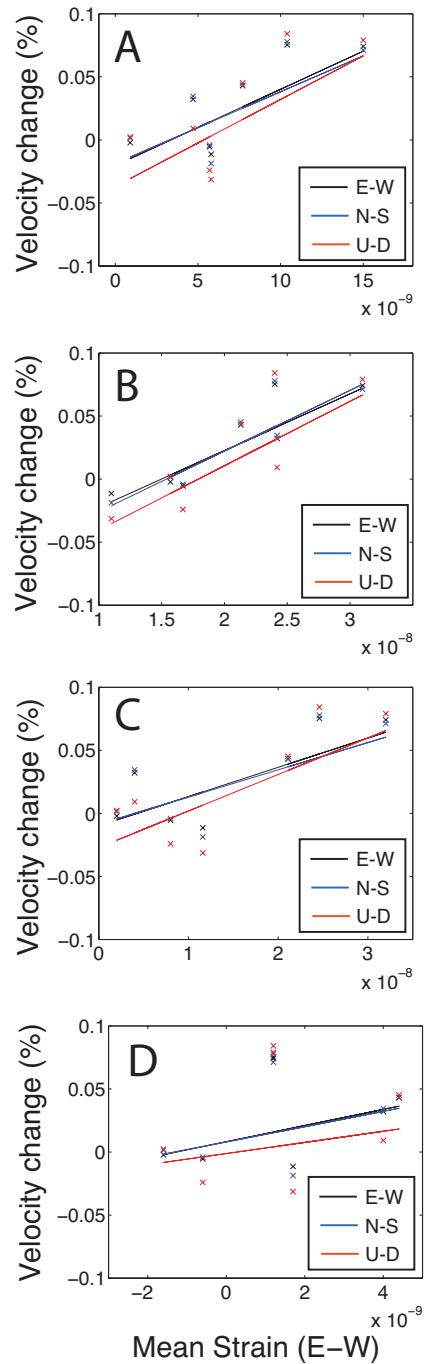


Figure 8.12: Linear regression between the E-W strain derived from E-W GPS detrended displacement and the individual components of average velocity change (E-W, N-S, and vertical components). The linear regression is computed using A, all the available GPS displacement, B, only the Basin and Range GPS displacements, C, only the Wasatch fault displacements, and D, only the Snake River Plain GPS displacements.

to and two days after the time of each blast. Table 8.3 and Figure 8.12 show the linear correlation with the estimated average velocity changes using 4 groups of the GPS stations. One group consists of all the available GPS stations while the other 3 groups use either only stations within the Snake River Plain, only stations within the Basin and Range, or only the stations close to the Wasatch fault. Comparison of the estimated average velocity changes from Case 2 with the average horizontal GPS strain using all the GPS stations shows a significant linear correlation, based on the R^2 values, of the velocity changes with the East-West strain (Table 8.3). For the strains derived from the Basin and Range GPS stations, there is a larger correlation of the velocity changes with the East-West strains compared to the strain derived from all the stations. Stations along the Snake River Plain region show negligible correlation ($R^2 < 0.23$) with the observed velocity change (Figure 8.12D, and Table 8.3). Fits with negative R^2 values here, suggests that the linear fit might be an incorrect model for those fits.

Seasonal variation in GPS displacement and therefore the seasonal variations in the strain can be induced by thermoelastic or hydrologic variations [104]. While hydrologic variations can induce localized changes, variations in the thermal conditions within the crust can be responsible for a broad crustal deformation [42]. Crustal deformation in the Basin and Range predominately creates normal fault and extensive structures striking in approximately north-south orientations. The correlation between the estimated average velocity changes and the calculated strain changes suggests that the velocity changes might be driven at least in part by the changes in the seasonal strain. With the inconsistent correlation we obtained between the average velocity and the groundwater level change, the strain changes here, might be driven by tectonic or thermoelastic stress changes. Given that the observed velocity changes correlate significantly with the strains aligned in the direction of the crustal deformation in the area, the velocity changes we observe might extend deep into the crust and therefore result in a small subsurface $\Delta v/v$. If the seasonal strains from the Basin and Range GPS detrended displacements are induced by crustal deformation, a significant part of the velocity

change observed might be driven by broad crustal deformation in the monitored region. The monitored region covers the eastern flank of the Basin and Range, which has been shown to have elevated thermal conditions [24] that might be responsible for broad active deformation in the region. Tectonic deformation of the region could induce velocity changes within the crust; however, these velocity changes are broader, more gradual, and extend deeper than the change due to other physical mechanisms such as variations in groundwater level or regional seismicity. Because of the broad and gradual properties of the crustal deformation-induced velocity changes, we expect larger values of h (volume of change) and lower subsurface relative velocity changes $\Delta v/v$. With a larger value of h , crustal deformation due to stress changes or elevated temperatures deep within the crust might explain, at least in part, the inverted values of $h\Delta v/v$ on the order of $1\%km$.

8.5.2 Local seismicity

Figure 8.13 shows the peak ground acceleration (PGA) due to local seismicity and the estimated velocity changes. We compute PGA (y) using its relationship with event magnitude given by Chiou et al. [17]:

$$\ln(y) = \ln(y_{ref}) + \phi \ln(V_{s30}) + f_{NL}(V_{s30}, y_{ref}) \quad (8.10)$$

where $\ln(y_{ref}) = c_1 - 2.1 \ln[R_f + C_{NS}] + (-0.5 + 2.1) \ln \sqrt{R_f + 50^2} + \gamma R_f$ and $C_{NS} = c_5 \cosh[c_6 \max(M - 3.0)]$. V_{s30} is the average shear wave velocity in the top $30m$, f_{NL} defines the nonlinear soil response of the monitored area, M is the event magnitude, and R_f is the distance to the fault rupture location in km . We use values for coefficients ϕ , γ , c_1 , c_5 , and c_6 reported by Pankow [73] for the Utah region. To compute PGA, we use the V_{s30} value of $230m/s$. The deviation of V_{s30} for each monitoring station from $230m/s$ will affect the magnitude of the PGA values and will affect negligibly the temporal variations of the PGA values. The temporal variations of the PGA values depends on the number and magnitude of the seismicity registered during each time period. We compute PGA for earthquake magnitudes and hypocenter parameters determined by the Utah Regional Seismic

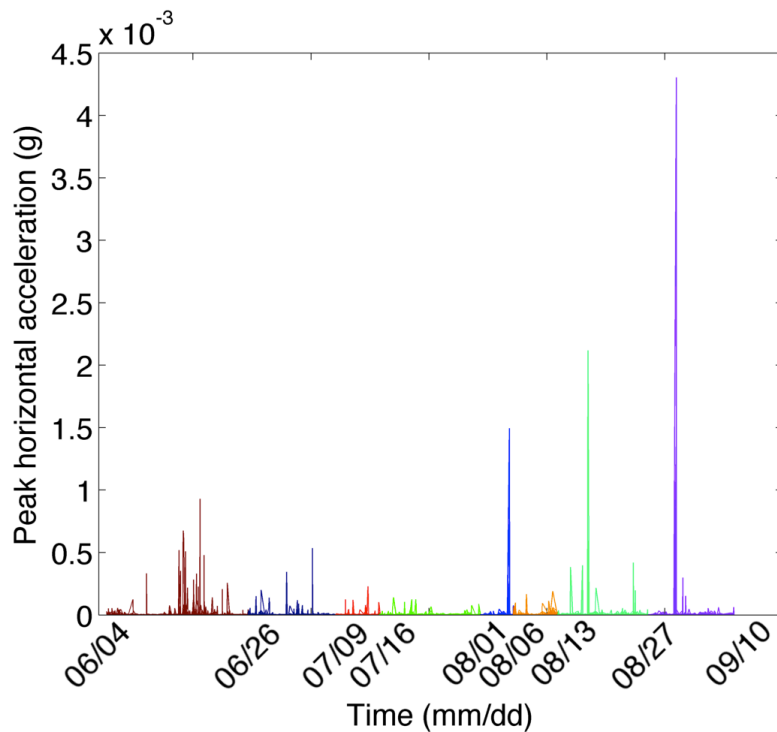
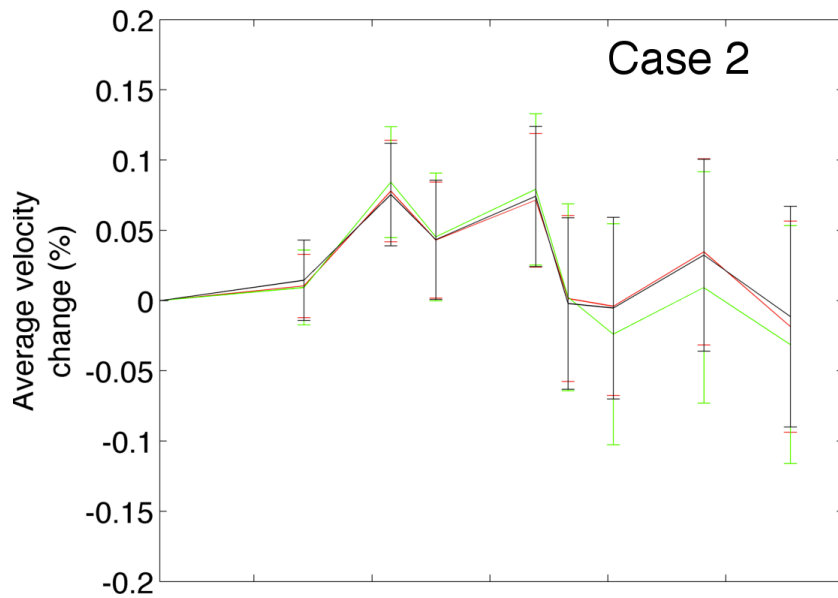


Figure 8.13: Comparison of the peak ground acceleration (PGA) with average relative velocity change estimated in Case 2. The PGA values are estimated from the local seismicity ($M > -0.36$) that occurred during the monitored time-lapse period. The PGA values are estimated using relationship between PGA and the magnitude of an earthquake Chiou et al. [17].

Network for seismic events in the monitoring region during the monitored time-lapse period (Figure 8.1).

The following time intervals contain days of relatively high spikes of PGA events: August 1 - August 6, August 13 - August 27, and August 27 - September 10 (Figure 8.13). Among these time periods, only the time period – August 27 - September 10 – has the anomalous PGA events occurring near the end of each time-lapse period. Comparing the PGA values with the estimated average velocity change, there is no clear correlation between the local seismicity induced PGA and the estimated average velocity changes. This insignificant correlation is suggested by the R^2 value of the linear fit between the PGA (total and average) values and the estimated average velocity changes (Table 8.4). The R^2 value of the linear fit for each of the average velocity changes is less than 0.32.

The effect of the local seismicity is expected to be constrained near the Wasatch fault which is situated in the eastern section of the monitored region. Therefore, local seismicity within the Wasatch fault system might be an unlikely cause for the observed velocity changes.

8.6 Discussion and Conclusions

The estimated velocity changes suggest that the eastern flank of the Basin and Range and the transition to the Middle Rocky Mountains and Colorado Plateau, are undergoing small but significant velocity changes within a short period of time. Correlation of the estimated velocity changes with groundwater level changes, seasonal tectonic strain changes and local seismicity indicates that the velocity change mostly might be induced by the East-West crustal deformation in the eastern Basin and Range. The magnitude of the estimated average velocity change varies from one time-lapse period to the other. The maximum of the absolute value of the estimated velocity change is 0.2%. Due to the averaging effect of coda interferometry, the volume and the magnitude of the velocity change are strongly correlated. We observe that the path-averaged velocity changes depend on the distance between the monitoring source and receivers. The estimated velocity changes generally decrease with source-receiver distance R_{sr} . This reduction in the estimated velocity change with source-

receiver distance is seen assuming 3D diffusion wave scattering. With the diffusion model and assuming a uniform scattering model, there is an inverse R_{sr} dependence of the estimated velocity changes $\langle\epsilon\rangle$. However, there is significant deviation of the estimated velocity changes $\langle\epsilon\rangle$ from the inverse R_{sr} relation. This deviation can result from heterogeneities in the subsurface $\Delta v/v$ or in the scattering properties of the subsurface. To obtain the inverse R_{sr} relation and consequently estimate the magnitude of the subsurface in-situ velocity change using the coda waves, we have made the following simplifying assumptions:

First, we assume that the coda waves we use for the time-lapse monitoring are described using the diffusion approximation for multiply scattered waves. This approximation is usually an over-simplification of the scattered waves especially in the early part of the coda. This approximation is likely to result in an erroneous estimation of the inverted values of $h\Delta v/v$. Also we assume a uniform diffusion model for the monitored area defined by an average diffusion constant in the subsurface. This diffusion constant is related to the distance between source and receivers using the diffusion model of the recorded intensities. If the average diffusion constant is uncharacteristic of the variation of the diffusion property of the monitored region, the inverted $h\Delta v/v$ will also be erroneous.

Second, we use a semi-infinite 3D subsurface with a fully reflecting free surface to invert for $h\Delta v/v$. The fully reflecting free surface may be a fair approximation of the free surface, but we ignore the presence of the Moho discontinuity. This boundary will change the magnitude of the sensitivity kernel of the coda because the crustal thickness is much less than the source-receiver distances used in estimating the velocity changes. Keller et al. [40] suggest that the crustal Basin and Range-Colorado Plateau transition has a thickness of about 25 km with a crustal thickness of 30 km for the Basin and Range [29]. Assuming an absorbing boundary at the crust-upper mantle interface will likely increase the magnitude of the sensitivity kernel [82]. Figure 8.14 shows that with a Moho interface at 25 km, the volumetric integral of the sensitivity kernel is increased by a factor of 1.25 to 1.80 depending on the source-receiver distance. This will result in a reduction of the value of the inverted

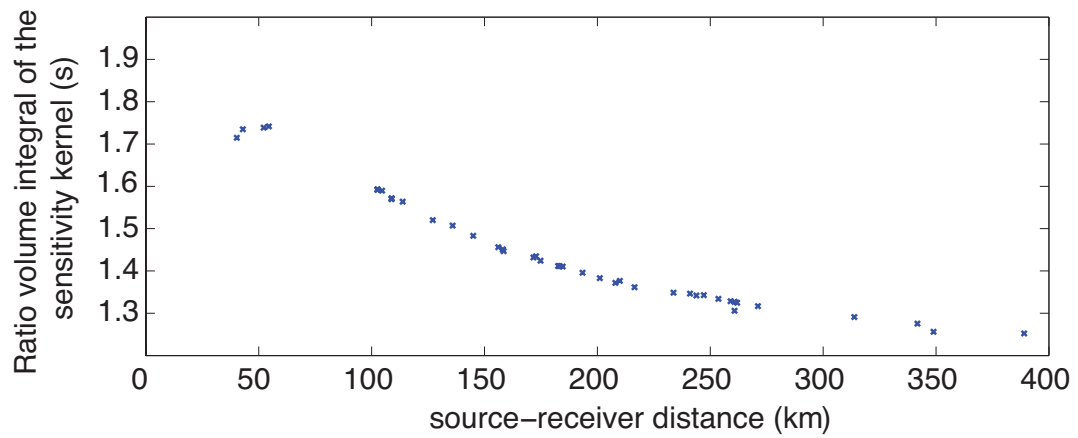


Figure 8.14: Increased sensitivity due to the presence of Moho interface at depth 25km based on the ratio of the volume integral of the sensitivity kernel with and without the Moho interface.

$h\Delta v/v$.

Third, we made a 2D approximation of the expression of Pacheco and Snieder [70] in equation E.6 by assuming that $h/R_{sr} \ll 1$. Therefore, the inverted $h\Delta v/v$ represents the true $h\Delta v/v$ within the subsurface if the velocity changes are restricted within the crust. If the observed velocity changes result from a deeper region of the subsurface, then the true values of $h\Delta v/v$ might deviate from the inverted values. Because of the large values of R_{sr} (several hundred kms), the approximation of $h/R_{sr} \ll 1$ is not likely to significantly affect the inverted values of $h\Delta v/v$.

Fourth, due to the extent of the monitored region, the recorded explosive signals are expected to generate surface waves. Due to conversion from body waves to surface waves, the surface waves can arrive within the coda wave time window especially for short source-receiver distances. In the recorded explosive signals, the surface waves mostly arrive after the coda waves. However, the relative arrival times of the coda wave and the surface wave are dependent on the source-receiver distances. In this study we have restricted the velocity changes analysis to the coda wave. The variation of the estimated velocity change across the coda (Figure 8.9) does not suggest a significant presence or contribution of surface-dominated scattered wave [67]. However, the presence of surface wave or surface dominated scattered waves in the coda will increase the sensitivity of the scattered waves to localized velocity change. This will result in lower values of $h\Delta v/v$. Therefore the inverted $h\Delta v/v$ values can be considered as the upper limit of the real $h\Delta v/v$ changes within the monitored region.

Finally, we assume a uniform lateral velocity change in the layer of velocity change across the monitored region. In reality it is likely that the velocity changes are localized in space both laterally and in depth. A heterogeneity in the subsurface velocity change likely explains the scatter in the estimated velocity changes. The inverted $h\Delta v/v$ can be seen as the average $h\Delta v/v$ of the true $h\Delta v/v$ within the monitored region. This means that in some areas of the monitored region the true changes will be higher or lower than the inverted values.

The above assumptions notwithstanding, the estimated velocity changes suggest that the crust underneath the region around the eastern Basin and Range is undergoing a path-averaged velocity change of the order of 0.1% within a short period of time. There might be a need to incorporate these velocity changes in any characterization of both the seismicity and deformation within the region. However, it would be useful to discern if these velocity changes are seasonal by incorporating measurements taken over several years or by applying coda wave interferometry to the coda waves generated from ambient noise correlations [33, 89].

8.7 Acknowledgments

We are grateful for the financial support of the Department of Energy (DOE) through grant DE-EE0002758. The explosive signals used in this study were obtained from the broadband USArray stations via IRIS.

Table 8.1: Estimated model parameters using the inverse R relation.

Event period	a (%km)	R^2	$h \frac{\Delta v}{v}$ (%km)
Period 1 (06/04-06/26)			
E-W	1.208 ± 4.6796	-0.0359	0.2796 ± 1.0830
N-S	1.227 ± 4.0842	-0.0244	0.2840 ± 0.9452
U-D	1.069 ± 4.9240	-0.02897	0.2474 ± 1.1396
Period 2 (06/26-07/09)			
E-W	8.272 ± 0.6536	0.3448	1.9144 ± 0.1514
N-S	8.358 ± 0.8643	-0.0987	1.9343 ± 0.2001
U-D	8.450 ± 1.1125	-0.3393	1.9556 ± 0.2576
Period 3 (07/09-07/16)			
E-W	-3.382 ± 0.3990	0.2096	-0.7827 ± 0.0924
N-S	-3.502 ± 0.4276	-0.0120	-0.8105 ± 0.0990
U-D	-3.574 ± 0.5839	-0.2823	-0.8271 ± 0.1352
Period 4 (07/16-08/01)			
E-W	4.677 ± 0.3941	0.4538	1.0824 ± 0.0913
N-S	4.141 ± 0.4903	-0.3588	0.9584 ± 0.1135
U-D	4.382 ± 0.4513	0.2150	1.0141 ± 0.1045
Period 5 (08/01-08/06)			
E-W	-9.001 ± 0.6926	0.09855	-2.0831 ± 0.1605
N-S	-8.038 ± 0.5898	0.2633	-1.8602 ± 0.1366
U-D	-7.889 ± 0.8625	-0.0293	-1.8258 ± 0.1997
Period 6 (08/06-08/13)			
E-W	-0.2111 ± 7.7143	0.00313	-0.0489 ± 1.7853
N-S	-0.9408 ± 6.9643	-0.0524	-0.2177 ± 1.6117
U-D	-4.062 ± 33.2908	0.1378	-0.9401 ± 7.7045
Period 7 (08/13-08/27)			
E-W	4.003 ± 0.5133	-0.3547	0.9264 ± 0.1188
N-S	3.949 ± 0.6128	-1.569	0.9139 ± 0.1418
U-D	4.019 ± 0.4722	0.06362	0.9301 ± 0.1093
Period 8 (08/27-09/10)			
E-W	-5.143 ± 0.9411	0.118	-1.1902 ± 0.2178
N-S	-6.538 ± 0.9513	-0.0716	-1.5131 ± 0.2202
U-D	-6.328 ± 3.2270	-0.2798	-1.4645 ± 0.7469

Table 8.2: Goodness of fit between average relative velocity changes and groundwater (GWL) subsidence based on the R^2 value (Case 2).

Velocity Components / GWL stations	S1	S2	S3	S4	S5	S6	S7	S8	S9
E-W	-0.1866	0.0367	0.3931	0.4412	0.3179	0.1779	0.5178	0.4376	0.4798
N-S	-0.1858	0.1071	0.4697	0.4743	0.3641	0.2612	0.5366	0.5125	0.5274
U-D	-0.2493	0.0297	0.3706	0.6005	0.4117	0.2057	0.6658	0.6142	0.6357

Table 8.3: Goodness of fit between average relative velocity changes and seasonal variation of (detrended) GPS displacement based on the R^2 value (Case 2).

GPS Component / Velocity Components	E-W	N-S	U-D
All GPS stations			
E-W	0.6106	0.5228	0.4993
N-S	-0.1240	-0.1401	-0.1828
Basin and Range stations			
E-W	0.7842	0.7982	0.6354
N-S	-0.1424	-0.1545	-0.1952
Wasatch fault stations			
E-W	0.6335	0.5442	0.6267
N-S	0.1476	0.1912	0.0750
Snake River Plain stations			
E-W	0.2261	-0.0052	-0.1200
N-S	-0.1127	-0.1491	-0.0770

Table 8.4: Goodness of fit between relative velocity change and PGA based on the R^2 value (Case 2).

Velocity Components	Total PGA soil	Mean PGA soil
E-W	0.2186	-0.0208
N-S	0.3158	0.0504
U-D	0.2060	0.0472

CHAPTER 9

CONCLUSION AND FUTURE WORK

The goal of my thesis work was to study the capability of imaging weak time-lapse changes and to develop imaging tools to image these changes. The time-lapse changes I considered range from velocity changes within mechanical and geo-mechanical structures to changes in the scattering strength of a scattering medium. The studies in the dissertation also focus on weak changes in which multiply scattered waves tend to provide higher sensitivity than singly scattered waves. These weak changes include velocity changes within the earth or mechanical structures which might result from naturally occurring events, induced stress changes, or thermal forcings. The changes also can result from various types of wear and tear in buildings, roads, and machines due to aging of these structures or to induced external forcings. The major contribution of this work is a technique for characterizing and localizing weak changes within any scattering medium using multiply scattered waves. This contribution extends the usual focus of coda wave interferometry, which is to detect weak changes within scattering media without providing significant information on the location of the detected change.

I developed an inversion algorithm that simultaneously detects and images localized weak changes within a scattering medium. The imaged localized change suggests that the resolution depends on the coda lapse time where the imaging data is extracted and on the monitoring source and receiver setup. We have explored a few topics in regard to detecting and imaging changes within a scattering medium such as determining the impact of the shifts in the properties of the sources generating the repeating coda waves, localizing change within a statistical heterogeneous medium, and characterizing the sensitivity of acoustic and elastic scattered waves. There remain a number of unexplored issues regarding the monitoring of localized weak changes using time-lapse coda waves.

There is need to extensively investigate the control that the source and receiver setup has on the inversion process. In Chapter 5, we show the effect of data averaging, which increases with coda lapse time, on the imaging process. However, the spread of the estimated change from the scattered waves across the source-receiver pairs depends on the placement of the source-receiver pairs relative to the time-lapse change to be imaged. An effective source-receiver geometry for monitoring includes source-receivers pairs for whom the ballistic waves traverse the anomaly, as well as source-receiver pairs for which the scattered waves sample the anomaly. Determining an optimal monitoring source-receiver setup that images a localized change will require a priori information about the general location of the change (if present) and about the scattering property of the medium.

In Chapter 4, we demonstrate the computation of the elastic sensitivity kernel and explain the characteristics of the sensitivity to perturbations in the P- and S-wave velocities. There is a need to apply these sensitivity kernels to imaging P- and S-wave velocity changes in real data problems such as those in the laboratory imaging problems found in Chapter 6. Because of the time constraint, we will leave the imaging with elastic kernels to future studies.

The sensitivity kernel both for acoustic and elastic wave scattering uses the scattered intensity field rather than the scattered wavefield. Utilizing the scattering intensity field allows us to formulate the imaging problem when we know only the statistical properties of the scattering model, without the need to know the precise locations and characteristics of the microscopic scatterers within the scattering medium. The question for future studies is, can we reformulate the imaging problem to use the scattered wavefield for computing the sensitivity kernel without using a priori the microscopic properties of the individual scatterers present within the scattering medium?

The numerical computation of the sensitivity kernel is dependent on knowledge of the statistical properties of the scattering medium. For a statistically homogeneous scattering medium, the scattering properties of the medium can be estimated by fitting and describing the envelope of the scattered intensity recorded by the receivers. However, for a heteroge-

neously scattering medium, more elaborate techniques will be needed to estimate the a priori scattering model for the kernel computations. We can estimate the a priori scattering model by describing the envelope of the time lapse coda when a dense monitoring array is present or by using imaged models from other geophysical imaging techniques such as migration velocity analysis, full waveform inversion and well-log measurements. For a weak velocity change and an accurate a priori scattering model, the sensitivity kernel is computed once and can be reused for subsequent time-lapse monitoring of a given medium. The question for future studies becomes, What is the impact of an error in the a priori scattering model on the computed sensitivity kernel and, in general, on the imaging of localized changes?

REFERENCES CITED

- [1] Aki, K. and L. Chouet, 1975, Origin of coda waves: source, attenuation, and scattering effects: *J. Geophys. Res.*, **80**, 3322–3342.
- [2] Aki, K. and P. G. Richards, 2002, *Quantitative seismology*: University Science Books.
- [3] Akkermans, E. and G. Montambaux, 2007, *Mesoscopic physics of electrons and photons*: Cambridge University Press. Cambridge Books Online.
- [4] Arts, R., O. Eiken, A. Chadwick, P. Zweigel, L. Van der Meer, and B. Zinszner, 2004, Monitoring of CO₂ injected at Sleipner using time-lapse seismic data: *Energy*, **29**, 1383–1392.
- [5] Asano, Y., T. Saito, Y. Ito, K. Shiomi, H. Hirose, T. Matsumoto, S. Aoi, S. Hori, and S. Sekiguchi, 2011, Spatial distribution and focal mechanisms of aftershocks of the 2011 off the Pacific coast of Tohoku earthquake: *Earth, Planets and Space*, **63**, 669–673.
- [6] Ashland, X. and R. E. Giraud, 2005, Groundwater level fluctuations in Wasatch front landslides and adjacent slopes, Northern Utah: Utah Geological Survey Open-File Report, **448**, 22.
- [7] Aster, R. C., B. Borchers, and C. H. Thurber, 2013, *Parameter estimation and inverse problems*: Academic Press.
- [8] Belkebir, K., P. C. Chaumet, and A. Sentenac, 2006, Influence of multiple scattering on three-dimensional imaging with optical diffraction tomography: *Journal of the Optical Society of America A*, **23**, 586–595.
- [9] Berkhout, A. and D. Verschuur, 2006, Imaging of multiple reflections: *Geophysics*, **71**, SI209–SI220.
- [10] Berkhout, A., D. Verschuur, and G. Blacquire, 2012, Illumination properties and imaging promises of blended, multiple-scattering seismic data: a tutorial: *Geophysical Prospecting*, **60**, 713–732.
- [11] Bouchon, M., C. A. Schultz, and M. N. Toksz, 1996, Effect of three-dimensional topography on seismic motion: *Journal of Geophysical Research: Solid Earth*, **101**, 5835–5846.

- [12] Brenguier, F., M. Campillo, C. Hadziioannou, N. Shapiro, and E. Larose, 2008a, Post-seismic relaxation along the San Andreas Fault at Parkfield from continuous seismological observations: *Science*, **321**, 1478–1481.
- [13] Brenguier, F., N. M. Shapiro, M. Campillo, V. Ferrazzini, Z. Duputel, O. Coutant, and A. Nercessian, 2008b, Towards forecasting volcanic eruptions using seismic noise: *Nature Geoscience*, **1**, 126–130.
- [14] Busch, K., C. M. Soukoulis, and E. N. Economou, 1994, Transport and scattering mean free paths of classical waves: *Physical Review B*, **50**, 93–98.
- [15] Chen, J. H., B. Froment, Q. Y. Liu, and M. Campillo, 2010, Distribution of seismic wave speed changes associated with the 12 May 2008 Mw 7.9 Wenchuan earthquake: *Geophysical Research Letters*, **37**.
- [16] Cheng, X., F. Niu, and B. Wang, 2010, Coseismic velocity change in the rupture zone of the 2008 Mw 7.9 Wenchuan earthquake observed from ambient seismic noise: *Bulletin of the Seismological Society of America*, **100**, 2539–2550.
- [17] Chiou, B., R. Youngs, N. Abrahamson, and K. Addo, 2010, Ground-motion attenuation model for small-to-moderate shallow crustal earthquakes in California and its implications on regionalization of ground-motion prediction models: *Earthquake Spectra*, **26**, 907–926.
- [18] Colin Cameron, A. and F. A. Windmeijer, 1997, An R-squared measure of goodness of fit for some common nonlinear regression models: *Journal of Econometrics*, **77**, 329–342.
- [19] Compton, S. and D. Hale, 2013, Estimating v_p/v_s ratios using smooth dynamic image warping: *Center for Wave Phenomena, Report 765*, 211–222.
- [20] Cowan, M. L., I. P. Jones, J. H. Page, and D. A. Weitz, 2002, Diffusing acoustic wave spectroscopy: *Physical Review. E, Statistical, Nonlinear, and Soft Matter Physics*, **65**. PMID: 12188849.
- [21] Daley, T., L. Myer, J. Peterson, E. Majer, and G. Hoversten, 2008, Time-lapse crosswell seismic and VSP monitoring of injected CO₂ in a brine aquifer: *Environmental Geology*, **54**, 1657–1665.
- [22] Davis, T. L., M. J. Terrell, R. D. Benson, R. Cardona, R. R. Kendall, and R. Winarsky, 2003, Multicomponent seismic characterization and monitoring of the CO₂ flood at Weyburn field, Saskatchewan: *The Leading Edge*, **22**, 696–697.
- [23] Draper, N. R. and H. Smith, 1981, *Applied regression analysis*: Wiley.

- [24] Eaton, G. P., 1982, The Basin and Range Province: Origin and tectonic significance: *Annual Review of Earth and Planetary Sciences*, **10**, 409–440.
- [25] Fichtner, A., F. Bleibinhaus, and Y. Capdeville, 2011, Full seismic waveform modelling and inversion: Springer.
- [26] Fleury, C., 2013, Increasing illumination and sensitivity of reverse-time migration with internal multiples: *Geophysical Prospecting*, **61**, 891–906.
- [27] Foldy, L. L., 1945, The multiple scattering of waves. I. General theory of isotropic scattering by randomly distributed scatterers: *Physical Review*, **67**, 107–119.
- [28] Gaburro, R., C. J. Nolan, T. Dowling, and M. Cheney, 2007, Imaging from multiply scattered waves: *Society of Photo-Optical Instrumentation Engineers*, 304–311.
- [29] Gilbert, H. J. and A. F. Sheehan, 2004, Images of crustal variations in the intermountain west: *Journal of Geophysical Research: Solid Earth*, **109**, B03306.
- [30] Godano, M., T. Bardainne, M. Regnier, A. Deschamps, and M. Valette, 2012, Spatial and temporal evolution of a microseismic swarm induced by water injection in the Arkema-Vauvert salt field (southern France): *Geophysical Journal International*, **188**, 274–292.
- [31] Grêt, A., R. Snieder, and U. Özbay, 2006, Monitoring in situ stress changes in a mining environment with coda wave interferometry: *Geophysical Journal International*, **167**, 504–508.
- [32] Groenenboom, J., 1995, Attenuation, dispersion, and anisotropy by multiple scattering of transmitted waves through distributions of scatterers: *The Journal of the Acoustical Society of America*, **98**, 3482–3492.
- [33] Hadziioannou, C., E. Larose, O. Coutant, P. Roux, and M. Campillo, 2009, Stability of monitoring weak changes in multiply scattering media with ambient noise correlation: Laboratory experiments: *Journal of the Acoustical Society of America*, **125**, 3688–3695.
- [34] Hale, D., 2013, Dynamic warping of seismic images: *Geophysics*, **78**, S105–S115.
- [35] Hale, D. and S. Compton, 2013, Smooth dynamic warping: *Center for Wave Phenomena*, **Report 764**, 201–210.
- [36] Haney, M. M., K. van Wijk, and R. Snieder, 2005, Radiative transfer in layered media and its connection to the O’Doherty-Anstey formula: *Geophysics*, **70**, T1–T11.

- [37] Hennino, R., N. Trégourès, N. Shapiro, L. Margerin, M. Campillo, B. Van Tiggelen, and R. Weaver, 2001, Observation of equipartition of seismic waves: *Physical Review Letters*, **86**, 3447–3450.
- [38] Kanu, C. and R. Snieder, 2014, Numerical computation of the sensitivity kernel for time-lapse monitoring with multiply scattered waves: Center for Wave Phenomena, **Report 816**, 291–306.
- [39] Kanu, C. O., R. Snieder, and D. O’Connell, 2013, Estimation of velocity change using repeating earthquakes with different locations and focal mechanisms: *Journal of Geophysical Research: Solid Earth*, **118**, 2905–2914.
- [40] Keller, G. R., R. B. Smith, and L. W. Braile, 1975, Crustal structure along the Great Basin-Colorado Plateau Transition from seismic refraction studies: *Journal of Geophysical Research*, **80**, 1093–1098.
- [41] Khatiwada, M., K. van Wijk, L. Adam, M. Haney, et al., 2009, A numerical sensitivity analysis to monitor CO₂ sequestration in layered basalt with coda waves: 79th Ann. Internat. Mtg. Soc. Expl. Geophys. Expanded Abstracts, 3865–3869.
- [42] Lachenbruch, A. H. and J. H. Sass, 1977, Heat flow in the United States and the thermal regime of the crust, in the earth’s crust: *Geophys. Monogr. Ser.*, edited by J. G. Heacock et al., **20**, 626–675.
- [43] Landrø, M., 2001, Discrimination between pressure and fluid saturation changes from timelapse seismic data: *Geophysics*, **66**, 836–844.
- [44] Larose, E. and S. Hall, 2009, Monitoring stress related velocity variation in concrete with a 2×10^{-5} relative resolution using diffuse ultrasound: *The Journal of the Acoustical Society of America*, **125**, 1853–1856. PMID: 19354358.
- [45] Levander, A., R., 1990, Seismic scattering near the earth’s surface: *Pure and Applied Geophysics*, **132**, 21–47.
- [46] Li, Y. and D. W. Oldenburg, 2000, Joint inversion of surface and three-component borehole magnetic data: *Geophysics*, **65**, 540–552.
- [47] Lipman, P., J. Lockwood, R. Okamura, D. Swanson, and K. Yamashita, 1985, Ground deformation associated with the 1975 magnitude-7.2 earthquake and resulting changes in activity of Kilauea volcano, Hawaii: U.S. Geological Survey Professional Paper 1276, 45 pp.
- [48] Lumley, D. E., 2001, Timelapse seismic reservoir monitoring: *Geophysics*, **66**, 50–53.

- [49] Luo, Y. and G. T. Schuster, 1991, Wave equation travelttime inversion: *Geophysics*, **56**, 645–653.
- [50] Maeda, T., K. Obara, and Y. Yukutake, 2010, Seismic velocity decrease and recovery related to earthquake swarms in a geothermal area: *Earth Planets and Space*, **62**, 685–691.
- [51] Mainsant, G., E. Larose, C. Brönnimann, D. Jongmans, C. Michoud, and M. Jaboyedoff, 2012, Ambient seismic noise monitoring of a clay landslide: Toward failure prediction: *Journal of Geophysical Research: Earth Surface* (2003–2012), **117**, F01030.
- [52] Malcolm, A. E., B. Ursin, and M. V. De Hoop, 2009, Seismic imaging and illumination with internal multiples: *Geophysical Journal International*, **176**, 847–864.
- [53] Margerin, L., M. Campillo, and B. van Tiggelen, 1998, Radiative transfer and diffusion of waves in a layered medium: New insight into coda Q: *Geophysical Journal International*, **134**, 596–612.
- [54] Margerin, L. and H. Sato, 2011, Reconstruction of multiply-scattered arrivals from the cross-correlation of waves excited by random noise sources in a heterogeneous dissipative medium: *Wave Motion*, **48**, 146–160.
- [55] Masera, D., P. Bocca, and A. Grazzini, 2011, Frequency analysis of acoustic emission signal to monitor damage evolution in masonry structures: *Journal of Physics: Conference Series*, **305**, 012134.
- [56] Matsumoto, S., K. Obara, K. Yoshimoto, T. Saito, A. Ito, and A. Hasegawa, 2001, Temporal change in P-wave scatterer distribution associated with the Mw 6.1 earthquake near Iwate volcano, northeastern Japan: *Geophysical Journal International*, **145**, 48–58.
- [57] McGuire, J. J., J. A. Collins, P. Goudard, E. Roland, D. Lizarralde, M. S. Boettcher, M. D. Behn, and R. D. van der Hilst, 2012, Variations in earthquake rupture properties along the Gofar transform fault, East Pacific Rise: *Nature Geoscience*, **5**, 336–341.
- [58] Meier, U., S. N.M., and F. Brenguier, 2010, Detecting seasonal variations in seismic velocities within Los Angeles basin from correlations of ambient seismic noise: *Geophys. J. Int.*, **181**, 985–996.
- [59] Miyazawa, M., A. Venkataraman, R. Snieder, and M. A. Payne, 2007, Analysis of microearthquake data at Cold Lake and its applications to reservoir monitoring: *SEG Technical Program Expanded Abstracts*, **26**, 1266–1270.
- [60] Montgomery, D. R. and M. Manga, 2003, Streamflow and water well responses to earthquakes: *Science* (New York, N.Y.), **300**, 2047–2049. PMID: 12829774.

- [61] Muñoz, A. and D. Hale, 2014, Automatic simultaneous multiple-well ties: Center for Wave Phenomena, **Report 788**, 41 pp.
- [62] Nakata, N. and R. Snieder, 2012, Estimating near-surface shear wave velocities in Japan by applying seismic interferometry to KiK-net data: *Journal of Geophysical Research: Solid Earth*, **117**, B01308.
- [63] Naus, D. J., 2006, The effect of elevated temperature on concrete materials and structures—a literature review: Technical report, Oak Ridge National Laboratory (United States). Funding organisation: ORNL work for others (United States).
- [64] Nishimura, T., N. Uchida, H. Sato, M. Ohtake, S. Tanaka, and H. Hamaguchi, 2000, Temporal changes of the crustal structure associated with the M6.1 earthquake on September 3, 1998, and the volcanic activity of Mount Iwate, Japan: *Geophysical Research Letters*, **27**, 269–272.
- [65] Niu, F., P. Silver, R. Nadeau, and T. McEvelly, 2003, Migration of seismic scatterers associated with the 1993 Parkfield aseismic transient event: *Nature*, **426**, 544–548.
- [66] Nolet, G., 1987, *Seismic tomography: With applications in global seismology and exploration geophysics*: Springer.
- [67] Obermann, A., T. Planès, E. Larose, C. Sens-Schönfelder, and M. Campillo, 2013, Depth sensitivity of seismic coda waves to velocity perturbations in an elastic heterogeneous medium: *Geophysical Journal International*, **194**, 372–382.
- [68] Oldenborger, G. A. and P. S. Routh, 2009, The point-spread function measure of resolution for the 3-D electrical resistivity experiment: *Geophysical Journal International*, **176**, 405–414.
- [69] Paasschens, J. C. J., 1997, Solution of the time-dependent Boltzmann equation: *Physical Review E*, **56**, 1135–1141.
- [70] Pacheco, C. and R. Snieder, 2005, Time-lapse travel time change of multiply scattered acoustic waves: *The Journal of the Acoustical Society of America*, **118**, 1300–1310.
- [71] ———, 2006, Time-lapse traveltime change of singly scattered acoustic waves: *Geophysical Journal International*, **165**, 485–500.
- [72] Page, J. H., H. P. Schriemer, A. E. Bailey, and D. A. Weitz, 1995, Experimental test of the diffusion approximation for multiply scattered sound: *Physical Review E*, **52**, 3106–3114.

- [73] Pankow, K. L., 2012, Instrumentally recorded ground motions in the Utah region since 2000: Selected topics in engineering and environmental geology in Utah: Utah Geological Association Publication, **41**, 1–8.
- [74] Pine, D. J., D. A. Weitz, P. M. Chaikin, and E. Herbolzheimer, 1988, Diffusing wave spectroscopy: *Physical Review Letters*, **60**, 1134–1137.
- [75] Planès, T., E. Larose, L. Margerin, V. Rossetto, and C. Sens-Schönfelder, 2014, Decorrelation and phase-shift of coda waves induced by local changes: multiple scattering approach and numerical validation: *Waves in Random and Complex Media*, 1–27, doi:10.1080/17455030.2014.880821.
- [76] Poupinet, G., W. L. Ellsworth, and J. Frechet, 1984, Monitoring velocity variations in the crust using earthquake doublets: An application to the Calaveras fault, California: *Journal of Geophysical Research*, **89**, 5719–5731.
- [77] Puskas, C. M., R. B. Smith, C. M. Meertens, and W. L. Chang, 2007, Crustal deformation of the Yellowstone-Snake river plain volcano-tectonic system: Campaign and continuous GPS observations, 1987-2004: *Journal of Geophysical Research: Solid Earth*, **112**, B03401.
- [78] Ripoll, J., M. Nieto-Vesperinas, and S. R. Arridge, 2001, Effect of roughness in nondiffusive regions within diffusive media: *Optical Society of America OCIS*, **18**, 940–947.
- [79] Robinson, D. J., M. Sambridge, and R. Snieder, 2011, A probabilistic approach for estimating the separation between a pair of earthquakes directly from their coda waves: *Journal of Geophysical Research*, **116**, B04309.
- [80] Robinson, D. J., R. Snieder, and M. Sambridge, 2007, Using coda wave interferometry for estimating the variation in source mechanism between double couple events: *Journal of Geophysical Research*, **112**, B12302.
- [81] Rossetto, V., 2013, Local time in diffusive media and applications to imaging: *Physical Review E*, **88**. arXiv:1307.4867.
- [82] Rossetto, V., L. Margerin, T. Planès, and E. Larose, 2011, Locating a weak change using diffuse waves: Theoretical approach and inversion procedure: *Journal of Applied Physics*, **109**, 903–911.
- [83] Roten, D., K. B. Olsen, J. C. Pechmann, V. M. Cruz-Atienza, and H. Magistrale, 2011, 3D simulations of M 7 earthquakes on the Wasatch fault, Utah, Part I: Long-Period (0-1 Hz) ground motion: *Bulletin of the Seismological Society of America*, **101**, 2045–2063.

- [84] Ryzhik, L., G. Papanicolaou, and J. B. Keller, 1996, Transport equations for elastic and other waves in random media: *Wave motion*, **24**, 327–370.
- [85] Sasaki, S. and H. Kaieda, 2002, Determination of stress state from focal mechanisms of microseismic events induced during hydraulic injection at the Hijiori hot dry rock site: *Pure and Applied Geophysics*, **159**, 489–516.
- [86] Sato, H., M. C. Fehler, and T. Maeda, 2012, *Seismic wave propagation and scattering in the heterogeneous earth: Second edition*: Springer.
- [87] Schaff, D. P. and G. C. Beroza, 2004, Coseismic and postseismic velocity changes measured by repeating earthquakes: *Journal of Geophysical Research: Solid Earth*, **109**, B10302.
- [88] Sens-Schönfelder, C. and U. Wegler, 2006, Passive image interferometry and seasonal variations at Merapi volcano, Indonesia: *Geophys. Res. Lett.*, **33**, L21302, doi:10.1029/2006GL027797.
- [89] ———, 2011, Passive image interferometry for monitoring crustal changes with ambient seismic noise: *Comptes Rendus Geoscience*, **343**, 639–651.
- [90] Shang, X. and L. Huang, 2012, Optimal designs of time-lapse seismic surveys for monitoring CO₂ leakage through fault zones: *International Journal of Greenhouse Gas Control*, **10**, 419–433.
- [91] Shapiro, N., M. Campillo, L. Margerin, S. Singh, V. Kostoglodov, and J. Pacheco, 2000, The energy partitioning and the diffusive character of the seismic coda: *Bulletin of the Seismological Society of America*, **90**, 655–665.
- [92] Shapiro, S. A. and G. Kneib, 1993, Seismic attenuation by scattering: Theory and numerical results: *Geophysical Journal International*, **114**, 373–391.
- [93] Shearer, P., M. and S. Earle, P., 2008, Observing and modeling elastic scattering in the deep earth: *Advances in Geophysics*, **50**, 167–194.
- [94] Silver, P. G., T. M. Daley, F. Niu, and E. L. Majer, 2007, Active source monitoring of cross-well seismic travel time for stress-induced changes: *Bulletin of the Seismological Society of America*, **97**, 281–293.
- [95] Smith, R. B. and W. J. Arabasz, 1991, Seismicity of the Intermountain Seismic Belt: Neotectonics of North America, *Geological Society of America, Decade Map*, **1**, 185–228.
- [96] Snieder, R., 2006, The theory of coda wave interferometry: *Pure and Applied Geophysics*, **163**, 455–473.

- [97] Snieder, R., A. Grêt, H. Douma, and J. Scales, 2002, Coda wave interferometry for estimating nonlinear behavior in seismic velocity: *Science*, **295**, 2253–2255.
- [98] Snieder, R. and J. Page, 2007, Multiple scattering in evolving media: *Physics Today*, **60** (5), 49–55.
- [99] Snieder, R. and M. Vrijlandt, 2005, Constraining the source separation with coda wave interferometry: Theory and application to earthquake doublets in the Hayward fault, California: *Journal of Geophysical Research*, **110**, B04301.
- [100] Spane, F. A., 2002, Considering barometric pressure in groundwater flow investigations: *Water Resources Research*, **38**, 1–18.
- [101] Spetzler, J., C. Sivaji, O. Nishizawa, and Y. Fukushima, 2002, A test of ray theory and scattering theory based on a laboratory experiment using ultrasonic waves and numerical simulation by finite-difference method: *Geophysical Journal International*, **148**, 165–178.
- [102] Stump, B., R. Burlacu, C. Hayward, K. Pankow, S. Nava, J. Bonner, S. Hock, D. Whiteman, A. Fisher, T. S. Kim, R. Kubacki, M. Leidig, J. Britton, D. Drobeck, P. O'Neill, K. Jensen, K. Whipp, G. Johnson, P. Roberson, R. Read, R. Brogan, and S. Masters, 2007, Seismic and Infrasonic energy generation and propagation at local and regional distances: Phase I-Divine Strake Experiment: Air Force Research Laboratory report, **AFRL-RV-HA-TR-2007-1188**.
- [103] Taillandier, C., M. Noble, H. Chauris, and H. Calandra, 2009, First-arrival traveltimes tomography based on the adjoint-state method: *Geophysics*, **74**, WCB1–WCB10.
- [104] Tsai, V. C., 2011, A model for seasonal changes in GPS positions and seismic wave speeds due to thermoelastic and hydrologic variations: *Journal of Geophysical Research: Solid Earth*, **116**, B04404.
- [105] Turner, J. A. and R. L. Weaver, 1994, Radiative transfer and multiple scattering of diffuse ultrasound in polycrystalline media: *The Journal of the Acoustical Society of America*, **96**, 3675–3683.
- [106] Van Leeuwen, T. and W. A. Mulder, 2010, A correlation-based misfit criterion for wave-equation traveltimes tomography: *Geophysical Journal International*, **182**, 1383–1394.
- [107] Vesnaver, A. L., F. Accaino, G. Bohm, G. Madrussani, J. Pajchel, G. Rossi, and G. D. Moro, 2003, Time-lapse tomography: *Geophysics*, **68**, 815–823.
- [108] Vlastos, S., E. Liu, I. G. Main, M. Schoenberg, C. Narteau, X. Y. Li, and B. Maillot, 2006, Dual simulations of fluid flow and seismic wave propagation in a fractured network: Effects of pore pressure on seismic signature: *Geophysical Journal International*, **166**, 825–838.

- [109] Weaver, R., 1982, On diffuse waves in solid media: *J. Acoust. Soc. Am.*, **71**, 1608–1609.
- [110] Weaver, R. L., C. Hadziioannou, E. Larose, and M. Campillo, 2011, On the precision of noise correlation interferometry: *Geophysical Journal International*, **185**, 1384–1392.
- [111] Wegler, U. and C. Sens-Schönfelder, 2007, Fault zone monitoring with passive image interferometry: *Geophysical Journal International*, **168**, 1029–1033.
- [112] Wesley, J. P., 1965, Diffusion of seismic energy in the near range: *Journal of Geophysical Research*, **70**, 5099–5106.
- [113] Yodh, A. and B. Chance, 1995, Spectroscopy and imaging with diffusing light: *Physics Today*, **48 (3)**, 34–41.
- [114] Yoshimoto, K. and H. Sato, 1997, Short-wavelength crustal heterogeneities in the Nikko area, Central Japan, revealed from the three-component seismogram envelope analysis: *Physics of The Earth and Planetary Interiors*, **104**, 63–73.
- [115] Young, J. F., S. Mindess, and D. Darwin, 2002, *Concrete*: Prentice Hall.
- [116] Zoback, M. and J. Zinke, 2002, Production-induced normal faulting in the Valhall and Ekofisk oil fields: *Pure and Applied Geophysics*, **159**, 403–420.
- [117] Zoback, M. D. and H.-P. Harjes, 1997, Injection-induced earthquakes and crustal stress at 9 km depth at the KTB deep drilling site, Germany: *Journal of Geophysical Research*, **102**, 18477–18491.

APPENDIX A - THE TIME PERTURBATION DUE TO A PERTURBED SOURCE

From Figure 2.1, the traveltime t_T for the signal along path T from the unperturbed source to the first scatterer along path T is given by

$$t_T = \frac{L_T}{V_o}, \quad (\text{A.1})$$

where V_o is the unperturbed medium velocity. The traveltime $t_{T'}$ for the signal along path T' from the perturbed source to the same first scatterer is given by

$$t_{T'} = \frac{L_{T'}}{V}. \quad (\text{A.2})$$

We assume that the signals from both sources after scattering by the first scatterer travel along the same path (Figure 1). We define $L_T = L_{T'} + \delta L$ and $V = V_o + \delta V$, where $\delta L = -(\hat{\mathbf{r}}_T \cdot \mathbf{D})$, with \mathbf{D} the perturbation of the source location and $\hat{\mathbf{r}}_T$ the take-off direction from the first source to the scatterer. The takeoff direction from the source $\hat{\mathbf{r}}_T$ in spherical coordinates is

$$\hat{\mathbf{r}}_T = \begin{pmatrix} \cos \psi \sin \theta \\ \sin \psi \sin \theta \\ \cos \theta \end{pmatrix}, \quad (\text{A.3})$$

where θ and ψ are colatitude and longitude in spherical coordinates, respectively. The traveltime for the signal along path T from the second source to the first scatterer can be re-expressed as

$$t_{T'} = \frac{L_{T'}}{V_o + \delta V} \quad (\text{A.4})$$

$$\simeq \left(\frac{1}{V_o} - \frac{\delta V}{V_o^2} + \dots \right) L_T - \left(\frac{1}{V_o} - \frac{\delta V}{V_o^2} + \dots \right) \cdot (\hat{\mathbf{r}}_T \cdot \mathbf{D}). \quad (\text{A.5})$$

Ignoring the terms of second order or higher in the velocity change and source displacement, equation A.5 gives,

$$t_{T'} \simeq \frac{L_T}{V_o} - \left(\frac{\delta V}{V_o} \right) \left(\frac{L_T}{V_o} \right) - \frac{(\hat{\mathbf{r}}_T \cdot \mathbf{D})}{V_o}, \quad (\text{A.6})$$

$$= t_T + t_{pv} + t_{pl}. \quad (\text{A.7})$$

Therefore, the time perturbation along path T' is given as

$$t_p^{T'} = t_{T'} - t_T = t_{pv} + t_{pl}, \quad (\text{A.8})$$

where t_{pv} = time shift due to velocity change and t_{pl} = time shift due to shift in source.

We need to derive the expression for $\langle t_p \rangle$. With equation 2.6 and equation A.8, the average time perturbation is given,

$$\begin{aligned} \langle t_p \rangle &= \frac{\sum_T A_T^2 t_p^{T'}}{\sum_T A_T^2} = \frac{-\sum_T A_T^2 \left(\left(\frac{\delta V}{V_o} \right) \left(\frac{L_T}{V_o} \right) + \left(\frac{\hat{\mathbf{r}}_T \cdot \mathbf{D}}{V_o} \right) \right)}{\sum_T A_T^2}, \\ &= \left\langle \frac{\delta V}{V_o} \right\rangle \frac{\int_T L_T / V_o \, d\Omega}{\int_T d\Omega} + \frac{\int_T (\hat{\mathbf{r}}_T \cdot \mathbf{D}) / V_o \, d\Omega}{\int_T d\Omega}, \end{aligned} \quad (\text{A.9})$$

where $\int_T \dots d\Omega$ denotes an integration over all take-off angles. In 3D, the integration limits of $d\theta$ and $d\psi$ are $[0, \pi]$ and $[0, 2\pi]$, respectively. Since $\int_T \hat{\mathbf{r}}_T \, d\Omega = 0$ and $\int_T (L_T / V_o) \, d\Omega / \int_T d\Omega = t$, where t is the traveltime of the scattered ray from the source to the receiver along path T , equation A.9 reduces to

$$\langle t_p \rangle = - \left\langle \frac{\delta V}{V_o} \right\rangle t. \quad (\text{A.10})$$

Hence to first order in D , the average traveltime perturbation depends only on the velocity changes within the explored medium.

APPENDIX B - VARIANCE OF THE TIME PERTURBATION

The variance of the travel time perturbation, using equation 2.6, is given by

$$\sigma_t^2 = \frac{\sum_T A_T^2 (t_p - \langle t_p \rangle)^2}{\sum_T A_T^2} = \langle t_p^2 \rangle - \langle t_p \rangle^2. \quad (\text{B.1})$$

where using equation A.7 $\langle t_p^2 \rangle$ is given by

$$\langle t_p^2 \rangle = \frac{\sum_T A_T^2 \left(-\left(\frac{\delta V}{V_o}\right) \left(\frac{L_T}{V_o}\right) - \frac{\hat{\mathbf{r}}_T \cdot \mathbf{D}}{V_o} \right)^2}{\sum_T A_T^2}. \quad (\text{B.2})$$

Expanding equation B.2 gives

$$\begin{aligned} \langle t_p^2 \rangle &= \sum_T A_T^2 \left(\left(\frac{\delta V}{V_o}\right)^2 \left(\frac{L_T}{V_o}\right)^2 + \left(\frac{\hat{\mathbf{r}}_T \cdot \mathbf{D}}{V_o}\right)^2 \right. \\ &\quad \left. + 2 \left(\frac{\delta V}{V_o}\right) \left(\frac{L_T}{V_o}\right) \left(\frac{\hat{\mathbf{r}}_T \cdot \mathbf{D}}{V_o}\right) \right) / \sum_T A_T^2. \end{aligned} \quad (\text{B.3})$$

In equation B.3,

$$\frac{\int_T (\hat{\mathbf{r}}_T \cdot \mathbf{D})^2 d\Omega}{\int_T d\Omega} = \frac{D^2}{C}, \quad (\text{B.4})$$

where $C = 1, 2, \text{ or } 3$ equals the dimension of the problem and

$$\frac{\int_T \hat{\mathbf{r}}_T \cdot \mathbf{D} d\Omega}{\int_T d\Omega} = 0, \quad (\text{B.5})$$

. Therefore, in 3D,

$$\langle t_p^2 \rangle = \left\langle \frac{\delta V}{V_o} \right\rangle^2 t^2 + \frac{D^2}{3V_o^2}, \quad (\text{B.6})$$

Combining equations B.6 and A.10, the total variance of the time perturbation is

$$\sigma_t^2 = \frac{D^2}{3V_o^2}. \quad (\text{B.7})$$

In the absence of additive noise, the variance of the travelttime perturbation thus depends only on the shift in the source location. With the estimate of the subsurface velocity, we can estimate the shift in the source location from equation B.7.

APPENDIX C - ERROR ESTIMATION

We estimate the error associated with the estimated relative velocity change using the data residuals from the L_2 norm. Using equation 2.7 and a Taylor series expansion of $\hat{U}(t+t_p)$ with respect to t in terms of $U(t)$,

$$\hat{U}(t+t_p) = \hat{U}(t-\epsilon t) \simeq U(t) - \epsilon t \frac{dU(t)}{dt}, \quad (\text{C.1})$$

where $\epsilon = \left\langle \frac{\delta V}{V_0} \right\rangle$. Here, we assume that ϵ is constant across the signal. Including additive errors $\delta U(t)$ in the data with standard deviation σ_U , equation C.1 gives

$$\hat{U}(t-\epsilon t) + \delta U(t) \simeq U(t) - (\epsilon + \delta\epsilon)t \frac{dU}{dt}, \quad (\text{C.2})$$

where $\delta\epsilon$ is the error of the relative velocity change due to the error in the data $\hat{U}(t+t_p)$. The relationship between the data error and the error in the relative velocity change, then gives

$$\sigma_U \simeq \sigma_{\delta v} t \frac{dU}{dt} \quad (\text{C.3})$$

where $\sigma_{\delta v}$ is the standard deviation of the error in the relative velocity change. Therefore, the error in the relative velocity change between the perturbed and unperturbed signals is

$$\sigma_{\delta v} = \|\hat{\epsilon} - \epsilon\|_2 \leq \frac{\sigma_U}{\|M\|_2}, \quad (\text{C.4})$$

where $\hat{\epsilon}$ and ϵ are the estimated and the exact relative velocity changes, respectively, and $\|M\|_2$ is $2\pi f_d t \|U\|_2$, with f_d the dominant frequency of the signal. Therefore, the error in the estimated relative velocity change $\sigma_{\delta v}$ is

$$\sigma_{\delta v} \leq \frac{\sigma_U}{\|U\|_2 2\pi f_d t}. \quad (\text{C.5})$$

In practice, t is the centertime of the used time window, $\|U\|_2$ is the amplitude of the data.

The error equation (equation C.5) depends on the dominant frequency of the signal, the length of the signals, and the amplitude difference between the signals $\hat{U}(t)$ and $U(t)$ which

is normalized by the amplitude of $U(t)$. The error in the data σ_U is due to any dissimilarity between the two signals $\hat{U}(t)$ and $U(t)$ resulting from either shift in the source location or the presence of additive noise.

APPENDIX D - COMPARATIVE TIME SHIFT BETWEEN CHANGES IN VELOCITY
AND SOURCE LOCATION

In this subsection, we compare phase shifts due to the shift in the source location to the phase shifts resulting from velocity change within the subsurface. If the phase of the wave that travels over a distance r from a source to a scatterer is $\exp(i\mathbf{k} \cdot \mathbf{r}_T)$, the phase change due to shift in the source location along path T is

$$\exp(-ik(\hat{\mathbf{r}}_T \cdot \mathbf{D})) = \exp(-ikD \cos \theta_T), \quad (\text{D.1})$$

where θ_T is the angle between the take-off ray of path T and the shift in the source location D , and $k = 2\pi/\lambda$. For $D/\lambda < 1$, we can approximate equation D.1 as

$$\exp(-ikD \cos \theta_T) \simeq 1 - ikD \cos \theta_T - \frac{1}{2}(kD \cos \theta_T)^2. \quad (\text{D.2})$$

The average value of the phase changes due to the shift in the source location is

$$\langle \exp(-ikD \cos \theta_T) \rangle \simeq 1 - ikD \langle \cos \theta_T \rangle - \frac{1}{2}(kD)^2 \langle \cos^2 \theta_T \rangle \quad (\text{D.3})$$

assuming we sum over all angles $\langle \cos \theta_T \rangle = 0$. For equal contribution from all take-off angles in 2D (the numerical simulations in subsection 2.4 are in 2D), $\langle \cos^2 \theta_T \rangle = \frac{1}{2}$. Therefore,

$$\langle \exp(-ikD \cos \theta_T) \rangle \simeq 1 - \frac{1}{4}k^2 D^2. \quad (\text{D.4})$$

Also, if the phase of the wave that travels over a time t is $\exp(-i\omega t)$, the phase change due to the change in the medium velocity is

$$\exp(-i\omega \Delta t) \simeq 1 - i\omega \Delta t - \frac{1}{2}(\omega \Delta t)^2, \quad (\text{D.5})$$

where Δt is the time shift due to velocity change. The second order terms contribute to the variance of the phase change. Therefore, for an accurate estimation of the velocity change,

$$\frac{1}{4}k^2 D^2 < \frac{1}{2}\omega^2 \Delta t^2. \quad (\text{D.6})$$

Equation D.6 implies that

$$\frac{D}{\lambda} < \sqrt{2}f|\Delta t|. \quad (\text{D.7})$$

But the average value of time shift due to velocity change $\langle \Delta t \rangle$ is

$$\langle \Delta t \rangle = -\left\langle \frac{\delta V}{V_o} \right\rangle t. \quad (\text{D.8})$$

Therefore, equation D.7 reduces to

$$\frac{D}{\lambda} < \sqrt{2}f \left| \left\langle \frac{\delta V}{V_o} \right\rangle \right| t. \quad (\text{D.9})$$

Equation D.9 shows that for an accurate estimation of relative velocity changes, the shift in the source location D has to satisfy equation D.9. For practical purposes, λ and f can be defined as the dominant wavelength and frequency of the processed signal, respectively. Also, t can be assigned as the centertime of the used time window.

APPENDIX E - ANALYTICAL APPROXIMATION OF THE MODEL OF PACHECO
AND SNIEDER [70]

The timeshift $\langle \tau(t) \rangle$ extracted from repeating coda (assuming the diffusion model) can be related to the localized velocity changes by the model of Pacheco and Snieder [70] as

$$-\frac{\langle \tau(t) \rangle}{t} = \langle \epsilon(t) \rangle = \int_V \frac{K(\mathbf{s}, \mathbf{x}_o, \mathbf{r}, t)}{t} \frac{\Delta v}{v}(\mathbf{x}_o) dV, \quad (\text{E.1})$$

where V in the integration volume and \mathbf{s} , \mathbf{x}_o , and \mathbf{r} are the source, arbitrary, and receiver locations, respectively. The sensitivity kernel $K(\mathbf{s}, \mathbf{x}_o, \mathbf{r}, t)$ is

$$K(\mathbf{s}, \mathbf{x}_o, \mathbf{r}, t) = \frac{\int_0^t P(\mathbf{s}, \mathbf{x}_o, t') P(\mathbf{x}_o, \mathbf{r}, t - t') dt'}{P(\mathbf{s}, \mathbf{r}, t)}, \quad (\text{E.2})$$

and $P(\mathbf{x}_1, \mathbf{x}_2, t)$ is the normalized intensity recorded at a receiver location x_2 due to a source at x_1 . Using the diffusion approximation for the normalized intensity in a 3D semi-infinite inhomogenous medium with a full reflecting surface boundary and where the source and receivers are located on the boundary, the normalized intensity is [82]

$$P(R, t) = \frac{2}{(4\pi Dt)^{3/2}} \exp\left(-\frac{R_{sr}^2}{4Dt}\right). \quad (\text{E.3})$$

Then the sensitivity kernel $K(\mathbf{s}, \mathbf{x}_o, \mathbf{r}, t)$ in a 3D medium with a full reflecting surface boundary is given by [82]

$$K(\mathbf{s}, \mathbf{x}_o, \mathbf{r}, t) = \frac{1}{2\pi D} \exp\left(\frac{R_{sr}^2 - (r + s)^2}{4Dt}\right) \left(\frac{1}{s} + \frac{1}{r}\right), \quad (\text{E.4})$$

where R_{sr} is the source-receiver distance, and r and s are distances from the receiver and source to \mathbf{x}_o , respectively. Therefore from equation E.1,

$$-\frac{\langle \tau(t) \rangle}{\langle t \rangle} = \langle \epsilon(t) \rangle = \int_x \int_y \int_0^h \frac{1}{2\pi D \langle t \rangle} \exp\left(\frac{R_{sr}^2 - (r + s)^2}{4D \langle t \rangle}\right) \left(\frac{1}{s} + \frac{1}{r}\right) \frac{\Delta v}{v}(\mathbf{x}_o) dz dy dx. \quad (\text{E.5})$$

Assuming $h/R_{sr} \ll 1$ and that the relative velocity change is constrained to the near surface slab such that $\Delta v/v(\mathbf{x}_o) = \Delta v/v$, then

$$-\frac{\langle \tau(t) \rangle}{\langle t \rangle} = \langle \epsilon(t) \rangle \simeq h \frac{\Delta v}{v} \int_x \int_y \frac{1}{2\pi D \langle t \rangle} \exp\left(\frac{R_{sr}^2 - (r+s)^2}{4D \langle t \rangle}\right) \left(\frac{1}{s} + \frac{1}{r}\right) dy dx. \quad (\text{E.6})$$

The travel time $\langle t \rangle$ associated with the estimated average velocity $\langle \epsilon(t) \rangle$ is [96]

$$\langle t \rangle = \frac{\int_{t'} w(t) t dt'}{\int_{t'} w(t) dt'}, \quad (\text{E.7})$$

where $w(t)$ is the intensity of the scattered waves. Because the intensity is higher in the early part of the coda rather than in the later, the weighted average time $\langle t \rangle$ lies close to the peak of the intensity. At the intensity peak,

$$\frac{\partial P(R_{sr}, t)}{\partial t} = 0. \quad (\text{E.8})$$

Based on equation E.3, $R_{sr}^2/6D \langle t \rangle = 1$.

In order to define equation E.6 with the major contributing variables, we express the variables as dimensionless quantities, let $x' = x/\sqrt{6D \langle t \rangle}$, $y' = y/\sqrt{6D \langle t \rangle}$, $R'_{sr} = R_{sr}/\sqrt{6D \langle t \rangle} = 1$, $r' = r/\sqrt{6D \langle t \rangle}$, and $s' = s/\sqrt{6D \langle t \rangle}$. Then,

$$-\frac{\langle \tau(t) \rangle}{\langle t \rangle} = \langle \epsilon(t) \rangle \simeq \frac{h \Delta v}{\pi v} \sqrt{\frac{3}{2D \langle t \rangle}} \int_{x'} \int_{y'} \exp\left(\frac{3}{2} (1 - (r' + s')^2)\right) \left(\frac{1}{s'} + \frac{1}{r'}\right) dy' dx'. \quad (\text{E.9})$$

Using $R_{sr}^2/6D \langle t \rangle = 1$, equation E.9 gives

$$-\frac{\langle \tau(t) \rangle}{\langle t \rangle} = \langle \epsilon(t) \rangle \simeq \frac{3}{\pi} \frac{h \Delta v}{R_{sr} v} \int_{x'} \int_{y'} \exp\left(\frac{3}{2} (1 - (r' + s')^2)\right) \left(\frac{1}{s'} + \frac{1}{r'}\right) dy' dx'. \quad (\text{E.10})$$

Let

$$\frac{3}{\pi} \int_{x'} \int_{y'} \exp\left(\frac{3}{2} (1 - (r' + s')^2)\right) \left(\frac{1}{s'} + \frac{1}{r'}\right) dy' dx' = \Sigma, \quad (\text{E.11})$$

then

$$-\frac{\langle \tau(t) \rangle}{\langle t \rangle} = \langle \epsilon(t) \rangle \simeq \frac{h \Delta v}{R_{sr} v} \Sigma. \quad (\text{E.12})$$

Equation E.12 allows for a parametric description of the estimated velocity change $\langle \epsilon(t) \rangle$ in terms of the model parameters h , $\Delta v/v$, and R_{sr} . Σ is a constant dimensionless parameter and the numerical solution for our study is equal to 4.32 ± 0.02 . The error in Σ is a numerical error.